Multiphase Galactic Outflows: Physical Properties and Feedback Effects

Andrin Fluetsch

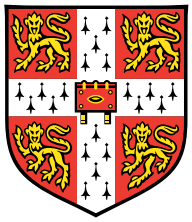

University of Cambridge,
Hughes Hall College,
Cavendish Laboratory Astrophysics Group
& Kavli Institute for Cosmology

This thesis is submitted for the degree of Doctor of Philosophy
July 2020

Declaration

This thesis is the result of my own work and includes nothing which is the outcome of work done in collaboration except as declared in the Preface and specified in the text. It is not substantially the same as any that I have submitted, or, is being concurrently submitted for a degree or diploma or other qualification at the University of Cambridge or any other University or similar institution except as declared in the Preface and specified in the text. I further state that no substantial part of my thesis has already been submitted, or, is being concurrently submitted for any such degree, diploma or other qualification at the University of Cambridge or any other University or similar institution except as declared in the Preface and specified in the text. It does not exceed the prescribed word limit for the relevant Degree Committee.

This thesis is based on material that has been submitted/published in:

- *Cold molecular outflows in the local Universe and their feedback effect on galaxies*, A. Fluetsch, R. Maiolino, S. Carniani, A. Marconi, C. Cicone, M. A. Bourne, T. Costa, A. C. Fabian, W. Ishibashi, G. Venturi, 2019, MNRAS, 483, 4586.
- *Properties of the Multiphase Outflows in Local (Ultra)luminous Infrared Galaxies*, A. Fluetsch, R. Maiolino, S. Carniani, S. Arribas, F. Belfiore, E. Bellocchi, S. Cazzoli, C. Cicone, G. Cresci, A. C. Fabian, R. Gallagher, W. Ishibashi, F. Mannucci, A. Marconi, M. Perna, E. Sturm, G. Venturi, arXiv: 2006.13232.

The work in these articles was conducted in collaboration with the listed co-authors.

In addition, the author has also been involved in the following papers during the course of his PhD:

- *The final data release of ALLSMOG: a survey of CO in typical local low-$M_\star$ star-forming galaxies*, Cicone, C.; Bothwell, M.; Wagg, J.; Møller, P.; De Breuck, C.; Zhang, Z.; Martín, S.; Maiolino, R.; Severgnini, P.; Aravena, M.; Belfiore, F.; Espada, D.; Fluetsch, A.; Impellizzeri, V.; Peng, Y.; Raj, M. A.; Ramírez-Olivencia, N.; Riechers, D.; Schawinski, K., 2017, A&A, 604, 45
- *AGN outflows and feedback twenty years on*, Harrison, C. M.; Costa, T.; Tadhunter, C. N.; Fluetsch, A.; Kakkad, D.; Perna, M.; Vietri, G., 2018, Nature Astronomy, 2, 198

- *Widespread QSO-driven outflows in the early Universe*, Bischetti, M.; Maiolino, R.; Carniani, S.; Fiore, F.; Piconcelli, E.; Fluetsch, A., 2019, A&A, 630, 19
- *Molecular outflows in local galaxies: Method comparison and a role of intermittent AGN driving*, Lutz, D.; Sturm, E.; Janssen, A.; Veilleux, S.; Aalto, S.; Cicone, C.; Contursi, A.; Davies, R. I.; Feruglio, C.; Fischer, J.; Fluetsch, A.; Garcia-Burillo, S.; Genzel, R.; González-Alfonso, E.; Graciá-Carpio, J.; Herrera-Camus, R.; Maiolino, R.; Schruba, A.; Shimizu, T.; Sternberg, A. Tacconi, L. J.; Weiß, A., 2019, A&A, 633, 35

Summary

Multiphase Galactic Outflows: Physical Properties and Feedback Effects

Andrin Fluetsch

Feedback mechanisms are invoked in theoretical models and cosmological simulations to regulate or even suppress star formation in galaxies. One feedback route is through galactic outflows, which eject large amounts of gas and thereby remove the fuel for future star formation. Such galactic outflows can be driven by active galactic nuclei (AGN) or processes associated with star formation such as supernovae or radiation pressure from young stellar populations. The goal of this thesis is to study outflows from an observational perspective in different phases to quantify their impact on their host galaxies comprehensively, primarily by using optical and millimetre band data from the Multi Unit Spectroscopic Explorer (MUSE) and the Atacama Large Millimeter/submillimeter Array (ALMA).

In the first part of this thesis, I study the physical mechanisms driving outflows as well as whether outflows are capable of suppressing star formation using a study of molecular gas outflows with ALMA and archival data. In a sample of 50 local galaxies with outflow signatures in low-J carbon monoxide (CO) transitions, I find most outflows are consistent with the radiation pressure-driven or the energy-driven (but with a low coupling efficiency) models. Furthermore, most outflows are unable to escape the galaxy's gravitational potential (with 5 % or less of outflowing gas exceeding the escape velocity), and the depletion time-scales of the galaxies' total gas reservoirs are typically of the order of 10^8 years or more. Based on these findings, I conclude that outflows are unlikely to quench their entire host galaxy but might affect the central regions of the galaxy.

Second, I investigate the physical conditions of the outflowing gas and the link between different gas phases in the galactic outflows. While there is observational evidence of outflows in many different phases, the connection between them and their relative importance is poorly understood. My results based on MUSE observations of 26 local (ultra)luminous infrared galaxies ((U)LIRGs) suggest that outflows have about three times higher electron density than

the galaxy's disc ($< n_{\rm e,disc} > \sim 150$ cm^{-3} and $< n_{\rm e,outflow} > \sim 500$ cm^{-3}), but they are less dust obscured than the galaxy's disc. Furthermore, I establish that the molecular phase is dominant in terms of mass and energy at all AGN luminosities, while the ionized gas phase is negligible in AGN host galaxies and at most a few per cent of the total mass or energy budget in star forming galaxies. The atomic neutral phase is slightly less massive and has lower kinetic power than the molecular phase.

Third, I analyse galaxies which exhibit positive feedback, which are instances where outflows trigger or enhance star formation. My results suggest that about 30 % of outflows show signs of star formation inside them, as the gas in these outflows is characterised by SF-like BPT diagnostics. The star formation rate inside these outflows is correlated with their ionized mass outflow rate. These findings suggest this mode of star formation might be more prominent at higher redshifts, and may contribute to the formation of the spheroidal component of galaxies.

Contents

Acknowledgements

First and foremost, I thank my PhD supervisor, Roberto Maiolino. I am incredibly grateful for his advice, his boundless enthusiasm and his insight. His phenomenal knowledge of astrophysics and his creativity in addressing research questions is inspiring. I would also like to thank him for making the Kavli Institute for Cosmology such a supportive and stimulating environment to conduct astrophysical research during his directorship.

In my first two years, I had the pleasure of working with Stefano Carniani. His expertise in extragalactic astronomy and knowledge of ALMA was a tremendous help for me. I also greatly appreciated his positive attitude and encouragement.

I also wish to thank Claudia Cicone for her instructive supervision leading up to my PhD at Cambridge and her continued help during my time as a doctoral student as a collaborator.

My time as a doctoral student would not have been the same had it not been for the other members of our research group. I will miss the collaborative spirit and their eagerness to help. The group meetings were always a friendly and instructive place to discuss scientific topics (with delicious chocolates as a bonus). In particular, I also thank my fellow PhD students Rob Gallagher, Simcha Brownson and James Trussler with whom I shared an office for a long time. I will miss our discussions, but even more so our lunch and coffee breaks. Thank you for being such amazing office mates and friends.

My PhD journey was full of interesting conversations and interactions with colleagues and collaborators in the field of extragalactic astronomy. I am honoured to have learned from you, both as a scientist and also personally: Francesco Belfiore, Enrica Bellocchi, Martin Bourne, Sara Cazzoli, Tiago Costa, Giovanni Cresci, Andrew Fabian, Wako Ishibashi, Alessandro Marconi, Filippo Mannucci, Michele Perna, Eckhard Sturm and Giacomo Venturi.

I am very grateful to Santiago Arribas for accompanying me to an observation trip to the ESO's Very Large Telescope and sharing his astrophysical and technical knowledge with me.

I wish to thank the administrators at the Kavli Institute of Cosmology and at Cavendish Astrophysics Group, in particular, Karen Scrivener and Steven Brereton for making sure my time as a PhD student was so positive.

I wish to express my thanks to the European Research Council for funding my doctoral

studies and all the work presented in this Thesis.

In addition, I would like to thank the University of Cambridge as whole and Hughes Hall College in particular for making my time in Cambridge truly special. The memories I shared with my friends there will stay with me forever. In particular, I would like to thank Joseph Wong, Roger de Belsunce, Daniel Wales and members of the Hughes Hall Boat Club.

Thank you, Liliane Stadler, for joining me on this PhD journey, your tireless support and the great memories we shared in Cambridge and Oxford over the last three and a half years.

I would like to conclude with a heartfelt thanks to my parents, Martin and Bettina Fluetsch, and my siblings, Flurina, Livia and Fabian, for their support, help and love. Without you, I would not have made it this far.

Chapter 1

Introduction

1.1 General Properties of Galaxies

Even though the first detection of galaxies outside of our own Milky Way dates back to the 18th century, the field of extragalactic astrophysics is barely 100 years old. At the end of the 18th century, Charles Messier and later, in the 19th century, also the British polymath John Herschel and John Louis Emil Dreyer catalogued a number of fuzzy objects, which were clearly distinct from the point-like stars. For many years, there was a discussion (which culminated in the Great Debate between Harlow Shapley and Heber Curtis) about whether these fuzzy objects ('nebulae'), resided inside the Milky Way or whether they were separate 'island universes'. Hubble settled this question conclusively by measuring the distance to 'spiral nebulae' using Cepheid variable stars with the 100-inch telescope at Mount Wilson Observatory. Cepheids are pulsating stars and their period of flux variations is linked to their intrinsic luminosity as found by Henrietta Leavitt (Leavitt 1908). Measuring the period of Cepheids and their apparent magnitude one can thus determine their distance. Hubble used this type of 'standard candle' to confirm the extragalactic nature of spiral nebulae and thereby started the research field of extragalactic astronomy.

Today we know that our Milky Way is just one of 2 trillion galaxies (Conselice et al. 2016), which range in mass from 10^6–10^{13} $M_\odot$ and come in a great variety of shapes and sizes. Our own Milky Way has a stellar mass of about $M_* = 6{\times}10^{10}$ $M_\odot$ (Licquia & Newman 2015) and a diameter of approximately 30 kpc (López-Corredoira et al. 2018).

Galaxies can be defined as gravitationally bound structures with stars, interstellar matter

such as gas and dust, stellar remnants (white dwarfs, neutron stars and black holes) and dark matter. A large part of the mass in galaxies is not visible (hence the name 'dark matter'), but we know of its existence because of its gravitational effect on visible matter. This dark matter constitutes about 90 per cent of the galaxy mass (Mulchaey 2000; Lovell et al. 2018), though its contribution might be smaller at higher redshifts (Genzel et al. 2017). It also has a great impact on several observables, such as for instance on the galaxy's rotation curve (see e.g. Zwicky 1937) or on the large-scale structure of galaxies such as seen by large-scale galaxy surveys such as Sloan Digital Sky Survey (SDSS) (York et al. 2000).

How galaxies form can only be understood in a cosmological context. In the standard cosmological model (called Lambda cold dark matter (ΛCDM)), gravity acts on very small initial density perturbations (on the order $\Delta\rho/\rho = 10^{-6}$) in the Universe, which is otherwise homogeneous and isotropic. The origin of these small primordial density fluctuations is likely inflation, a period of rapid, exponential expansion in the early Universe (Guth 1981). These initial perturbations are nearly scale-invariant (i.e. the primordial density fluctuations scale as $P(k) \propto k$), Gaussian and adiabatic (Harrison 1970; Zeldovich 1972; Bardeen et al. 1983). With time, the initial perturbations grow through gravity. High density regions collapse if they reach the Jeans instability (Jeans 1902) and attract further material, while low-density regions become emptier. In the ΛCDM paradigm small structures form first and successively larger structure is built up. This eventually gives rise to massive dark matter (DM) halos and a filamentary structure between them. This mass distribution is called the cosmic web. These DM halos appear between redshift 10–30 with masses around 10^5–10^8 $M_\odot$ (Tegmark et al. 1997; Planelles et al. 2015). DM halos grow hierarchically as smaller halos merge together and form larger ones. Luminous galaxies can then form in dark matter halos through cooling and condensation of gas within their potential wells (White & Rees 1978). Comparing results from numerical simulations 'boxes' of the whole Universe (e.g. the Millenium (Springel et al. 2005) or Illustris simulations (Vogelsberger et al. 2014)) with large-scale galaxy survey such as the 2 degree Field Galaxy Redshift Survey (2dFGRS) (Colless et al. 2001) or the SDSS (York et al. 2000), one finds a remarkably similar distribution of galaxies (Springel et al. 2006; Vogelsberger et al. 2014). However, reproducing the physical properties of the baryonic component of galaxies (stellar mass, star formation, gas content, age of stellar population, chemical enrichment etc.) is still very challenging both for analytical models and hydrodynamical cosmological simulations as these properties require incorporating complex phenomena associated with the baryonic matter (heating and cooling, radiative processes, shocks, fragmentation etc.).

The first attempt to classify the enormous number of galaxies in categories or groups was made by Edwin Hubble himself with the 'Hubble tuning-fork' diagram (Hubble 1926, 1936). The distinctive feature to classify galaxies was their morphology, i.e. their visual appearance.

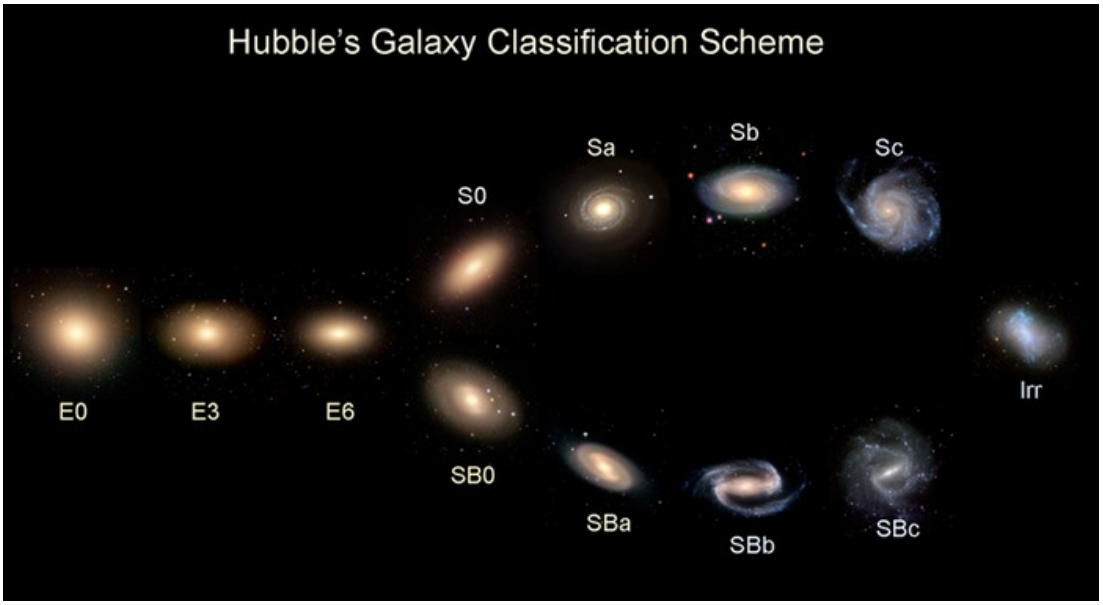

Figure 1.1: Hubble tuning-fork diagram. Elliptical galaxies are displayed on the left (assigned the letter 'E') spirals are shown on the right (assigned the letter 'S'). Spirals are further divided into barred spirals (bottom) and spiral galaxies without bars (top). Irregular galaxies ('Irr') with disturbed morphologies cannot be classified with this simple framework. From University of Iowa.

According to the tuning-fork diagram, galaxies are divided into ellipticals (which are assigned the letter E and numbers 0–7) and spirals (with the capital letter S and letters from a–c). Lenticular galaxies (S0) are at the transition point between the two groups. For ellipticals, the numbers 0–7 characterise the ellipticity, with 0 being almost round and 7 very elliptical. The letters a-c for spiral galaxies describe how tightly wound their spirals arms are (a being very tightly and c more loosely wound). Spiral galaxies are further separated into barred spirals, which have a 'B' in their classification name, and normal spiral galaxies. In barred spirals, the spiral arms are usually connected to the central bar. The Hubble tuning-fork failed, however, at classifying galaxies with more peculiar shapes such as dwarf galaxies or irregular galaxies. For some time, the Hubble diagram was erroneously interpreted as an evolutionary track, such that galaxies move from elliptical shapes to spirals. Thus, galaxies from E0–E7 and S0 are also referred to as 'early-type' and spiral galaxies as 'late-type'. We now know that elliptical galaxies do not evolve into spirals (and it is actually the other way around). Elliptical galaxies have a factor of 4-7 lower specific angular momentum than spirals (Romanowsky & Fall 2012) and will not spontaneously begin rotating and even in case of a collision of ellipticals, it is very unlikely that the angular momentum of the two ellipticals are exactly aligned and the collision will probably further reduce the angular momentum. Despite this, the (possibly misleading) nomenclature of 'early-type' and 'late-type' galaxies is still used.

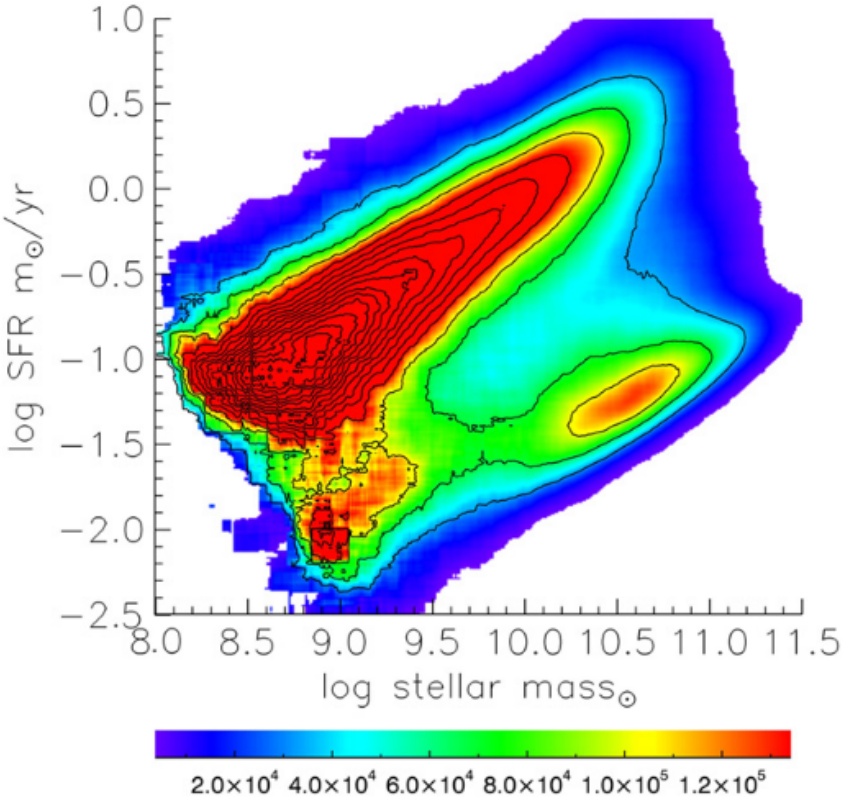

Figure 1.2: Distributions of the galaxies in the SFR-stellar mass diagram. The contours represent the number densities of galaxies. The star forming galaxies at high SFRs form the main sequence, while the high number density of galaxies at high stellar mass and low SFR is the quenched population. Figure from Renzini & Peng (2015).

Today, we often classify galaxies based on their location in the colour–magnitude diagram. The colour of a galaxy refers to the difference in magnitude in two wavelength bands, for instance u–g. The colour–magnitude diagram of large galaxy surveys shows two, clearly distinct populations: the 'blue cloud' and the 'red sequence' (Strateva et al. 2001; Baldry et al. 2004, 2006). In Fig. 1.3, this bimodality is illustrated in the $u - r$ colour–stellar mass plot. This bimodality is also apparent in the colour–concentration (Driver et al. 2006) or colour–morphology (Bamford et al. 2009) diagrams. These measured quantities, colour and magnitude, correspond to physical parameters of the galaxy since the colour is a proxy of recent star formation (or the age of the stellar population) and the absolute magnitude is related to the stellar mass. That means that galaxies in the blue cloud tend to have smaller stellar masses (mostly below $10^{10.5} M_\odot$) and red galaxies are preferentially found at the high-mass end of the colour–magnitude (or colour–mass) diagram. Furthermore, blue galaxies show a tight relation between their star formation rates (SFRs) and their stellar mass, dubbed the 'main sequence' of star forming galaxies, which extends also to high redshifts, although its normalisation increases

out to about $z \sim 1$–2. (see e.g. Salim et al. 2007; Speagle et al. 2014; Renzini & Peng 2015). Since they have comparatively large SFR (a large number of bright OB stars and hence the blue colour), galaxies in the blue cloud are called 'star forming'. The main sequence of star forming galaxies is shown in the stellar mass-SFR diagram in Fig. 1.2. Red sequence galaxies, on the other hand, have little or no ongoing star formation and we refer to them as passive, quiescent or 'quenched'. This bimodality extends further to other galaxy properties: quenched galaxies tend to be devoid of gas and have old stellar populations, whereas star forming galaxies are preferentially gas-rich and have young stellar populations. Most blue galaxies have late-type morphology, while red galaxies are mostly early-type galaxies. But there exists a small number of blue early-type as well as red late-type galaxies (Schawinski et al. 2014) (see also Fig. 1.3). As in general red galaxies tend to be more massive and to have an old stellar population, it is thought that they must have formed significant amounts of stars in the past. Therefore, it seems reasonable to assume that galaxies from the blue cloud evolve into red galaxies and not the other way around as initially thought.

There is a much smaller population of galaxies lying between the blue cloud and the red sequence in a region we refer to as the green valley. These galaxies appear to be in transition from one population to the other. The low number of green valley galaxies is often interpreted as evidence for a rapid transition between the two populations or that the fraction of galaxies leaving the main sequence towards quiescence at any given time is small. Recent observations have argued that possibly only a small fraction of galaxies experience a rapid quenching on time-scales of < 250 Myr, due to a mechanism that quickly heats or removes the gas reservoir, such as AGN feedback (see Section 1.2). In most galaxies star formation seems to be suppressed more gradually on time-scales of > 1 Gyr (Schawinski et al. 2014). This slow quenching is probably due to a cutoff of gas inflows ('starvation', Peng et al. (2015)).

The galaxy bimodality extends to higher redshifts, at least up to $z \sim 2.5$ (Brammer et al. 2009, 2011). Furthermore, there are fewer quenched galaxies at higher redshifts, confirming that blue galaxies evolve into 'red-and-dead' galaxies with cosmic time (Ilbert et al. 2013; Muzzin et al. 2013).

The processes responsible for halting star formation in galaxies and making them move towards the red sequence is often referred to as quenching. The question of what is the mechanism responsible for quenching star formation in galaxies is one of the most pressing issues in the field of galaxy evolution and investigating one specific proposed quenching mechanism is one of the main focus of this thesis.

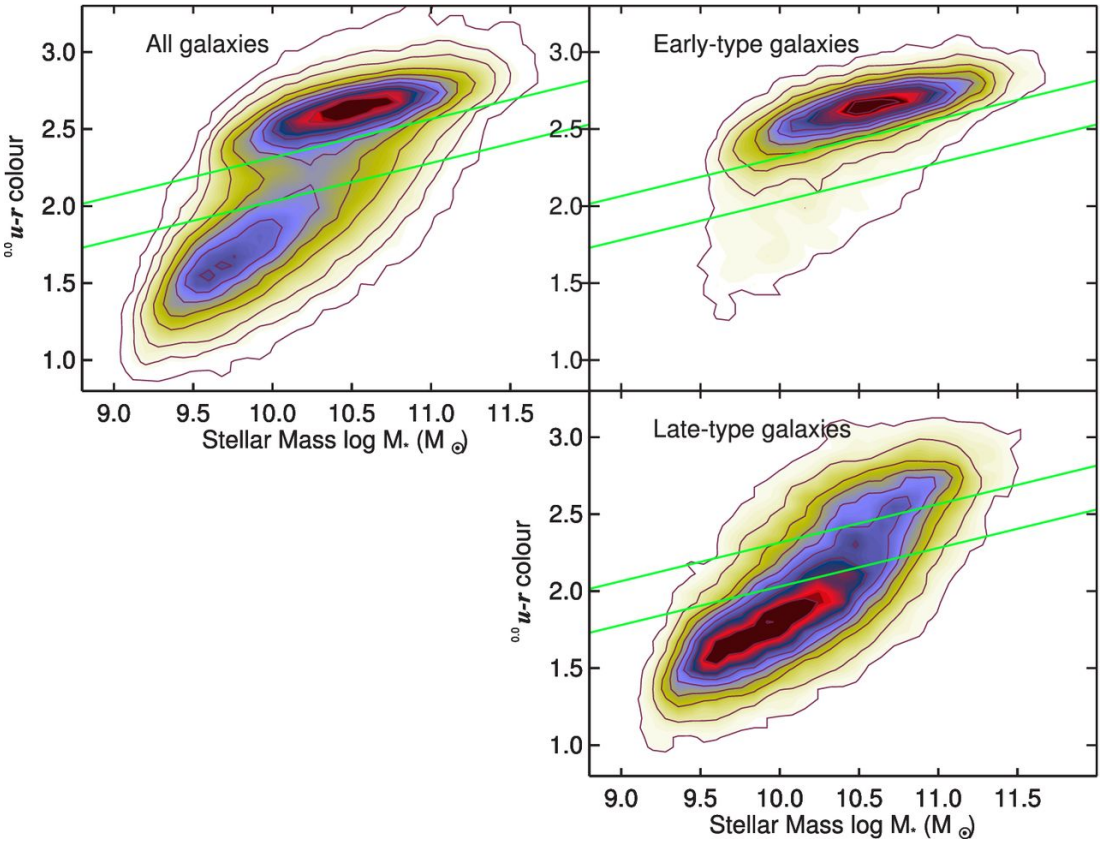

Figure 1.3: u- r colour–stellar mass diagram from Schawinski et al. (2014). The top left plot shows all galaxies and there is clearly bimodal distribution, with the blue cloud at the bottom left and the red sequence at the top. The two plots on the right illustrate that early-type morphologies are predominantly found in the red sequence (top right), whereas late-type galaxies are mostly in the blue cloud. However, there is a significant number of red late-type galaxies and also a number of blue early-type objects. Between the green solid lines lies the green valley with fewer galaxies.

1.2 Feedback in Galaxy Evolution

Supermassive black holes are a constituent of most if not all massive galaxies (Magorrian et al. 1998). They are much more massive than solar mass black holes (hence 'supermassive') and typically range in masses from $M_{\rm BH} = 10^5$–10^9 M$_\odot$ (Kormendy & Ho 2013). These supermassive black holes might have evolved from the remnants of the first generation of stars, metal-free Population III stars. Alternative theories suggest they form through gas-dynamical instabilites (through the direct collapse of dense gas) or via stellar-dynamical processes (Volonteri 2012). In either scenario, black holes grow through the accretion of matter, which forms an accretion disc around the black hole. With a temperature of $T \sim 10^6$ K, accretion discs emit large amounts of radiation in the ultraviolet (UV) and optical part of the electromagnetic spectrum. During

times of intense activity (i.e. powerful accretion), we refer to these objects as active galactic nuclei (AGN). AGN are exceptionally luminous and can outshine their host galaxy by orders of magnitude (Farrah et al. 2003; Nardini et al. 2009). Estimates suggest about 20 % of galaxies in the local Universe host AGN, however, this is highly dependent on the luminosity threshold and wavelength band used for selecting them (Miller et al. 2003; Best et al. 2005). Mass accretion onto SMBH was found to be the source to explain both the unusually broad and strong emission lines in Seyfert galaxies (Fath 1909; Seyfert 1943) and also the highly collimated jets seen in radio observations of (by their standards) high redshift (i.e. $z > 0.1$) 'quasi-stellar objects' (quasars) (Matthews & Sandage 1963). The broad emission lines originate in the broad-line region (BLR), where gas clouds feel the gravtitational effect of the BH directly. Due to high electron densities ($n_e > 10^8$ cm^{-3}), collisional de-excitation is more dominant than radiative de-excitation for forbidden optical lines (such as [OIII]λ5007) and thus most forbidden lines are not emitted efficiently in the broad line regions (Peterson 2006). Indeed, nebular emission lines such as [OIII] do not have a broad component associated with the BLR, but only a narrow component produced by the much more extended narrow-line region (NLR). AGN are divided into two classes, type I and type II AGN, based on the presence (type I) or absence (type II) of broad recombination emission lines. These two types of AGN can be unified using a single physical model (Antonucci 1993; Urry & Padovani 1995). According to this model, the difference between type I and type II AGN is that they are intrinsically the same kind of object, viewed from different angles. In type I AGN, the observer is able to see the broad-line region unobscured, while in type II AGN the broad-line region is obscured by a dusty torus.

Despite being only about 0.1 % as massive as their host galaxy and their minute extent, there is evidence that AGN profoundly affect the evolution of galaxies. Their importance was mainly realised due to three pieces of indirect evidence: a) the striking similarity between the star formation rate history (SFH) and the black holes accretion rate (BHAR) history across cosmic time, b) the tight correlations between the mass of the black hole (M_{BH}) and properties of the bulge of the host galaxy and c) the success of AGN feedback in accounting for the discrepancy between the dark matter halo and the observed stellar mass function at high masses in semi-analytical models and cosmological simulations. In the following, I will discuss these three reasons for invoking AGN feedback in more detail.

a) similarity of star formation and black hole accretion rate histories: Both the SFR and the BHAR experience a sharp increase from z=0 to z=1 and they both have a peak around redshift 2–3 ('cosmic noon') and then decline again steeply to higher redshifts (Madau et al. 1996; Shankar et al. 2009; Madau & Dickinson 2014; Heckman & Best 2014). For the last 11 Gyr, the ratio of these two growth rates has been constant and about of order 1500, which is also in agreement with the 10^{-3} factor in the local M_{BH}-M_{bulge} scaling relation (see point b)).

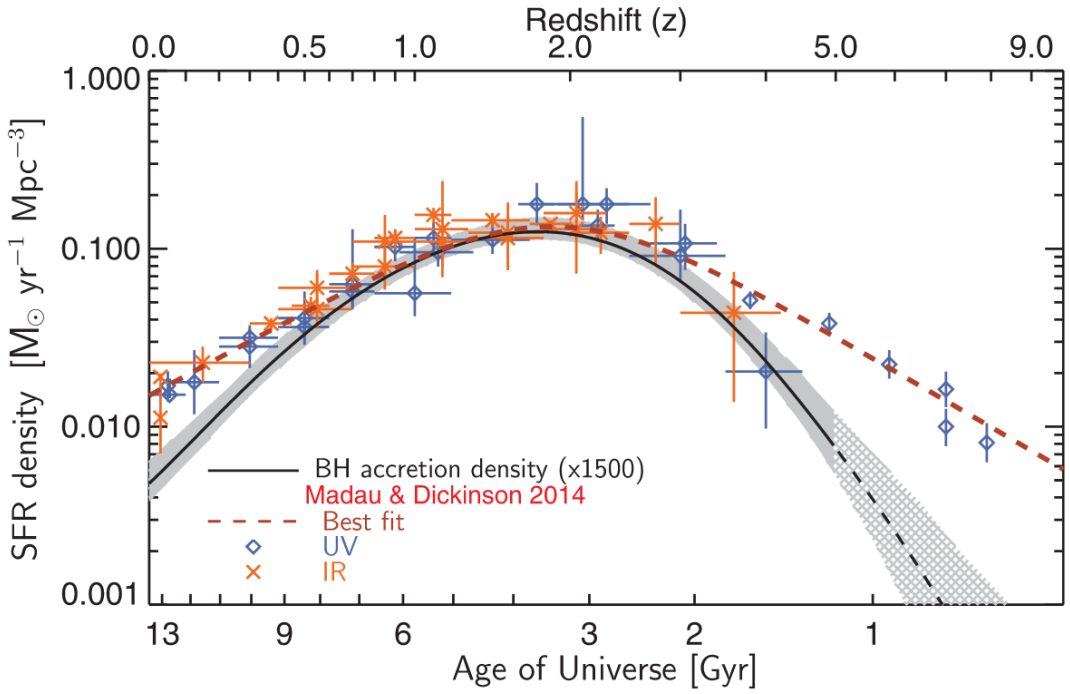

Figure 1.4: Black hole accretion rate density (solid black line) in comparison with the star formation rate density (dark red dashed line) as a function of redshift. The black hole accretion rate density is scaled by a factor of 1500 for visualization purposes. The blue and orange data points are estimates of the star formation rate density from UV and IR data, respectively. Figure from Aird et al. (2015).

This is illustrated in Fig. 1.4, where the black hole accretion density is shown as a solid black line and the star formation rate density is represented by a dashed dark red line. The black hole accretion density is multiplied by a factor of 1500 for better visualization. The histories of black hole and star formation share further similarities. The most massive galaxies form in intense starbursts at higher redshifts, whereas less massive galaxies gained their mass in longer periods of star formation at lower redshifts. This form of growth is called anti-hierarchical growth or downsizing (Cowie et al. 1996) and it is also mirrored in the growth of SMBH. The most massive BH formed at high redshifts during intense accretion periods, while less massive black holes formed during lower Eddington accretion times at much lower redshift (Ueda et al. 2003; Merloni 2004; Barger et al. 2005). This finding seems to suggest that there is a link between black hole accretion and star formation. However, it is not obvious whether the co-evolution is due to the fact that a) the star formation rate affects the black hole growth or b) the black hole accretion has an influence on the galaxy's star formation or c) a third process affects both, star formation and black hole accretion.

b) correlation between the black hole mass and properties of the bulge of the host

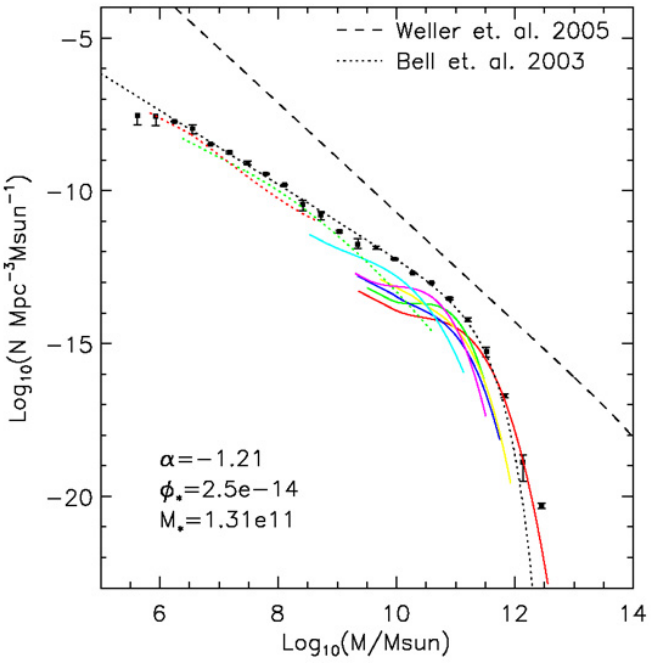

Figure 1.5: The dark matter mass function (dashed line) from numerical simulations of Weller et al. (2005) in comparison to the observed galaxy stellar mass function (black data points). The coloured line are spline fits to functions of galaxies from different Hubbles Types. Figure from Read & Trentham (2005).

galaxy: The SMBH mass, $M_{\rm BH}$, was found to correlate tightly with several host bulge properties, as for instance the velocity dispersion ($M_{\rm BH} \sim \sigma^{4-5}$), luminosity ($M_{\rm BH} \sim L_{\rm bulge}^{1.1}$) or mass of the bulge ($M_{\rm BH} \sim 10^{-3}\ M_{\rm bulge}$) (Gebhardt et al. 2000; Häring & Rix 2004; Ferrarese & Ford 2005; Kormendy & Ho 2013; McConnell & Ma 2013). For ellipticals, the bulge contains the entire galaxy, for spiral galaxies it only refers to the central bulge. The correlations hold over several orders of magnitude and have been interpreted as evidence for a causal connection between the central SMBH and its host galaxy. Such a connection cannot be gravitational in nature, though, since the sphere of influence of the black hole ($r = GM_{\rm BH}/\sigma^2$, which is typically < 1 pc) is very small compared to the extent of its host galaxy (tens of kpc). However, AGN feedback is not the only possible explanation for these correlations. Galaxy mergers of initially uncorrelated BH mass and stellar mass distribution could give rise to the observed correlation without invoking a coupling between the central BH and its host galaxy (Jahnke & Macciò 2011). This makes the interpretation of the $M_{\rm BH}$-σ and other black hole mass-bulge relations non-trivial. Since host galaxy and black holes are correlated even at earlier epochs (as explained under point a)), it seems likely that AGN feedback plays at least some role, but the emergence of such tight correlations might be further helped by galaxy mergers.

c) strong discrepancy between the dark matter halo mass function predicted by ΛCDM

and the observed galaxy stellar mass function both at the low- and high-mass end: The dark matter halo function is characterised by a power law with a steep slope of about –0.9 (in the halo mass range hosting galaxies). The stellar mass function, on the other hand, is well fit by a Schechter function (Schechter 1976) with a characteristic stellar mass of $M_* = 10^{10.5}$ $M_\odot$ and with a slope much shallower than the halo mass function at low masses. That means that at low and high masses, there are significantly fewer galaxies than expected from the number of dark matter halos. This is shown in Fig. 1.5, where the dashed line represents the dark matter halo mass function (scaled by the stellar to dark matter mass ratio) and the dotted line the fit to data points (black) of the stellar mass function. Early papers in the 70s (Binney 1977; Rees & Ostriker 1977) argued that this is due to varying cooling efficiencies at different halo masses. Halos with masses between 10^9 $M_\odot$ – 10^{12-13} $M_\odot$ cool efficiently and collapse at the free fall rate, whereas above and below this is not the case. However, we know that the progenitors of massive halos today could have cooled in the past when they were less massive. Another problem with this argument was that these models predicted that at low redshifts the gas would have cooled efficiently and we would see efficient star formation in massive galaxies. In reality, many large galaxies are already quiescent at redshift 2 (e.g Glazebrook et al. 2004; Werner et al. 2019). Varying cooling efficiencies can thus not fully explain the characterstic mass scale of galaxies. Therefore, feedback mechanisms have been invoked. Feedback from supernovae and stellar winds can reconcile the difference between the observations and the halo mass function at the low-mass end (Dekel & Silk 1986). In galaxies with masses $M_\star < 10^{10.5}$ $M_\odot$ and hence with a shallow gravitational well, supernovae are efficient at removing gas from the galaxy's reservoir (the fuel for star formation) and thus capable of suppressing or at least regulating star formation. At around $M_* = 10^{10.5}$ $M_\odot$, the discrepancy between ΛCDM predictions and the observed stellar mass function is smallest. To explain the gap between the two mass functions at high stellar masses, AGN feedback is invoked. Simulations including AGN feedback have successfully reproduced the exponential suppression of star formation at high masses through a combination of heating, jets and outflows (Bower et al. 2012; Puchwein & Springel 2013).

Together these findings have made AGN feedback one of the main candidates to explain the suppression of star formation (quenching) in massive galaxies. There are other quenching mechanisms associated with the environment in which galaxies live (such as ram pressure stripping (e.g. Gunn & Gott J. Richard 1972) and 'strangulation' (which could, however, be caused by an AGN, but also by tidal interactions) (Peng et al. 2015; Trussler et al. 2020)). Another quenching mechanism is shock heating of the gas accreting onto the massive haloes (e.g. Dekel & Birnboim 2006; Dekel et al. 2009), which tends to prevent cold accretion which in turn is required to replenish the galaxy with fresh gas for star formation. However, simulations have shown that this mechanism is little effective in quenching star formation as dense cold

streams can still pierce the hot halo and deliver gas onto the galaxy. This form of AGN feedback discussed in this section, referred to as negative feedback, is different from the positive (AGN) feedback discussed in Section 1.2.3.

1.2.1 AGN Feedback Modes

AGN feedback can operate in two different modes depending on the accretion rate of the black hole (which is related to the luminosity of the AGN). These two modes should not be seen as two separate pathways, but rather as complementing each other. It has been proposed that the quasar mode shapes the evolution of the galaxy early on, whereas the radio mode maintains that situation at lower redshifts (Churazov et al. 2005; Fabian 2012).

The radiative (or quasar or wind) feedback mode is seen in high luminosity AGN, accreting material at a rate close to the Eddington limit (Silk & Rees 1998). The Eddington luminosity is defined as the luminosity, whose radiation pressure on the accreting gas is equal to the gravitational force. This mode is characterised by a short ($\tau \sim 10^7$ yr), but very intense phase of black hole accretion. In this case, the energy released by the AGN can couple to the surrounding ISM and drive powerful outflows which expel gas out of the galaxy (King & Pounds 2015). This process can potentially deplete the galaxy of its gas reservoir for star formation. This mode may be responsible for the observed $M_{\rm BH}$ - σ and other black hole mass - host galaxy relations (see Section 1.2). Probably, this mode is most effective during the peak of AGN and SF activity around redshifts 1–3 (see Fig. 1.4) when galaxies were gas-rich (Fabian 2012; Heckman & Best 2014). High accretion rates lead to large inflows of gas into the centre of the AGN. This accreted gas (mainly at X-ray energies) and dust (UV–IR wavelengths) often cause the AGN itself to be obscured (Fabian 1999; Hickox & Alexander 2018), making observations of this phenomenon more challenging. Often the inflow of gas also causes a starburst near the AGN (< 100 pc) which might further contribute to the obscuration (Hickox & Alexander 2018).

The second mode, called the jet (or kinetic or radio) mode is thought to act at later times ($z \lesssim 1$), in low luminosity AGN (i.e. $L_{\rm AGN} < 0.01\ L_{\rm Edd}$). According to popular models, after the expulsion of gas through the wind mode, the jet mode ensures the galactic halo remains hot by driving powerful jets which heat the circumgalactic and halo gas (Silk & Mamon 2012). Thus it prevents re-accretion onto the galaxy and as a consequence also reignition of star formation. The jet mode is prominent in the centres of groups and clusters of galaxies. Perhaps the strongest piece of evidence of this mode (and AGN feedback in general) is found in cool-core clusters, where large X-ray cavities have been observed (McNamara & Nulsen 2007, 2012). The cavities are spatially coincident with emission from the radio lobes suggesting that radio jets are the cause for the expanding bubbles and for energy injection into the halo. That could imply that the power provided by the radio jet suppresses gas cooling and thus star formation.

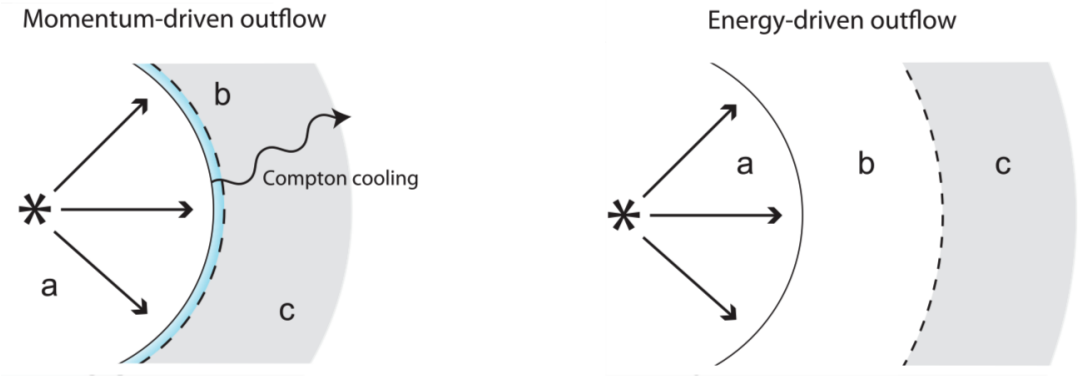

Figure 1.6: Momentum- vs energy-driven outflows (from Costa et al. (2014)). According to both models, the outflow is driven by an inner wind in region a. In the momentum-driven case (left), the wind cools efficiently as it hits the ISM and region b is therefore thin. In the energy-driven scenario (right), no efficient cooling is possible and the wind expands as an adiabatic bubble (region b).

1.2.2 Radiative (Negative) Feedback Models

Three different models of AGN radiative feedback have been put forward: a) momentum-driven outflows, b) energy-driven outflows and c) radiation pressure-driven outflows, which directly act onto the dusty clouds.

a) Momentum-driven winds: Momentum-driven outflows start with a sub-relativistic ($v_{\rm w}$ $\approx$ 0.1c), highly-ionized inner wind, which is powered primarily by the radiation generated by accretion onto the black hole. This in turn is thought to happen predominantly through radiation pressure onto the highly ionized gas via line locking on metal ions. This inner wind collides with the ISM and generates two shocks: a) a forward shock that thrusts into the ambient ISM and b) a reverse shock because the wind has to decelerate rapidly. If the gas now cools efficiently and faster than its flow time (=r/v), we have a 'momentum-driven' wind. The inner wind does, however, transfer its momentum fully in this collision. Outflowing gas in the momentum-driven mode is usually confined to scales of a few 100 pc (King & Pounds 2015). In this mode, the black hole mass is proportional to the stellar velocity dispersion, $M_{\rm BH} \propto \sigma^4$, close to the observed exponent of 4.3 (Kormendy & Ho 2013). Furthermore, the momentum-driven scenario gives a normalization which agrees with the observed value of the $M_{\rm BH}$–σ relation (Debuhr et al. 2011). However, more realistic cosmological simulations by Costa et al. (2014) showed that the momentum input provided by this model does not suppress the cold gas infall. To be consistent with the $M_{\rm BH}$–σ relation, the winds have to become energy-driven at small (i.e. $\lessapprox$ 100 pc) scales. Momentum-driven winds inject energy, which is only about 10 % of the bulge gas binding energy (King & Pounds 2015). In this mode, the black hole can grow steadily. The momentum-driven outflow scenario is shown on the left of Fig. 1.6. An inner

wind originating in region a creates a reverse shock in region b. This shell remains thin.

b) Energy-driven winds: Like the momentum-driven mode, the energy-driven feedback mode starts with the highly-ionized inner wind, which hits the ISM. The main difference is that in this case the wind is not able to lose its thermal energy efficiently. Instead, it retains all its mechanical energy and drives an adiabatic expansion of a hot shocked wind bubble (shown as region b on the right-hand side of Fig. 1.6). This expanding bubble drives the ambient ISM (region c) further out. The energy-driven scenario is more extreme and could expel most of the gas in the spheroidal component. This model of feedback leads to the black hole mass being proportional to σ^5, slightly larger than the observed value.

c) Radiation pressure-driven winds: An alternative mechanism for driving large-scale outflows is radiation pressure directly pushing the dust grains in the molecular clouds of the ISM in the host galaxy. Provided gas and dust are efficiently coupled, radiative momentum can be transferred to the gas by dust, which is partially ionized due to the radiation. The dusty gas which is being driven by radiation pressure is strongly radiating in the IR and remains at temperatures $T \ll 10^4$, whereas the outer shell is shocked to higher temperatures ($T \sim 10^6$–10^7 K). Typically, radiation pressure-driven outflows are confined to small scales < 1 kpc (Thompson et al. 2015; Costa et al. 2018b), where gas is optically thick in the infrared. Radiation pressure-driven models are only capable of driving gas to ~ kpc scales in the case of dense circumnuclear gas, which can result in efficient photon trapping (Costa et al. 2018b). Photon trapping causes multiple photon scattering which in turn results in a momentum boost.

1.2.3 Positive Feedback

While AGN feedback has been invoked to explain the suppression of star formation and this has to be the overall dominating effect, recent models and observations strongly suggest that AGN feedback can also *induce* star formation (Ishibashi & Fabian 2012; Silk 2013a; Zubovas et al. 2013b; Mukherjee et al. 2018). Observational verification of this phenomena become only recently possible due to the advent of integral field spectroscopy instruments such as the Multi Unit Spectroscopic Explorer (MUSE), which allowed the study of star formation and winds driven by an AGN or by star formation on a spatially resolved basis. Positive feedback is predicted to act through two different modes.

In the first mode, the outflow driven by AGN feedback is theorised to compress the ambient ISM (Nayakshin & Zubovas 2012; Nayakshin 2014). If the molecular gas in the ISM is driven beyond the Jeans limit (Jeans 1902), gravitational collapse is induced and stars can be formed. Hence this first mode could enhance star formation in the disc of the host galaxy or even in clouds in the circumgalactic medium. Observational evidence of an outflow leading to fragmentation and gravitational cloud collapse was found in a few galaxies (e.g. Centaurus A (Salomé et al.

2017) and NGC 5643 (Cresci et al. 2015a)). This phenomenon has also been observed at higher redshifts. Cresci et al. (2015b) studied a QSO at $z \sim 1.6$, which shows signs of quenching in the direction of the outflowing gas, but a boost of star formation at the edges of the outflow, where it hits the surrounding ISM and presumably leads to compression. However, a recent re-analysis cast doubt on this interpretation (Scholtz et al. 2020), finding extended Hα and not just along the edges.

According to the second mode of positive feedback, gas within the outflowing gas itself undergoes cooling and fragmentation, eventually leading to star formation (Ishibashi & Fabian 2012; Zubovas et al. 2013a, 2014; Decataldo et al. 2019; Yu et al. 2020). Indeed, observations have shown that a large fraction of outflowing gas is often molecular (Cicone et al. 2014; García-Burillo et al. 2015). In addition, measurements of dense gas tracers such as HCN or HCO^+ transitions proved that the HCN/CO ratio is enhanced in winds indicating the outflow consists to a large part of dense ($n > 10^4$ cm^{-3}) and clumpy gas (Aalto et al. 2012, 2015; Oosterloo et al. 2017; Cicone et al. 2020). In other words, the conditions in at least some outflows seem suitable for star formation. A number of works have provided evidence for star formation inside the outflow by combining analysis of the dominant excitation mechanism (e.g. Baldwin, Phillips & Terlevich (BPT) diagrams) and arguments based on the ionization parameter (Maiolino et al. 2017; Gallagher et al. 2019; Rodriguez del Pino et al. 2019)

Positive feedback might have far-reaching implications as it could explain the size evolution of the spheroidal component of galaxies (Ishibashi et al. 2013; Dugan et al. 2014) and the presence of high-velocity stars (potentially capable of escaping the galaxy) (Dugan et al. 2014) because they have intrinsically high radial velocities. Through supernovae explosions, stars formed in the outflow could also contribute to the chemical enrichment of the circumgalactic and intergalactic medium. Furthermore, positive feedback can contribute significantly to the global star formation rate of the galaxy, as evidenced by the observation of IRAS 23128-5919, where the star formation in the outflow amounts to about 25 % of the total SFR (Maiolino et al. 2017).

1.3 Outflows from Stellar Feedback and AGN

In Section 1.2, I have summarized the evidence that points towards a co-evolution between SMBH activity and star formation. So far, there is no consensus on whether this co-evolution is non-causal or whether there is a physical mechanism linking the two. However, both of these processes are driven by the (shared) cold gas reservoir. This reservoir, in turn, is determined by the interplay of supply of cold gas (feeding) and the removal or heating of cold gas (feedback) (e.g. Harrison 2017). Since BH accretion and star formation impart momentum and energy

into the host galaxy through radiation, winds and jets, these are natural candidates for feedback.

For more than three decades, we have known that feedback from processes associated with star formation can affect the evolution of galaxies through outflows. These outflows are powered by mechanical energy and momentum from stellar winds and supernovae. During the initial starburst phase, this energy is mainly supplied by winds from hot, massive OB stars (< 3 Myr). Later, winds from Wolf-Rayet stars contribute (3–6 Myr) predominantly and finally core collapse type II supernovae are the main driver (until 40 Myr) of stellar feedback (Veilleux et al. 2005).

As highlighted in Section 1.2, stellar feedback is not able to explain the lack of very massive galaxies seen in the galaxy stellar mass function. AGN feedback is instead invoked in these massive galaxies as AGN are very powerful energy sources. If a black hole with mass $M_{\rm BH}$ has grown through the accretion of gas (Soltan 1982), it has released an energy of the order of $E_{\rm BH} \approx \eta M_{\rm BH} c^2$. For an accretion efficiency of $\eta = 0.1$ and a BH of mass 10^8 $M_\odot$, this amounts to $E_{\rm BH} \approx 2{\times}10^{61}$ erg. The binding energy of the bulge of a galaxy is $E_{\rm bulge} \approx M_{\rm bulge}\sigma^2$. Applying the known correlation between black hole and bulge mass ($M_{\rm bulge} \approx 10^3 M_{\rm BH}$) (see Section 1.2), the binding energy for a bulge hosting a black hole with mass 10^8 $M_\odot$ is $E_{\rm bulge} \approx 8{\times}10^{58}$ erg. Therefore, the energy released by the black hole exceeds the binding energy of the bulge by two or three orders of magnitude. If only the binding energy of the gas, $E_{\rm gas} \sim 0.16\ E_{bulge}$ is considered, the potential of the black hole to affect the gas becomes even more apparent (King & Pounds 2015). Clearly, the energy released by the black hole during its accretion phase can potentially have a devastating effect on its host galaxy, to the point of completely quenching star formation and maybe also drive (or at least contribute to) the galaxy bimodality.

Although the mechanisms of starburst- and AGN-driven winds are very different, the difference when observing them is not as clear-cut. On average, AGN-driven outflows will be more powerful, with higher outflow rates and higher velocities (Cicone et al. 2014). Despite this, many outflows can not be put clearly into one category and might be driven by a combination of the two (e.g. Gowardhan et al. 2018)

The combined effect of outflows from star formation processes and AGN activity can reconcile the discrepancy between observed stellar mass function with the expectation from dark matter halos.

1.3.1 Multiphase Nature of Outflows

The last 30 years have seen an increased observational effort to understand starburst- and AGN-driven feedback associated with galactic outflows. Initial works pioneered the field by observing very powerful galaxies with massive and fast outflows. Combined, these studies have found that outflows are common, albeit to what extent they affect their host galaxy is still debated. Most of

Table 1.1: Overview of different outflow gas phases

Gas phase	Tracers	$\langle T_{\rm gas} \rangle$ [K]	$\langle n_{\rm gas} \rangle$ [cm^{-3}]	spatial scale [pc]
Highly ionized	X-ray absorption lines	10^6–10^7	10^6–10^8	< 1 pc
Ionized	[OIII], Hα	10^3–10^4	10^2–10^4	10–10000
Neutral atomic	HI, Na ID, [CII]	10^2–10^3	1–10^2	10–1000*
Molecular	CO, OH, H_2, [CII]	10–10^2	$\geq 10^3$	10–10000

Adapted from Cicone et al. (2018), *: neutral outflows are likely to be more extended given the sizes of the molecular outflows, but since they rely on absorption (Na ID and HI) or weaker lines ([CII]) than CO, they have mainly been detected at smaller radii.

the first outflow observations targeted the ionized phase, either the hot ionized phase (through X-ray) or the warm ionized phase (through optical emission lines) (Heckman et al. 1990). In the last 10-15 years, many studies managed to detect outflows in other phases, most importantly the atomic neutral phase and the molecular phase. This discovery of the molecular outflow phase is interesting because it concerns the phase out of which stars are formed and could provide an insight into how feedback through outflows affects the host galaxy's star formation. These findings have also revealed the complexity and multiphase nature of outflows, not unlike what we know about the structure of the normal ISM. The various phases trace outflows at different spatial scales (from sub-pc to tens of kpc), evolving on different time-scales and with different physical conditions (such as density and temperature). This also highlights the importance of using a multi-wavelength approach to provide a comprehensive understanding of the physical processes at work, connecting the sub-pc winds with the driving of large-scale outflows and potentially the quenching of galaxies. Comparing observations to predictions from models and simulations also requires us to know in detail the *total* mass and energy budget of the outflow as this is often the predicted property by recent simulations. Many observations, however, focus on one single phase, which might lead to a significant underestimation of the impact of outflows. The next subsections will provide an overview of different wind and outflow phases from an observational perspective.

1.3.2 Ultra-fast Outflows

Ultra-fast outflows (UFOs) are probably driven by wide-angle winds from the accretion disc around the AGN, which are accelerated by radiation pressure. They are usually traced through absorption lines of highly ionized Iron atoms in the K-band such as Fe XXV or Fe XXVI, where they show a P Cygni profile. This spectroscopic feature consists of blueshifted absorption and redshifted emission and is interpreted as a signature of outflowing gas. UFOs are very fast ($v \approx$

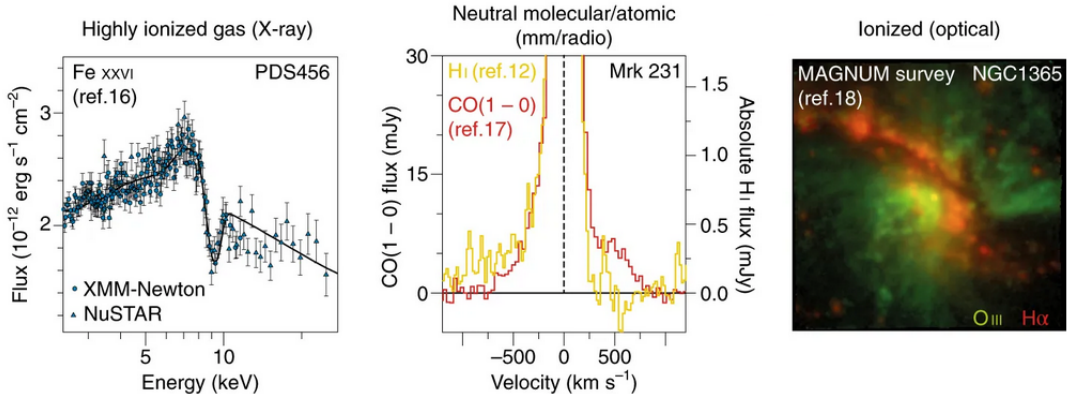

Figure 1.7: Outflows have been observed in several different phases. Left: UFO detected in a Fe absorption line through a P Cygni profile. Centre: Neutral atomic (HI, yellow) and molecular (CO(1–0), red) profiles showing broad emission line wings indicative of outflowing gas. Right: Ionized outflow traced by [OIII] (green), perpendicular to the galactic disc probed by Hα (red) (from Cicone et al. (2018)).

0.1–0.25 c), have large column density ($N_{\rm H} \sim 10^{22}$–10^{24} cm^{-2}) and high ionization parameters (log(ξ/(erg cm s^{-1})) = ~ 3–5) (King & Pounds 2015). Mass outflow rates are moderate ($\dot{M}_{\rm OF}$ ~ 0.01–1 M$_\odot$/yr), but high kinetic powers ($\dot{E}_{\rm OF} \sim 10^{42}$-$10^{45}$ erg s^{-1}), typically corresponding to ≈ 0.5 % of the AGN bolometric luminosity, suggest (according to models) that UFOs might be capable of significantly affecting the ISM in the host galaxy. UFOs are prevalent with an incidence of about 35-50 % (Gofford et al. 2013; Tombesi et al. 2014).

Even though UFOs act on sub-pc scales, models attest them a crucial role in driving the galactic-scale outflows because they likely represent the inner wind described in theoretical models (see Section 1.2.2). Recent works (Feruglio et al. 2015; Tombesi et al. 2015; Veilleux et al. 2017) have attempted to demonstrate the coupling between UFOs and large-scale molecular outflows in a small number of objects. There is still some debate about whether these are consistent with the energy- or momentum-driven scenario.

In addition, galactic scale outflows are predicted to be observable through spatially extended (~ kpc) emission in the soft X-ray (Nims et al. 2015). Unfortunately, current X-ray facilities lack the spectral and spatial resolution to detect this diffuse X-ray signature except for some of the closest and most powerful outflows. However, they will be detectable through future X-ray mission such as the Advanced Telescope for High Energy Astrophysics (Athena) or the X-ray Imaging and Spectroscopy Mission (XRISM).

1.3.3 Ionized Outflows

The warm ($T \sim 10^4$ K) ionized outflow phase is mainly traced through blueshifted and asymmetric forbidden optical emission lines, such as the [OIII]λ5007 line, or through recombination lines such as Hα. The blueshift in these lines is interpreted as outflowing gas approaching along the line of sight. The absence or suppression of observational signatures from the receding cone (redshifted emission) can be explained by partial or complete obscuration by the galactic disc. Ionized outflows typically have velocities of a few 100 km s^{-1} up to several 1000 km s^{-1} (Harrison et al. 2014) and their mass outflow rates are mostly moderate but can reach hundreds of M$_\odot$/yr in very luminous AGN host galaxies (Bischetti et al. 2017). Longslit and integral field spectroscopy have found ionized outflow extending up to 10 kpc (Harrison et al. 2014). Ionized outflows tend to be faster and more massive with increasing AGN bolometric luminosity (Fiore et al. 2017) but also with higher radio luminosity (Mullaney et al. 2013). Warm ionized outflows occur in about 30-50 % of AGN host galaxies (Harrison et al. 2014; Woo et al. 2016). Constraining the ionized mass and energy budget is challenging because of uncertainties mainly associated with the electron density, n_e, (the outflow mass is inversely proportional to the electron density) and the extent of the outflow (see Section 1.4).

One of the most convincing pieces of evidence for outflows quenching star formation comes also from observations of ionized outflows. Studies targeting galaxies at $z \sim 2$ noticed a spatial anti-correlation between the outflowing part of the galaxy traced by [OIII] and star formation in the galaxy traced by Hα (Cano-Diaz et al. 2012; Carniani et al. 2016), although a recent study debates this finding and interpretation (Scholtz et al. 2020). This study confirms the existence of a powerful outflow, but finds no spatial anti-correlation between the outflow and star-forming regions.

1.3.4 Neutral Atomic Outflows

A blueshift in the sodium doublet absorption lines (Na ID) traces the neutral atomic phase of the outflow. Sodium can probe the cool ($T < 10^4$ K), metal-enriched gas given a strong continuum source in the background. The presence of outflowing gas traced by Na ID is almost exclusively found in face-on galaxies and absent in edge-on galaxies, suggesting that outflows are perpendicular to the galaxy disc. This finding would also be consistent with the fact that in edge-on galaxies sodium inflows have been found (Roberts-Borsani & Saintonge 2019). However, these results could also be explained by a selection effect as face-on galaxies have a strong continuum on a larger projected area than edge-on galaxies and thus facilitate outflow detection with Na ID at larger projected radii. Furthermore, neutral atomic outflow traced by Na ID are not more prevalent or more massive in AGN host galaxies compared to inactive

galaxies. (Concas et al. 2019; Roberts-Borsani & Saintonge 2019).

Recently, also neutral hydrogen absorption, HI, has been used to trace fast ($\sim$ 1000 km s^{-1}) outflowing gas (Morganti et al. 2005, 2013). The HI absorption feature might be connected to the radio power or, more specifically, the radio jet of the host (Geréb et al. 2015; Morganti et al. 2015).

Another increasingly used outflow tracer is the fine structure transition [CII] 157.74 μm line, which is sensitive to the ionized and neutral outflow phases having an ionization potential of 11.3 eV (compared to 13.6 eV for hydrogen). The majority of [CII] emission is believed to stem from photon-dominated regions (PDRs), where the bulk of the gas is in the neutral atomic phase. However about 20 % is generally coming from CO-dark molecular gas and about 30 % can come from the partly ionized phase (Pineda et al. 2013). The [CII] transition is a promising outflow tracer at high redshifts, as it is a very strong line and less affected by CMB attenuation than for instance low-J CO transitions (see Section 1.3.5, da Cunha et al. (2013)). Indeed, outflows studies have successfully detected broad [CII] wings at low- (Janssen et al. 2016) and high-redshifts ($z \sim 6$, Cicone et al. 2015; Bischetti et al. 2019b) indicative of outflowing gas.

1.3.5 Molecular Outflows

Most molecular gas is found in H_2 clouds, but H_2 itself is not a good tracer of the (outflowing) molecular gas mass. It requires high temperatures ($\sim$ 100–1000 K, Roussel et al. (2007)) to be excited while most molecular clouds are cool ($T \sim$ 10–20 K) (Kennicutt & Evans 2012). Instead, cold molecular gas outflows are predominantly studied using either sub-mm observations of low-J transition of carbon monoxide (CO) or observations of far-IR hydroxyl (OH) transitions. Some of the first molecular outflows were found by detecting a P Cygni profile in OH (Fischer et al. 2010; Sturm et al. 2011) (see Section 1.3.2). Together with interferometric observations of CO (Feruglio et al. 2010), which showed extended, broad wings, these observations revealed the existence of massive molecular outflows with velocities of the order of $v_{OF} = 10^2$–10^3 km s^{-1}. The mass outflow rates in the molecular phase are high with values up to 1000 $M_\odot$/yr, significantly higher than most ionized outflows. CO traces the bulk of molecular gas with densities $n \geq 10^3$ cm^3. More recent works have also successfully detected denser ($n \sim 10^4$–10^7 cm^{-3}) molecular gas using more complex molecules as tracers, as for instance rotational transitions of HCN and HCO$^+$ (Aalto et al. 2012, 2015; Walter et al. 2017).

Some studies (Emonts et al. 2014; Tadhunter et al. 2014; Emonts et al. 2017) have successfully detected evidence of outflowing gas in the profile of the rotational-vibrational H_2 1–0 S(1) emission line at 2.12 μm. However, as mentioned, these transitions only trace the very hot molecular gas, which accounts only for a tiny fraction of the molecular gas. Recent models (e.g.

Richings & Faucher-Giguère 2018) have revealed that the molecular gas in galactic outflows can be warmer than the molecular gas in galactic discs, with temperatures of a few 100 K, which could be detected with rotational H_2 transitions in the mid-IR. The James Webb Space Telescope (JWST) will be able to map such transitions with high sensitivity and high angular resolution.

1.4 Measurement of Outflow Properties

This section will give an overview of the main observational challenges when assessing the impact of outflows and of the uncertainties in this process.

A property which is commonly studied to infer the outflow's capabilities to affect the gas reservoir (and thus star formation) is the mass outflow rate, $\dot{M}_{\rm OF}$. It can be inferred through the following equation:

$$\dot{M}_{\rm OF}[{\rm M}_\odot\ {\rm yr}^{-1}] = C\frac{M_{\rm OF}v_{\rm OF}}{r_{\rm OF}}, \tag{1.1}$$

where $M_{\rm OF}$ is the gas mass in the outflow, $r_{\rm OF}$ the extent of the outflow and $v_{\rm OF}$ its velocity. C is either 1 or 3 depending on assumptions about the geometry and whether the outflow rate is measured instantaneous or time-averaged. Assuming a time-averaged thin expelled shell or clumps requires $C = 1$. In this thesis I adopt $C = 1$, as this guarantees mass conservation for outflows with a constant velocity (Veilleux et al. 2017). If we instead assume a spherical or multi-conical volume with a uniform filling factor then this implies $C = 3$ (Maiolino et al. 2012). Often, the mass outflow rate is compared to the SFR of the galaxy. For this purpose, the loading factor is defined as $\eta = \dot{M}_{\rm OF}/{\rm SFR}$. Assuming η remains constant one can infer whether gas is expelled at a faster rate than stars are being formed ($\eta > 1$) or not ($\eta < 1$). I will now discuss the properties used in determining the mass outflow rate in more detail.

The outflow velocity, $v_{\rm OF}$, is often measured using a nth percentile of the total emission line, e.g. the 10th percentile, v_{10} (e.g. Perna et al. 2017). The advantage of this definition is that it is model-independent (i.e. it does not depend on the line fitting procedure). Alternatively, a combination of the offset between the systemic disc and outflow component and the the velocity line width is used (Rupke et al. 2005b; Fiore et al. 2017). The measurements of the outflow velocities suffers from a number of uncertainties. First, the outflow velocity is often measured in projection, which can lead to an underestimation of the true value. Second, the velocity may vary within the outflow itself (e.g. Walter et al. 2017; Venturi et al. 2018).

Measuring the extent of the outflow, $r_{\rm OF}$, is another major challenge of outflow studies. Many (especially early) studies did not resolve the outflow and can thus only provide an upper limit for the outflow radius (and hence a lower limit for the mass outflow rate). Even modern

integral field spectroscopy measurements can generally spatially resolve outflows only in the local Universe ($z \sim 0$). For instance, at a redshift of $z = 2$, a resolution of one arcsec corresponds to ~ 8 kpc, much larger than most observed ionized and molecular outflows. An exception to this are a number of adaptive optics-assisted observations at higher redshift (e.g. Brusa et al. 2016; Herrera-Camus et al. 2019; Kakkad et al. 2020). Another issue, even for low-redshift sources, is the ambiguous definition of the radius of the outflow. Some works measure the maximum distance (e.g. Cresci et al. 2015b; Rupke et al. 2017; Venturi et al. 2018), whereas others take the average (luminosity-weighted) distance of outflowing gas (e.g. Querejeta et al. 2016; Gowardhan et al. 2018). Beam-smearing effects are important when measuring outflow radii, in particular in type I AGN. Husemann et al. (2016) found that failing to take into account point spread function (PSF) effects in type I AGN host galaxies can lead to an overestimation of outflow energetics by up to two orders of magnitude.

The mass of the outflowing gas is usually determined based on the line luminosity. For warm ionized outflows, the mass is given by

$$M_{\mathrm{OF,ion}} = f \frac{L_{\mathrm{OF}}}{n_{\mathrm{e}}} \tag{1.2}$$

where L_{OF} is the line luminosity of the outflow, n_{e} the electron density and f a proportionality constant. Because of their insensitivity to elemental abundances in the outflow gas and to the ionization state, usually recombination lines, such as Hα or Hβ are used. Some studies use [OIII]λ5007 instead, but this can lead to an underestimation of the true outflow mass, partly because it does not take into account the fraction of ionized gas that does not emit [OIII] because oxygen is in lower ionization stages. An additional reason might be that the [OIII]-emitting region is smaller than the Hβ-emitting region as found by some works (Carniani et al. 2015). There are three main sources of uncertainty in determining the outflow mass. By far the largest uncertainty is the electron density. It can vary from a few cm^{-3} up to 10^4 cm^{-3} and can thus lead to estimates which differ by orders of magnitude (Harrison et al. 2018). Fortunately, the density can be constrained for galaxies with measurements of the [SII]λ6716/λ6731 doublet and various other ways (Davies et al. 2020). We shall discuss the different density estimates in more detail in Chapter 3. The second source of error is the uncertainty on the luminosity of the outflow. Often, there is no straightforward way to disentangle the outflow and the systemic component, especially in galaxies, where outflows are not very powerful and fast (e.g. Mingozzi et al. 2019). As a consequence, the luminosity of the outflow could be over- but also underestimated. In type I AGN there is an additional complication because recombination permitted lines have a third, very broad, component, which makes the fitting of these lines even more complicated. This is because the quasar can easily outshine the host galaxy and also because these lines are very broad and hence many emission lines are blended (e.g Rupke et al. 2017). Finally, the

constant f is temperature dependent and its precise value therefore not well determined.

Many molecular outflow studies rely on interferometric mapping of low-J CO (typically J = 1–0 or 2–1) transition. In this case, the molecular gas mass can be calculated as

$$M_{\rm OF,mol} = \alpha_{\rm CO} L_{\rm CO}(1-0) \tag{1.3}$$

with $L_{\rm CO}$(1–0) the line luminosity of the CO(J=1–0) rotational transition and $\alpha_{\rm CO}$ the CO-to-H_2 conversion factor. Similarly to the warm ionized phase, it is difficult to distinguish outflowing gas from the gas in the disc in the CO line profile and this is one major uncertainty. Furthermore, the CO-to-H_2 conversion factor, $\alpha_{\rm CO}$, is highly uncertain and, depending on the system, values between 0.15 and 4.5 $M_\odot$ (K km s^{-1} pc^2)$^{-1}$ have been used. The CO-to-H_2 conversion factor is critical for our understanding of molecular emission in general and has been subject to debate (for a detailed discussion see e.g. Bolatto et al. 2013). Traditionally a conversion factor of $\alpha_{\rm CO}$ = 0.8 $M_\odot$ (K km s^{-1} pc^2)$^{-1}$ has been employed for outflowing gas. This stems from the fact that the gas excitation of the outflow in the type I AGN Mrk 231 is similar to that in its host galaxy, which is an ULIRG (for which an $\alpha_{\rm CO}$ = 0.8 $M_\odot$ (K km s^{-1} pc^2)$^{-1}$ is generally assumed). However, some observational studies point to a larger value. For instance, Leroy et al. (2015) derive a conversion factor of about 1-2.5 $M_\odot$ (K km s^{-1} pc^2)$^{-1}$ in the starburst-driven outflow of M82. Another recent study by (Cicone et al. 2018), found a higher value of 2.1 ± 1.2 $M_\odot$ (K km s^{-1} pc^2)$^{-1}$ for outflowing gas in NGC 6240 by combining CO (1–0) data with measurements of the [CI](1–0) transition. Additionally, we should note that some hydro-chemical simulations find a value that is ∼ 6 times smaller (0.13 $M_\odot$ (K km s^{-1} pc^2)$^{-1}$) (Richings & Faucher-Giguère 2018). Another caveat in the determination of the conversion factor is the assumption that the CO (1–0) transition is optically thick. This might not hold in turbulent gas and also not in outflowing as. Indeed, through multi-transition analysis some works have found that the CO(1–0) outflow in IC 5063 is optically thin (e.g. Dasyra et al. 2016; Oosterloo et al. 2017). In the optically thin case, the conversion factor would be much lower. For a typical excitation temperature of $T_{\rm ex}$ = 30 K, $\alpha_{\rm CO}$ is 0.34 $M_\odot$ (K km s^{-1} pc^2)$^{-1}$. However, other molecular outflows do not appear to have optically thin CO gas as found by Lutz et al. (2020), who instead suggest a conversion factor around 2 $M_\odot$ (K km s^{-1} pc^2)$^{-1}$.

A further complication is that for many sources, especially at high redshift, only higher J-transitions of CO are observed. These line luminosities from high-J transtions, $L_{\rm CO}$(J–J-1), have to be converted into $L_{\rm CO}$(1–0), often without sufficient knowledge of the CO excitation ladder.

The impact of winds is often quantified using the kinetic power of the outflow, which is related to the mass outflow rate and velocity via:

$$\dot{E}_{\rm OF} = \frac{\dot{M}_{\rm OF} v_{\rm OF}^2}{2} \tag{1.4}$$

or the momentum rate, $\dot{P}_{\rm OF}$,

$$\dot{P}_{\rm OF} = \dot{M}_{\rm OF} v_{\rm OF}. \tag{1.5}$$

The above properties can be used to to distinguish between different models of radiative feedback (see Section 1.2.2) as they predict different momentum rates and coupling efficiencies. Energy-driven outflows typically assume the kinetic power of the outflow to be ~ 5 % of the AGN bolometric luminosity and a momentum rate of $\dot{P}_{\rm OF} \sim 20 L_{\rm AGN}/c$ (Zubovas & King 2012; Faucher-Giguère & Quataert 2012; King & Pounds 2015), unless the coupling efficiency with the ISM is much smaller than unity. Momentum-driven outflow models predict a lower momentum rate of $\sim L_{\rm AGN}/c$ and as a consequence the kinetic power is also lower, typically $\dot{E}_{\rm OF}/L_{\rm AGN} \sim 0.08$–$0.3$ % for plausible outflow velocities between 500–2000 km s^{-1} (Costa et al. 2014). For outflows driven by radiation pressure on dusty clouds, models expect a superlinear relation between the kinetic luminosity and the AGN luminosity: $\dot{E}_{\rm OF} \propto L_{\rm AGN}^{3/2}$ (Ishibashi et al. 2018). At high AGN luminosity, the kinetic power can amount up to 1 % of $L_{\rm AGN}$.

1.5 Thesis Aims and Overview

In this introduction, I have highlighted the importance of feedback in galaxy evolution and also discussed some of the observational evidence of galactic outflows, which is one possible manifestation of feedback.

The first aim of this thesis is to characterise the molecular outflow phase in detail in a much larger sample than in previous works, where often only individual objects were studied. I will study how outflow properties are related to properties of the host galaxy (such as the SFR or AGN luminosity). The goal is to find the physical mechanisms responsible for driving large-scale winds and compare different theoretical models (see Section 1.2.2). Furthermore, I will assess whether molecular outflows are capable of affecting star formation in the host galaxy as some studies of powerful outflows suggest.

A second goal of this thesis is to quantify the properties of the ionized outflow phase. In addition, I will shed light on the connection between different outflow phases to allow comparisons to simulations and arrive at a comprehensive picture of outflows and their potential negative feedback effect onto their host galaxies.

In the last part of the thesis, I will investigate the prevalence of positive feedback and try to understand its importance in galaxy evolution. More broadly, I will also look at the BPT diagnostics of outflows and how they influence other outflow properties.

1.5.1 Thesis Outline

Chapter 2 of this thesis investigates molecular outflows in a sample of about 50 local ($z < 0.2$) galaxies. We collect published molecular outflows and combine them with previously unpublished archival ALMA observations targeting low-J CO transitions. As part of this work, we study the driver of these molecular outflows (SF vs AGN-driven) and compare their energetics to theoretical models of outflows, such as energy-, momentum- or radiation pressure-driven models. Furthermore, we assess whether outflows escape the galaxy's gravitational potential and whether they are capable of quenching the galaxy's star formation.

Chapter 3 looks at the properties of multiphase outflows in a sample of local (ultra)luminous infrared galaxies ((U)LIRGs). For this purpose, MUSE data of a sample of ~ 25 local (U)LIRGs is analysed and complemented with observations of ionized and neutral atomic outflows from the literature. In the first part, the properties of the ionized outflow such as electron density and visual extinction are presented. In the second part, the ionized outflow phase is compared to the molecular and neutral atomic outflow phases in terms of mass and energetics as well as on a spatially resolved basis.

Chapter 4 studies further evidence for positive feedback in (U)LIRGs using a combination of BPT diagnostics and analysis of their properties (electron density, ionization parameter). For this analysis, the same sample as in Chapter 3 of ~ 25 local (U)LIRGs is used. This chapter also looks at how outflow properties vary as a funciton of their BPT classification.

Chapter 5 presents the conclusions of the work in this thesis as well as an overview of open questions and further avenues for research into outflows and their impact on host galaxies.

Chapter 2

Cold Molecular Outflows in the Local Universe and Their Feedback Effect on Galaxies

This chapter is adapted from 'Cold molecular outflows in the local Universe and their feedback effect on galaxies', A Fluetsch et al., 2019, MNRAS, 483, 4586

As explained in Chapter 1, outflows have been observed in many different phases. Of particular interest is the molecular phase as it is the phase out of which stars form. Hence, molecular outflows are possibly a direct link how feedback mechanisms can affect star formation in the host galaxy, namely by expelling the fuel for future star formation. In this chapter we study molecular outflows in a sample of 45 local galaxies, including both star forming galaxies and active galactic nuclei, primarily by using CO data from the Atacama Large Millimeter/submillimeter Array (ALMA) archive and from the literature.

2.1 Introduction

The purpose of this chapter is to explore the scaling relations between molecular outflows and galaxy properties. This will shed light on the driving mechanisms of outflows and their effect on the host galaxies. We improve relative to previous studies by significantly increasing the statistics with a sample size of nearly 50 galaxies (which is more than twice that of previous molecular outflow studies using CO data) and by tackling some of the biases and selection

effects. We use interferometric CO measurements that allow us to determine the velocity and spatial extent of the outflows. We specifically investigate the relations between outflow and galaxy properties such as star formation rate, stellar mass, and AGN luminosity.

Throughout this chapter, a $H_0 = 70$ km s^{-1} Mpc^{-1}, $\Omega_M = 0.27$ and $\Omega_\Lambda = 0.73$ cosmology is adopted.

2.2 Sample and Data Analysis

2.2.1 The Atacama Large Millimeter/submillimeter Array (ALMA)

As this chapter extensively uses data obtained with the Atacama Large Millimeter/submillimeter Array we will provide a brief introduction to the telescope and the basic principle of interferometers.

ALMA is an interferometer located on the Chajnantor plateau in northern Chile at an altitude of 5000 m above sea level. It consists of a large array of 64 12-m antennas, reaching baselines up to 16 km and a compact array with 7-m and 12-m antennas. Different receiver bands currently allow observations from 84 GHz (band 3) to 950 GHz (band 10). Interferometers have the huge advantage that they overcome the resolution limitation given by the size of the main dish in a single-dish telescope. For a single-dish telescope, the angular resolution (in radians), θ, is

$$\theta = 1.22\frac{\lambda}{D}, \tag{2.1}$$

where λ is the observed wavelength and D the diameter of the telescope. The larger the diameter, the greater the resolution. However, in radio astronomy the wavelengths (λ) are longer and resolution is therefore much lower than for optical telescopes. In addition, building telescopes with very large diameter is not practical. Currently, the largest single-dish telescope is the Five-hundred-meter Aperture Spherical radio Telescope (FAST) in the southwest of China (with a 500 m diameter as the name suggests, Nan et al. (2011)). These two factors limit the angular resolution of traditional single-dish radio telescopes.

Interferometry circumvents this resolution limitation by combining signals from several antennas, separated from each other. This allows very high angular resolution observations of objects on the sky. For an interferometer the angular resolution, θ, is given not by the size of the main dish, but by the largest baseline ($D_{\rm baseline}$), i.e. the maximum distance between two antennas:

$$\theta = 1.22\frac{\lambda}{D_{\rm baseline}}, \tag{2.2}$$

where λ is the observed wavelength. For instance, for the most extended configurations of ALMA, the resolution is therefore between 20 mas at 230 GHz to 43 mas at 110 GHz.

ALMA, like other interferometers, combines signals from different antennas using aperture synthesis. Radiation from the source travels to the antennas, but because they are physically separated, the light has to travel different distances and is out of phase. This creates an interference pattern for each pair of antennas, which we call visibility. If, as in the case of ALMA, many different pairs of antennas are included, one can obtain a set of visibilities in the so-called uv-plane, where u and v are the coordinates of the projected baseline separations in units of wavelength. According to the van Cittert-Zernike theorem (see e.g Rohlfs & Wilson 2004), these visibilities are the 2D Fourier transform of the brightness on the sky. That means the brightness on the sky is the inverse Fourier transform of the visibilities. Since there is a limited number of antennas, the visibilities are not perfectly sampled in the uv-plane. In particular, if two antennas are a distance d apart, they are only sensitive to emission on scales smaller than $\sim 1/d$, any larger structures would be resolved out. Thus, in order to be sensitive to a range of structures in the celestial object, a combination of short and long baselines is needed. In addition, longer exposure also leads to a better sampling of the uv plane as the motion of the target on the sky results in different projected baselines.

This set of visibilites can be mapped onto an image with the CLEAN algorithm (Högbom 1974), which we use also use in this chapter. First, the visbilities are inverse Fourier transformed to obtain a 'dirty image'. At the same time, a 'dirty beam' is created from the visibility plane sampling distribution. The CLEAN algorithm then assumes that the image can be modelled with a combination of point sources (delta functions). It starts with the pixel with the highest intensity in the dirty image, models it as a delta function and adds this to the clean components. This clean component is convolved with the dirty beam and subtracted from the dirty image. This process is repeated until all residual emission in the field is below a certain level (e.g. 3σ). In the final step, all the modelled emission (i.e. all clean components) is convolved with the clean beam, which is obtained by fitting a 2D Gaussian to the primary lobe of the dirty beam. During this process, the visibilites can be weighted equally (natural weighting) which results in the lowest noise level but gives poor resolution with rather high sidelobes. Alternatively, the weights are inversely proportional to the sampling density function, which gives low side lobes and provides high resolution but also relatively high noise levels. In our work, we opted for Briggs weighting (Briggs et al. 1999), which is a compromise between these two extremes (natural and uniform weighting) and simultaneously optimizes noise levels, sidelobe levels and angular resolution. The Briggs robust parameter allows us to vary smoothly between uniform (robust parameter of -2) and natural (robust parameter of 2) weighting. We used a robust parameter of 0. The channel widths vary between 20–100 km s^{-1} and whenever possible (i.e. within the ALMA windows), we map the line to high velocities ($|v| > 1500$ km s^{-1} from the CO line core) to detect possible wings.

2.2.2 Sample Selection

We have characterised molecular outflows by collecting data both from the literature and from an extensive analysis of ALMA archival data. We set an upper limit of $z < 0.2$ on the redshifts of the targets, since beyond this redshift the angular resolution of most ALMA archival observations ($>0.3''$) probes scales too coarse (>1 kpc) to enable a proper characterisation of outflows. We search the ALMA archive for low-J transitions (i.e. CO(1–0), CO(2–1) and CO(3–2)) of all local galaxies observed in these transitions and with publicly available data in the archive as of 1st April, 2018. As a result, we have analysed about 100 galaxies from the ALMA archive. However, most of these data have turned out to have sensitivities too low to enable the detection of putative faint broad CO transitions associated with outflows. However, we have detected outflow signatures in seven of these galaxies, according to the procedure described in Section 2.2.3.

We generally do not use the ALMA observations for which there is no outflow detection to set upper limits on the outflow properties (e.g. outflow rate, kinetic power, and momentum rate), since these would need knowledge of both outflow size and velocity, which is not known a priori. Yet, we can infer tentative upper limits in three cases for which the outflow is detected in other phases (in particular the ionized phase) by assuming that the (undetected) molecular outflow has the same size and velocity as those observed in the detected outflow phases. As a consequence, from the ALMA archive we have obtained molecular outflow information for a total of 10 galaxies (7 detections and 3 upper limits).

For what concerns the literature sample, we have searched for published molecular outflows at $z < 0.2$ obtained through the analysis of the CO(1–0) and CO(2–1) emission lines. We have compiled a total of 31 galaxies with published molecular outflows (five of which are upper limits). The observational parameters of these measurements are summarised in Table 2.1, where we provide the size of the synthesized beam, the observation time and the telescope used for the observation of the CO transition.

We also include four ULIRGs from González-Alfonso et al. (2017) in our sample. In these cases, the molecular outflow properties have been determined based on the FIR transitions of OH observed through the Herschel/PACS spectrometer. Their mass outflow rates are calculated assuming a single expulsion of gas, which is analogous to what we assume in this chapter (as it will be described in Section 2.2.4). For an additional four galaxies of the González-Alfonso et al. (2017) sample, the molecular outflow rates inferred from OH have been measured also through CO observation and in these cases they are in reasonable agreement (typically within a factor of 2).

Table 2.1: Literature sample

Galaxy	synthesized beam (arcsec)	on source time (hrs)	telescope
CO Literature data			
IRAS F08572+3915	3.1×2.7	20	IRAM PdBI
IRAS F10565+2448	3.5×2.9	10	IRAM PdBI
IRAS 23365+3604	3.1×2.6	10	IRAM PdBI
Mrk 273	5.0×4.0	12	IRAM PdBI
IRAS F23060+0505	5.3×4.5	3	IRAM PdBI
Mrk 876	6.0×3.9	6	IRAM PdBI
I Zw 1	4.7×3.7	8	IRAM PdBI
Mrk 231	3.2×2.8	7.4	IRAM PdBI
NGC 1266	0.7×0.6	NA	CARMA
M82	3.6×3.6	NA	OVRO millimetre array
NGC 1377	0.7×0.5	NA	SMA
NGC 6240	1.4×0.7	10	IRAM PdBI
NGC 3256	1.0×0.6	13	SMA
NGC 3628	3.0×2.4	40	NMA
NGC 253	4.0×4.0	7.5	SMA
NGC 6764	1.3×1.3	NA	IRAM PdBI
NGC 1068	0.5×0.5	NA	IRAM PdBI
IC 5063	NA*	2.4	APEX*
NGC 2146	3.4×2.8	44	NMA
IRAS 17208-0014	0.6×0.5	NA	IRAM PdBI
NGC 1614	1.5×0.8	NA	IRAM PdBI
Circinus Galaxy	2.7×2.1	NA	ALMA
SDSS J1356+1026	1.9×1.3	2.2	ALMA
ESO 320-G030	0.3×0.2	0.4	ALMA
NGC 1808	2.3×1.2	0.7	ALMA
NGC 1433	0.6×0.4	2	ALMA
M51	1.2×1.0	127	IRAM PdBI
4C 12.50	4.0×3.8	13	IRAM PdBI
IRAS 05081+7936	5.0×4.7	4	IRAM PdBI
IRAS 10035+4852	6.4×4.4	4	IRAM PdBI
IRAS F11119+3257	3.5×2.2	1.9	ALMA

Continued on next page

Table 2.1: (1): galaxy name, (2): synthsized beam size (in arcsec), * for IC 5063, the beamsize is not given, as this information relies on single-dish observations. The size of the outflow has been estimated based on the neutral outflow (see Morganti et al. 2013), (3): on source observation time in hours, (4): telescope used for the observation

The total sample used in this chapter consists of 45 galaxies whose properties, such as redshift, luminosity distance, optical classification, SFR, AGN luminosity, AGN contribution to the bolometric luminosity ($\alpha_{\rm bol} = L_{\rm AGN}/L_{\rm bol}$), molecular and atomic gas content and radio parameter $q_{\rm IR}$ are listed in Table 2.2. This sample is homogenised as described in Sections 2.2.4 and 2.2.5, i.e. the properties of the host galaxy and the outflow are calculated in a consistent way across the entire sample. We stress that even though we have not used any other selection criteria, our sample is still heavily biased, as most of the ALMA observing programmes (as well as results from the literature) have primarily targeted samples with enhanced star formation (ULIRGs or, more generally, starbursts) or with a known AGN. Nevertheless, we have significantly enlarged the sample relative to previous CO outflow studies by more than doubling its size and by including galaxies that are more representative of the massive star forming galaxy population, as they feature also lower velocity outflows and much less extreme objects than in previous studies. In particular, we have included targets from the ALMA archive culled from observing programmes that were not aimed at extreme classes of galaxies (starbursts or AGN), and this has resulted in a less biased sample than in previous studies.

However, we emphasize, once more, that the goal of this chapter is not to provide an unbiased census of the occurrence of molecular outflows in galaxies. The primary goal of this work is to explore the relations between molecular outflows and galaxy properties by sampling the broadest possible range of galaxy properties, such as SFR, mass, activity type and AGN luminosity.

To illustrate the range of SFRs and galaxy stellar masses, Fig. 2.1 shows the galaxies in our sample in the stellar mass – star formation rate plane. We also overplot the contours of the distribution of galaxies from the Sloan Digital Sky Survey Data Release 7 (SDSS DR7) release. This figure illustrates the sample selection and the biases affecting our study, but also how this work improves on earlier studies by sampling a larger part of the stellar mass – star formation rate plane. The grey points indicate galaxies from a previous study on molecular outflows by Cicone et al. (2014), the blue points show the new, additional galaxies added in this work. Different symbols indicate different optical spectral classification, as discussed more in detail

later on. The sample spans about two orders of magnitude in stellar mass and nearly four orders of magnitude in SFR. Clearly, the galaxies in our sample are not distributed uniformly over these ranges and do not even follow the distribution traced by SDSS galaxies. As a consequence of the selection biases, our sample is skewed towards massive galaxies and mainly sampling galaxies above the main sequence, hence (probably merger-driven) starbursts. Hence, we likely select galaxies which are more likely to host fast and powerful outflows. However, our sample also probes the main sequence and a few galaxies located in the green valley. Due to the selection of galaxies from published works and archival data, quiescent galaxies are not included by our sample.

In addition, the fraction of AGN in our sample ($\approx$ 50 %) is higher than in other local complete surveys, where about 10–20 % are unambiguously AGN (although the actual number might be anything up to 40 %, depending on the AGN luminosity threshold and the selection band) on the AGN luminosity threshold and the selection band) (Maiolino & Rieke 1995; Miller et al. 2003). However, this enables us to properly probe different level and types of AGN activity. The AGN in our sample probe a wide range of bolometric AGN luminosities, from very weak AGN ($\sim 10^{40}$ erg s^{-1}), to powerful AGN in the quasar regime ($\sim 10^{46}$ erg s^{-1}).

2.2.3 Identification of Outflows

The ALMA archival data have been calibrated and imaged using the CASA software version 4.7 (McMullin et al. 2007). We have ensured that the data cubes have a spectral window broad enough to find possible wings (covering at least 1500 km s^{-1}). We analyse the ALMA CO data initially by searching for outflow signatures by fitting a single or a double Gaussian profile to the CO emission integrated over the whole galaxy. Whether only one or two Gaussians are required is determined by comparing the reduced chi-square ($\chi^2_{\rm red}$) value of the respective fits. If two Gaussians lead to a decrease in $\chi^2_{\rm red}$ of 10 % or more, then we consider this as an initial clue for the possible presence of an outflow. In these cases, we also visually verify whether we can clearly distinguish a narrow ($\sigma_{\rm narrow} \lesssim 100$ km s^{-1}) and a broad component ($\sigma_{\rm broad}$ ranging from $\sim$100 km s^{-1} to several 100 km s^{-1}, depending on the galaxy). In these candidate cases, we tentatively identify the broad component as emission from an outflow. With the third criterion (see below) we ensure that broad component's flux is above 3σ.

We then verify the presence of outflows by inspecting the position–velocity (pv) diagram and producing a map of the line wings. Position–velocity diagrams are generated by extracting a 2D spectrum along a pseudo-slit placed along the major and minor axes of the galaxy and plotting the velocity as a function of the position along the pseudo-slit. The typical slit width is about 0.6 arcsec, but it is set to one beam width and hence might be larger. This is because an interferometer is not able to resolve structures smaller than the synthesized beam and a larger

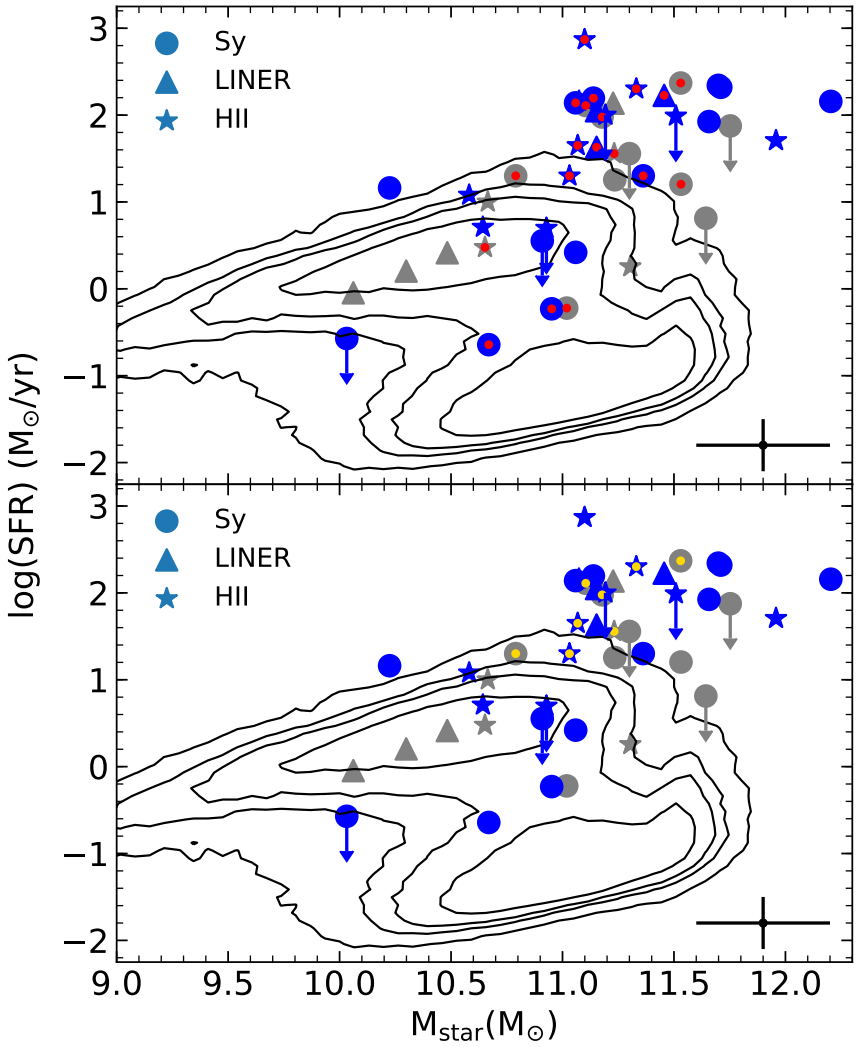

Figure 2.1: Distribution of our sample in the stellar mass-SFR diagram, compared to the SDSS galaxies (contours). The grey points show the galaxies in the sample of Cicone et al. (2014), the blue galaxies represent the additional galaxies added to that sample. The SDSS contours show the levels 100, 300, 500, 1000 galaxies. The red dot in the upper panel marks galaxies with measurements of ionized outflows, the yellow dot in the lower panel galaxies with observed neutral atomic outflows.

slit (wide-slit pv diagram) would wash out structures or patterns. Rotation-dominated galaxies show a characteristic S-shape in the pv diagram (along the major axis), whereas outflows are identified by an excess of high-velocity gas on top of normal rotation. Line wings maps are also produced by integrating over the spectral range, where the broad component (i.e. outflow component) is dominant. We determine the root mean square (rms) of the line maps and identify the wings as significant when they are detected at a significance level of $> 5\sigma$. The line wings are identified as due to outflows if they have velocities in excess of two times the width of the

narrow component and are not located in the direction of rotation. In Appendix 2.6, we show for each galaxy the spectrum integrated over the whole galaxy (defined as the region where the flux is above 3σ) including the narrow and the broad component, the pv diagrams along the major and minor axes and the line maps of the wings.

2.2.4 Outflow Properties

We calculate the outflow mass based on the flux of the broad line component, which can be converted into a CO line luminosity $L'_{\rm CO}$. This CO line luminosity is defined as the product of the velocity-integrated source brightness temperature, $T_{\rm b}\Delta v$, and the source area, $\Omega_{\rm s} D_{\rm A}^2$. $D_{\rm A}$ is the angular size distance and equal to $D_{\rm L}/(1+z)^2$ (Solomon & Vanden Bout 2005). $\Omega_{\rm s}$ is the solid angle subtended by the source. The beam-diluted brightness temperature is related to the observed integrated line intensity, $I_{\rm CO}$ via $I_{\rm CO} = \int T_{\rm mb}\, dv$ and hence $T_{\rm b}\Delta v \Omega_{\rm s} = I_{\rm CO}\Omega_{\rm s\star b}(1+z)$. Therefore, the line luminosity in K km s^{-1} is (Solomon & Vanden Bout 2005):

$$L'_{\rm CO} = 23.5 \Omega_{\rm s\star b} D_{\rm L}^2 I_{\rm CO} (1+z)^{-3}, \tag{2.3}$$

where $\Omega_{\rm s\star b}$ is in arcsec^2, the luminosity distance in Mpc and $I_{\rm CO}$ in K km s^{-1}. Alternatively, for a source of any size in terms of the total line flux, $S_{\rm CO}\Delta v$ in Jy km s^{-1} (Solomon & Vanden Bout 2005):

$$L'_{\rm CO} = 3.25 \times 10^7 S_{\rm CO} \Delta v \nu_{\rm obs}^{-2} D_{\rm L}^2 (1+z)^{-3}, \tag{2.4}$$

where $\nu_{\rm obs}$ is the observed frequency of the CO transition (in GHz), $D_{\rm L}$ the luminosity distance (in Mpc) and z the redshift. $L'_{\rm CO(1-0)}$ can in turn be converted into molecular mass of the outflow ($M_{\rm outf}(H_2)$) via $M_{\rm outf}(H_2) = \alpha_{\rm CO} L'_{\rm CO}$, where $\alpha_{\rm CO}$ is the CO-to-H_2 conversion factor. For outflows we conservatively assume a CO-to-H_2 conversion factor of 0.8 $M_\odot$/(K km s^{-1} pc^2) for consistency with previous work. This is the value typically adopted for the molecular ISM of ULIRGs (Bolatto et al. 2013). The reason for this choice is explained in Section 1.4.

For outflows observed in higher-J transitions, we assume that the CO emission is thermalized and optically thick, hence $L'_{\rm CO(3-2)} = L'_{\rm CO(2-1)} = L'_{\rm CO(1-0)}$. This is consistent, within the errors, with what was found in Mrk 231 (Feruglio et al. 2015). The double-component fitting allows us to directly estimate the outflow velocity ($v_{\rm outf}$) using the prescription of Rupke et al. (2005b): $v_{\rm outf} = {\rm FWHM_{broad}}/2 + |v_{\rm broad} - v_{\rm narrow}|$, where $\rm FWHM_{broad}$ is the full width at half maximum of the broad component, and $v_{\rm broad}$ and $v_{\rm narrow}$ are the velocity centroids of the broad and narrow components, respectively. The spatial extent of the outflow is calculated based on the line maps of the broad wings. We fit a 2D-Gaussian profile to the wing map and use the beam-deconvolved major axis (FWHM) divided by two as the radius of the outflow.

The mass outflow rate, $\dot{M}_{\rm outf}(H_2)$, is calculated assuming time-averaged thin expelled shells or clumps (see Section 1.4):

$$\dot{M}_{\rm outf}(H_2) = \frac{v_{\rm outf}(H_2) M_{\rm outf}(H_2)}{r_{\rm outf}(H_2)}. \tag{2.5}$$

where $v_{\rm outf}(H_2)$, $r_{\rm outf}(H_2)$ and $M_{\rm outf}(H_2)$ are the velocity, radius, and molecular gas mass of the outflow, respectively. This formula assumes that the outflow started at point -$t_{\rm outf}$ = -$r_{\rm outf}/v_{\rm outf}$ and has a constant mass outflow rate (Lutz et al. 2020). This description allows us a better comparison with models than the assumption of spherical (or multi-conical) volume with uniform filling factor (Cicone et al. 2015; Pereira-Santaella et al. 2016; Veilleux et al. 2017). It has also been argued that the formula above is more realistic because the emission does not brighten at large radius as we would expect for the model of a spherical outflow with uniform filling factor (Lutz et al. 2020). It can be shown that between the two scenarios, there is a difference of a factor of 3 in the estimates of the outflow rate (and derived quantities such as kinetic power and momentum rate), which does not alter our conclusions significantly. Projection effects certainly plague the estimation of the outflow radius and velocity. However, as discussed in Cicone et al. (2015), since the orientations of outflows are distributed randomly, it can be shown that the resulting average correction factor is unity, hence statistically the (unknown) projection correction factors cancel out on average, though they certainly introduce scatter. In line with Cicone et al. (2014), we assume a 50 % error on the outflow velocity due to projection effects. The different estimates of $\alpha_{\rm CO}$ for the outflowing gas lie within a factor of $\sim$ 3 assuming optically thick emission as found in most galaxies by Lutz et al. (2020) (for details see Section 1.4). By combining all sources of uncertainty, we infer that the average uncertainty on the mass outflow rate is about 0.3 dex. The errors on the associated outflow properties (kinetic power, momentum rate) is estimated to be as large as 0.5 dex because the mass outflow rate is multiplied again with the outflow velocity (and its error). The outflow properties of all 45 galaxies are shown in Table 2.3. In this table, we provide mass outflow rate, outflow radius, outflow velocity and associated outflow properties. Furthermore, ionized and neutral mass outflow rate as well as escape fractions are also included in this table.

2.2.5 Ancillary Information

In this section, we provide ancillary information on the host galaxy, which are summarized in Table 2.2.

2.2.5.1 Optical Classification

In terms of activity classifications, we refer to galaxies as 'star forming', 'Seyfert', and 'LINER' based on their optical spectroscopic classification, and in particular through the [SII]-BPT diagram (Kewley et al. 2006). The nature of galaxies classified as 'LINER' is not always clear, and this classification appears to include a mixed population. It has been shown that the 'LINER' emission can extend on kpc-scales across a large fraction of passive and green valley galaxies (hence renaming this class as 'LIER', i.e. dropping the 'N' which stands for 'Nuclear' in the original acronym) and correlates with the old stellar population, and this can be explained in terms of excitation by the hard radiation field produced by evolved post-AGB stars (e.g. Sarzi et al. 2010; Belfiore et al. 2016). However, in the nuclear regions, LI(N)ER-like emission can also be associated with excitation by weak, radiatively inefficient AGN (e.g. Ho et al. 1993). Yet, in LIRGs, ULIRGs, and other galaxies characterised by prominent outflows, which are most of the LINER-like galaxies in our sample, LI(N)ER-like diagnostics are likely associated with shock excitation (e.g. Monreal-Ibero et al. 2006). Many authors broadly group Seyfert and LI(N)ER-like diagnostics into a generic 'AGN' category. As discussed above, this rough classification can be misleading as in many galaxies the LINER classification is not associated with an AGN at all; however, in the case of our sample, it is true that many LINER-like galaxies do host an AGN based on the X-ray or mid-IR properties; therefore in a few instances in the chapter (e.g. Section 2.3.1) we will adopt this classification as well. Regardless of the optical classification, the role of the AGN, if present, will be clarified by the AGN fractional contribution to the bolometric luminosity, as discussed in the following.

2.2.5.2 AGN Luminosity

AGN bolometric luminosities were derived from the hard X-ray flux (2–10 keV) by using the relation given in Marconi et al. (2004): $\log[L_{\rm AGN}/L\ (2\text{-}10\ {\rm keV})] = 1.54 + 0.25\mathcal{L} + 0.012\mathcal{L}^2 - 0.0015\mathcal{L}^3$, where $\mathcal{L} = (\log L_{\rm AGN} - 12)$ and $L_{\rm AGN}$ is the AGN bolometric luminosity in units of $L_{\odot}$. Typically, X-ray-based AGN luminosities have a scatter of ~ 0.1 dex (Marconi et al. 2004). In a few cases where no X-ray data are available, or the source is Compton-thick, we used the [OIII]λ5007 luminosity. In this case, the AGN luminosity is inferred from the relation $L_{\rm AGN} \sim 3500\ L_{\rm [OIII]}$ (Heckman et al. 2004). In some cases for which [OIII]λ5007 is not available, or where the object is heavily obscured in the optical, we estimated the AGN luminosity by using the AGN contribution to the bolometric luminosity, $\alpha_{\rm bol}$, as inferred from various mid-IR diagnostics in the literature (Veilleux et al. 2009; Nardini et al. 2009, 2010). Nardini et al. (2009) and Nardini et al. (2010) use spectral features in the wavelength range of 5-8 μm that allow them to disentangle AGN and starburst contribution. Veilleux et al. (2009)

use six different IR-based methods, as for instance the equivalent width of the PAH feature at 7.7 μm and the continuum ratio of f_{30}/f_{15}, and average them to calculate the AGN contribution. Using the AGN fraction, we can then calculate the AGN luminosity via $L_{\rm AGN} = \alpha_{\rm bol} L_{\rm bol}$, where in most cases $L_{\rm bol} \approx L_{\rm IR}$ (although for ULIRGs $L_{\rm bol} \sim 1.15\ L_{\rm IR}$ (Veilleux et al. 2009)). In the rest of the chapter, $\alpha_{\rm bol} = L_{\rm AGN}/L_{\rm bol}$ refers to the AGN contribution to the total IR luminosity, which generally dominates in most of our galaxies, although in a few, more quiescent galaxies the stellar optical/NIR light may contribute significantly. The uncertainty of the IR luminosity consists of the contribution from uncertainties on the IR fluxes at 12, 25, 60, and 100 μm, which are generally below 10 % and the scatter in the calculation of the total IR luminosity, $L_{\rm IR}$, based on these IRAS fluxes, which is about 10-20 % (Takeuchi et al. 2005). In total, we therefore conservatively assume 30 % uncertainty on $L_{\rm IR}$.

2.2.5.3 Star Formation Rate

To compute the total star formation, we use the $L_{\rm IR}$-SFR relation given in Kennicutt & Evans (2012), which assumes a Chabrier initial mass function (IMF) and the total IR luminosity from 8 to 1000 μm, corrected for the AGN contribution through the $\alpha_{\rm bol}$ factor. The uncertainty in SFRs stems from uncertainties on $L_{\rm IR}$ (which is discussed above and amounts to $\sim$ 30 %) and on $\alpha_{\rm bol}$. $\alpha_{\rm bol}$ has similar values using various techniques and they usually agree within 10-15 % (Veilleux et al. 2009). We assume this as the typical error. The conversion of IR luminosity to SFR comes with a 30 % calibration uncertainty (Kennicutt 1998). For SFR estimates, we therefore conservatively infer a typical uncertainty of 0.3 dex.

2.2.5.4 Gas Content

The molecular gas mass in the host galaxy is inferred from the CO(1-–0) (narrow) line luminosity, $L'_{\rm CO}$, as discussed above. The CO-to-H_2 conversion factor is one of the major uncertainties in the calculation of the molecular gas mass and depends heavily on the metallicity and physical state of the molecular ISM (Bolatto et al. 2013). We adopt three different CO-to-H_2 conversion factors depending on the type of galaxy. For ULIRGs, we adopt $\alpha_{\rm CO} = 0.8\ {\rm M}_\odot\ ({\rm K\ km\ s^{-1}\ pc^2})^{-1}$, for LIRGs we use $\alpha_{\rm CO} = 1.2\ {\rm M}_\odot\ ({\rm K\ km\ s^{-1}\ pc^2})^{-1}$ and for all other galaxies we use a Milky Way-type conversion factor of $4.4\ {\rm M}_\odot\ ({\rm K\ km\ s^{-1}\ pc^2})^{-1}$ (Bolatto et al. 2013).

For about half of the galaxies 21 cm HI, single dish observations are also available that provide the atomic gas mass in the host galaxy.

2.2.5.5 Stellar Mass

Stellar masses are calculated for all galaxies in this sample by using the K-band magnitude and a colour correction (e.g. B-V) (Bell et al. 2003). K-band magnitudes are taken from the extended source catalogue of 2MASS (Skrutskie et al. 2006).

However, the presence of an AGN can potentially contaminate the observed fluxes. For Seyfert II galaxies, the direct continuum radiation from the accretion disc is obscured along our line of sight, but the hot dust heated by the AGN can still contribute significantly to the light observed in the K-band. Therefore, in the case of Seyfert II galaxies, in order to avoid the latter issue, we use J-band magnitudes that are not affected by AGN-heated circumnuclear dust emission, and estimate the K-band magnitude by assuming J–K=0.75, which is the average colour (with little scatter) found by Mannucci et al. (2002).

For Seyfert I galaxies in our sample, a contamination by the AGN might be very high also in the J-band and optical bands (because the radiation from the accretion disc is directly observable) and, therefore, we need to use a different approach. For Mrk 231 and IRAS F11119 + 3257, the contribution of the AGN to the total magnitudes has been estimated in Veilleux et al. (2002) and we simply subtract this nuclear contribution to estimate the stellar masses in these two galaxies. For the other three Seyfert I galaxies, we compute the stellar mass by using the H-band magnitude of the host (which does not include nuclear contribution by the AGN) inferred by Zhang et al. (2016) and the mass-to-light correction given in their paper.

For non-type I AGN, the colours for the mass-to-light ratio correction are obtained from the literature. We combine different colours, u-g for galaxies with SDSS photometry, B-V from VERONCAT, the Veron Catalogue of Quasars and AGN (Véron-Cetty & Véron 2010), or from the GALEX survey (Gil de Paz et al. 2007) and B-R from the APM catalogue[a]. In a few cases where no information about colours is available, we assume an average logarithmic mass-to-light correction of –0.08 (Bell et al. 2003; Zhang et al. 2016). Our final errors on the stellar mass comprises errors on the photometry of the host galaxy (H, J or K-band) and the uncertainty of the $M_\star/L$ ratio. The K-band magnitudes are estimated to have an 0.1 mag uncertainty based on comparison between different samples (Bell et al. 2003). In the J and H-band, the typical uncertainty is 0.2 mag (Zhang et al. 2016). Our estimates of $M_\star/L$ ratios have a typical systematic error of about 25 % that stems from uncertainties in galaxy age, dust extinction, and the impact of SF bursts on the star formation history (Bell et al. 2003). Furthermore, for AGN host galaxies, additional uncertainties might be introduced by the corrections applied here. A different approach by Zibetti et al. (2009) based on a library of model galaxies and $M_\star/L$ derived from the colours of those, finds a different colour-$M_\star/L$ relations. These can be

[a] http://www.ast.cam.ac.uk/~mike/apmcat/

as large as 0.5 dex at the bluest colours (which are usually not found in our sample). However, results by Taylor et al. (2011) suggest that these differences are likely smaller if a different prescription for dust reddening is used. Therefore, we obtain an average error of 0.2 dex on the stellar masses. Although the use of different colours for some of the galaxies may potentially be a matter of concern, Bell & de Jong (2001) and Taylor et al. (2011) have shown that there is no systematic uncertainties on the inferred stellar masses when different colours and different (IR/red) bands are used.

2.2.5.6 Radio Emission

In order to investigate the potential link between outflows and radio jets, we have also collected data about the radio power in galaxies at 1.4 GHz, mostly by using the database provided by NED. Since in normal star forming galaxies the radio luminosity simply scales with the SFR as traced by the IR luminosity (e.g. Yun et al. 2001; Ivison et al. 2010), the contribution from a radio jet can be inferred in terms of excess relative to the radio-to-IR ratio observed in normal star forming galaxies. Therefore, in Table 2.2 we provide the quantity $q_{\rm IR}$, which is the ratio between the rest frame 8-to-1000 μm flux and the 1.4 GHz monochromatic radio flux (Ivison et al. 2010).

2.3 Results

In this section, we report the main results obtained through our sample of molecular outflows, in combination with the ancillary data. A more extensive analysis of the results and of their interpretation is given in Section 2.4.

2.3.1 Mass Outflow Rate Scaling Relations

In this section, we start investigating the scaling relations between the molecular outflow rate and galaxy properties, with the goal of obtaining a first indication of the driving mechanism in different regimes.

2.3.1.1 Dependence on SFR and $L_{\rm AGN}$

Figure 2.2 shows the molecular mass outflow rate, $\dot{M}_{\rm outf}(H_2)$, as a function of the SFR, colour-coded by the AGN contribution to the bolometric luminosity, $\alpha_{\rm bol}$. Similar to what was found in smaller samples in previous works (Cicone et al. 2014; García-Burillo et al. 2015), the star forming/starburst galaxies have a mass-loading factor $\eta = \dot{M}_{\rm outf}(H_2)/{\rm SFR}$ consistent with unity or slightly lower. In this chapter we assume that in star forming galaxies the contribution to the

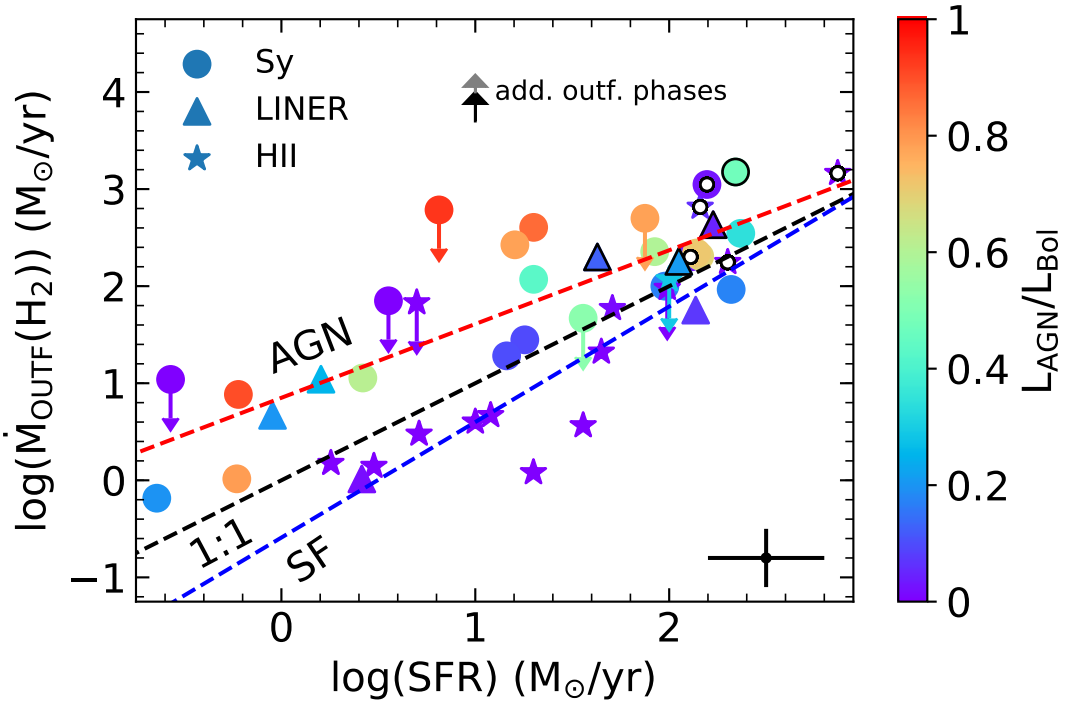

Figure 2.2: Mass outflow rate as a function of SFR. The black dashed line shows the relation for an outflow mass-loading factor of $\eta = \dot{M}_{\rm outf}({\rm H_2})/{\rm SFR} = 1$. The red and blue dashed lines represent the best fits to AGN hosts and star forming/starburst galaxies, respectively. The vertical black and grey arrows indicate the average correction of the outflow rate, for AGN and star forming galaxies, respectively, once the atomic (ionized and neutral) phase average contributions to the outflow rate (for details see Chapter 3) are included. The data points are colour-coded according to their AGN contribution ($L_{\rm AGN}/L_{\rm bol}$), as given in the colour bar on the right. The data points with black edges are molecular outflows inferred from OH measurements by González-Alfonso et al. (2017). The symbols with a central white dot are the candidate 'fossil' outflows (see Section 2.4.3).

total mass-loss rate is similar for different gas phases (ionized/neutral atomic and molecular). By including all the gas phases, the total mass-loss rate increases roughly by 0.5 dex, which is indicated by the grey arrow, and which brings the total loading factor closer to (or exceeding) unity for star forming galaxies. A more detailed analysis of multiphase outflows and the relative importance of different gas phases will be provided in Chapter 3. However, for the moment we focus on the molecular outflow rate. The best fit of the relation between molecular outflow rate and SFR for SF galaxies (shown as a dashed blue line in Fig. 2.2) is $\log(\dot{M}_{\rm outf}({\rm H_2})/({\rm M_\odot\ yr^{-1}})) = 1.19^{+0.16}_{-0.16}\log({\rm SFR}/({\rm M_\odot\ yr^{-1}})) - 0.59^{+0.28}_{-0.28}$. This and the following fits are performed by using linmix (Kelly 2007), considering the error bars both in x and y direction and including upper limits.

The AGN host galaxies have a mass-loading factor larger than unity, especially those that

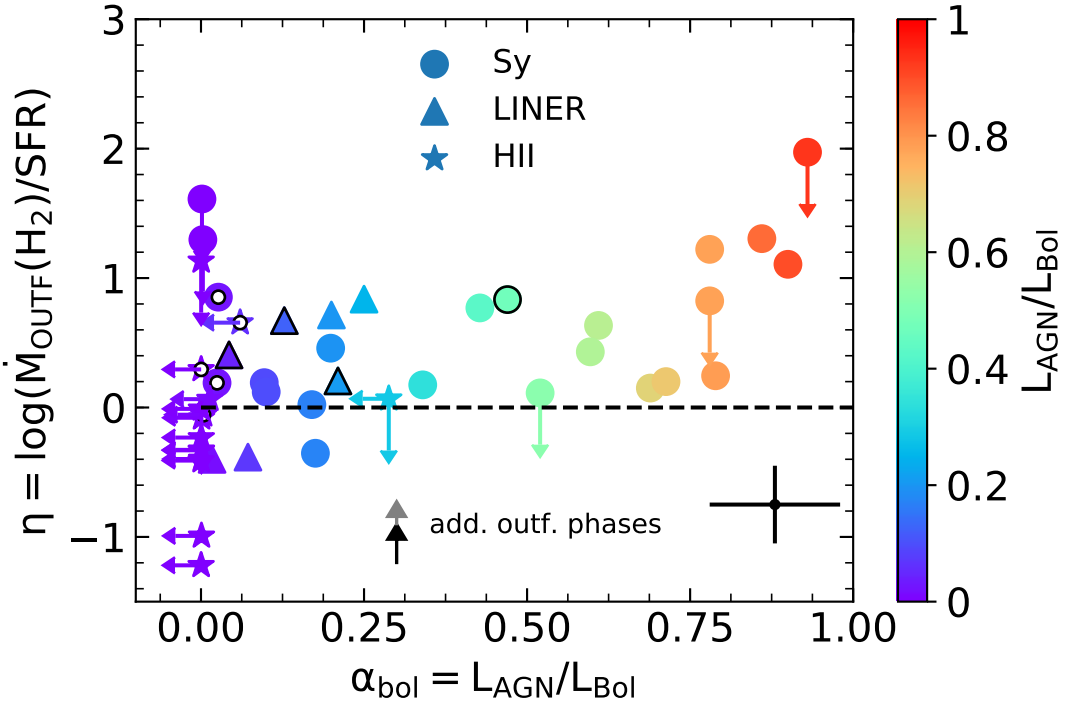

Figure 2.3: Mass-loading factor $\eta = \dot{M}_{outf}(H_2)/SFR$ as a function of AGN fractional contribution to the bolometric luminosity, L_{AGN}/L_{bol}. The black dashed line shows the relation for an outflow mass-loading factor $\eta = 1$. Colour-coding and symbols are the same as in Fig. 2.2.

are AGN dominated, and η ranges from a factor of a few up to a hundred. The best-fitting relation for AGN host galaxies is $\log(\dot{M}_{outf}(H_2)/(M_\odot\ yr^{-1})) = 0.76^{+0.11}_{-0.11}\log(SFR/(M_\odot\ yr^{-1})) + 0.85^{+0.18}_{-0.18}$ and is shown with a red dashed line in Fig. 2.2. As we will discuss in Chapter 3, in AGN host galaxies the atomic phase makes, on average, a comparable contribution to the outflow rate as the molecular phase, while the ionized phase is generally negligible, at least in the luminosity range probed by us. To account for all phases in the outflow rate of AGN host galaxies, we therefore add 0.3 dex to the molecular mass outflow rate (shown as black arrow in Fig. 2.2). The effect of including the atomic component of the outflow for AGN is shown with a black arrow.

The outflow properties inferred in star forming galaxies are in good agreement with models predicting a mass-loading factor η close to 1 (e.g. Finlator & Davé 2008; Davé et al. 2011; Heckman et al. 2015), where feedback from supernovae (SNe) is the main outflow driver and required to properly regulate star formation in galaxies.

Galaxies containing an AGN have loading factors larger than 1, indicating that gas is removed at a faster rate than stars are formed. In particular, the presence of a strong AGN in the galaxy increases the (molecular) outflow mass-loading factor substantially. In particular, the

higher the AGN contribution ($\alpha_{\rm bol}$, see colour-coding in Fig. 2.2), the higher their mass-loading factor η. This is illustrated even more clearly in Fig. 2.3, where the relation between the outflow loading factor, i.e. $\eta = \dot{M}_{\rm outf}({\rm H_2})/{\rm SFR}$, and $\alpha_{\rm bol} = L_{\rm AGN}/L_{\rm bol}$ is shown. However, a correlation is seen only at $L_{\rm AGN}/L_{\rm bol} > 0.7$, while at $0.1 < L_{\rm AGN}/L_{\rm bol} < 0.7$, the loading factor η simply scatters between 1 and 10 for AGN. As we will discuss further later on, this is probably due to two effects: (1) additional contribution from star formation to the outflow rate (which, however, is expected to contribute only with $\eta \sim 1$); 2) the fact that the outflow has much longer time-scale ($> 10^6$ yr) than the AGN accretion variability ($\sim$ 10–10^5 yr) (Gilli et al. 2000; Schawinski et al. 2015), hence the outflow is expected to generally outlast an AGN that has recently switched off, or decreased in luminosity.

Figure 2.4 shows the correlation between the mass outflow rate and $L_{\rm AGN}$. The dashed line shows the best fit to the AGN host galaxies (LINERs, Seyfert I and Seyfert II), excluding purely star forming galaxies (optically classified as star forming/starburst), which gives the following relation: $\log(\dot{M}_{\rm outf}/({\rm M_\odot\ yr^{-1}})) = 0.68^{+0.10}_{-0.10}\ \log(L_{\rm AGN}/({\rm erg\ s^{-1}})) - 28.5^{+4.6}_{4.6}$. Comparing with the predictions from chemo-hydrodynamic simulations (Richings & Faucher-Giguère 2018), the observed values are about 1 dex higher at $L_{\rm AGN} = 10^{44}$ erg s^{-1}, but are consistent with simulations at $L_{\rm AGN} \approx 10^{46}$ erg s^{-1} within the errors. Although Seyfert galaxies show a correlation between AGN luminosity and molecular mass outflow rate, suggesting that these outflows are AGN driven, this correlation is looser and with a larger scatter than previously found in the literature (e.g. Cicone et al. 2014; Fiore et al. 2017), probably as a consequence of our sample being less biased. Nevertheless, this is still supportive of the scenario in which luminous AGN boost the outflow rate by a large factor and nearly proportionally to the AGN radiative power. It is interesting to note that Fig. 2.4 clearly shows the presence of a significant fraction of galaxies (indicated by symbols with a central white dot) with high outflow rates but little AGN contribution and, for those classified as AGN, clearly not following the correlation observed for the bulk of luminous AGN host galaxies. As discussed above, this is partly due to contribution by star formation, but the bulk of the effect may be due to 'fossil' AGN-driven outflows as will be clarified in Section 2.4.

2.3.1.2 Dependence on Galaxy Stellar Mass

Fig. 2.5 shows the outflow rate as a function of stellar mass. This plot shows some correlation, which may be indirectly linked to the correlation between outflow rate and SFR, through the stellar mass-SFR relation for galaxies on the 'main sequence'. An important prediction of theoretical models of feedback from star formation is that the outflow loading factor should anticorrelate with the galaxy stellar mass as $\eta \propto M_\star^{-0.5}$, as a consequence of the deeper gravitational potential well in more massive galaxies (Mitra et al. 2015; Somerville et al. 2015;

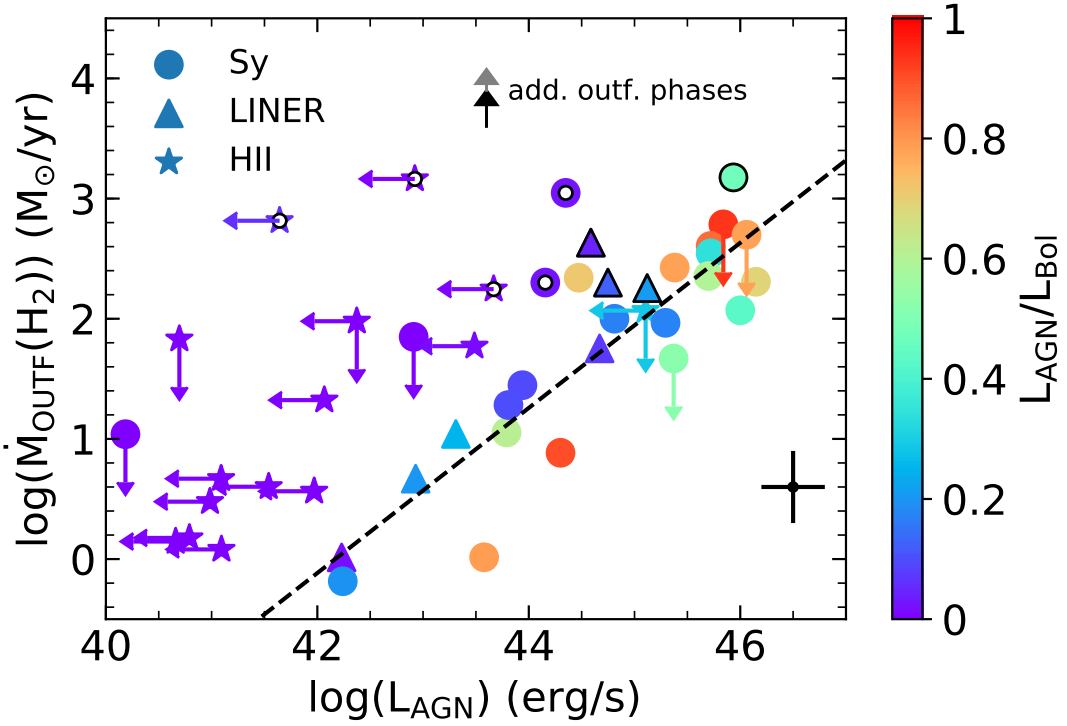

Figure 2.4: Mass outflow rate as a function of AGN (bolometric) luminosity. The dashed line indicates the fit to the AGN host galaxies (LINERs, Seyfert I and II). Colour-coding and symbols are the same as in Fig. 2.2.

Chisholm et al. 2017). Figure 2.6 shows the dependence of the mass-loading factor η on the stellar mass. Clearly, the observed relation between outflow mass-loading factor and stellar mass is very scattered. A linear regression indicates that there is only a weak anticorrelation of the form $\log(\eta) = -0.18\ ^{+0.24}_{-0.24}\log(M_\star/M_\odot) + 2.3^{+2.7}_{-2.6}$. This is only marginally consistent with theoretical predictions. However, before invoking any tension with theoretical models one should be aware of three main issues: (1) we include AGN-driven and star formation-driven outflows, whereas the models make predictions about outflows driven by SNe and stellar radiation pressure, (2) the range of stellar masses is probably too narrow to properly test the theoretical predictions, especially given that the dependence of the outflow rate on mass is weak (slope of –0.5 in log), (3) the simple relation of outflow rate with stellar mass is convolved with the dependence on SFR and with the AGN contribution, which likely dominate the scatter of any relation with $M_\star$. We address the last issue in the following subsection.

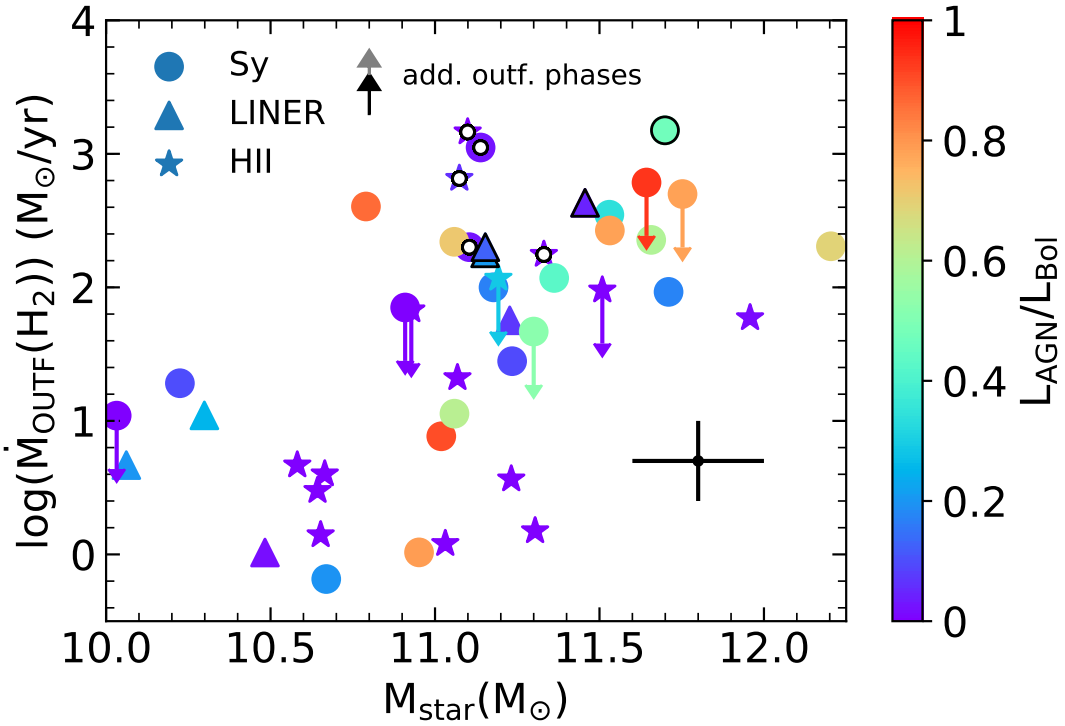

Figure 2.5: Molecular mass outflow rate as a function of galaxy stellar mass. Colour-coding and symbols are the same as in Fig. 2.2.

2.3.1.3 Disentangling the Outflow Dependence on Host Galaxy Parameters

In the previous subsections, we have shown how the outflow rate depends on galaxy properties (such as stellar mass, SFR, and the luminosity of the AGN). However, it is difficult to isolate the role played by each of these quantities, especially given that they are correlated. In this section, we attempt to disentangle the contribution of these different factors.

For this purpose, we performed a regression as follows:

$$\log(\dot{M}_{\rm outf}) = \mathrm{x}\ \log(\alpha \mathrm{SFR} + \beta L_{\rm AGN}) + \mathrm{y}\ \log M_{\star}, \tag{2.6}$$

and finding the values of the parameters that minimize the dispersion around this relation. The reason for using this expression is that for starburst galaxies we only have an upper limit on the AGN luminosity. Combining the SFR and AGN in the term in parenthesis ensures that this term never diverges to very negative values in log, i.e. it ensures that when we investigate galaxies with outflows there is always a driving mechanism, either SF or AGN. We have excluded our candidate fossil outflows, as they are expected not to follow a relation with AGN or SFR, although AGN variability will still be a source of scatter.

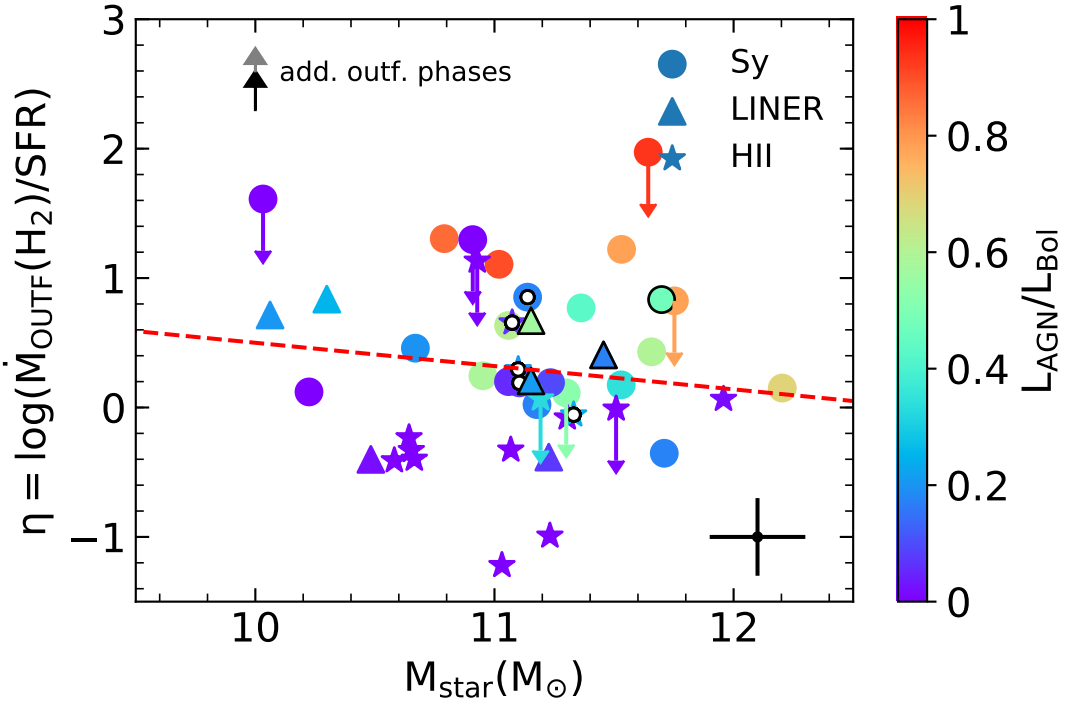

Figure 2.6: Mass-loading factor as a function of stellar mass. The red dashed line shows the best fit to the data. Colour-coding and symbols are the same as in Fig. 2.2.

The resulting best fit is:

$$\log(\dot{M}_{\rm outf}({\rm H_2})/({\rm M_\odot\ yr^{-1}})) = 1.14\log\Big(0.52\frac{\rm SFR}{\rm M_\odot\ yr^{-1}} + 0.51\frac{L_{\rm AGN}}{10^{43}{\rm erg\ s^{-1}}}\Big) - 0.41\log\Big(\frac{M_\star}{10^{11}{\rm M_\odot}}\Big), \quad (2.7)$$

with one standard deviation errors on the four parameters being Δ(x, α, β, y) = (0.12, 0.19, 0.25, 0.25). The resulting relation is shown in Fig. 2.7. In this figure, we show the molecular mass outflow rate as a function of the stellar mass, SFR and AGN luminosity of their host galaxies. Clearly, the large dispersion seen in the previous plots (outflow rate versus $L_{\rm AGN}$, versus SFR and versus $M_\star$ separately) is greatly reduced in this relation, indicating that we are simultaneously capturing the contribution of these three factors to the outflow rate. Very interestingly, this relation enables us to disentangle (at least partly) the contribution of the three factors to the outflow rate. The dependence on stellar mass is now seen more clearly: the dependence has a power-law index of –0.41, which is very close to the value expected by theory of –0.5 for outflows driven by star formation. As our sample also includes AGN-driven outflows, it is likely that these have mass-loading factors that decrease with stellar mass, too. In such an analysis we cannot disentangle the power-law index of the dependence on AGN luminosity and SFR separately. With the functional form adopted by us the combined dependence has a

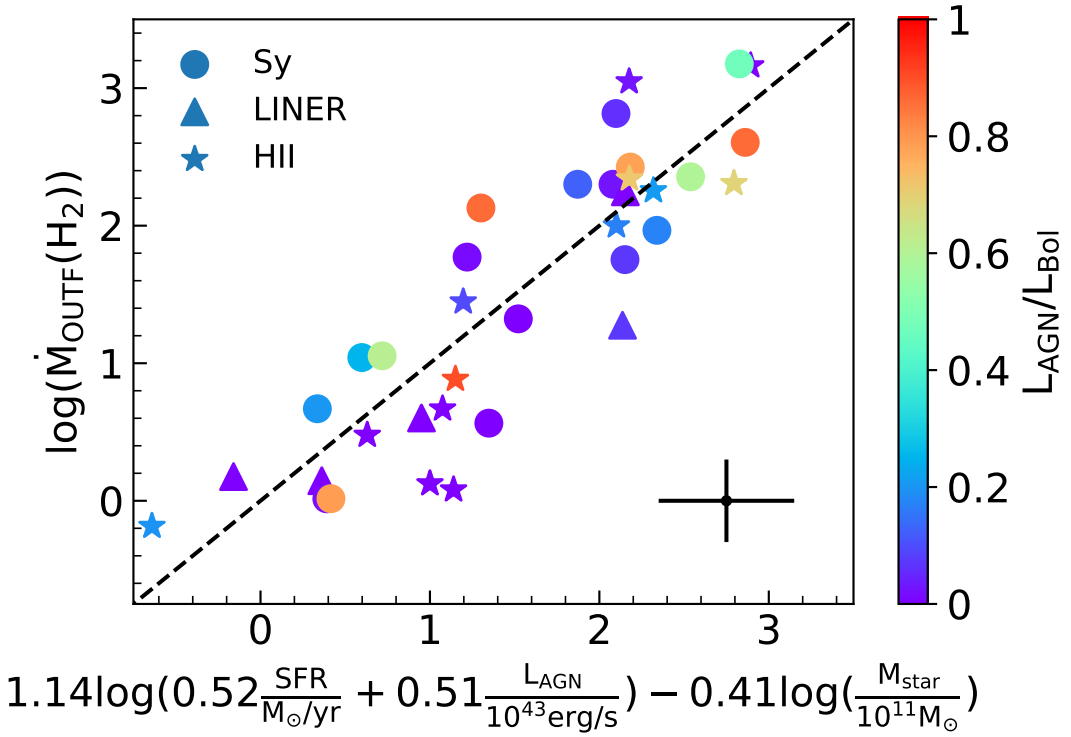

Figure 2.7: Simultaneous multiple linear regression fit of the molecular outflow rate as a function of SFR, stellar mass, and AGN luminosity, as given in equation 2.7. Colour-coding and symbols are the same as in Fig. 2.2.

power-law index of 1.1, i.e. a nearly linear relation, as expected in many models at least for the SFR.

However, this relation only accounts for the molecular phase of the outflow. Including the atomic-neutral and ionized phases is difficult because we do not have enough statistics in terms of galaxies that have all three outflow phases measured. As mentioned in Section 2.3.1, we can roughly account for these two phases by including a factor of 3 for star forming galaxies (as they have an ionized and atomic outflow rates that are similar to the molecular outflow rate) and a factor of 2 for AGN-dominated galaxies (as they have an atomic outflow rate similar to the molecular outflow rate and a negligible contribution from the ionized outflow rate, at least in our luminosity range (see Chapter 3)). In this case, the resulting best fit for the *total* outflow rate is given by

$$\log(\dot{M}_{\rm outf}({\rm tot})/({\rm M}_\odot\ {\rm yr}^{-1})) = 1.13\ \log\Big(1.29\frac{\rm SFR}{{\rm M}_\odot\ {\rm yr}^{-1}} + 0.81\frac{L_{\rm AGN}}{10^{43}{\rm erg\ s}^{-1}}\Big) - 0.37\ \log\Big(\frac{M_\star}{10^{11}{\rm M}_\odot}\Big), \tag{2.8}$$

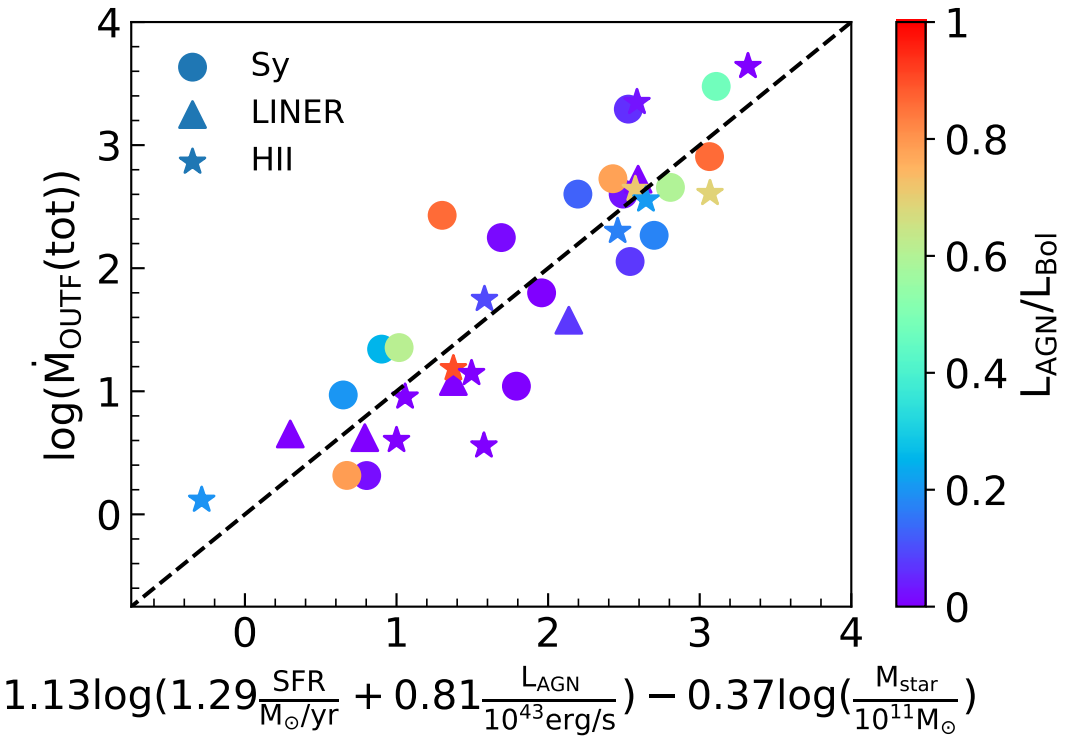

Figure 2.8: Simultaneous multiple linear regression fit of the *total* outflow rate as a function of SFR, stellar mass, and AGN luminosity, as given in equation 2.8. Colour-coding and symbols are the same as in Fig. 2.2.

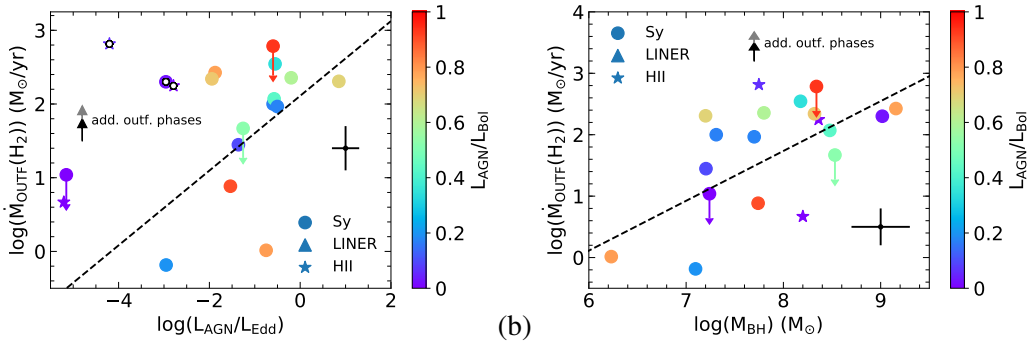

Figure 2.9: (a): Outflow rate as a function of Eddington ratio, i.e. L_{AGN}/L_{Edd}. (b): Outflow rate as function of black hole mass. Colour-coding and symbols are the same as in Fig. 2.2.

with one standard deviation errors on the four parameters being Δ(x, α, β, y) = (0.55, 0.45, 0.12, 0.24). The resulting fit is shown in Fig. 2.8, which has a scatter even smaller than in Fig. 2.7.

These *global* relations can be used to infer the expected outflow rate in any kind of galaxies, and provide an appropriate comparison for the theoretical models and simulations.

2.3.1.4 Dependence on Eddington Ratio

In the previous subsections, we have investigated the dependence on nuclear activity in terms of AGN absolute luminosity. However, both in energy-driven outflows and radiation pressure-driven outflows (the two main mechanisms proposed for AGN outflows), the most fundamental quantity is the AGN luminosity relative to the Eddington limit, $L_{\rm AGN}/L_{\rm Edd}$. This quantity is more difficult to determine as it requires an estimate of the black hole mass. The latter has been inferred only for about half of the galaxies in our sample with a variety of methods (primarily through virial estimators) and these measurements are subject to large uncertainties. The major contribution to this uncertainty stems from the virial coefficient f, which shows a scatter of 0.44 (Woo et al. 2010). The left-hand side of Fig. 2.9 shows the outflow rate as a function of Eddington ratio. If one excludes SF-dominated galaxies, which are driven by a different mechanism (see also discussion in the next sections), the plot shows some correlation between outflow rate and Eddington ratio, although with a few points subject to large scatter. Such a scatter could partly be accounted for by the uncertainties in the black hole masses. Additional discussion on this dependence will be given in Section 2.4.

2.3.1.5 Dependence on Black Hole Mass

In Fig. 2.9 on the right, we also show the outflow rate as a function of black hole mass. In principle, one should not expect any correlation of the outflow rate with the black hole mass, but the plot clearly shows a significant correlation. Such a correlation was already identified by Rupke et al. (2017), although with lower statistics. One interpretation is that this correlation is simply a consequence of the correlation between outflow rate and stellar mass (Section 2.3.1.2), through the black hole-galaxy mass relation. However, another possibility is that the correlation between outflow rate and black hole mass traces the average driving effect that the black hole has during its intermittent accretion phases. Indeed, if one assumes that the black hole accretes at a given Eddington fraction $L_{\rm AGN}/L_{\rm Edd}$ (e.g. at the average Eddington fraction of the AGN population) and with an average duty cycle, then the black hole mass may be a tracer of the average AGN activity over the past $\sim 10^6 - 10^8$ yr, i.e. on time-scales closer to the outflow dynamical time-scale, hence resulting in the observed correlation. We discuss the effects of the

AGN flickering further in the next sections.

2.3.1.6 Dependence on Radio Power

Galactic outflows are seen to also be linked with the presence of radio jets. The connection appears to be common for what concerns the ionized phase of outflows (Mullaney et al. 2013). Furthermore, clear indications that some molecular and atomic outflows are associated with radio jets have been found (e.g. Morganti et al. 2013, 2015; Dasyra et al. 2015, 2016). However, it is not yet clear how common this association is among molecular outflows.

We have explored this connection in our sample by investigating the correlation of the outflow rate with the excess of radio power relative to the value expected from the radio-SFR correlation, which is traced by the parameter $q_{\rm IR}$, defined as the ratio between the FIR flux and the monochromatic flux at 1.4 GHz (Section 2.2.5.6). Fig. 2.10 shows the molecular outflow rate as a function of the parameter $q_{\rm IR}$. The vertical dashed line indicates the average value for star forming galaxies, while the solid vertical line indicates the limit below which galaxies are considered to have a significant radio excess associated with a radio jet (Ivison et al. 2010; Harrison et al. 2014).

Most galaxies in our sample are consistent with the radio luminosity being associated with star formation. Actually it seems that, on average, $q_{\rm IR}$ in our sample is even higher than typically observed in normal galaxies, possibly reflecting the bias towards star-bursting systems, or the contribution of powerful AGN to the IR emission in some of the galaxies of our sample.

Fig. 2.10 shows that two of the three galaxies with radio excess ($q_{\rm IR} < 1.8$) do have strong outflows. However, the plot shows no clear correlation between molecular outflow rate and excess of radio emission relative to the SFR-radio relation. This finding suggests that, statistically, the presence of radio jets does not seem to be a primary driving mechanism of the majority of galactic molecular outflows in our sample. However, this does not imply that strong radio jets cannot cause outflows. In fact, as already discussed at the beginning of this section, radio jets have been seen as the origin of powerful outflows in a few specific galaxies.

2.3.2 Depletion Time

In the following, we estimate the outflow depletion time-scale, defined as $\tau_{\rm depl,outf} = M_{\rm gas}/\dot{M}_{\rm outf}$, i.e. the time required to remove all gas from the galaxy with the current mass outflow rate assuming no fresh supply of additional gas is delivered to the galaxy. We first focus on the depletion time of the molecular gas, i.e. $\tau_{\rm depl,outf}(H_2) = M(H_2)/\dot{M}_{\rm outf}(H_2)$, as we have this information for all galaxies in the sample and we will then discuss the total gas depletion time for galaxies that have information on their HI content. In Fig. 2.11, we show the

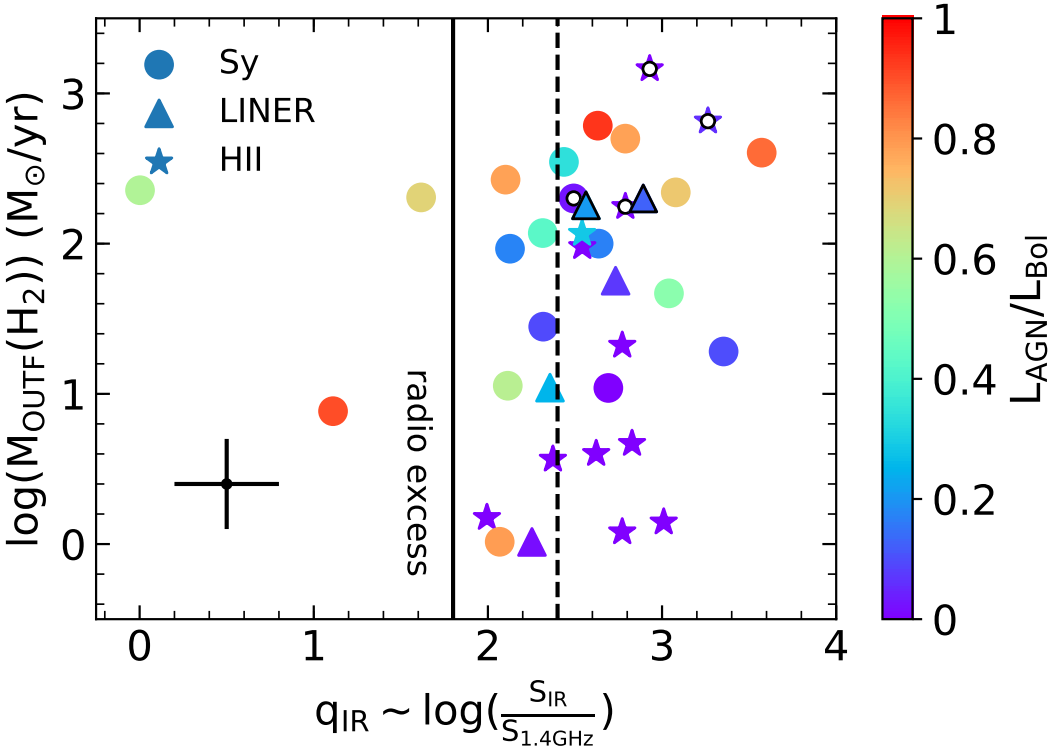

Figure 2.10: Molecular outflow rate as a function of the parameter $q_{\rm IR}$ defined as the ratio between the FIR flux and the radio monochromatic flux at 1.4 GHz (Section 2.2.5.6). The vertical dashed line indicates the average value for star forming galaxies, while the solid vertical line indicates the limit below which galaxies are considered to have a significant radio excess associated with a radio jet (Ivison et al. 2010; Harrison et al. 2014). Colour-coding and symbols are the same as in Fig. 2.2.

relation between molecular depletion time-scales and AGN luminosity. While we do observe an anticorrelation between depletion time-scales and AGN luminosity, and with AGN contribution to the bolometric luminosity, the trend is much more scattered than in previous studies (Sturm et al. 2011; Cicone et al. 2014). The depletion time-scale of molecular gas for the most powerful AGN is between a few times 10^6 and 10^8 yr.

Fig. 2.12 shows the depletion time due to outflows compared to the depletion time-scale due to star formation. For star forming galaxies, the depletion time due to star formation is similar or shorter than the depletion time due to outflowing gas. For AGN hosts, the depletion is dominated by outflows rather than by gas consumption due to star formation, implying that AGN-driven outflows play a key role in regulating star formation in galaxies.

For about half of the galaxies, we also have information on the atomic gas content, hence we can estimate the total depletion time: $\tau_{\rm depl}({\rm tot}) = M({\rm H_2} + {\rm HI})/\dot{M}_{\rm outf}(H_2)$. This is shown in Fig. 2.13, which shows the total depletion time-scale with increasing AGN luminosity. This figure

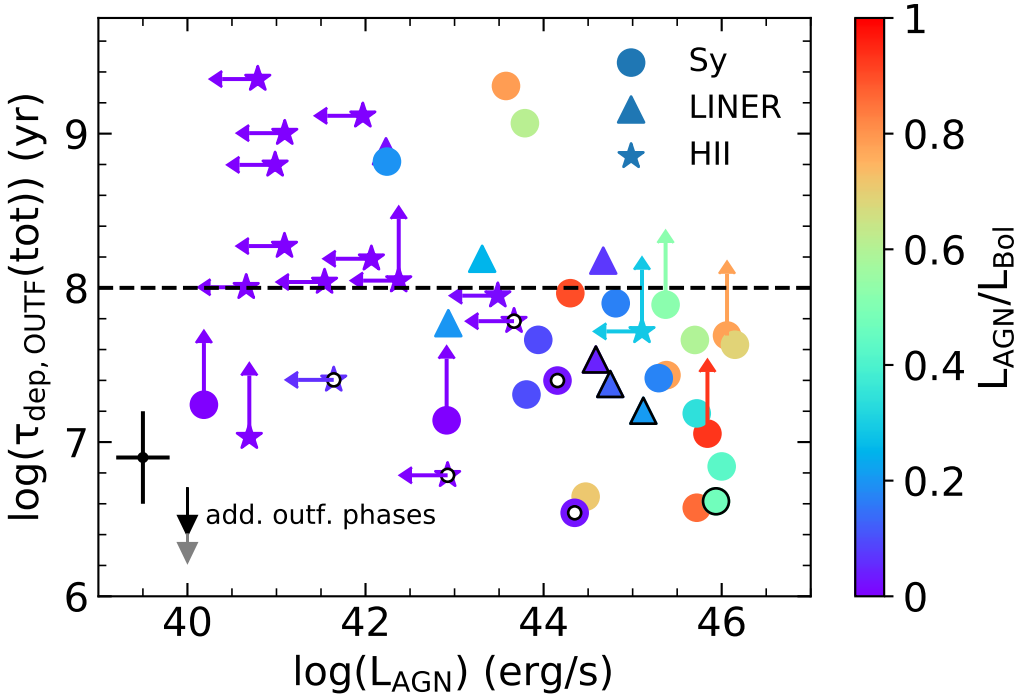

Figure 2.11: Molecular gas depletion time-scale due to outflows as a function of AGN luminosity. Colour-coding and symbols are the same as in Fig. 2.2.

illustrates that the total depletion time-scale is much longer, and generally exceeding 10^8 yr even in most AGN (even if the other gas phases are included, as shown by the black arrow), implying that the AGN is unlikely to clear the galaxy of its total gas content.

The combination of these various results indicates that AGN-driven outflows are capable of clearing the central parts of galaxies, where the gas content is dominated by the molecular phase, but the AGN is unlikely to clear the entire galaxy of its gas content.

2.3.3 Kinetic Power

It is important to investigate the properties of outflows such as their kinetic power and momentum rate, as different models make different predictions for these quantities. In this section, we briefly discuss the observational results for what concerns the kinetic power. In the next section, we will discuss the momentum rate, while a detailed analysis of implications and comparison with models will be given in Section 2.4.2.

Fig. 2.14 shows the kinetic power of the outflow (=0.5 v^2 $\dot{M}_{\rm outf}$) as a function of the radiative power of the AGN. Clearly, for AGN host galaxies the kinetic power correlates with the AGN luminosity, although the correlation appears to be superlinear. Moreover, our more extended,

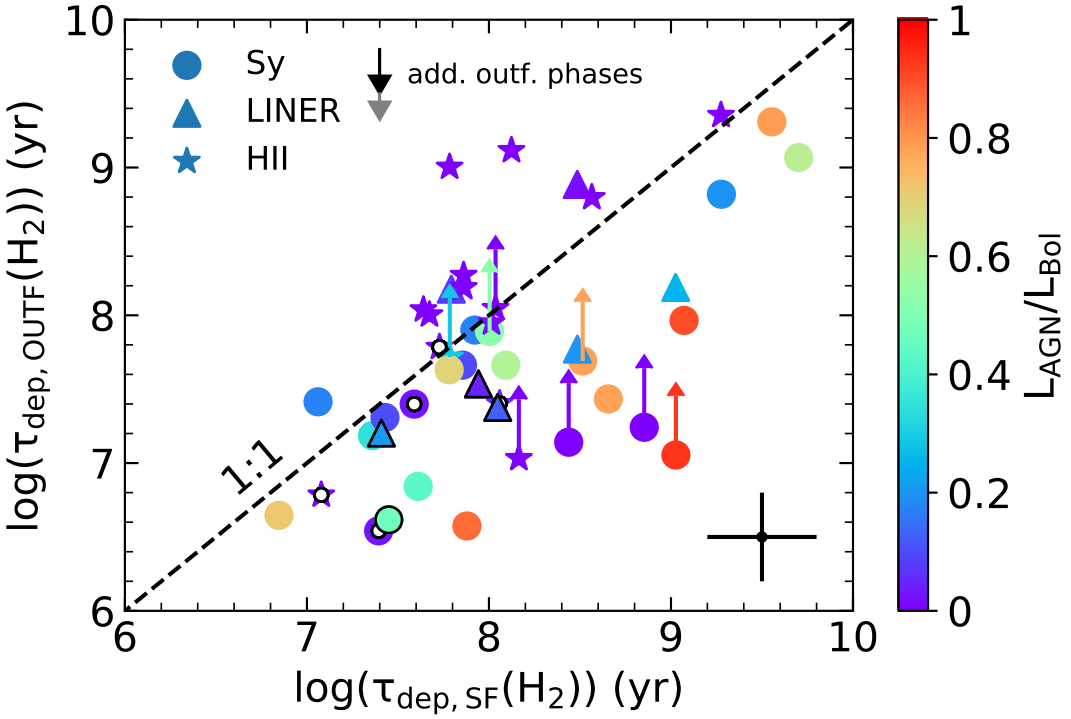

Figure 2.12: Molecular gas depletion time-scale due to outflows versus depletion time-scale due to star formation. Colour-coding and symbols are the same as in Fig. 2.2.

and less biased sample, with respect to previous studies, reveals a large scatter.

Star forming galaxies follow a different trend compared to AGN, as expected since in these sources the observed outflows cannot have originated from a currently active AGN episode. To test whether star formation can explain why these galaxies are outliers, in Fig. 2.15 we compare the kinetic power of the outflow with the power expected to be generated by SNe ($P_{\rm K,SF}$ = $7{\times}10^{41}$ SFR ($M_\odot$ yr^{-1}), Veilleux et al. (2005)). In star forming galaxies, especially those with low values of $P_{\rm K,SF}$, the kinetic power of the outflow can be explained by SNe by assuming a coupling efficiency of only 0.5 % (except for a few SF galaxies with extreme outflows discussed further below). However, accounting for the contribution of the ionized and atomic phases increases the kinetic power of SB-dominated outflows by a factor of $\sim$ 3 (Section 2.3.1), as indicated by the grey arrow, suggesting a coupling efficiency of SN ejecta with the ISM higher than 1 %. Conversely, in AGN host galaxies a coupling of $\sim$ 10 % or, in some cases, much more is needed; as this is significantly larger than expected by models of SN outflows (especially if accounting for the other outflow phases, as indicated with the black arrow), this indicates, as expected, that SNe are not powerful enough to drive the outflow in these objects and that the outflow must be mostly driven by the AGN.

Figs 2.14 and 2.15 also clearly indicate that there are a few galaxies for which the kinetic

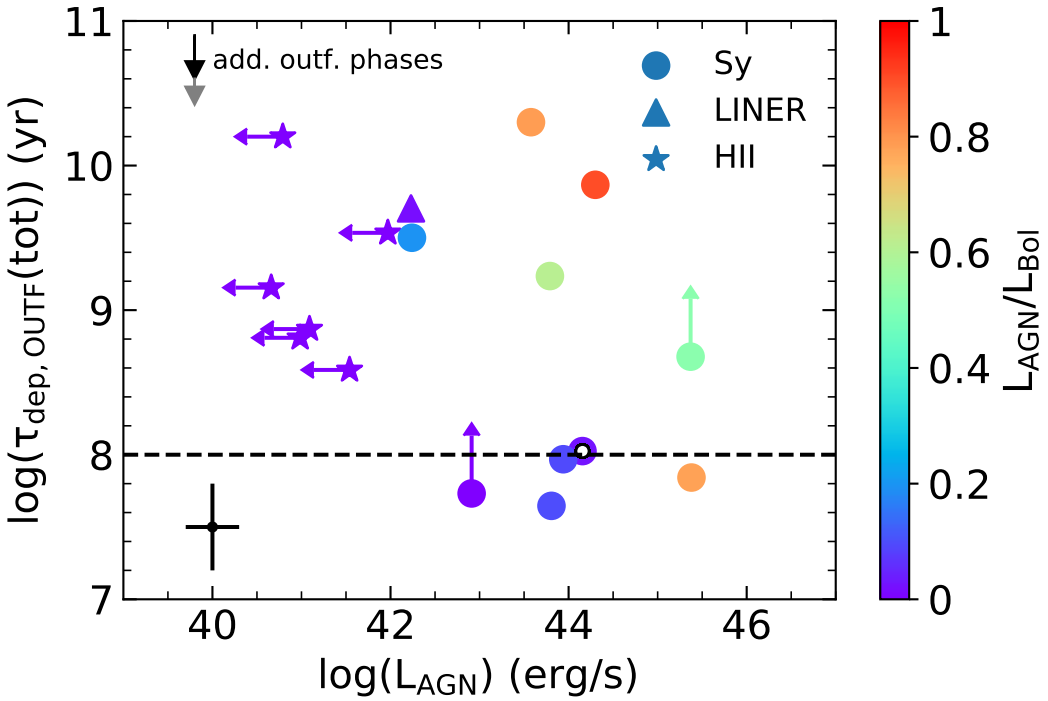

Figure 2.13: Total gas (HI+H_2) depletion time-scale as a function of AGN luminosity. Colour-coding and symbols are the same as in Fig. 2.2.

power greatly exceeds what is expected from the AGN energy-driven scenario and also in excess of what is expected by the SNe-driven scenario, as a coupling efficiency higher than 10 % would be required. In these cases (objects marked by white dot in their centre), the outflow is likely due to a past, more active phase of the AGN. This will be discussed further in Section 2.4.3.

2.3.4 Momentum Rate

The outflow momentum rate is plotted as a function of the AGN radiative momentum rate L_{AGN}/c in Fig. 2.16, illustrating a tight correlation between these two quantities for AGN host galaxies, further indicating that AGN play a significant role in driving galactic outflows. However, also in this case it is clear that the scatter is significantly larger than in previous studies.

Galaxies classified as star forming are all outliers in this relation since they are powered by a different mechanism (i.e. SNe feedback and/or radiation pressure from the stellar UV radiation field). In Fig. 2.17, we analyse the dependence of outflow momentum rate on *total* photon momentum rate of the galaxy, L_{bol}/c. For strong AGN hosts, $L_{bol} \approx L_{AGN}$, but for AGN with lower AGN contribution and star forming galaxies, L_{bol} is much larger than L_{AGN}. In this plot,

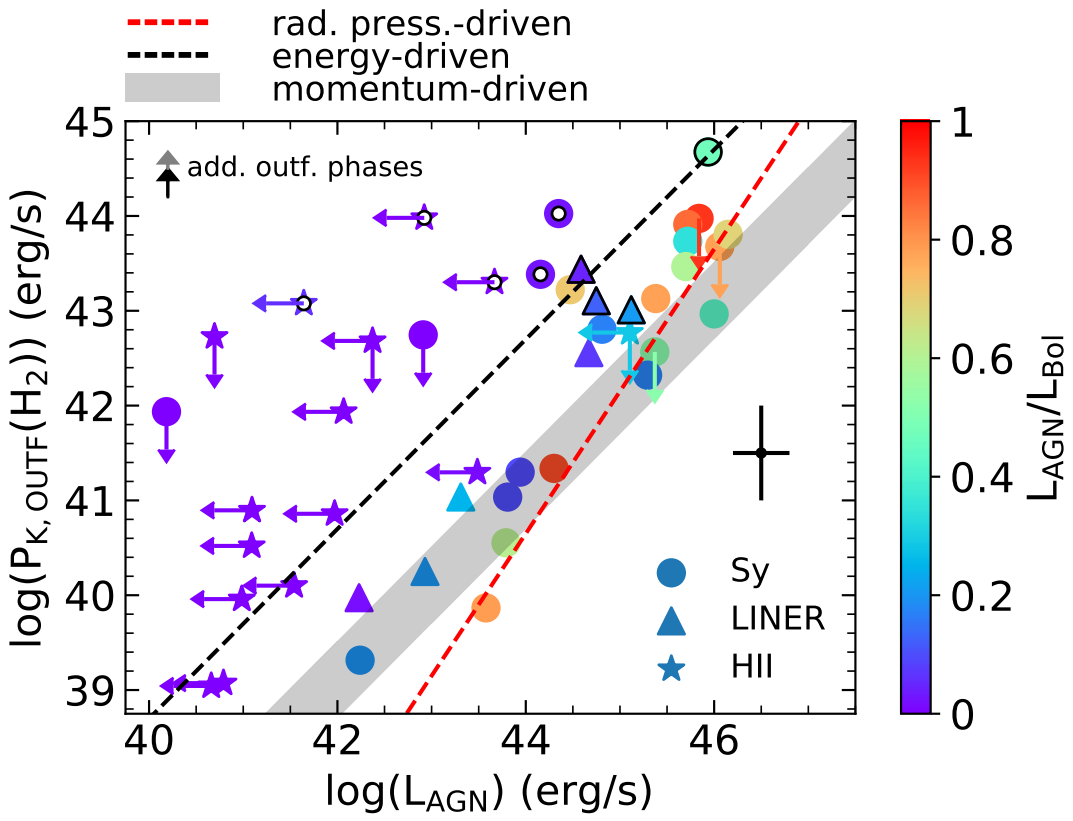

Figure 2.14: Kinetic power ($P_{\rm K,outf}$) of the outflow as a function of the AGN luminosity. The dashed black line indicates the theoretical prediction of $P_{\rm K} = 0.05 L_{\rm AGN}$ for an energy-driven outflow, assuming a coupling efficiency of 100 % between the outflow and the ISM. The prediction for momentum-driven outflows and some models of radiation pressure-driven outflows is shown as a shaded region. The red dashed line shows the predicted relation for the radiation pressure-driven outflow presented in Ishibashi et al. (2018). Colour-coding and symbols are the same as in Fig. 2.2.

it is interesting to note that for some star forming galaxies, especially at high luminosities (i.e. high SFR) the momentum rate is close to $\sim 0.5\ L_{\rm bol}/c$, suggesting that radiation pressure on dusty clouds by the radiation field of young stars can be an additional significant contributor to the driving mechanism of outflow in starburst galaxies, as predicted by some models (Thompson et al. 2015), although a coupling efficiency of at least 50 % would be required.

In some star forming galaxies, the momentum rate of the outflow is close to or exceeding $L_{\rm bol}/c$ (which would imply an unrealistic coupling efficiency of 100 % or higher), indicating that other mechanisms or other phenomena may be at work. This is also seen in some AGN: a few AGN hosts have outflows which, when compared with $L_{\rm AGN}/c$, are characterised by momentum boosts well in excess of what expected by any theory (see Fig. 2.16). As we will discuss later on, most of these outflows with extreme momentum rates can be explained in terms of fossil

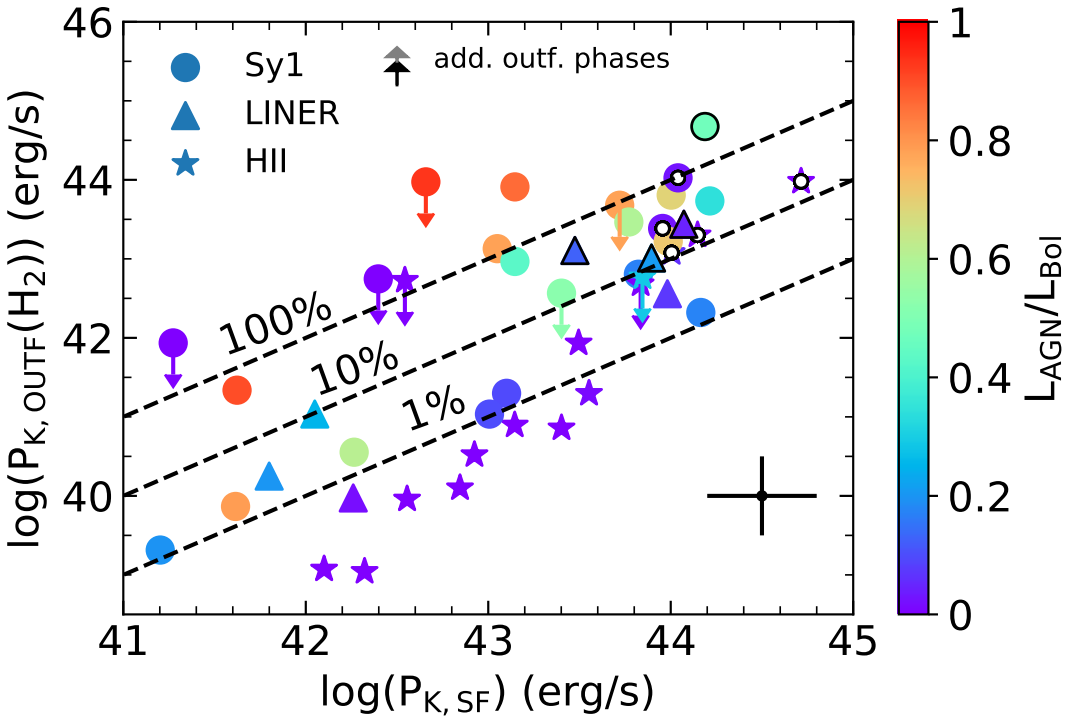

Figure 2.15: Kinetic power of the outflow as a function of the kinetic power generated by SNe, as inferred from the SFR. The black dashed lines indicate coupling efficiencies of 1, 10, and 100 %. Colour-coding and symbols are the same as in Fig. 2.2.

outflows resulting from a much stronger past AGN activity.

2.4 Discussion

2.4.1 Driving Mechanisms in AGN

Three different mechanisms have been proposed for powering AGN-driven outflow: an energy conserving blast wave (so-called energy-driven), a momentum conserving blast wave (so-called momentum-driven), and direct radiation pressure on to the dusty clouds of the galactic ISM (so-called radiation pressure-driven). These are discussed in greater detail in Chapter 1. Briefly, the energy-driven scenario predicts the outflow kinetic power to be about 5 % of the AGN radiative power, if the AGN is accreting close to the Eddington limit and if a 100 % thermal-to-kinetic conversion efficiency and high gas covering fractions are assumed (i.e. 100 % coupling between the blast wave and the ISM in the host galaxy) (King 2010; Faucher-Giguère & Quataert 2012; Zubovas & King 2012; Costa et al. 2014; King & Pounds 2015; Richings & Faucher-Giguère 2018). In the momentum-driven mode the outflow kinetic energy is expected to be of the order of 0.1 % of the AGN radiative luminosity, or less (King & Pounds 2015). And in the

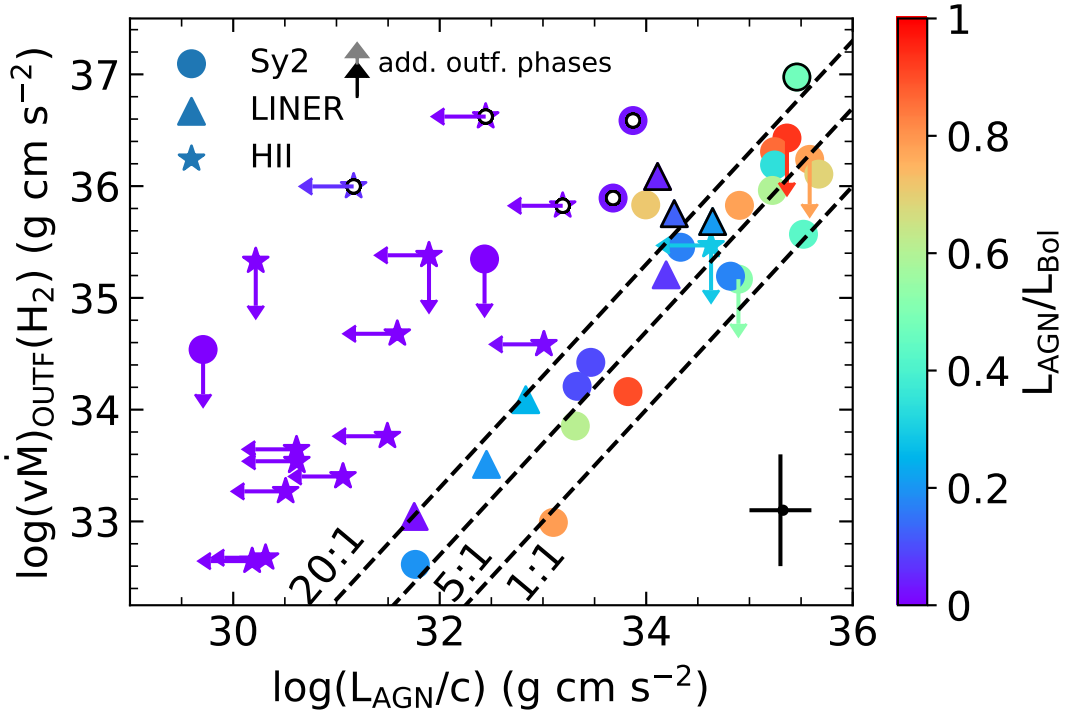

Figure 2.16: Relation between outflow momentum rate ($v_{\rm outf}\dot{M}_{\rm outf}(H_2)$) and AGN radiative momentum rate ($L_{\rm AGN}/c$). The theoretical predictions ($v_{\rm outf}\dot{M}_{\rm outf}$)/($L_{\rm AGN}/c$) ~ 20:1 (energy-driven) and 1:1 (momentum-driven) are shown as a dashed lines, respectively. Radiation pressure-driven outflows can reach ($v_{\rm outf}\dot{M}_{\rm outf}$)/($L_{\rm AGN}/c$) ~ 5:1. Colour-coding and symbols are the same as in Fig. 2.2.

radiation pressure-driven mode of AGN feedback, the kinetic power of the outflows can be as high as ~ 1 % of the AGN luminosity. Furthermore, radiation pressure-driven models predict a superlinear relation between outflow kinetic power and AGN luminosity in the form $P_{\rm K,outf} \propto L_{\rm AGN}^{3/2}$. This has been derived by Ishibashi et al. (2018) by solving the equation of motion for the velocity, v:

$$\frac{d}{dt}[M_{\rm sh}(r)v] = \frac{L}{c}(1 + \tau_{IR} - e^{\tau_{UV}}) - \frac{GM(r)M_{sh}(r)}{r^2}, \tag{2.9}$$

where $M_{\rm sh}$ is the shell mass, $M(r)$ is the total mass distribution and L the central luminosity (in our case the AGN luminosity). Assuming a isothermal potential ($M = \frac{2\sigma^2 r}{G}$ with the velocity dispersion σ) and fixed-mass shell (i.e. $M_{\rm sh}$(r) = $M_{\rm sh}$), one obtains $v \propto L^{1/2}$ and hence $P_{\rm K,outf} \propto L_{\rm AGN}^{3/2}$.

Many theoretical models expect that the most effective feedback process is obtained through AGN-driven outflows that are energy conserving (i.e. energy-driven) if the coupling between the blast wave and the ISM is high enough. Yet, more detailed 3D, non-spherically symmetric

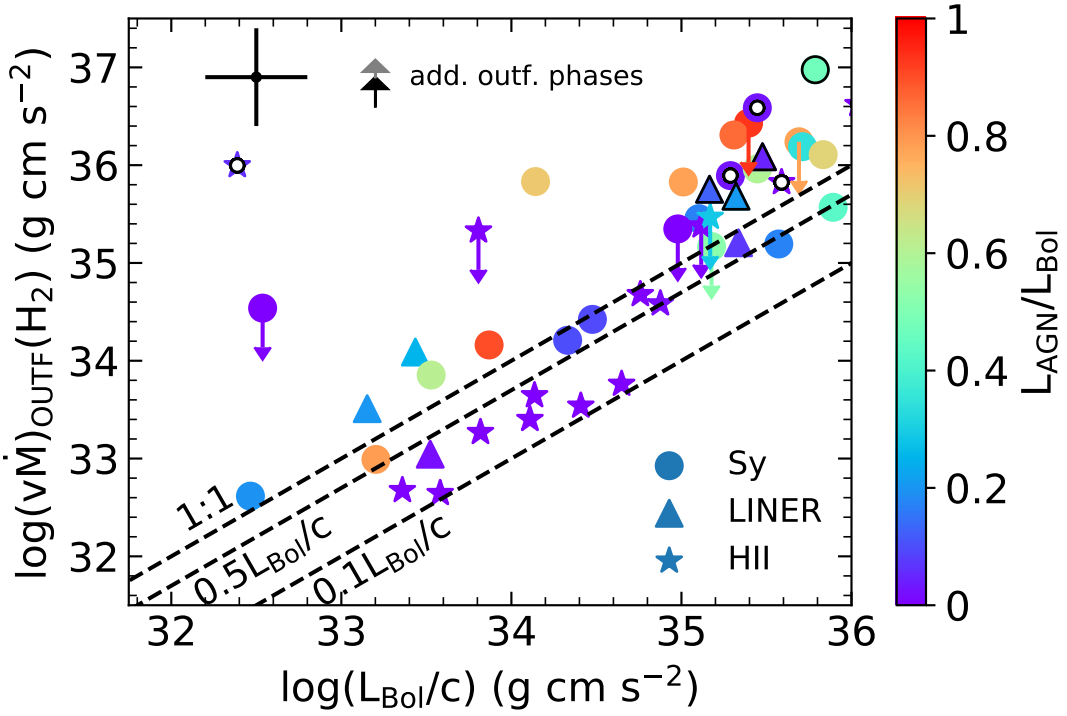

Figure 2.17: Dependence of the outflow momentum rate ($v_{\rm outf}\dot{M}_{\rm outf}$) on the total photon momentum output of the galaxy (i.e. from AGN *and* star formation). The top dashed line indicates the 1:1 relation between momentum rate and bolometric luminosity, while lower dashed lines indicate lower ratios. Colour-coding and symbols are the same as in Fig. 2.2.

simulations have suggested that the coupling can be significantly lower than 100 %, with dense clumps of the ISM remaining unaffected and the outflow escaping along the directions of least resistance (Bourne et al. 2014; Gabor & Bournaud 2014; Bourne et al. 2015; Costa et al. 2015; Roos et al. 2015).

On the other hand, momentum-driven outflows (in which the energy of the shocked wind is quickly dissipated on small scales via radiation losses) are generally expected to be much less effective in driving outflows.

An additional class of models suggests that direct radiation pressure of the UV, optical, and IR photons on the dusty clouds of the ISM can be effective enough to drive massive outflows (Fabian 2012; Thompson et al. 2015; Ishibashi et al. 2017; Bieri et al. 2017; Ishibashi et al. 2018; Costa et al. 2018a,b). In this case, there is a broad range of expected outflow properties. If the central dusty region in which acceleration takes place is optically thick to IR radiation, then the kinetic power of the outflows can be as high as $\sim$ 1 % of the AGN luminosity (this applies also when the source of radiation is a compact starburst); however, in less extreme cases, the outflow kinetic power is expected to be lower than this value. Recently, Ishibashi et al. (2018)

developed the model of radiation pressure-driven outflows further. They predict a superlinear relation between outflow kinetic power and AGN luminosity in the form $P_{\rm K,outf} \propto L_{\rm AGN}^{3/2}$.

By looking at the results reported in Section 2.3.3 and Fig. 2.14, where the prediction of different models are also shown, it is clear that outflows in AGN host galaxies span a broad range of properties. Although AGN 'flickering' can account for some of the scatter, as discussed in the next section, the very broad range of $P_{\rm K,outf}/L_{\rm AGN}$ suggests that these outflows are driven by a combination of different driving mechanisms and/or a broad range of coupling efficiencies with the ISM. Some AGN are consistent with the energy-driven scenario, and full coupling between the outflow and the ISM. However, the majority of AGN are significantly below the $P_{\rm K} = 0.05\ L_{\rm AGN}$ relation (which assumes all thermal energy of the putative expanding hot bubble is converted into kinetic energy of the outflow) and so the respective outflows are more consistent with a momentum-driven or radiation pressure-driven mechanism; alternatively, they are energy-driven, but poorly coupled with the galaxy ISM. However, the momentum-driven scenario can probably be excluded as the observed outflows are mostly on kpc-scales, while momentum-driven outflows should be confined within the central few 100 pc (King & Pounds 2015).

As shown in Fig. 2.14, at high AGN luminosities, galaxies lie closer to the expected value for the energy-driven mode though still mostly below the value expected from energy-driven outflows. This seems to indicate that different driving mechanisms may be at work at different AGN luminosities. Specifically, at high luminosities energy-driven outflows (though with poor coupling) may dominate, while at low luminosities radiation pressure may be the dominant mechanism driving outflows.

The superlinear relation between outflow kinetic power and AGN luminosity in the form $P_{\rm K,outf} \propto L_{\rm AGN}^{3/2}$ expected by the radiation pressure model of Ishibashi et al. (2018) (dashed orange line in Fig.2.14) is consistent with the observed relation in terms of slope. Therefore, this model can potentially account also for the high $P_{\rm K,outf}/L_{\rm AGN}$ values (~1 %) observed at the highest luminosities, and the decreasing values of this ratio at lower luminosities. However, the model also expects the outflow rate to follow a relation $\dot{M}_{\rm outf} \propto L_{\rm AGN}^{1/2}$, which is somewhat shallower than what we observe for molecular gas (see Fig. 2.4).

In terms of momentum rate, in the energy-driven case models expect that the momentum rate is boosted to about 15-20 $L_{\rm AGN}/c$ (Faucher-Giguère & Quataert 2012; Zubovas & King 2012). Momentum-driven winds are expected to result in momentum rates of $\sim L_{\rm AGN}/c$ (King 2010). Direct acceleration of the ISM through the action of radiation pressure on dusty clouds generates momentum rates ranging from ~ 1 up to 5 $L_{\rm AGN}/c$, the latter in the case that the medium that is being accelerated is optically thick to IR radiation, resulting in multiple scattering that boosts the momentum rate (Ishibashi & Fabian 2015; Thompson et al. 2015; Bieri et al. 2017; Costa

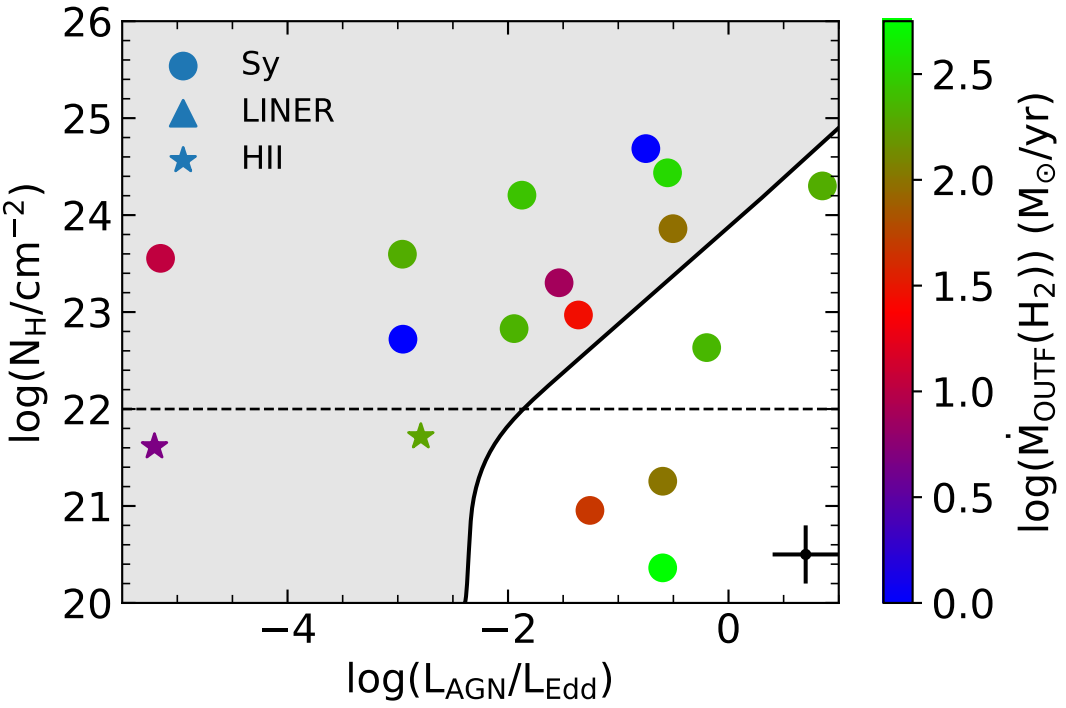

Figure 2.18: Gaseous column density along our line of sight, as inferred from X-ray spectra, versus L_{AGN}/L_{Edd}, with symbols colour-coded by outflow rate (right-hand side colour bar). The solid line delimitates the area (non-shaded) where radiation pressure on dust is expected to overcome gravity (i.e. where the effective Eddington luminosity for a dusty medium is exceeded) hence producing powerful outflows. Symbols are the same as in Fig. 2.2.

et al. 2018a; Ishibashi et al. 2018).

In Fig. 2.16 the upper dashed line represents the theoretical prediction for the energy-driven model (with 100 % coupling), while the lower dashed lines indicate the values expected for the momentum-driven and radiation pressure-driven models. Some of the galaxies with an AGN do follow the theoretical prediction for energy-driven outflows within the errors, but most galaxies hosting an AGN have momentum rates scattered between the energy-driven case and the momentum/radiation pressure-driven cases, further suggesting the contribution of different driving mechanisms and/or energy-driven outflows with poor coupling.

An additional route to study the driving mechanism is to investigate the relation between the outflow rate, the AGN luminosity and the gas column density of the circumnuclear gas. Indeed, in the context of radiation pressure-driven outflows, the effective Eddington luminosity is dominated by radiation pressure on dust, which drastically reduces the Eddington limit. Fabian et al. (2008) and Ricci et al. (2017) have pointed out that the effective Eddington limit ($L_{Edd,eff}$) is higher at higher gas column densities as larger amounts of material need to be pushed out. Hence, these authors expect a region in the L_{AGN}/L_{Edd} vs N_H plane where radiation pressure on

dust dominates over gravity and where this kind of outflows should be most effective. This is explored in Fig. 2.18, where the column density (as inferred from X-ray observations) is shown as a function of the Eddington ratio, $L_{\rm AGN}/L_{\rm Edd}$, and colour-coding is according to the outflow rate. The region on the right-hand side of the plot, delimited by the solid line, is where the effective Eddington luminosity for a dusty medium is exceeded, and therefore where we expect powerful outflows that are driven by radiation pressure on dust. As pointed out by Fabian et al. (2008) and Ricci et al. (2017), this region is underpopulated, indeed empirically confirming that the effective Eddington ratio is exceeded in this region. The few galaxies of our sample located in this region do indeed show among the highest outflow rates, suggesting that these extreme outflows may be driven by radiation pressure on dust. We note that in the scenario discussed by Fabian et al. (2008) and Ricci et al. (2017) AGN with $N_{\rm H} < 10^{22}$ cm^{-2} are not considered, as these low column densities are thought to be associated with dust lanes in the host galaxy and not directly linked with the AGN process; however, our analysis shows that the three objects in this region are characterised by strong outflows, suggesting that also in these cases the outflow is driven by radiation pressure on dust. For the other galaxies, located on the left-side of the solid line (grey shaded area) there is not much correlation between the outflow rate and the AGN's location on the diagram. In particular, there are galaxies with high outflow rates also below the boundary expected by the model. These outflows could be driven by a different mechanism.

To summarize, our results indicate that AGN-driven outflows are either consistent with predictions from direct radiation pressure models or with the energy-conserving blast-wave scenario, but with a coupling with the ISM of the host galaxy that varies from galaxy to galaxy and generally is lower than 100 %.

2.4.2 Driving Mechanisms in Star Forming Galaxies

As discussed in Section 2.3.3 only about ∼1–2 % of the kinetic power released by SNe appear to be converted into the kinetic power of the outflow. A low coupling efficiency of the kinetic energy between SN ejecta and ISM is expected by the fact that most of the energy is radiated away in the dense interstellar medium in which most SNe are expected to explode. Yet, models and simulations expect still higher coupling efficiencies, of the order of 5 % (Walch & Naab 2015). Although there is some tension, this is mostly within the errors. However, if this tension is confirmed with more accurate data it may indicate that radiation losses during the SN–ISM interaction are higher than expected (possibly because the ISM is denser than assumed in the simulations).

However, in addition to the kinetic power injected by SNe, outflows in star forming galaxies can also be driven by radiation pressure on to the dusty clouds (Thompson et al. 2005, 2015).

The correlation in Fig. 2.17 between the outflow momentum rate and radiative momentum from the bolometric luminosity of star forming galaxies suggests that indeed radiation pressure may play a role. However, one should also be aware that such a correlation is also degenerate with the kinetic power injected by SNe, since the SN rate is linked to the SFR which is in turn related to the bolometric luminosity. Moreover, it is important to note that most star forming galaxies have a ratio between momentum rate and radiation momentum between 0.5 and 0.1 (Fig. 2.17), implying that, if this driving process is at work, the coupling efficiency must be less than 50 %.

2.4.3 Fossil Outflows

There are a few galaxies with outflows that are characterised by anomalously high kinetic powers and momentum rates compared to their AGN luminosity and SFR, which are difficult to explain with any driving mechanism. More specifically, Figs 2.14 and 2.15 indicate that for some galaxies (marked with a white dot in these and other figures) the kinetic power is greatly in excess of what is expected even from the AGN energy-driven scenario, even assuming 100 % coupling, and is also in excess of what is expected by the SNe-driven scenario, unless assuming an unrealistically high coupling efficiency of the SNe (larger than 10 %, especially if accounting for all outflow phases). In Fig. 2.16 it is clear that these objects have also very high momentum rate, even larger than expected in the case of energy-driven outflows and 100 % coupling. It is unlikely that in these objects the SFR or AGN power is not estimated properly, as the observational constraints are quite good. It is also unlikely that these outflows are driven by a radio jet, as these objects do not show any radio excess in Fig. 2.10. In these cases, as already hinted in the previous sections, the most likely explanation is that we are observing 'fossil' outflows that outlast a formerly powerful AGN, which has recently faded. This interpretation is further supported by the low Eddington ratios ($\log(L_{\rm AGN}/L_{\rm Edd}) \lesssim -3$) seen in the three fossil outflow objects for which a black hole mass estimate is available.

Fossil outflows are expected from theory in large numbers. It has been shown that outflows can remain visible for a time about 10 times longer than the driving phases and up to 10^8 yr in total (King et al. 2011). Theoretical considerations have suggested that in M82 a powerful AGN might have been present until about 17 Myr ago and may have been responsible for driving the outflow currently observed (Zubovas 2015). Even more simply, without invoking detailed and extensive theoretical simulations, the dynamical time-scales of the outflows ($t_{\rm dyn} \sim R/v$) are in the range of 10^6-10^8 yr, while we know that AGN have a 'flickering' time-scale ranging from a few years (e.g. Gilli et al. 2000) up to 10^5 yr (Schawinski et al. 2015; King & Pounds 2015). Therefore, a large number of fossil AGN is naturally expected. The outliers we see here are possible manifestations of this scenario and are likely the tip of the iceberg of a much

larger population of fossil outflows. If this is true, then one should be careful when comparing observational outflow properties with theoretical models as possibly a large fraction of galaxies (in our sample 10–20 %) display fossil outflows.

The reason why in the past such fossil outflows had not been identified is likely because previous observations had targeted primarily known, strong AGN hence biasing the sample towards outflows that are in the phase of being powered. Instead, in our study we have collected data of galaxies from the ALMA archive, many of which had been observed independently of their activity, hence reducing such biases.

Table 2.4 gives the list of fossil outflows identified by us. Their properties have no peculiarities relative to other galaxies in the sample.

2.4.4 Do Outflows Escape the Galaxy and the Halo?

If outflow velocities are high enough to escape the potential of the galaxy (and possibly even the halo), then these outflows can effectively clear the galaxy of its gas content. But this also depends on how much gas the outflows sweep up as they move out of the galaxy and on whether they collide with inflowing material. We ignore the latter effects here, because, as it turns out, most outflowing material should not escape the galactic halo purely due to its insufficient velocity. Limited mass-loading and a potential interaction with gas infall would only strengthen our conclusions.

In principle, one should use the velocity rotation curve of galaxies to infer the mass distribution radial profile of the associated gravitational potential. Unfortunately, at the moment, this information is not available for the vast majority of the galaxies in our sample. Information on the rotation curve is available only for very few galaxies, primarily from the CO interferometric data, and only in the central region of the galaxy. As a consequence, we have to rely on some simple assumptions and use scaling relations with the stellar mass.

We consider the stellar mass as determined in Section 2.2.5. We use the relation by McIntosh et al. (2005) at $z = 0$ to relate the stellar mass to the half-light radius, r_{50}:

$$\log(\bar{r}_{50}/\mathrm{h}^{-1}\mathrm{kpc}) = 0.56 \log\left(M_\star \mathrm{h}^2/\mathrm{M}_\odot\right) - 5.52. \tag{2.10}$$

We approximate the stellar mass distribution adopting a Hernquist profile (Hernquist 1990) for the density

$$\rho(r) = \frac{M}{2\pi}\frac{a}{r}\frac{1}{(r+a)^3} \tag{2.11}$$

where a is related to the effective radius $r_{\rm eff}$ via $r_{\rm eff} \approx 1.8135a$. We can now compute the escape velocity for galaxies in our sample. The escape velocity is given by

$$v_{\rm esc} = \sqrt{2|\Phi(r)|} = \sqrt{\frac{2GM}{r+a}}. \tag{2.12}$$

The escape fraction is then defined as the fraction of the outflow that has a velocity higher than the escape velocity. Unfortunately, this calculation can be done only for those outflows for which we have the data in electronic form, as it requires estimating the integral of the fraction of the broad wings with velocity higher than the escape velocity (i.e. this calculation cannot be done for the data in the literature for which an electronic version of the spectrum is not available). This part of the outflow will eventually leave the galaxy. In Fig. 2.19, the escape fraction is shown for the galaxies as a function of the AGN luminosity. Only in IRAS 20100–4156, and maybe in 4C 12.50, 10 % or more of the gas in the outflow will escape the galaxy using these simple assumptions. For all other galaxies, the escape fraction is smaller or even negligible and there is no clear dependence on AGN luminosity. We should note, however, that the equations here only hold if we consider ballistic motions. This is a simplification and probably not true since the outflow is driven by pressure (especially in the energy-driven or radiation pressure-driven scenario). If the AGN fades, there is still residual gas pressure, which can drive the outflow (King & Pounds 2015). Simulations of multiphase outflows have also failed to reproduce warm outflows at higher velocities assuming a ballistic model (but they successfully reproduce the low-velocity outflows) (Vijayan et al. 2020). If the outflows are still driven and therefore further accelerated, they are more likely to escape the galaxy potential. The error in the escape fraction is as large as 50 % as inferred by running a Monte Carlo simulation, taking into account errors in fitting the line profile, stellar mass, and outflow radius.

Therefore, despite galactic outflows being very massive and energetic, especially those driven by AGN, most of the expelled gas will quickly re-accrete on to the galaxy and be available again for future star formation. Hence, the ejection of gas, at least in this molecular phase, does not really contribute to the global quenching of star formation in galaxies. However, these outflows can still have a dramatic effect in the central region of galaxies (especially in the bulge region), where they can locally suppress or even quench star formation. Moreover, even if the ejective aspect of outflows does not directly contribute to the global quenching of galaxies on large galactic scales, this does not mean that outflows do not play a role at all on the global evolution of galaxies on large scales. By injecting energy, outflows can keep the halo gas hot and prevent it from cooling on to the galaxy, hence effectively resulting into a delayed quenching of star formation in the galaxy as a consequence of starvation (e.g. Gilli et al. 2017; Costa et al. 2018a).

The escape fractions inferred above are for molecular outflows. Ionized outflows, although

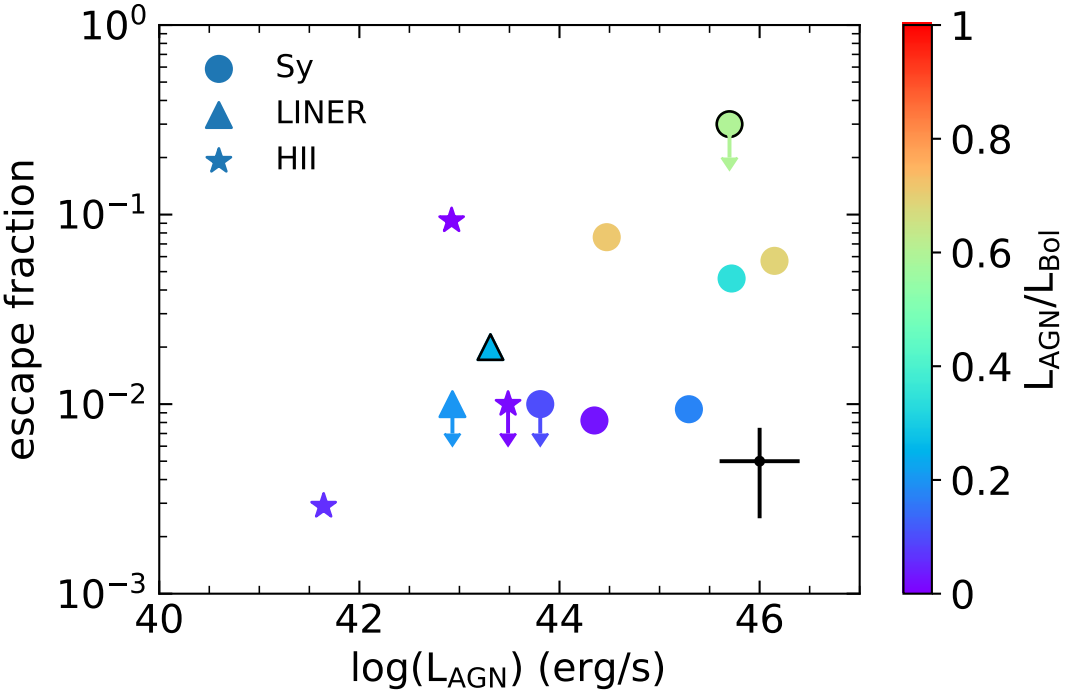

Figure 2.19: Fraction of the molecular outflow that escapes the galaxy as a function of AGN luminosity. The two data points with a black contour are taken from the literature and use slightly different definitions of escape velocity.

generally contributing much less to the outflow rate, are expected to have higher escape fractions (Costa et al. 2015). This can be investigated for several galaxies whose outflow has been mapped in the ionized phase, but we defer this kind of analysis to a later study.

We note that the escape fraction discussed above refers to the escape velocity from the galaxy. The escape fraction from the galaxy dark matter halo are even smaller, but also more difficult to compute. We can attempt to estimate the velocities needed to escape the halo by making a few approximations in the following.

We use the Navarro–Frenk–White (NFW) profile (Navarro et al. 1995) to describe the density in the halo of the galaxy:

$$\rho(r) = \frac{\rho_{\rm crit}\delta_{\rm c}}{r/r_{\rm s}(1+r/r_{\rm s})^2} \tag{2.13}$$

where $\rho_{\rm crit} = 3H^2/8\pi G$ is the critical density and $r_{\rm s} = r_{200}/c$ is the characteristic radius (c being the concentration parameter). The mass of the halo (M_{200}) can be inferred from the stellar mass using a stellar mass-halo mass relation from abundance matching (Moster et al. 2013). To find the mass concentration from the halo mass, we use the relation by Duffy et al. (2008) at $z = 0$:

$$\log c_{200} = 0.76 - 0.1 \ \log M_{200}. \tag{2.14}$$

Similar to what we found in Section 2.4.4, the escape velocity is:

$$v_{\rm esc} = \sqrt{2|\Phi(r)|} = \sqrt{\frac{2M_{200}G}{r(\ln(1+c) - c/(1+c))}\ln(1 + r/r_{\rm s})} \tag{2.15}$$

This allows us to compute the escape fractions of gas out of the halo. As expected, we generally obtain escape fractions from the halo much smaller than the escape fractions from the galaxy, typically much smaller than 1 %, further indicating that the bulk of the outflowing gas will remain in the gravitational potential of the system and will eventually re-accrete on to the galaxy. We note, however, that our sample does not include low-mass galaxies ($M_\star < 10^{10}\ M_\odot$), for which models expect a large fraction of the outflowing gas to leave the galaxy and its halo, hence enriching the IGM (Koudmani et al. 2019). Detailed observations targeting this class of galaxies are needed in order to test these expectations.

2.4.5 Effectiveness of AGN-driven Outflows in Quenching Star Formation

AGN-driven outflows have been claimed to be one of the primary candidates for cleaning galaxies of their gas content hence quenching star formation and transforming them into passive systems. The 'blast-wave' energy-conserving mode, with 100 % coupling with the ISM, has generally been regarded as the most effective mode to remove galaxies of their gas content (Zubovas & King 2012). We have, however, obtained various results indicating that such 'ejective' mode is probably not effective in clearing the whole galaxy of its gas content, even at high luminosities. Indeed, most observational properties of the AGN-driven outflows are below the expectations from energy-conserving mode, suggesting either poor coupling efficiency (as suggested by some models and numerical simulations, (e.g. Gabor & Bournaud 2014; Costa et al. 2015; Richings & Faucher-Giguère 2018) or that other driving mechanisms, such as direct radiation pressure on to the ISM dusty clouds, are also at work (Thompson et al. 2015; Costa et al. 2018a; Ishibashi et al. 2018). We have shown that the outflow depletion time-scales for the total gas mass are very long, beyond the typical lifetime of AGN. Thus, these outflows are unlikely to expel the whole amount of gas in the galaxy. Finally, as illustrated in the previous section, only a small fraction of the outflowing gas actually escapes the galaxy (and even less the halo); hence, most of the expelled gas re-accretes on the galaxy to fuel star formation.

Although, the AGN 'ejective' mode does not seem capable of quenching the entire galaxy, it can likely clean and quench the central region. Indeed, the outflow depletion time associated with the (mostly centrally concentrated) molecular gas is much shorter ($\sim 10^7$ yr), especially in luminous AGN. Therefore, the ejective AGN mode (especially when occurring at high redshift) may actually be an important route for quenching star formation in the bulge region.

The AGN-driven outflow may also have an additional indirect effect on larger scales. Although the ejective mode is likely confined to the central regions, the energy injected by the outflow into the halo can contribute to keep it hot, hence preventing further gas accretion on to the galaxy and therefore resulting in a 'delayed' quenching, by starvation, once star formation has used up the gas available in the disc (Costa et al. 2015, 2018a). This 'preventive', delayed mode is supported by various statistical properties of the local population of galaxies (Peng et al. 2015; Woo et al. 2017; Cresci & Maiolino 2018).

2.5 Conclusions

In this chapter, we have quantified the energetics of molecular outflows in a sample of 45 local ($z < 0.2$) galaxies including AGN host galaxies as well as star forming/starburst galaxies. The sample spans a range in AGN luminosity from $\log(L_{\rm AGN}) \sim 41$ up to ~ 46 erg s^{-1} and in star formation rate from ~ 0.1 up to several 100 M$_\odot$ yr^{-1}. Molecular outflow properties are inferred from interferometric observations of low-J CO lines (apart from four galaxies, for which OH absorption from Herschel is used). We collect data of molecular outflows from the literature and recalculate outflow and host galaxy properties in a consistent manner. Furthermore, we also analyse all public ALMA archival data of low-J (1–0, 2–1 and 3–2) CO lines in local galaxies and look for signatures of outflowing gas. This is the largest sample to date for which molecular outflows in CO have been investigated, and includes also less powerful outflows than previous studies. Our sample improves with respect to previous studies not only in terms of statistics but also by reducing the bias favouring very active galaxies that have been preferentially targeted in the past.

Our main findings can be summarized as follows:

- The molecular mass-loading factor ($\eta = \dot{M}_{\rm outf}({\rm H_2})/{\rm SFR}$) for star forming galaxies is consistent with unity, as expected by models of star formation feedback.
- The molecular mass-loading factor is higher in AGN host galaxies compared to star forming galaxies, although a significant boost (with $\eta > 10$) is only seen in galaxies in which the AGN luminosity is high relative to the bolometric luminosity ($L_{\rm AGN}/L_{\rm bol} > 0.7$).
- In AGN, the outflow rate correlates with the AGN luminosity and with the Eddington ratio, $L_{\rm AGN}/L_{\rm Edd}$, although with large scatter, further indicating that the AGN plays a role in driving outflows. We also observe a correlation with the black hole mass, which can be seen as tracing a link between the outflow (which has a dynamical time-scale of $10^6 - 10^8$ yr, much longer than the AGN flickering time-scale) and the integrated, average past activity of the black hole.

- We highlight that the dependence of the outflow properties on AGN luminosity, SFR, and galaxy stellar mass makes it difficult to isolate the individual dependencies, as each these properties are can be mutually correlated in galaxies. Therefore, we have derived a relation of the outflow rate simultaneously fitting the dependence of AGN luminosity, SFR, and stellar mass. The resulting fit is much tighter than the individual relations and enables us to disentangle, at least partially, the individual dependencies. In particular, we obtain a scaling of the outflow rate on stellar mass as $\propto M_{\star}^{-0.41}$, which is very close to the dependence expected by models of outflows driven by SNe and stellar winds. We also suggest that the inferred empirical (four-dimensional) relation between outflow rate, $L_{\rm AGN}$, SFR and $M_{\star}$ can be very efficiently used to predict the strength of outflows in a variety of galaxies and for comparison with models.
- We find that the majority of the molecular outflows studied here show no excess of radio emission relative to the SFR–radio relation. In addition, there is no correlation between molecular outflow rate and IR-to-radio luminosity ratio, indicating that the majority of molecular outflows are not driven by radio jets, at least within the luminosity range probed by us. However, this does not exclude that radio jet may have an important role in driving molecular outflows in a few specific galaxies, as indeed observed.
- The depletion time-scale associated with outflow (i.e. $\tau_{\rm depl} = M_{\rm gas}/\dot{M}_{\rm outf}$) anticorrelates with AGN luminosity, i.e. is shorter in more luminous AGN. The depletion time-scale for molecular gas ($\tau_{\rm depl,outf}(H_2)= M(H_2)/\dot{M}_{\rm outf}(H_2)$) can be as short as a few, or a few tens million years, much shorter than the depletion time-scale associated with star formation only. However, when considering also the atomic component, the depletion time-scale for the total gas content ($\tau_{\rm depl,outf}(\rm tot)= M(H_2 + HI)/\dot{M}_{\rm outf}(H_2)$) is typically of the order, or longer than 10^8 yr, i.e. longer than the typical AGN lifetime. This indicates that AGN-driven outflows are generally capable of quickly removing the gas from the central regions (which are dominated by the molecular phase), but unlikely to clean the entire galaxy from its gas content.
- For AGN host galaxies the outflow kinetic power, $P_{\rm K,outf}(H_2)$, shows a much larger scatter than in previous studies and spans from 0.1 to 5 % of $L_{\rm AGN}$. The ratio $P_{\rm K,outf}(H_2)/L_{\rm AGN}$ increases with AGN luminosity. The momentum rate spans from 1 to 30 times $L_{\rm AGN}/c$. These results suggest that the AGN-driven outflows can be both energy-driven (with a broad range of coupling efficiencies with the ISM) and radiation pressure-driven.
- We estimate that the fraction of outflowing gas with a high enough velocity to escape the galaxy and the dark matter halo is less than 5 %. This indicates that although outflows can remove gas from the central region, most of the expelled gas re-accretes on to the galaxy.

- The results on the kinetic power, on the momentum rate, on the depletion time-scale and on the fraction of escaping case, considered all together, indicate that the AGN 'ejective mode' is unlikely to be effective in cleaning the galaxy of its gas content, at least in the mass range probed by us ($M_\star > 10^{10}$ M$_\odot$). However, AGN outflows are likely capable of cleaning the gas content, hence quench star formation, in the central (bulge) region. Moreover, AGN-driven outflows can inject energy into the halo hence keeping it hot and preventing further gas accretion, therefore resulting in a delayed feedback that quenches the galaxy through starvation (Peng et al. 2015; Woo et al. 2017).
- In star forming galaxies, the kinetic power is only 1–2 % of the kinetic power generated by SNe, indicating very fast cooling of SN ejecta in the dense ISM in which they explode, hence poor efficiency in driving outflows, as expected by some models. In star forming galaxies, the momentum rate of outflows correlates with the bolometric luminosity, and it is about 0.3 $L_{\rm bol}/c$, suggesting that radiation pressure can also contribute to drive outflows in star forming galaxies.
- We also identify about 10 % of the galaxies whose outflow significantly exceeds the maximum theoretical values of kinetic power and momentum rate expected for both AGN and SB-driven cases. Our proposed explanation is that these are 'fossil outflows' resulting from the activity of a past strong AGN, which has now faded. Theoretical models expect such fossil outflows to be present in large numbers, also simply based on the fact that the outflows dynamical time-scales is of the order of $10^6 - 10^8$ yr while the AGN has a much shorter variability ($1 - 10^6$ yr). Previous outflow surveys have not identified such fossil outflows because they may have been biased towards powerful AGN and powerful starburst galaxies in order to maximize the probability of detecting outflows. Our sample is less biased in this sense (as it includes galaxies that were not selected specifically with the goal of detecting outflows), which has enabled us to detect this phenomenon. However, our sample is still biased, hence the fraction of fossil outflow found by us is probably still the tip of the iceberg of a larger population.

Table 2.2: List of galaxies in the sample analysed in this work, together with some of their basic properties

Galaxy	type	z	D_L [Mpc]	SFR [$M_\odot$ yr^{-1}]	$\log(L_{AGN})$ [erg s^{-1}]	$\log(M_\star)$ [$M_\odot$]	α_{bol}	$\log(M(H_2))$ [$M_\odot$]	$\log(M(HI))$ [$M_\odot$]	q_{IR}	Ref.
(1)	(2)	(3)	(4)	(5)	(6)	(7)	(8)	(9)	(10)	(11)	(12)
CO Literature data											
IRAS F08572+3915	Sy2	0.05821	265	20	45.72	10.79	0.86	9.18		3.57	α, A, a
IRAS F10565+2448	Sy2	0.04311	196	95	44.81	10.66	0.170	9.90		2.64	α, A, a
IRAS 23365+3604	LINER	0.06438	285	137	44.67	11.23	0.072	9.93		2.73	α, A, a
Mrk 273	Sy2	0.03777	169	139	44.16	11.10	0.080	9.70	10.21	2.49	α, A, a
IRAS F23060+0505	Sy2	0.17300	831	75	46.06	11.75	0.780	10.39		2.79	α, A, a
Mrk 876	Sy1	0.12900	607	6.5	45.84	11.64	0.930	9.84		2.63	α, A, a
I Zw 1	Sy1	0.06114	259	36	45.37	11.30	0.520	9.56	10.27	3.04	α, A, a
Mrk 231	Sy1	0.04217	189	234	45.72	11.53	0.340	9.73		2.44	α, A, a
NGC 1266	LINER	0.00719	28.6	1.6	43.31	10.30	0.250	9.23		2.36	α, A, a
M82	HII	0.00068	4.03	10	$\leq$41.54	10.66	$\leq$0.0009	8.64	9.04	2.62	α, A, a
NGC 1377	LINER	0.00578	23.9	0.9	42.93	10.06	0.200	8.44	9.89		α, A, a
NGC 6240	Sy2	0.02448	107	16	45.38	11.53	0.780	9.86	10.05	2.10	α, A, a
NGC 3256	HII	0.00926	44.6	36	$\leq$41.97	11.23	$\leq$0.0007	9.68	9.89	2.37	α, A, a
NGC 3628	HII	0.00280	17.1	1.8	$\leq$40.79	11.30	$\leq$0.0009	9.53	10.31	2.00	α, A, a
NGC 253	HII	0.00081	2.77	3	$\leq$40.66	10.65	$\leq$0.0004	8.15	9.27	3.01	α, A, a
NGC 6764	LINER	0.00807	32.6	2.6	42.23	10.48	0.017	8.90	9.64	2.25	α, A, a
NGC 1068	Sy2	0.00379	13.1	18	43.94	11.23	0.097	9.11	9.12	2.32	α, A, a
IC 5063	Sy2	0.01100	47.2	0.6	44.30	11.02	0.9	8.85	10.75	1.11	α, A, a
NGC 2146	HII	0.00298	12.5	12	$\leq$41.09	10.58	$\leq$0.0003	8.94	9.41	2.83	α, A, a

Continued on next page

Table 2.2 – *Continued from previous page*

Galaxy	type	z	D_L [Mpc]	SFR [$M_\odot$ yr^{-1}]	log(L_{AGN}) [erg s^{-1}]	log($M_\star$) [$M_\odot$]	α_{bol}	log($M(H_2)$) [$M_\odot$]	log(M(HI)) [$M_\odot$]	q_{IR}	Ref.
IRAS 17208-0014	HII	0.0428	189	200	≤43.67	11.33	≤0.24	10.03		2.79	β, B, b
NGC 1614	HII	0.0159	68.3	45	≤42.07	11.07	≤0.0006	9.51		2.77	β,γ, C, b
Circinus Galaxy	Sy2	0.0014	8.34	0.6	43.57	10.95	0.59	9.32	10.27	2.07	δ, D, b
SDSS J1356+1026	Sy2	0.1230	579	20	46	11.36	0.43	8.91		2.32	ϵ, E, b
ESO 320-G030	HII	0.0108	51.1	20	≤41.09	11.03	≤0.0001	9.08		2.77	ζ, F, b
NGC 1808	HII	0.0033	10.8	5.1	≤40.98	10.64	≤0.0005	9.28	7.70		β, C, b
NGC 1433	Sy2	0.0036	14.5	0.23	42.24	10.67	0.20	8.63	9.22		η, G, b
M51	Sy2	0.0020	11.1	2.6	43.79	11.06	0.61	10.12	9.80	2.11	θ, H, b
4C 12.50	Sy2	0.1217	573	84	45.70	11.66	0.60	10.02		0.002	β ,I,b,c
IRAS 05081+7936	HII	0.0537	239	98	≤42.37	11.51	≤0.0006	10.03		2.54	ι, J, d
IRAS 10035+4852	HII	0.0648	294	100	≤45.11	11.19	≤0.33	9.79		2.54	ι, J, d
IRAS F11119+3257	Sy1	0.189	929	144	46.2	12.20	0.689	9.94		1.62	κ, K, c
CO ALMA archival data											
IRAS 20100-4156	HII	0.129583	605	330	≤42.93	11.10	≤ 0.0007	9.95		2.93	σ, O, b
PG 0157+001	Sy1	0.16311	777	209	45.29	11.71	0.18	9.38		2.13	τ, P, b
IRAS 15115+0208	HII	0.095482	441	50.9	≤43.49	11.96	≤0.1	9.72			υ, J, b
IRAS 05189-2524	Sy2	0.042563	189	146	44.47	11.06	0.05	8.99		3.08	χ, Q, b
NGC 4418	Sy2	0.007268	36.4	14.5	43.81	10.22	≤0.0005	8.59	8.66	3.35	η, S, b
IRAS 13120-5453	Sy2	0.030761	138	157	44.35	11.14	0.173	9.59			η, N, c, f
IRAS 22491-1808	HII	0.077760	348	145	≤41.64	11.07	≤0.06	10.22		3.26	ψ, Q, h
NGC 1386	Sy2	0.002895	11.1	0.27	40.19	10.03	0.0015	8.28		2.69	λ, L, b
NGC 6810	HII	0.006775	28	5.0	40.70	10.93	0.0003	8.86			μ, C, b

Continued on next page

Table 2.2 – *Continued from previous page*

Galaxy	type	z	D_L [Mpc]	SFR [$M_\odot$ yr^{-1}]	$\log(L_{AGN})$ [erg s^{-1}]	$\log(M_\star)$ [$M_\odot$]	α_{bol}	$\log(M(H_2))$ [$M_\odot$]	$\log(M(HI))$ [$M_\odot$]	q_{IR}	Ref.
NGC 5643	Sy2	0.003999	20.1	3.6	42.91	10.90	0.0029	8.99	9.42		ν, H, b
OH outflows (González-Alfonso et al. 2017)											
IRAS F03158+4227	Sy2	0.13459	632	220	45.94	11.70	0.55				ξ, o, C, e
IRAS F14348-1447	LINER	0.08257	382	169	44.59	11.46	0.17	10.17			o, M, e
IRAS F14378-3651	LINER	0.067637	308	112	45.12	11.15	0.21	9.46		2.56	o, π, N, e
IRAS F20551-4250	LINER	0.04295	187	43	44.75	11.15	0.13	9.67		2.89	β, C, e

Table 2.2: Outflow properties: (1) galaxy name, (2) outflow mass, (3) outflow radius, (4) outflow velocity (following the prescription in Rupke et al. (2005a)), (5) mass outflow rate, (6) depletion time due to outflows, (7) kinetic power divided by AGN luminosity, (8) momentum rate boost, (9) ionized mass outflow rate, (10) neutral outflow rate using Na I D absorption, (11) neutral outflow rate using [CII], (12) fraction of the outflowing gas escaping the galaxy (*these values are taken from the literature and their definition of outflow velocity is slightly different from the one used here), (13): references: (a) Cicone et al. (2014), (b) García-Burillo et al. (2015), (c) Zschaechner et al. (2016), (d) Sun et al. (2014), (e) Pereira-Santaella et al. (2016), (f) Salak et al. (2016), (g) Combes et al. (2013), (h) Querejeta et al. (2016), (i) Dasyra et al. (2014), (j) Leroy et al. (2015), (k) Veilleux et al. (2017), (l) this work, includes information about which CO transition is used (m): González-Alfonso et al. (2017), (14) CO transition used for calculation of outflow properties.

Table 2.3: Outflow properties of the sample

Galaxy	$\log M_{\rm outf}(H_2)$	$R_{\rm outf}$	$v_{\rm outf}$	$\dot{M}_{\rm outf}(H_2)$	$\log \tau_{\rm depl,outf}(H_2)$	$\frac{P_{\rm K,outf}(H_2)}{L_{\rm AGN}}$	$\frac{\dot{M}_{\rm outf}(H_2)v}{L_{\rm AGN}/c}$	$\dot{M}_{\rm outf}$(ion)	$\dot{M}_{\rm outf}(HI)_{\rm NaID}$	$\dot{M}_{\rm outf}(HI)_{\rm [CII]}$	ef.	Ref.	Trans.
	$[M_\odot]$	[pc]	$[kms^{-1}]$	$[M_\odot yr^{-1}]$	[yr]			$[M_\odot yr^{-1}]$	$[M_\odot yr^{-1}]$	$[M_\odot yr^{-1}]$	[%]		
(1)	(2)	(3)	(4)	(5)	(6)	(7)	(8)	(9)	(10)	(11)	(12)	(13)	(14)
Literature data													
IRAS F08572+3915	8.61	820	800	403	6.57	0.016	11	0.32	25	130		(a)	1-0
IRAS F10565+2448	8.37	1100	450	100	7.90	0.0010	13	0.54	65	180		(a)	1-0
IRAS 23365+3604	8.17	1230	450	57	8.18	0.008	10					(a)	1-0
Mrk 273	8.24	550	620	200	7.40	0.17	160	0.66	7.9	110		(a)	1-0
IRAS F23060+0505	≤9.56	≤4050	(550)	≤500	≥7.69	≤0.004	≤4.5					(a)	1-0
Mrk 876	≤9.48	≤3550	(700)	≤610	≥7.05	≤0.014	≤12					(a)	1-0
I Zw 1	≤7.67	≤500	(500)	≤47	≥7.90	≤0.0016	≤1.9					(a)	1-0
Mrk 231	8.47	600	700	350	7.19	0.01	8.8	0.05	180	250	4.6	(a)	1-0
NGC 1266	7.93	450	177	11	8.19	0.005	18				2*	(a)	1-0
M82	8.08	800	100	4	8.04	≥0.036	≥218					(a)	1-0
NGC 1377	7.29	200	110	5	7.77	0.0021	11				<1	(a)	2-1
NGC 6240	8.61	650	400	267	7.43	0.006	8.4			≤1300		(a)	1-0
NGC 3256	7.34	500	250	4	9.12	≥0.08	≥190	3.6	26			(a)	2-1
NGC 3628	7.36	400	50	1.5	9.35	≥0.019	≥230					(a)	1-0
NGC 253	6.32	200	50	1.4	8.00	≥0.024	≥290	0.60				(a)	2-1
NGC 6764	6.52	600	170	1	8.89	0.006	20					(a)	1-0
NGC 1068	7.26	100	150	28	7.66	0.0023	9.1					(a)	2-1
IC 5063	7.37	500	300	8	7.97	0.0011	2.2	0.21				(a)	2-1
NGC 2146	7.68	1550	150	5	8.27	≥0.27	≥1100					(a)	1-0
IRAS 17208-0014	7.66	160	600	176	7.78	≥0.43	≥430	46	34			(b)	2-1
NGC 1614	7.51	560	360	21	8.19	≥0.74	≥1200	13	22			(b)	1-0
Circinus Galaxy	6.48	450	150	1	9.31	0.0002	0.78	0.07				(c)	1-0
SDSS J1356+1026	7.84	300	500	118	6.84	0.0009	1.1	2.7				(d)	3-2
ESO 320-G030	6.81	2500	455	1.2	9.00	≥0.63	≥840	1.6	24			(e)	2-1
NGC 1808	7.48	1000	98	3	8.80	≥0.094	≥580					(f)	1-0
NGC 1433	5.81	100	100	0.7	8.82	0.0012	7.1	0.07				(g)	3-2
M51	6.61	37	100	11	9.07	0.0006	3.5					(h)	1-0
4C 12.50	7.72	150	640	227	7.66	0.006	5.5				<30*	(i)	3-2
IRAS 05081+7936	≤8.01	≤500	(400)	≤95	≥8.05							(j)	1-0
IRAS 10035+4852	≤8.15	≤500	(400)	≤117	≥7.72							(j)	1-0
IRAS F11119+3257	9.14	7000	1000	203	7.63	0.0046	2.7				5.7	(k)	1-0
ALMA archival data													

Continued on next page

Table 2.3 – *Continued from previous page*

Galaxy	$\log M_{\rm outf}(H_2)$ [$M_\odot$]	$R_{\rm outf}$ [pc]	$v_{\rm outf}$ [kms^{-1}]	$\dot{M}_{\rm outf}(H_2)$ [$M_\odot$yr^{-1}]	$\log \tau_{\rm depl,outf}(H_2)$ [yr]	$\frac{P_{\rm K,outf}(H_2)}{L_{\rm AGN}}$	$\frac{\dot{M}_{\rm outf}(H_2)v}{L_{\rm AGN}/c}$	$\dot{M}_{\rm outf}$(ion) [$M_\odot$yr^{-1}]	$\dot{M}_{\rm outf}(HI)_{\rm NaID}$ [$M_\odot$yr^{-1}]	$\dot{M}_{\rm outf}(HI)_{\rm [CII]}$ [$M_\odot$yr^{-1}]	ef. [%]	Ref.	Trans.
IRAS 20100-4156	9.31	663	456	1457	6.78	≥11	≥15000	2.5			9.3	(l)	1-0
PG 0157+001	8.39	729	268	93	7.41	0.001	2.4				0.94	(l)	3-2
IRAS 15115+0208	8.82	1174	103	59	7.95	≥0.006	≥38				<1	(l)	1-0
IRAS 05189-2524	8.87	189	491	219	6.64	0.060	69	7.0		480	7.6	(l)	3-2
NGC 4418	7.90	569	134	19	7.31	0.0017	7.6				<1	(l)	2-1
IRAS 13120-5453	8.55	179	549	1115	6.54	0.47	520			680	0.82	(l)	3-2
IRAS 22491-1808	8.73	202	241	654	7.40	≥27	≥68000				0.29	(l)	2-1
NGC 1386	≤6.23	80	500	≤17	≥7.24	≤56	≤68000					(l)	1-0
NGC 6810	≤7.20	120	500	≤64	≥7.03	≤107	≤130000					(l)	1-0
NGC 5643	≤6.92	60	500	≤85	≥7.14	≤0.68	≤820					(l)	1-0
OH outflows (González-Alfonso et al. 2017)													
IRAS F03158+4227	8.70	335	1000	1500	6.62	0.055	33					(m)	
IRAS F14348-1447	8.62	355	450	420	7.54	0.07	95			≤1500		(m)	
IRAS F14378-3651	8.07	255	425	180	7.20	0.008	11					(m)	
IRAS F20551-4250	8.00	175	450	200	7.37	0.023	31	0.40				(m)	

Table 2.3: Outflow properties: (1) galaxy name, (2) outflow mass, (3) outflow radius, (4) outflow velocity (following the prescription in Rupke et al. (2005a)), (5) mass outflow rate, (6) depletion time due to outflows, (7) kinetic power divided by AGN luminosity, (8) momentum rate boost, (9) ionized mass outflow rate, (10) neutral outflow rate using Na I D absorption, (11) neutral outflow rate using [CII], (12) fraction of the outflowing gas escaping the galaxy (*these values are taken from the literature and their definition of outflow velocity is slightly different from the one used here), (13): references: (a) Cicone et al. (2014), (b) García-Burillo et al. (2015), (c) Zschaechner et al. (2016), (d) Sun et al. (2014), (e) Pereira-Santaella et al. (2016), (f) Salak et al. (2016), (g) Combes et al. (2013), (h) Querejeta et al. (2016), (i) Dasyra et al. (2014), (j) Leroy et al. (2015), (k) Veilleux et al. (2017), (l) this work, includes information about which CO transition is used (m): González-Alfonso et al. (2017), (14) CO transition used for calculation of outflow properties.

Table 2.4: Fossil Outflow candidates

Galaxy	$P_{\mathrm{K,outf}}(\mathrm{H_2})/L_{\mathrm{AGN}}$	$(\dot{M}_{\mathrm{outf}}(\mathrm{H_2})\ v)/(L_{\mathrm{AGN}}/\mathrm{c})$	$P_{\mathrm{K,outf}}(\mathrm{H_2})/P_{\mathrm{K,SF}}(\mathrm{H_2})$ [%]
Mrk 273	0.17	160	27
IRAS 17208-0014	≥0.43	≥430	14
IRAS 20100-4156	≥11	≥15000	18
IRAS 13120-5453	0.47	520	97
IRAS 22491-1808	≥27	≥68000	12

Table 2.4: Outflow properties: (1): galaxy name, (2): ratio of kinetic power of the outflow and the bolometric luminosity of the AGN, (3): momentum boost factor, (4): kinetic energy outflow compared to kinetic energy due to supernovae.

2.6 Appendix: ALMA Archival Data

In Figs 2.20–2.26 of this appendix, we show the ALMA archival data of galaxies in which we have found evidence for outflows. Each figure shows on the top panels the integrated spectrum along with a zoom in the y-axis, and where the blue dashed line shows the narrow component and the red dashed line the broad component tracing the outflow. The central panel shows the position–velocity diagram along the major axis (left) and along the minor axis (right). The bottom panels show the map of the broad wings, i.e. the flux integrated in the velocity ranges where the broad component is stronger than the narrow component (specific velocity ranges are indicated on top of each panel).

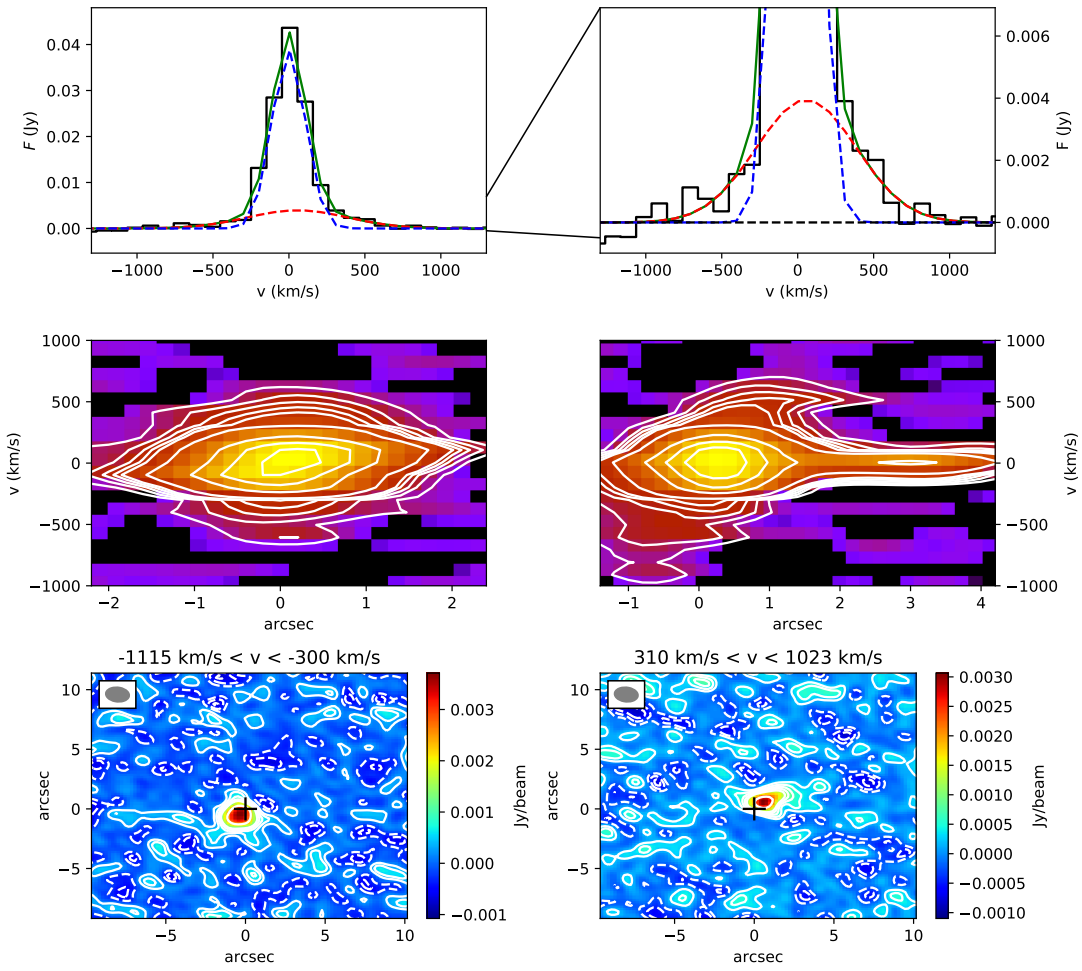

Figure 2.20: IRAS 20100-4156: The top panels show the CO line emission and the fit to the line, where the blue dashed line represents the narrow emission and the red dashed line is the broad component. The two middle panels show the position-velocity diagrams along the major (left) and minor (right) axis with (1,2,3,4,5,10,30,50,70)σ contours as white lines. In the bottom panel, the linemaps of the wings are depicted (produced by integrating over the spectral range where the broad component, i.e. outflow component, is dominant). The black cross indicates the peak of the narrow emission. Positive contours are shown as white lines (1,2,3,4,5,10)σ and negative contour are represented by white dashed lines (-1,-2,-3)σ.

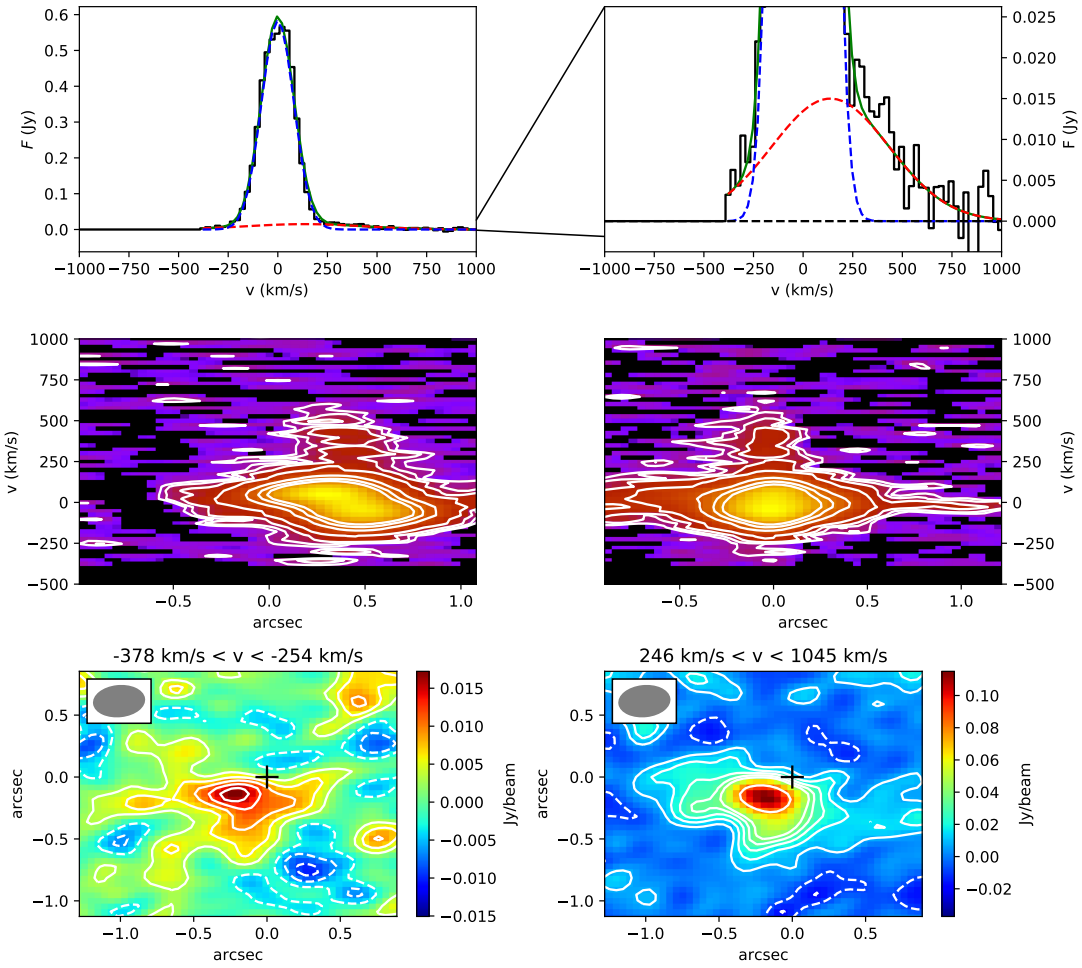

Figure 2.21: IRAS 05189-2524: see caption of Fig. 2.20, but contours in p–v diagrams (middle panel) are (2,3,5,10,30,50,70)σ.

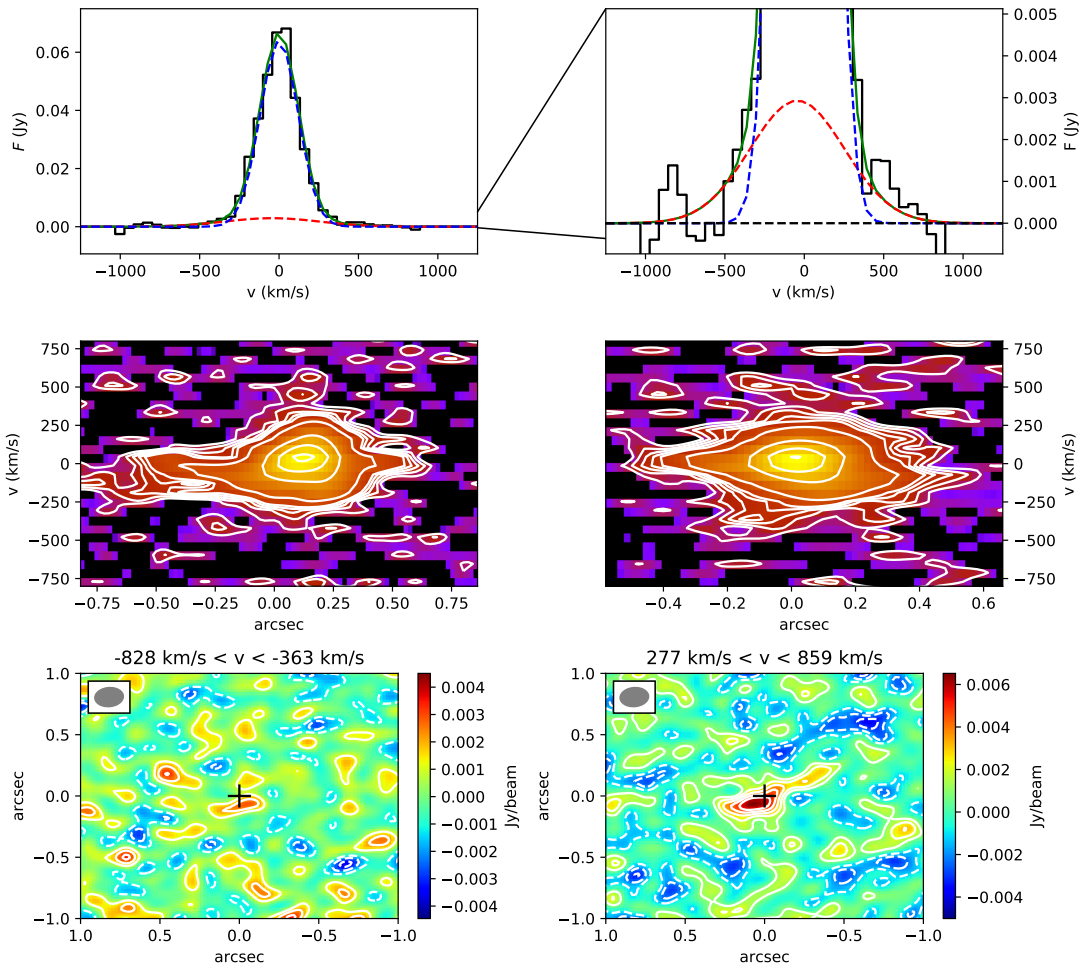

Figure 2.22: PG 0157+001: see caption of Fig. 2.20

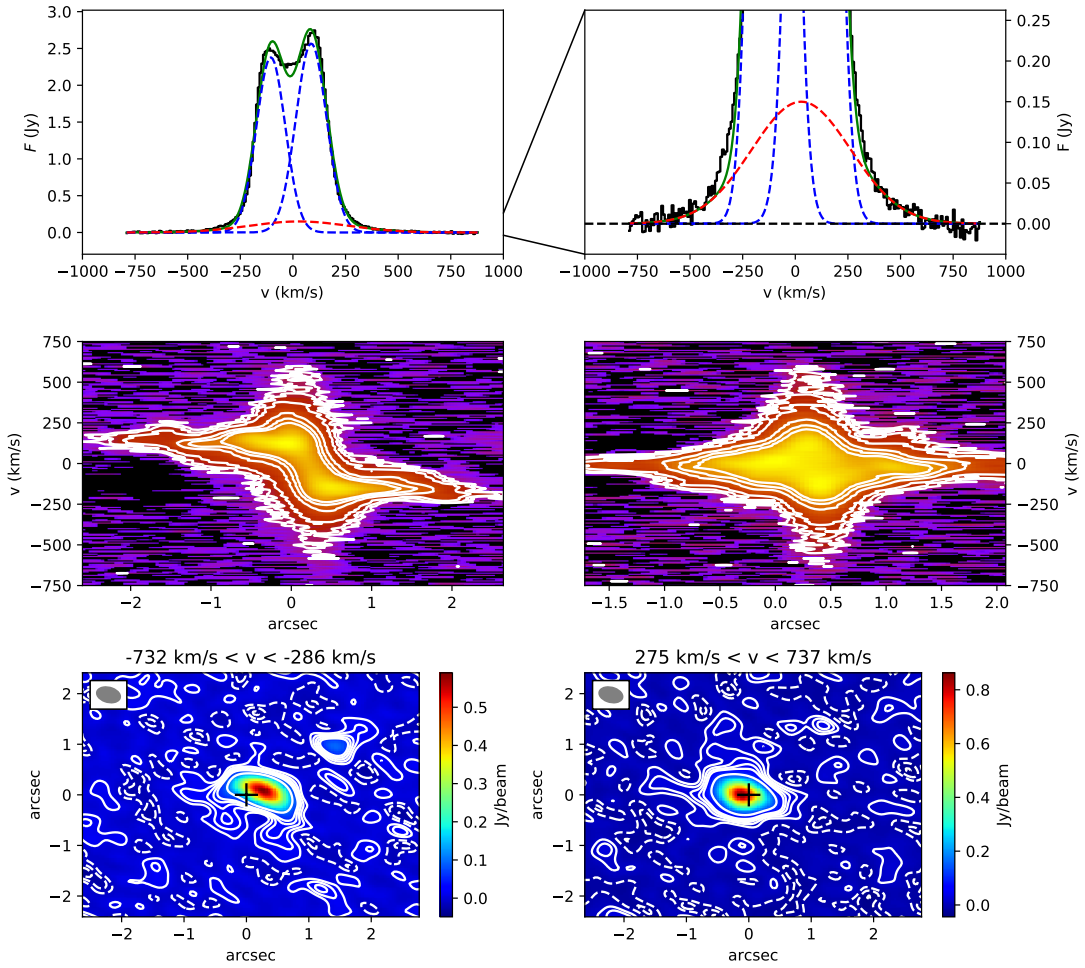

Figure 2.23: IRAS13120-5453: see caption of Fig. 2.20, but contours in p–v diagrams (middle panel) are (3,5,10,30,50,70)σ.

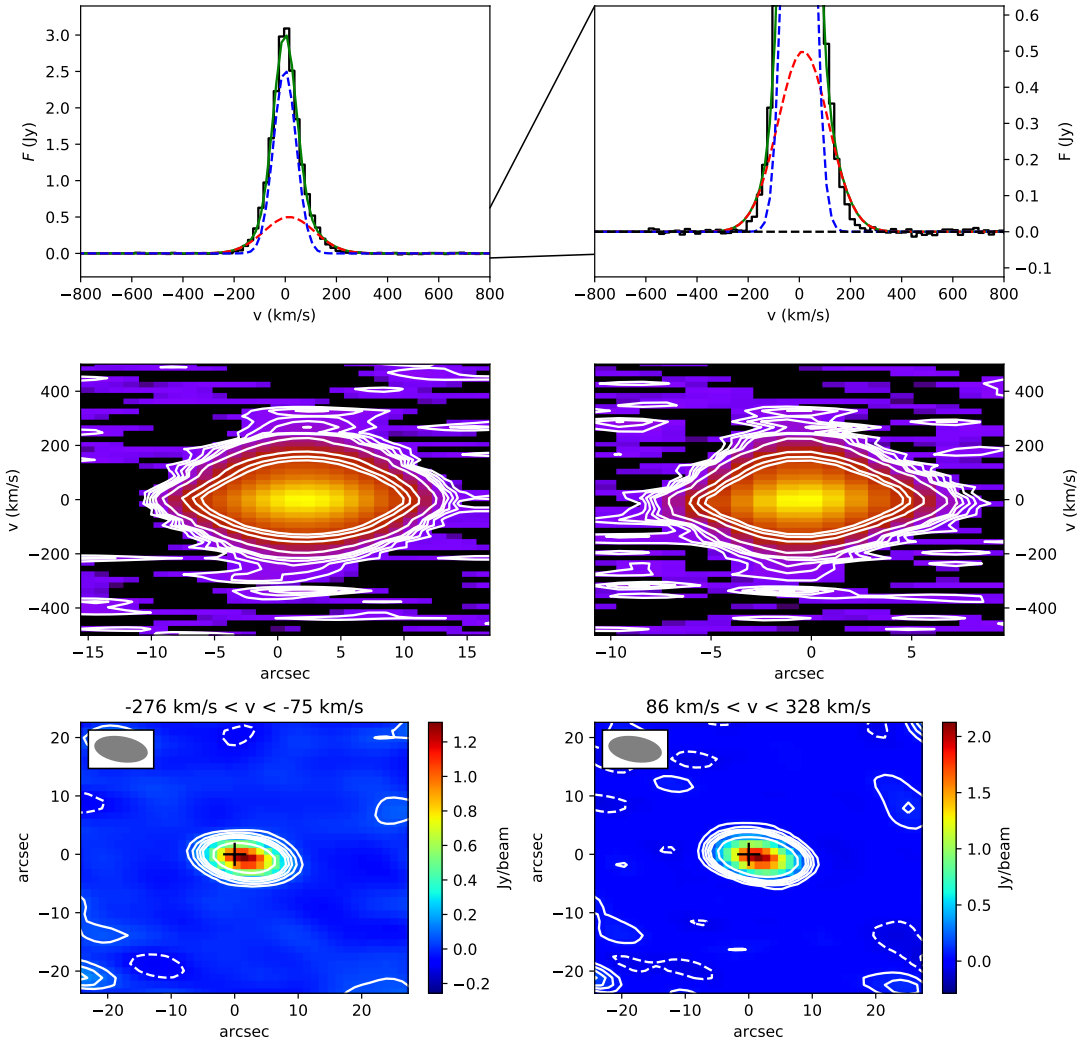

Figure 2.24: NGC4418: see caption of Fig. 2.20

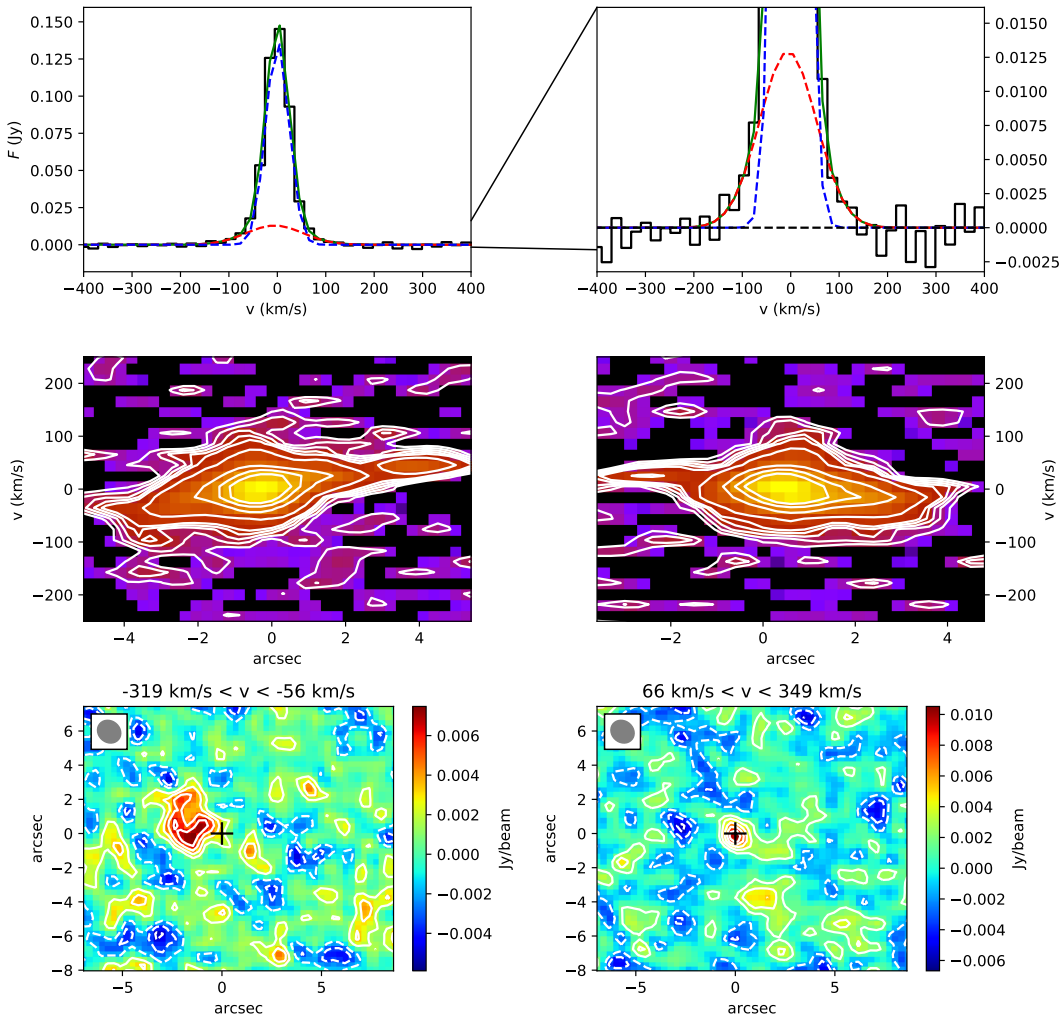

Figure 2.25: IRAS15515+0208: see caption of Fig. 2.20

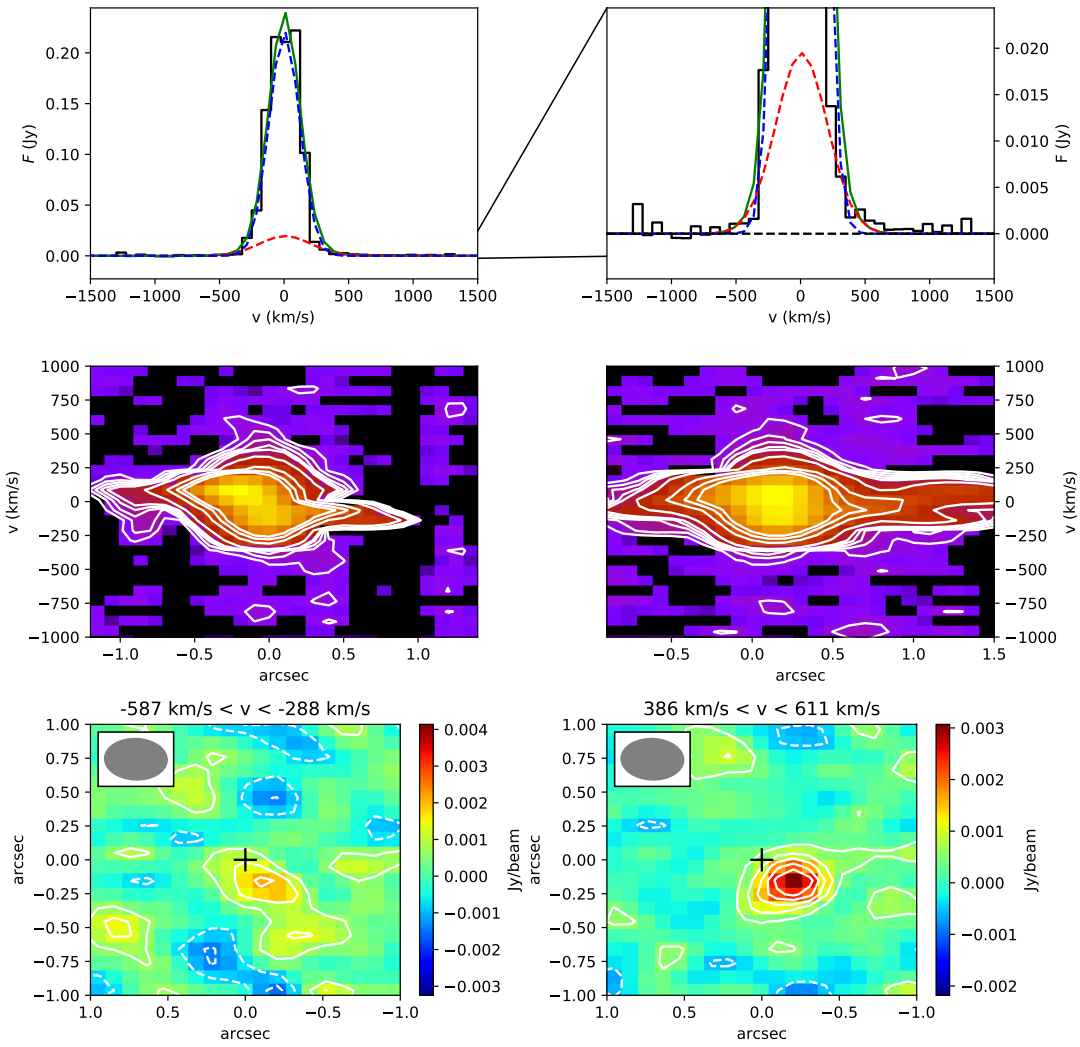

Figure 2.26: IRAS 22491-1808: see caption of Fig. 2.20

Chapter 3

Properties of the Multiphase Outflows in Local (Ultra)luminous Infrared Galaxies

This chapter is adapted from 'Properties of the Multiphase Outflows in Local (Ultra)luminous Infrared Galaxies', A Fluetsch et al., 2020, arXiv: 2006.13232

In recent years, galactic winds and outflows have been observed in several different gas phases, including in the hot highly-ionized, the warm ionized, the neutral atomic phase and the molecular gas phase (details are given in Chapter 1). These measurements trace outflows at different spatial scales (from sub-pc in the X-ray to tens of kpc in the cold molecular and ionized phase) and in different physical conditions (e.g. they are sensitive to different temperatures and densities). Especially in low-redshift Seyfert galaxies, several studies have been able to resolve gas kinematics and outflows down to $\sim$ 10 pc (Alonso-Herrero et al. 2018; Shimizu et al. 2019; Slater et al. 2019). Some of these works successfully detected very weak outflows with mass outflow rates << 1 $M_{\odot}$/yr, acting only on small-scales (e.g. Finlez et al. 2018; Shimizu et al. 2019).

The vast majority of outflow studies, however, focus on one single outflow phase. Only a small number of works have studied several phases in a single galaxy and found that galactic outflows are multiphase and can be as complex as the normal ISM. For instance, in the Seyfert galaxy IC 5063, a remarkable kinematic similarity between the ionized, neutral atomic and the molecular phase was found (Morganti et al. 2015; Oosterloo et al. 2017), suggesting a link between the different phases. Similarly, HE 1353-1917 (Husemann et al. 2019) and IRAS F08572+3915 (Herrera-Camus et al. 2020) also display co-spatiallity between the molecular

and the ionized outflow phase. In other galaxies, such as Mrk 231 (Feruglio et al. 2015), the interplay between gas phases appears to be much more complex and there might have been several feedback episodes. In a sample of Seyfert I galaxies, it was found that the spatial correlation between neutral atomic outflows traced by the sodium doublet and the ionized outflow varies greatly from galaxy to galaxy, but overall, the different phases seem to be unrelated (Rupke et al. 2017).

Despite these efforts to detect multiphase outflows, the connection (if there is any) between the different outflow phases and therefore the physical mechanism driving them remains mostly unknown (Cicone et al. 2018). One major open question is the relative contribution of different phases to the total mass or energy budget of the outflow. It is crucial to know the *total* outflow mass and energy as only this will enable a thorough comparison to simulations of AGN or star formation-driven feedback (e.g. Biernacki & Teyssier 2018; Nelson et al. 2019) and allow us to distinguish between different driving mechanisms (i.e. energy-driven, momentum-driven or radiation-pressure driven) (see e.g. Fabian 2012; Costa et al. 2014).

Several observational studies have suggested that the molecular phase is dominant with a mass that is a factor of 10–100 larger than that in the ionized phase (Carniani et al. 2015; Fluetsch et al. 2019; Ramos Almeida et al. 2019), although the uncertainties in both phases are significant. Fiore et al. (2017) confirmed with disjoint samples that the molecular mass outflow rate is significantly higher than the ionized mass outflow rate, but suggested that at high AGN luminosity, the ionized phase becomes more prominent and almost comparable in outflow rate at luminosities above $L_{\rm AGN} \sim 10^{47}$ erg s^{-1}. By only selecting objects with measurements of both gas phases instead of disjoint samples, Fluetsch et al. (2019) were unable to reproduce the increasing contribution of the ionized outflow phase at high AGN luminosities. However, most galaxies in Fluetsch et al. (2019) have AGN luminosities below 10^{46} erg s^{-1} and might therefore not properly test the regime discussed in Fiore et al. (2017).

3.1 Introduction

In this chapter, we investigate multiphase outflows in a sample of 26 local ($z < 0.2$) (ultra)luminous infrared galaxies ((U)LIRGs). ULIRGs, formally defined as a class of galaxies with an infrared luminosity $>10^{12}$ $L_\odot$ (ULIRGs) (or $>10^{11}$ $L_\odot$ for LIRGs), are galaxies with a strong AGN, starburst activity or a combination of the two. Usually, (U)LIRGs are (advanced) mergers and have large amounts of gas and dust (Lonsdale et al. 2006; Kartaltepe et al. 2010). This makes them suitable laboratories to study feedback as they are likely to exhibit fast and massive outflows (see e.g. Rodríguez-Zaurín et al. 2013; Rose et al. 2017) and resemble massive active galaxies at higher redshift, where we expect feedback processes to be enhanced. Fur-

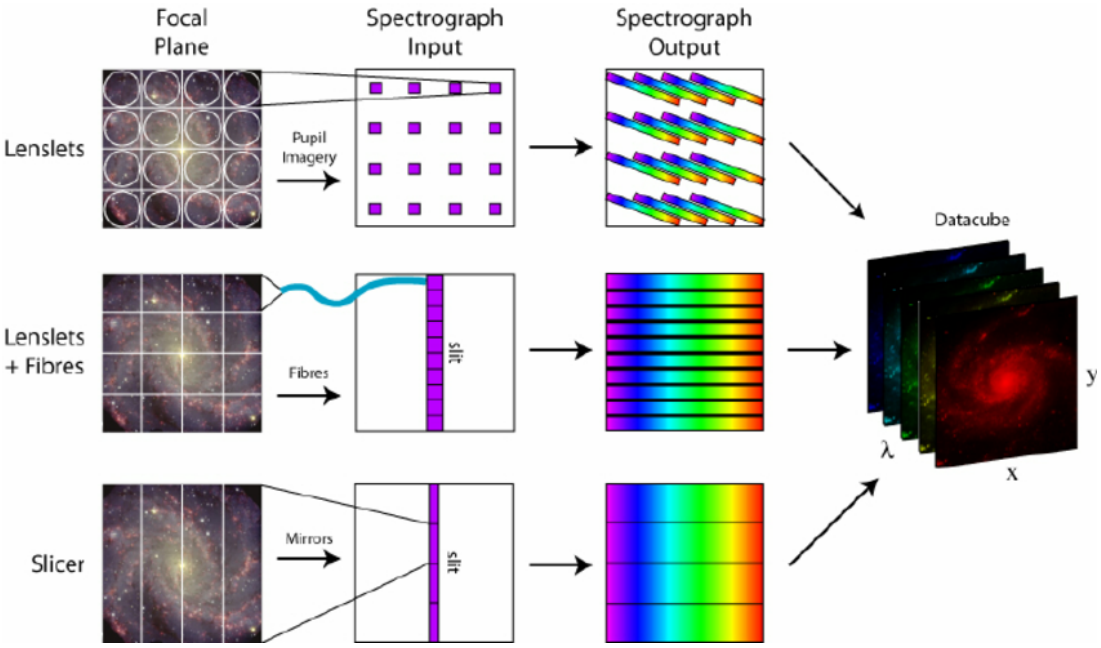

Figure 3.1: Illustration of the techniques used in integral field spectroscopy. The focal plan on the left is sample using either a) lenslets (top row), b) lenslets and fibres (middle row) or c) an image slicer (bottom row). The data product is a 3D data cube with two spatial dimensions (x and y) and a wavelength channel (λ). Figure from Westmoquette et al. (2009).

thermore, we supplement our sample with multiphase outflows from the literature, increasing our total sample size to 31 galaxies with multiphase outflows. This makes our work the largest spatially resolved multiphase outflow study to date.

The goal of this chapter is twofold. First, we aim to characterise the multiphase outflows in our sample of local (U)LIRGs in terms of morphology, kinematics and outflow properties (e.g. electron density). Second, we shed light on the connection between the different gas phases as well as their relative contribution, both on a spatially resolved basis and in terms of global properties such as mass outflow rate or kinetic power of the outflow.

As in Chapter 2, we assume a $H_0 = 70$ km s^{-1} Mpc^{-1}, $\Omega_M = 0.27$ and $\Omega_\Lambda = 0.73$ cosmology.

3.2 Methods

3.2.1 Integral Field Spectroscopy and MUSE

The results in this and the following chapter were obtained using the Multi Unit Spectroscopic Explorer (MUSE) at the Very Large Telescope (VLT). We will therefore briefly explain the principles of integral field spectroscopy in this section. IFS is a type of spectroscopy that allows to obtain a spatially resolved spectra of an astrophysical object. IFS solves some long-standing

issues of traditional long-slit spectroscopy, such as slit losses due to mismatched slit and object size or the difficulty of obtaining position-dependent information about an astrophysical source. Current IFS instruments operate at optical and infrared wavelengths. The basic components of an IFS are an integral field unit (IFU), which samples the field of view into separate spatial components, and a spectrograph, which is responsible for dispersing the incoming light onto a Charge Coupled Device (CCD). IFUs divide the 2D spatial plane with lenslet arrays (e.g. SAURON on the William Herschel Telescope (Bacon et al. 2001)), bundles of fibre-optic cables (e.g. MaNGA (Bundy et al. 2015)) or with an image slicer. MUSE uses an image slicer, where the light from the object on the sky encounters an array of mirrors, which are arranged at slighly different angles to segment the picture into smaller strips, which are fed through a spectrograph onto an array of 24 CCDs. The mechanism of IFS instruments is illustrated in Fig. 3.1, where the different types of IFUs (lenslets, lenslet and fibre-optic cables, and slicer) are shown on the right. The individual spatial components are then fed into a spectrograph, which disperses the light. Finally, the individual spectra are combined to create a 3D data cube (on the left).

For each spatial pixel (called spaxel), the signal is sent to a spectrograph and the resulting spaxels are combined into a 3D data cube at the data processing stage (described below). These data cubes consist of two spatial dimensions (x and y or RA and Dec) and a velocity or wavelength dimension (λ in Fig. 3.1).

3.2.2 Sample

Our sample consists of 26 local ($z < 0.2$) (U)LIRGs. These are galaxies with a strong AGN, significant star formation or a combination of the two. The sample includes both, AGN and star formation-dominated objects. The objects span several order of magnitude in AGN luminosity, from $\lesssim 10^{42}$ erg s^{-1} to $\sim 10^{46}$ erg s^{-1}. These galaxies were observed as part of several different ESO Multi Unit Spectroscopic Explorer (MUSE) observing programmes at the Very Large Telescope. 11 galaxies were observed under programme 101.B.0368 (PI: Maiolino). Four galaxies are from the programme 102.B.0617 (PI: Fluetsch). The remaining targets are taken from a variety of different programmes: three targets from 095.B-0049, two targets from each 094.B-0733 and 096.B-0230, and one target from each of the following observing programmes 60.A.9315, 097.B.0165, 097.B-0313 and 094.B-0733.

3.2.3 Data Analysis

The MUSE data cubes are used in their reduced form after running the MUSE pipeline. The full description of the pipeline is provided in Weilbacher et al. (2020). Briefly, the MUSE pipeline consists of two stages. In the first stage, the data of the individual 24 CCD is calibrated

and pre-processed. In this stage, bias, dark current and flat field corrections are applied. In addition, the wavelength is calibrated and the sky subtracted. In the second stage the IFUs of one or more exposures are combined into the final data cube.

This produces a data cube of about 300 × 300 spaxels which cover the MUSE field of view (1' × 1' in the Wide Field Mode) with a spatial sampling of 0.2" × 0.2". The point spread function (PSF) of MUSE is roughly circular in shape and has a FWHM of 0.66 arcsec at 7000 Å. It decreases from about 0.75 arcsec at 5000 Åto 0.60 arcsec at 9000 Å(Bacon et al. 2015). The wavelength coverage of MUSE cubes ranges from 4650 Å to 9300 Å and, at the redshift of the targets, covers all the main optical emission lines of interest (from Hβ to [SII]$\lambda\lambda$6716,6731). It achieves a resolution between 1750 (at 4650 Å) and 3750 (at 9300 Å). The field of view covers between ∼10 kpc to ∼170 kpc of the galaxy depending on its redshift. The spatial resolution, $FWHM_{\rm seeing}$ ranges from 0.55–2.0" across the same and the average of these in the sample is about 1". The typical observation time for the targets is approximately 40 mins.

In a first step, the data cubes are binned using Voronoi tessellation (Cappellari & Copin 2003) to achieve an average signal-to-noise ratio (SNR) of 30–40 (this varies from galaxy to galaxy) per wavelength channel in each bin in the r-band (5405–6982 Å). In this step, all spaxels with a SNR < 3 in the r-band are discarded to avoid noisy spectra in the Voronoi bins.

The stellar continuum is modelled using the MILES stellar library templates, which include about 1000 stars, which range across a large number of atmospheric parameters (such as ages and metallicities) (Sánchez-Blázquez et al. 2006). These templates cover the wavelength range from 3525–7500 Å, which includes all nebular lines which are of interest for our analysis. The fitting is performed using an adapted Penalized Pixel-Fitting (pPXF) routine (Cappellari & Emsellem 2004; Cappellari 2017) and allowing an additive Legendre polynomial to correct the shape of the the template continuum. The main emission lines (Hβ, [OIII]$\lambda\lambda$4959,5007, [OI]$\lambda\lambda$6300,6366, Hα, [NII]$\lambda\lambda$6548,6584 and [SII]$\lambda\lambda$6717,6732) are fitted simultaneously with the stellar continuum to allow optimal recovery of the total flux of emission lines, in particular the Balmer lines (see e.g. Sarzi et al. 2006). We fit with one, two or three Gaussian emission line components. During this step, we mask five strong sky emission lines (5577.4 Å, 5889.9 Å, 6157.7 Å, 6300.3 Å and 6363.7 Å) as well as the Na ID absorption lines (at 5889.9 Å and 5895.9 Å) at the target's redshift since this might not exclusively originate from stars in these galaxies, but also from absorption by neutral atomic gas in the ISM (see Section 3.2.5). As the best fit we select the model with the lowest $\chi^2_{\rm red}$. Next we subtract the stellar continuum from the total spectra in each spaxel, scaling the fit from bin to each spaxel according to their r-band flux. We performed visual checks of the fits for a sub-sample of spaxels to verify that the stellar continuum subtraction works well.

3.2.4 Ionized Gas

The resulting continuum-subtracted data cube is fitted on a spaxel-by-spaxel basis using the Python library lmfit (Newville et al. 2014). Lmfit provides non-linear optimisation and is built on the Levenberg-Marquardt algorithm (Levenberg 1944; Marquardt 1963). We fit the same emission lines as in the simultaneous fitting with one or two Gaussian components. For Seyfert I galaxies, we allow a third, very broad component for the Balmer lines to account for emission from the AGN broad line region (BLR). To accurately estimate the extent of outflows in Seyfert I galaxies a PSF correction is required (see e.g Husemann et al. 2016). For the Seyfert I galaxy IRAS 00509+1225, the only type I AGN in our sample with an outflow, this means that the outflow extent could be overestimated due to beam smearing. However, the radius we find in this galaxy agrees very well with results from Rupke et al. (2017) who did an elaborate PSF subtraction. To fit the very broad component, we first fit the central spaxel and use the results as the initial guess for width and velocity offset of this component. For galaxies with just two components, the width (σ) of the narrow component has to be smaller than 200 km s^{-1} and the broad component has to have a width of at least 125 km s^{-1} and has to be larger than the narrow component. For each component (narrow, broad and very broad if needed), we tie velocity centroid and dispersion, while the amplitudes are allowed to vary freely. Exceptions are the amplitudes of [OIII]$\lambda\lambda$4959,5007; [OI]$\lambda\lambda$6300,6366; and [NII]$\lambda\lambda$6548,6584, for which the ratio of the doublets is given by the Einstein coefficients. The ratio of the two emission lines of the [SII] doublet is allowed to vary between 0.44 and 1.5 (Osterbrock & Ferland 2006). For each spaxel we employ the reduced χ^2 (Andrae et al. 2010), $\chi^2_{\rm red}$, to determine whether a model with one, two or three components is preferred. We then select the model with the lowest $\chi^2_{\rm red}$ value. If based on the $\chi^2_{\rm red}$ metric, we find two or more components, we classify the broad component as a signature of an ionized outflow only if it is kinematically clearly distinct from the narrow component. In addition, we require the broad component to be larger than 3σ in the integrated spectrum in at least two lines. The integrated spectrum is calculated over the whole galaxy where SNR is larger than 3σ in the r-band. Finally, to get the intrinsic fluxes for all emission lines, we use the Balmer decrement and we apply a Calzetti et al. (2000) attenuation curve for a galactic diffuse ISM ($R_{\rm V}$ = 4.05) to correct for dust reddening. This should account for the mixing between dust and gas emitting regions in star forming galaxies.

3.2.5 Neutral Atomic Gas

To study the neutral atomic gas, we analyse the Na I doublet (at 5889.9 Å and 5895.9 Å) profile in the data cube obtained by dividing the original data cube by the continuum fit (for details see Rupke et al. 2005a). The Na ID line probes neutral gas (i.e. HI), thanks to the low

ionization potential of the associated transition, which is 5.14 eV. One caveat of the sodium absorption technique is that the detection of outflowing gas requires a strong background of stellar continuum light and hence outflows outside the projected stellar disc or far from the galaxy's bright centre might be missed. Residual stellar contribution (even after running pPXF) to the Na ID as well as contamination from Na ID emission and from the nearby He Iλ5876 emission line may further complicate the measurement.

As the sodium absorption feature is rather weak, we apply Voronoi binning to this data cube. We require a typical SNR of $>$ 10–15 for all targets on the sodium absorption feature in the stellar-continuum subtracted cube. We then fit the sodium absorption profile in each Voronoi bin.

Our fitting approach is based on a model of partially overlapping Na atoms (see Rupke et al. 2005a) with the analytical form:

$$I(\lambda) = 1 - C_{\rm f} + C_{\rm f} \times e^{-\tau_{\rm B}(\lambda) - \tau_{\rm R}(\lambda)} \tag{3.1}$$

with $C_{\rm f}$ being the covering fraction and $\tau_{\rm B}$ and $\tau_{\rm R}$ being the optical depths of the blue and the red Na I lines (5889.9 Å and 5895.9 Å). The optical depth of a line, $\tau(\lambda)$ is given by a Gaussian:

$$\tau(\lambda) = \tau_0 e^{-(\lambda - \lambda_0 + \Delta\lambda_{\rm offset})^2 / ((\lambda_0 + \Delta\lambda_{\rm offset}) b_{\rm D}/c)^2}, \tag{3.2}$$

where τ_0 and λ_0 are the central optical depth and wavelength of each line component and $b_{\rm D}$ is the Doppler linewidth. $\Delta\lambda_{\rm offset}$, the wavelength offset, is linked to the velocity offset: $\Delta\lambda_{\rm offset}$ = $\Delta {\rm v} \lambda_0$/c with c being the speed of light. The doublet is fit with one, two or three absorption components and up to one sodium emission component. We allow for simultaneous fitting of the emission and absorption components. This simultaneous fitting can lead to degeneracy. In order to minimize that, we tie the width of the Na ID emission component to the He I emission line width. The ratio of the central optical depths of the sodium doublet is fixed to $\tau_{0,B}/\tau_{0,R}$ = 2 for all absorption components which is given by the ratio of the Einstein parameters for the two transitions (Morton 1991). We require the covering fractions to be between 0 and 1. Simultaneously we also fit the He I emission line (5876 Å). This is important as the sodium absorption profile sometimes extends bluewards and its true amplitude might be underestimated if He λ5876 is not considered. To fit several components, we multiply the different $I_{\rm i}(\lambda)$'s, e.g. for two components $I(\lambda) = I_1(\lambda)\ I_2(\lambda)$, where $I_1(\lambda)$ and $I_2(\lambda)$ are of the form given in equation 3.1 with different covering fractions and optical depths for each component.

As in the emission line fitting, we use the lmfit library (Newville et al. 2014). The best fit is determined using the Bayesian information criterion (BIC). The BIC selects the best fit while taking into account the complexity of the model (i.e. models with more parameters are penalized) (Liddle 2007).

We use the 50th percentile, v_{50}, of the whole sodium absorption profile, as a measure of outflow velocity. Similar to Rupke et al. (2005a), we classify a component as outflowing if it has a velocity shift of $\Delta v < -50$ km s^{-1}. We adopt this conservative assumption to account for possible errors in the fitting. Redshifted sodium emission may also be additional evidence of receding, outflowing gas (see e.g. Rupke & Veilleux 2015; Roberts-Borsani & Saintonge 2019).

The advantage of this model is that the optical depth can be related to the sodium column density, N(Na I), via:

$$N(\mathrm{Na\ I}) = \frac{\tau_0 b_\mathrm{D}}{1.497 \times 10^{-15} \lambda_0 f}. \tag{3.3}$$

$\lambda_0 = 5897.55$ Å and $f = 0.318$ are the vacuum wavelength and the oscillator strength, respectively. b_D is the Doppler parameter, which is related to the velocity dispersion via $b_\mathrm{D} = \sqrt{2}\sigma$.

The hydrogen column density, N(H), is then given by:

$$N(\mathrm{H}) = N(\mathrm{Na\ I})(1-y)^{-1} 10^{-(a+b)}, \tag{3.4}$$

where y is the ionization fraction, a the galaxy's Na abundance and b the depletion onto dust. We assume the following values: $y = 0.9$, $a = -5.69$ and $b = -0.95$ (Savage & Sembach 1996; Rupke et al. 2005a). The hydrogen column density can then be used to calculate the outflow mass (see Section 3.2.7). Typical errors for the covering fraction and the velocity are around 20 % and 20 km s^{-1} (Rupke et al. 2005b), respectively, and we therefore conservatively assume an error of 0.5 dex on the neutral atomic mass outflow rate.

3.2.6 Ancillary Properties

In this chapter, we compare the neutral atomic, the ionized and the molecular outflow phases. The properties of the molecular outflows (velocity, radius and mass of the outflow as well as derived properties) are taken from Chapter 2. This chapter uses the same cosmology, the same definition of mass outflow rate and the same convention for the measurement of outflow radius and velocity as we do here and hence allows direct comparison.

The AGN luminosity, L_AGN, is provided in Chapter 2, where we use the absorption-corrected X-ray luminosity in the range from 2–10 keV and the bolometric correction by Marconi et al. (2004) to determine the AGN bolometric luminosity, L_AGN, in most cases. If no X-ray data is available, then the AGN bolometric luminosity is inferred from the extinction-corrected [OIII] luminosity using the relation given in Heckman et al. (2004).

We calculate the AGN contribution, $\alpha_\mathrm{bol} = L_\mathrm{AGN}/L_\mathrm{bol}$, where L_bol is the bolometric luminosity of the galaxy, which for ULIRGs is given by $L_\mathrm{bol} \approx 1.15\ L_\mathrm{IR}$ (Veilleux et al. 2009).

The star formation rates (SFRs) from Chapter 2 are used if possible. The calculation is based on the total infrared luminosity (8–1000 μm), taking into account the AGN fraction, $\alpha_{\rm bol}$ (Sturm et al. 2011). Otherwise, we calculate the SFR ourselves using the same prescription. There are a few exceptions: for HE 1351-1917, zC400528, 3C 298 we use the SFRs provided in the respective papers (see Table 3.2) based on spectral energy density (SED) fitting due to the lack of reliable IR data.

The optical classification in star forming, LI(N)ER and Seyfert galaxies is based on the galaxy's BPT diagrams, which will be presented in Chapter 4. An overview of the sample including ancillary data of the galaxies can be found in Table 3.2.

3.2.7 Calculation of Outflow Properties

In order to perform a comparison to previous outflow studies, we calculate the outflow properties in the integrated spectrum. To calculate the integrated spectrum we sum all spaxels with a r-band SNR > 3. In our analysis, we use the broad Hα component to calculate outflow properties. Some studies have used [OIII] instead, which gives lower outflow rate values (Carniani et al. 2015), likely because it does not properly account for the lower ionization phases of the outflow. The ionized mass outflow rate can be inferred from the Hα luminosity in the outflow (i.e. broad component), $L_{\rm H\alpha,OF}$, and the electron density, $n_{\rm e}$, as follows (Carniani et al. 2016):

$$M_{\rm OF,ion}[{\rm M}_\odot] = 6.1 \times 10^8 \left(\frac{L_{\rm H\alpha,OF}}{10^{44}\ {\rm ergs}^{-1}}\right)\left(\frac{n_{\rm e}}{500\ {\rm cm}^{-3}}\right)^{-1}. \tag{3.5}$$

We then obtain the mass outflow rate at radius $r_{\rm OF,ion}$ by dividing the outflowing gas mass by the dynamical time-scale, $\tau_{\rm OF}$:

$$\dot{M}_{\rm OF,ion} = \frac{M_{\rm OF,ion}}{\tau_{\rm OF,ion}} = \frac{M_{\rm OF,ion} v_{\rm OF,ion}}{r_{\rm OF,ion}}, \tag{3.6}$$

where $v_{\rm OF,ion}$ and $r_{\rm OF,ion}$ are the velocity and extent of the ionized outflow, respectively. We define the outflow velocity $v_{\rm OF} = \Delta v + {\rm FWHM}_{\rm broad}/2$ to be consistent with previous works (e.g. Rupke et al. 2005a; Fluetsch et al. 2019).

The radius of the ionized outflow is defined as the radius which encompasses 50 % of the total flux of the broad Hα component above 3σ. By directly determining the electron density in the outflow (see Section 3.3.2.1), we can drastically reduce the main uncertainty of this computation. Hence, the typical uncertainty on the ionized mass outflow rate is estimated to be $\sim$ 0.3 dex, mainly due to projection effects which affect the velocity and radius measurements as well as uncertainties in determining the electron density. The kinetic power of the outflow is given by $0.5 v_{\rm OF}^2\ \dot{M}_{\rm OF}$ (see Section 1.4).

The mass outflow rate of the neutral atomic outflow can be computed using equation 4.1 and using the neutral outflow velocity, radius and mass. Using the hydrogen column density obtained in Section 3.2.5, the neutral mass outflow rate is given by:

$$\dot{M}_{\mathrm{OF,neu}}[\mathrm{M_\odot yr^{-1}}] = 11.5 \sum_{i=1}^{N} \left(\frac{C_\Omega}{0.4} C_\mathrm{f}\right) \left(\frac{r}{10\ \mathrm{kpc}}\right) \times \left(\frac{N(\mathrm{H})}{10^{20}\ \mathrm{cm^{-2}}}\right) \left(\frac{\Delta v}{200\ \mathrm{km\ s^{-1}}}\right), \tag{3.7}$$

where we sum over all outflowing components, from $i = 1$ to N. C_f and C_Ω are the local (see eq. 3.1) and large-scale covering factor, respectively. Following Rupke et al. (2005a), we assume $C_\Omega = 0.4$ for LIRGs and $C_\Omega = 0.8$ for ULIRGs. $N(\mathrm{H})$ is the hydrogen column density along the line of sight and r is the radius.

Similar to the ionized outflow, we also calculate the properties of the neutral atomic outflow in the integrated spectrum. The spatial extent of the outflow, r_OF, is assumed to be 5 kpc as in Rupke et al. (2005b), which in turn is motivated by observations of by their data of ULIRGs and measurements of local starbursts. For the Seyfert I galaxies (2 objects) we do not fit the sodium absorption doublet because of the degeneracy caused by the strong quasar continuum (see Section 3.5.5).

3.2.8 Extended Sample

To study the relation between different outflow phases, we include galaxies studied in the literature with outflows detected in several phases. We refer to these galaxies combined with our galaxies with multiphase outflows as the *extended sample*. In total, the extended sample consists of 31 galaxies with outflows studied in multiple phases. Our extended sample includes the multiphase outflows studied by Rupke & Veilleux (2013), Rupke et al. (2017), Fluetsch et al. (2019) and Husemann et al. (2019). We also add three targets with redshifts $z > 1$, which all have measurements of outflows in several phases: zC400528 (Herrera-Camus et al. 2019), XID2028 (Cresci et al. 2015b; Brusa et al. 2018) and 3C 298 (Vayner et al. 2017).

The outflow measurements in these galaxies are homogenised to allow a fair comparison to our MUSE sample. In particular, to re-calculate the properties of the ionized outflows, we use the same

- formula to calculate mass outflow rate (eq. 4.1), i.e. without the factor of three as used in some other works
- electron density ($n_\mathrm{e} = 500\ \mathrm{cm^{-3}}$, average electron density of outflows, see below)
- definition of outflow velocity if possible ($v_\mathrm{OF} = \Delta v + \mathrm{FWHM}/2$)
- attenuation curve to correct for extinction (Calzetti et al. 2000) with $R_\mathrm{V} = 4.05$

- tracer of outflowing gas, i.e. Hα instead of [OIII] (see Section 3.2.7)
- conversion from Hα luminosity into outflow mass, i.e. equation 3.5.

For the calculation of neutral atomic outflow properties, we adopt the same

- formula to calculate mass outflow rate (eq. 4.1), i.e. without the factor of three as used in some other works
- values for the ionization fraction, galaxy's sodium abundance and the depletion onto dust (see Section 3.2.5).

Finally, to ensure that molecular outflow rates and energetics are calculated consistently across the sample, we assume the same

- formula to calculate mass outflow rate (eq. 4.1), i.e. without the factor of three as used in some other works
- same conversion factor (α_{CO} = 0.8 $M_\odot$ (K km s^{-1} $pc^2)^{-1}$)
- definition of outflow velocity if possible ($v_{OF} = \Delta v$ + FWHM/2).

3.3 Results

3.3.1 Prevalence of Outflows

Out of the 26 galaxies analysed, 12 galaxies show clear signs of an ionized outflow and 11 show evidence of neutral atomic outflowing gas, 8 galaxies have outflows in both phases. The number of neutral outflows may be larger than this number as any sodium absorption in Seyfert I galaxies (see Section 3.2.7) might be overshadowed by broad He I lines. However, we found in other objects a more extended Na ID outflow could partially absorb the He I emission line (see e.g. Fig. 3.16).

In our study, we find that most galaxies with outflows have outflow signatures in both phases, but there are a few exceptions. For instance, IRAS 23128-5919 has a clear ionized outflow, but no detectable neutral atomic gas at high velocity. However, one should be aware, that the discrepancy might be due to sensitivity in the different phases rather than due to the physical properties of the outflow. For each galaxy we present maps of the ionized and neutral atomic phases and the integrated spectra in Section 3.5.5.

3.3.2 Characterisation of Outflows

3.3.2.1 Electron Density

In this section, we compare the electron density of the outflowing gas and the disc. This not only informs our understanding of the physical conditions of the ionized ISM, but it is also important to calculate the mass and kinetic energy of the ionized outflow (which are both

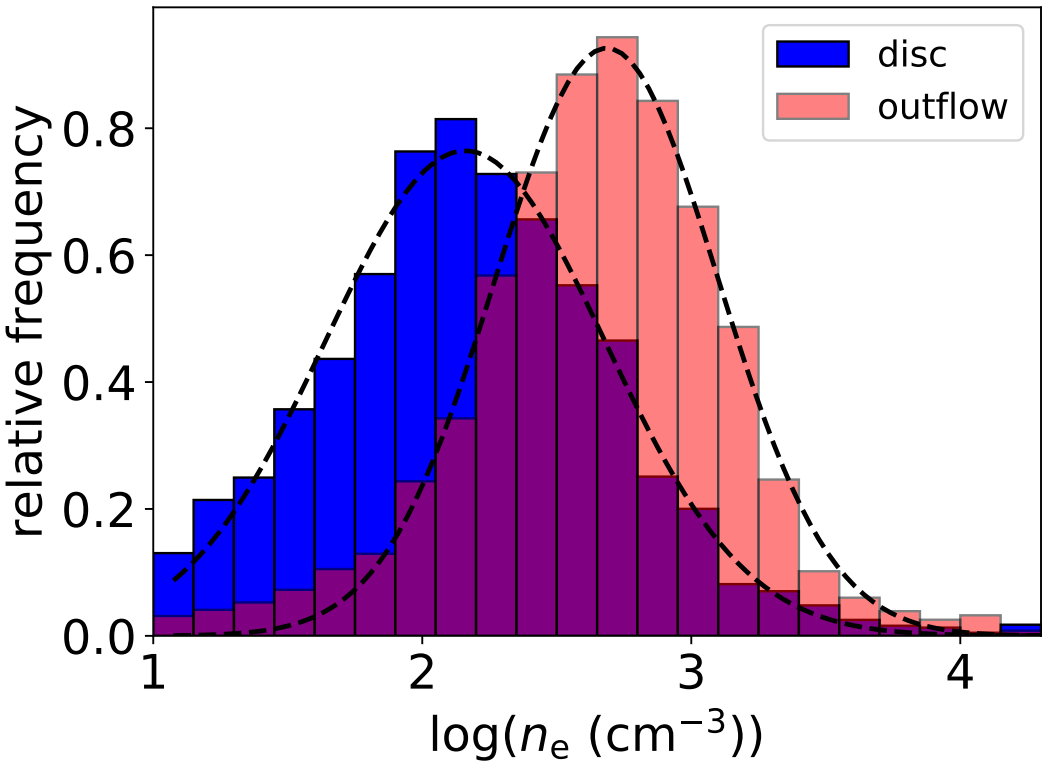

Figure 3.2: In blue and red, the distribution of the electron densities (n_e) of the narrow (disc) and broad (outflow) components of all galaxies with ionized outflows are shown, respectively. The dashed lines are the Gaussian fit to the distributions.

inversely proportional to the electron density, n_e, see Section 3.2.7). Indeed, the electron density has been one of the main uncertainties in these calculations (Harrison et al. 2018).

We estimate the electron density based on the [SII]λ6717/[SII]λ6731 ratio, assuming a temperature of $T_e = 10^4$ K (Osterbrock & Ferland 2006). The density is calculated for each spaxel in a galaxy using the prescription in Sanders et al. (2015):

$$n_e = \frac{cR - ab}{a - R}, \tag{3.8}$$

where R = [SII]λ6717/[SII]λ6731 and $a = 0.4315$, $b = 2107$, $c = 627.1$. The [SII] ratio is sensitive to density in the range $50 < n_e < 5000$ cm^{-3} (Osterbrock & Ferland 2006). Below and above these limits, the [SII] ratio varies little and is not suitable to accurately determine densities.

We would like to stress that electron densities determined using this method are about 1–2 orders of magnitude lower than electron densities derived from trans-auroral [OII] and [SII] lines, which both have higher critical densities and trace a different gas phase (for details see

Harrison et al. 2018). A recent study by Davies et al. (2020) also found that electron density derived from [SII] are significantly lower than those estimated from auroral or trans-auroral lines.[a] Even if it turned out that the [SII] densities underestimate the true electron densities, it would not change our comparison between disc and outflow as we compare *relative* densities. It would, however, lower the ionized outflow rates (and indeed this is the same point made by Davies et al. (2020), see Section 3.3.3)

In Fig. 3.2 we show the electron density distribution of all spaxels of the narrow and broad components which trace dynamically quiescent gas in the disc and gas in the outflow, respectively. The blue and red distributions show the electron density values for the narrow and broad components, respectively. For each [SII] component we require a SNR of at least 2 for both sulphur lines. To account for the fact that for nearby galaxies we have more spaxels and therefore the distribution might be biased towards them, we weigh spaxels of each galaxy differently. We do that in such a manner that each galaxy contributes equally to the final histogram regardless of the number of spaxels in the broad and narrow components. This is done by weighing each spaxel by the inverse of the total number of spaxels in the galaxy to which this spaxel belongs. The distributions in Fig. 3.2 are wide because we add up several galaxies with different densities, but there is also a considerable range of densities in each individual galaxy as well as the uncertainty associated to individual measurements. We fit these distributions with Gaussians (shown as black dashed lines in Fig. 3.2) and obtain the following centroids: $\mu_{\rm broad}$ = 485 cm^{-3} and $\mu_{\rm narrow}$ = 144 cm^{-3}, and dispersions $\sigma_{\rm broad}$ = 0.41 dex and $\sigma_{\rm narrow}$ = 0.52 dex. The density of the outflowing gas is on average a factor of three higher than the density of the disc. This trend remains even if we do not weigh spaxels differently as described above. The trend is also robust if we consider spaxels where both components are present (i.e. we include only parts of the disc where we also have an outflowing component). The density of the broad component also does not change if we apply more stringent criteria for the identification of the outflowing gas, such as we require a minimum blueshift of –100 km s^{-1} and a width of $\sigma_{\rm broad}$ >150 km s^{-1} for the broad component to ensure we only trace outflowing gas with the broad component. The finding is equally clear both in galaxies with higher AGN fraction ($\alpha_{\rm bol}$>0.5) and with lower AGN fraction ($\alpha_{\rm bol}$<0.5). The galaxies with stronger AGN show slightly higher densities (~ 0.1–0.2 dex higher) for both the narrow and the broad components. In Section 3.11, we show that AGN host galaxies have on average a higher disc electron density than star forming galaxies. In Chapter 4, we will show the electron densities in several individual galaxies.

[a] They also estimate the electron density with a method based on the determination of the ionization parameter, $U = Q_{\rm Lyc}/4\pi r^2 c n_{\rm H}$, and with this method, they find much higher gas densities. However, we deem this method little reliable as it depends quadratically on the distance r, which is uncertain due to projection effects. Moreover, they do not have spatially resolved information to estimate this quantity.

In addition, we observe the trend that outflows are denser than the disc in all individual galaxies apart from IRAS 21453-3511 (discussed below) and IRAS 15115+0208 (although in this galaxy the number of spaxels with sufficient SNR (i.e. > 3) is not high enough to definitely confirm this).

This result qualitatively agrees with several previous studies (Holt et al. 2011; Arribas et al. 2014; Villar-Martín et al. 2014; Perna et al. 2017; Rose et al. 2017; Mingozzi et al. 2019; Davies et al. 2020), who all found outflowing gas to be denser than gas in the disc. The simplest explanation for dense gas in the outflow is that the expelled gas is compressed (e.g. Bourne et al. 2015; Decataldo et al. 2019). Our average values are similar to the ones found by Arribas et al. (2014), who found densities of $n_{\mathrm{e,broad}} = 459 \pm 66$ cm^{-3} and $n_{\mathrm{e,narrow}} = 296 \pm 29$ cm^{-3} also in a sample of (U)LIRGs. Villar-Martín et al. (2014) and Perna et al. (2017) find a higher electron density than this work of $\gtrsim 1000$ cm^{-3} in the outflowing gas, likely because they focus on more extreme objects, considering only AGN hosts or higher redshift targets.

As mentioned above, although this trend seems robust over a range of galaxy properties, there are few rare individual objects, where the density in the disc is similar or higher than in the outflow. For instance, in IRAS 21451-3511, the density of the disc and outflow are very similar. This is shown in Fig. 3.12, where the distribution of the two histograms have centroids $n_{\mathrm{e,broad}} = 10^{2.44}$ cm^{-3} and $n_{\mathrm{e,narrow}} = 10^{2.46}$ cm^{-3}. Another isolated case is NGC 6810, where some parts of the outflow are less dense than the disc (see Venturi et al. 2020 (in prep.)). We cannot yet explain why some galaxies show this trend, but it seems to be unique to sources that are classified as star forming galaxies according to their [SII]-BPT diagrams. We can only speculate that possibly some star formation driven outflows do not lead to enhanced densities in the outflowing gas due to a different mechanism at play.

3.3.2.2 Dust Extinction

We compare the dust extinction, A_{V}, of the narrow and broad components. We estimate the extinction using the Balmer decrement Hα/Hβ and assuming the Calzetti et al. (2000) attenuation law with $R_{\mathrm{V}} = 4.05$. The intrinsic flux ratio of Hα/Hβ is little dependent on density and temperature and any significant deviation in the observed ratio can thus by attributed to interstellar dust extinction. We assume an intrinsic Hα/H$\beta = 2.86$ for $T = 10^4$ K (Osterbrock & Ferland 2006). Furthermore, we require the SNR on Hβ to be >3. As in any external galaxy, the observed Balmer decrement (or colour excess) does not trace a dusty screen but dust in the ISM mixed with the ionized regions emitting Hα and Hβ.

The resulting extinction distributions are shown in Fig. 3.3 with the narrow component shown in blue and the broad component in red. The narrow component has a visual extinction more than twice as large as the broad component. The centres of the Gaussian fit to the

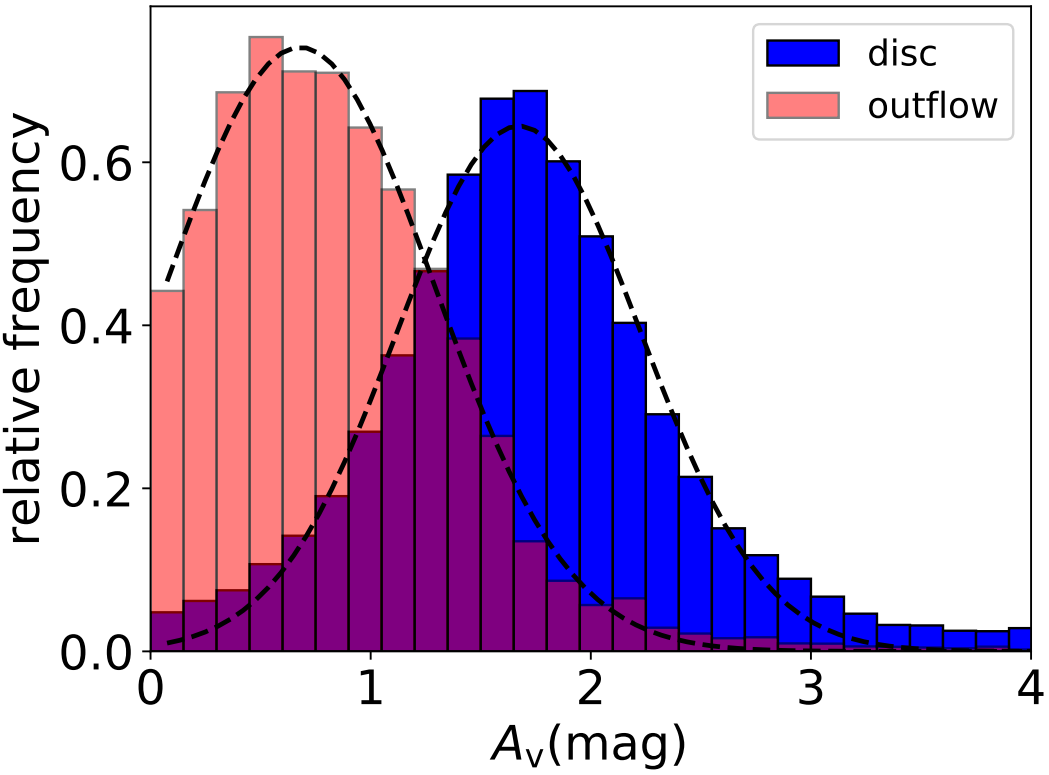

Figure 3.3: Distribution of the values of visual extinction of the narrow (disc, in blue) and broad components (outflow, in red). The centroids of the Gaussian fit to these distributions are A_V = 1.67 mag and A_V = 0.68 mag for the narrow and broad components, respectively.

distributions are $A_{V,broad}$ = 0.68 mag and $A_{V,narrow}$ = 1.67 mag. The median extinction values for different galaxies range from ~1 to ~ 4 mag in the narrow component and from ~0.4 mag to ~2.7 mag in the broad component. The difference in extinction between narrow and broad components, ΔA_V, varies considerably across the sample and this will be discussed in more detail below.

Some works (Rose et al. 2017; Mingozzi et al. 2019) confirm the finding that outflows are less affected by extinction than the disc, others find the opposite result (Holt et al. 2011; Villar-Martín et al. 2014). These results can be explained by a combination of two effects. First, the near side of the outflow is generally less obscured than the disc, while the far side may be extinct by the disc to such a degree that it cannot be detected at optical wavelengths in many galaxies. This seems to be the main explanation for galaxies with lower extinction in the outflow than in the disc. Second, as there are a large number of objects with lower extinction in the disc as e.g. in Villar-Martín et al. (2014), it seems likely that at least some outflows are very dusty, and dustier than the disc. This has indeed been proposed to explain very high

UV luminosities as a consequence of dust scattering in the outflows of the starburst galaxies NGC 253 and M82 (e.g. Hoopes et al. 2005). Radiation pressure-driven models of feedback also predict that dusty gas should preferentially be expelled by powerful outflows (Murray et al. 2005; Ishibashi & Fabian 2016). Unequivocal observational evidence of dust in most or all outflows would also help us greatly to understand molecular outflows. The presence of dust in the outflow is a requisite in many models to explain molecule formation in the outflow (Richings & Faucher-Giguère 2018). To quantify these effects, one would determine the extinction for the approaching and receding outflow part separately. This could be achieved by separate fitting of the red and blue components of the Balmer emission lines (see Venturi et al. 2018). Such an analysis suffers from additional fitting degeneracy and will therefore not be discussed in more detail in this thesis.

In Chapter 2, we discussed radiation pressure-driven winds as one possible outflow mechanism. To explain observations of high momentum ratios (several L/c) as presented in Chapter 2 this mechanism requires high IR optical depths ($\tau_{\rm IR}$). This is because the radiation force is proportional to $\tau_{\rm IR}$ (Ishibashi & Fabian 2012; Costa et al. 2018a). High IR optical depth in turn would likely be due to dust extinction and high $A_{\rm V}$ values (Calzetti 2001). The outflows in our sample in this chapter with low dust extinction are hence probably not driven by radiation pressure, especially if the have high kinetic powers or momentum rates. Another explanation is that some of the measured extinction probes outflows on larger scales (> 1 kpc), whereas the radiation-pressure driven scenario could still work if the outflows are optically thick (and have high extinction values) in their centre (i.e. central hundreds of parsecs) and the optical depth falls off rapidly further away from the centre (Ishibashi & Fabian 2012).

To evaluate the driver of different extinction values in the broad and narrow components, we look at how the galaxy's median $\Delta A_{\rm V}$ = $A_{\rm V,broad}$ - $A_{\rm V,narrow}$ scales with integrated outflow or galaxy properties. For this analysis, we use our own data and combine it with results from Rose et al. (2017) and Husemann et al. (2019). For the objects of Rose et al. (2017), outflow mass rates are provided but the gas masses are not. Therefore, there is a different number of data points in the two plots in Fig. 3.4 and Fig. 3.5. There is no clear correlation between $\Delta A_{\rm V}$ and $\alpha_{\rm bol}$, SFR, the neutral atomic or the molecular outflow mass or mass rate. However, the ionized mass outflow rate ($\dot{M}_{\rm OF}$) correlates with $\Delta A_{\rm V}$ (with a Pearson correlation coefficient of ρ = 0.84) as shown in Fig. 3.4 on the left. This correlation appears to be driven by the mass of the ionized outflow (right-hand side of Fig. 3.4), as this leads to an even tighter correlation with $\Delta A_{\rm V}$ (correlation coefficient ρ = 0.93). Intuitively one might assume that this trend is mainly driven by $A_{\rm V,broad}$, which is proportional to the outflow mass. Higher $A_{\rm V,broad}$ gives a higher intrinsic Hα luminosity for the same observed Hα flux. This Hα luminosity in turn is proportional to the outflow mass (see equation 3.5). In order to test this hypothesis, we plot

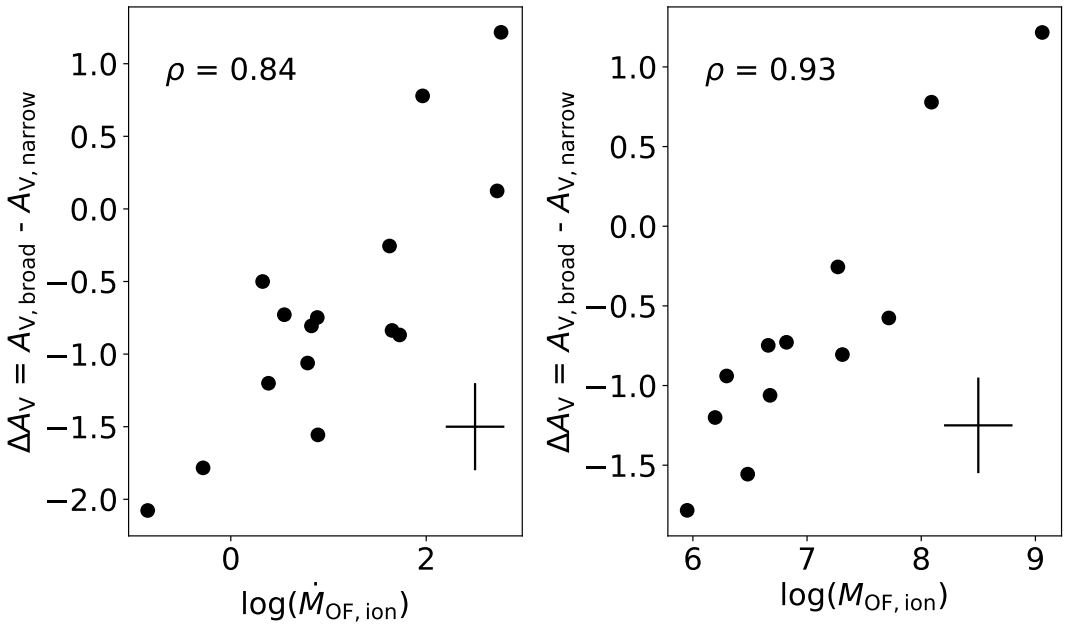

Figure 3.4: Difference in extinction between the narrow and broad components, ΔA_V = $A_{V,broad}$ - $A_{V,narrow}$, as a function of ionized mass outflow rate (left) and ionized outflowing gas mass (right). The typical error is given by the black cross. There are fewer data points in the left figure as for some galaxies the outflowing gas mass was not provided (for details see text).

the extinction of the broad component ($A_{V,broad}$) as a function of the ionized mass outflow rate and ionized outflow mass in Fig. 3.5. The trends in 3.5 are much weaker than in Fig. 3.4, hence indicating that the latter are not purely driven by a potential co-variance between the two axes through Hα_{broad}. Part of this might be explained by errors in measuring both the visual extinction and the outflow mass (rate). To quantify the effect of errors leading to a spuriously higher correlation, we run a Monte Carlo simulation, assuming errors of 0.3 dex on outflow mass (rate) and 0.3 dex on A_V and there is only a 2 % chance that the tighter correlation as seen here with ΔA_V than with $A_{V,broad}$ is due to errors. Hence, it seems unlikely, that errors are solely responsible for the tighter correlation in Fig. 3.4. Instead it seems the ionized outflow mass does drive the *difference* in extinction between broad and narrow components. In other words, the most massive ionized outflows have comparatively more dust in the outflow than in the disc. In these outflows, mainly dusty gas might be expelled, enhancing the extinction in the outflow while simultaneously lowering the extinction in the disc. This could be further indication that dust plays an important role in outflows, especially for the most massive of them.

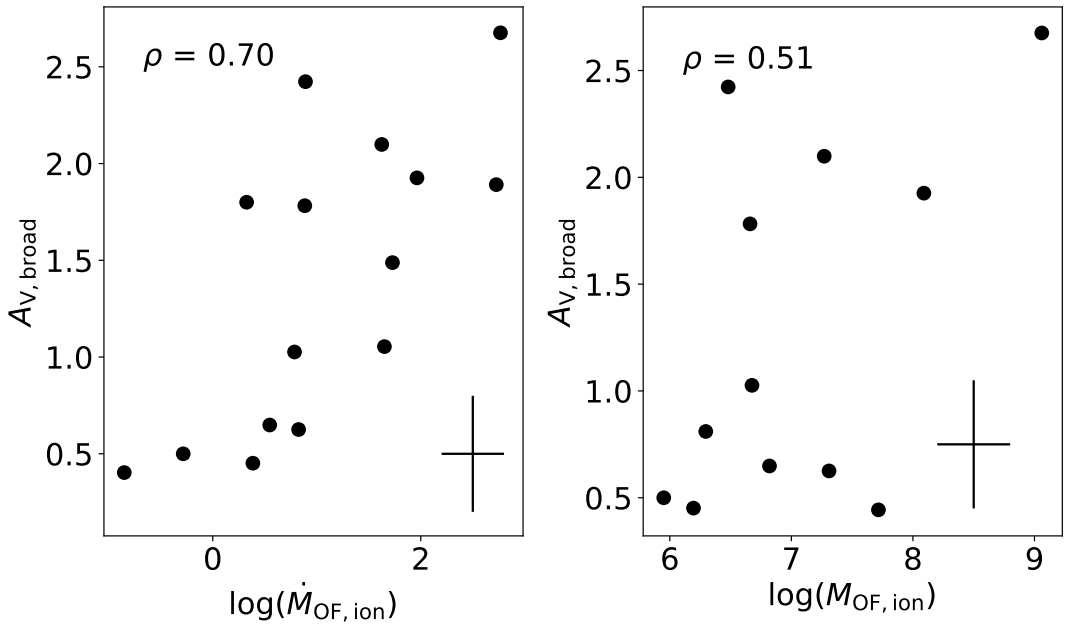

Figure 3.5: Extinction of the broad component, $A_{V,broad}$, as a function of ionized mass outflow rate (left) and ionized gas mass (right). The typical error is given by the black cross. There are fewer data points in the left figure as for some galaxies the outflowing gas mass was not provided (for details see text).

3.3.3 Comparison of Outflow Phases

In this subsection we compare the ionized and neutral atomic outflows to the molecular outflow properties.

For the following analysis, we also add the extended sample described in Section 3.2.8. which includes 31 galaxies with at least two outflow phases and 13 galaxies with all three outflow phases (excluding galaxies which have only an upper limit in at least one phase).

We first test how much each phase (molecular, ionized and neutral atomic) contributes to the total outflow rate for galaxies with measurements of all outflow phases. This is important to allow for a fair comparison to predictions of models and simulations of galaxy evolution, which look at the total impact of the outflow, while most observations focus on one single phase instead and thus might underestimate outflow properties. The outflow masses were homogenised according to the procedure outlined in Section 3.2.8. The relative contributions of different phases to the total outflow rate are shown in Fig. 3.6, where the molecular contribution is shown in blue, the neutral atomic and the ionized in red and green, respectively. The galaxies are sorted by AGN luminosity which increases from left to right. The molecular mass outflow rate amounts to more than half the total mass outflow rate in 11 out of the 13 galaxies. The two galaxies where this is not the case are both classified as star forming galaxies.

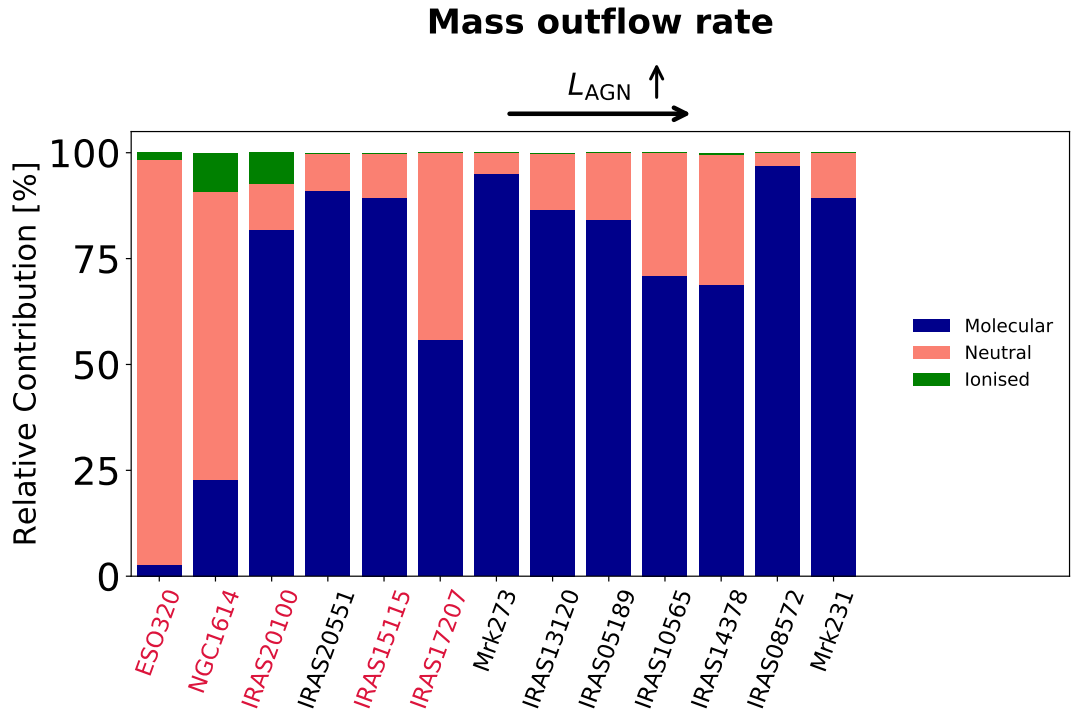

Figure 3.6: Relative contribution of the molecular (blue), ionized (green) and neutral atomic (red) phases to the total mass outflow rate. The galaxies whose names are in red are star forming galaxies. The galaxies are sorted by increasing AGN luminosity from left to right.

Some star forming galaxies, whose names are shown in crimson in Fig. 3.6, display larger mass outflow rate contributions from the ionized and the neutral atomic phase than AGN and LI(N)ER galaxies. The ionized phase is negligible (< 5 % of the total outflow rate) in AGN and LI(N)ER galaxies and is only larger than 20 % in one star forming object (IRAS 20100-4156).

A similar picture emerges if we study the relative contribution of different phases to the total kinetic power. The kinetic power is given by $P_{OF} = \dot{M}_{OF} v_{OF}^2/2$ (see Section 1.4). The associated distribution is shown in Fig. 3.7, where the relative contribution of the molecular (blue), neutral atomic (red) and ionized phases (green) are displayed. Star forming galaxies have significant contributions from the ionized and neutral atomic phases, ranging from ~40 % to >95 % of the total kinetic power. In AGN and LI(N)ER galaxies, the molecular component is more dominant than in star forming galaxies. There is, however, significant variation from galaxy to galaxy. Studying the relative contribution of different phases to the outflow rate and the kinetic power as a function of SFR or α_{bol} revealed no clear trends (see e.g. Section 3.13).

Next we investigate the mass outflow rate of the three different phases, ionized, neutral atomic and molecular for galaxies which have measurements (or upper limits) for at least two phases. This comparison can be seen in Fig. 3.8, where we plot the different mass outflow

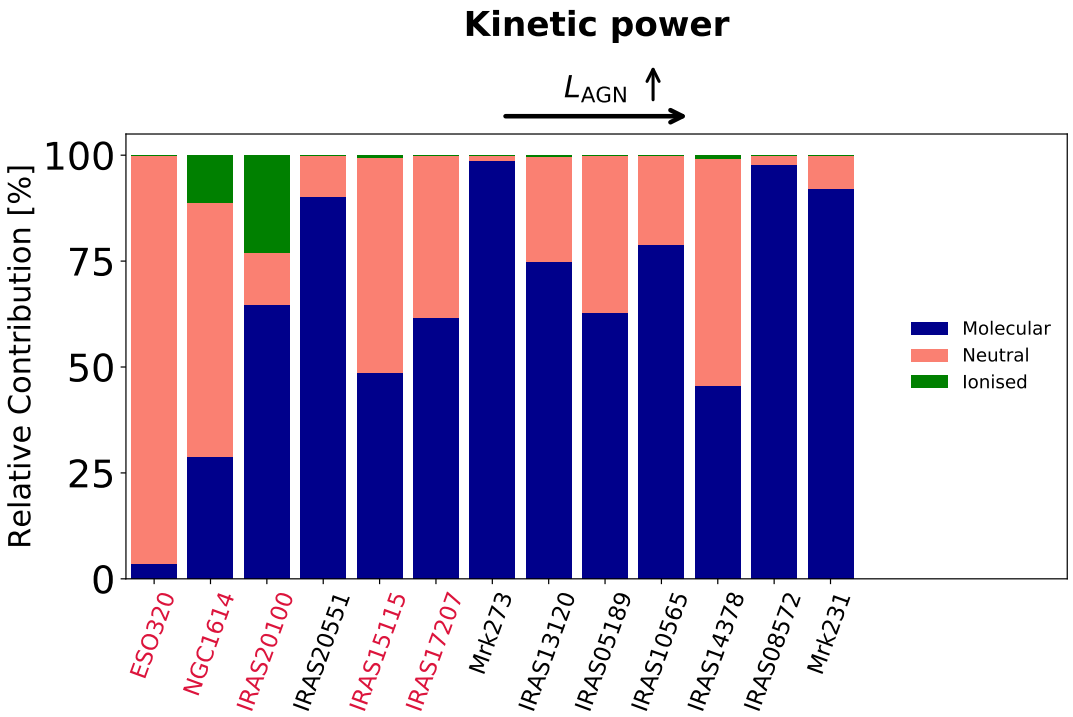

Figure 3.7: Relative contribution of the molecular (blue), ionized (green) and neutral atomic (red) phases to the total kinetic power of the outflow. The galaxies whose names are in red are star forming galaxies.

rates against each other. The samples in the three plots are slightly different. To increase the statistics, in each plot we show the galaxies with measurements in both of the phases plotted. We distinguish between high-redshift sources ($z > 1$, green) and low-redshift sources ($z < 0.2$, black). The data points with a red edge have no reliable extinction correction for the ionized phase and thus should be treated as lower limits. These figures clearly show that the ionized mass outflow rate is much smaller (up to 2–3 orders of magnitude smaller) than the neutral atomic or molecular mass outflow rate. A major caveat is that some ionized outflow rates might be underestimated because of an uncertain extinction correction. But even if these points are ignored, the ionized outflow rates are significantly lower (cf. Fig. 3.6, which only includes galaxies with proper extinction correction). This confirms previous findings which estimate the ionized phase to contribute only minimally (Rupke & Veilleux 2013; Carniani et al. 2015; Ramos Almeida et al. 2019). The figure on the top right highlights that outflow rates in the molecular and neutral atomic phase are similar (usually within 1 dex). This picture might be slightly skewed, however, as we include upper limits in the molecular and ionized, but not in the atomic neutral outflow phase. However, the relative contribution of the ionized outflow rate to the total outflow rate varies from galaxy to galaxy (from $\leq$ 1 % to 10's of %) and a simple

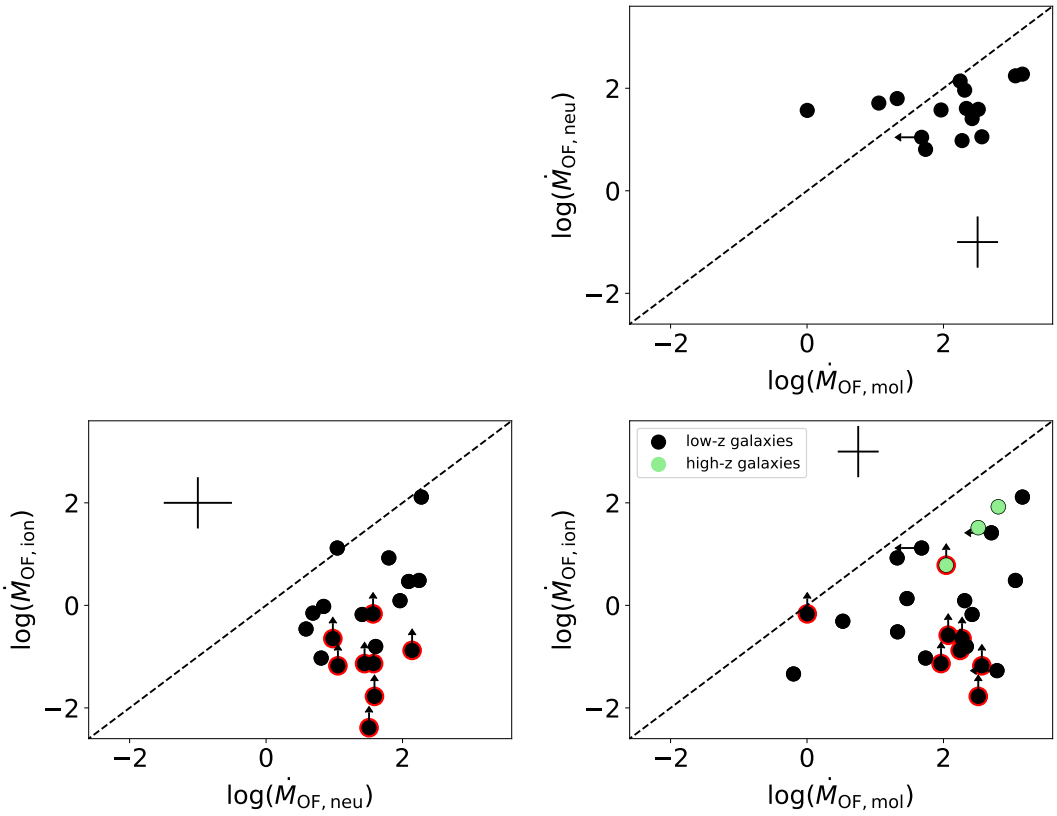

Figure 3.8: Comparison between the outflow rates in the ionized, molecular and neutral gas phases. The black symbols represent the low-redshift ($z < 0.2$) sources while the green symbols are the high-redshift ($z > 1$) targets. The dashed black line in all plots shows the 1:1 correlation. Typical errors are given by the black crosses. The data points with red edges have an uncertain or no extinction correction in the ionized outflow phase and should be treated as lower limits.

prescription as in Fluetsch et al. (2019) might not be fully appropriate to determine the total outflow budget. If electron densities from auroral or trans-auroral lines are a better estimate than the densities based on the [SII] doublet (as suggested by Davies et al. (2020), see Section 3.3.2.1), then the contribution of the ionized phase would drop even further by additional 1–2 orders of magnitude and hence it would become negligible also in star forming galaxies.

Another open question is also how the relative contribution of ionized and molecular gas to the total outflow rate changes with increasing AGN luminosity. Previous studies suggested that the ionized gas contribution to the total mass outflow rate becomes increasingly important with higher AGN luminosity and is similar to the molecular outflow rate above AGN luminosities of 10^{46} erg s^{-1} (Fiore et al. 2017; Bischetti et al. 2019a). However, these studies worked with disjoint samples, with a limited number of sources or by restricting the AGN luminosity range. We study this trend in Fig. 3.9, where we plot the ratio $\dot{M}_{\rm OF,ion}/\dot{M}_{\rm OF,mol}$ as a function of the

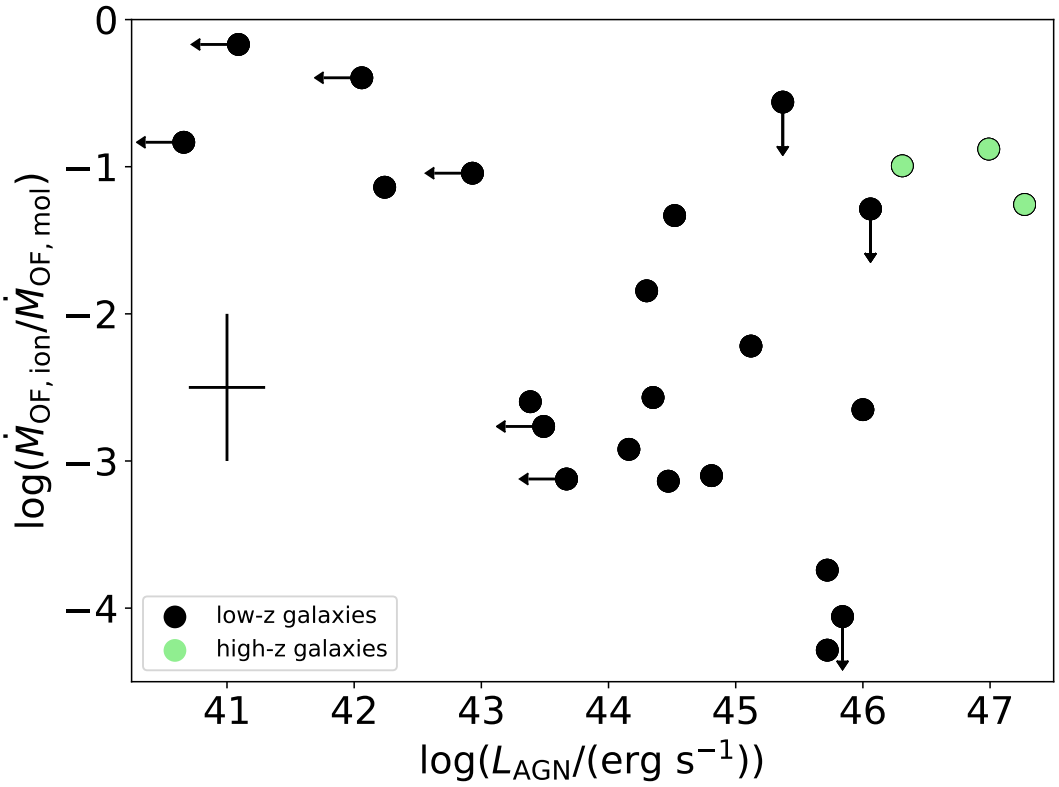

Figure 3.9: Ratio of ionized and molecular mass outflow rate as a function of AGN luminosity. The green data points represent the high-redshift sources and the black data points the low-redshift targets.

AGN luminosity, L_{AGN}. The green data points represent galaxies above redshift 1, whereas low-redshift objects are shown as black data points. Contrary to some previous studies, we do not find that the ionized phase becomes more prominent at higher AGN luminosities. Instead, there is no clear trend. The contribution of the ionized mass outflow rate might actually decrease at higher L_{AGN}. The three high-redshift sources all seem to have large ionized outflow rates, which are almost comparable to their molecular ones. They are also the only objects with $L_{AGN} > 10^{46}$ erg s^{-1} and are consistent with the results by Fiore et al. (2017). However, given the small sample, it is impossible to establish whether higher redshifts targets indeed have a fundamentally different outflow composition or whether objects with higher AGN luminosities have comparatively higher ionized outflow rates. An additional factor possibly contributing to the deviation of high-z galaxies is that they suffer from observational limitations, such as reduced sensitivity to low-surface brightness and high-velocity gas.

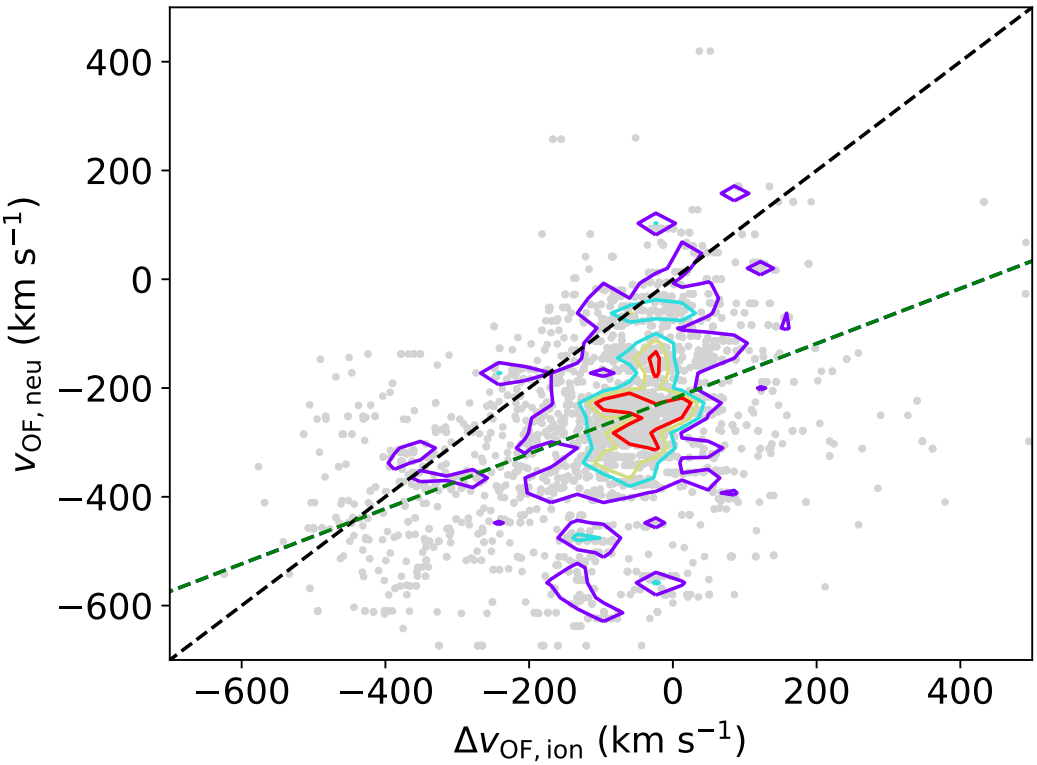

Figure 3.10: Neutral outflow velocity (v_{50}) versus ionized outflow blueshift for all spaxels of all galaxies. The dashed black line indicates the 1:1 correlation, the green dashed line is the best fit to the data points.

3.3.4 Spatial and Velocity Comparison of Outflow Phases

MUSE has the capability to resolve the gas kinematics with excellent spatial resolution and we therefore also attempt to compare the different outflow phases on a spatially resolved basis. The maps of all 14 galaxies (with outflows) are presented in Section 3.5.5. What is striking is that galaxies with outflows in the ionized and in the neutral atomic phase display similar morphology and kinematic structures. For instance, in IRAS 13120-5453, the velocity gradient across the field of view is very similar for the two phases. In addition, the two phases are co-spatial for large parts of the galaxy, displaying similar blueshifts.

In order to quantify this better, in Fig. 3.10 we compare the outflow velocity of the neutral phase with that of the ionized phase for each spaxel, where we find outflows in both phases. The dashed black line indicates the 1:1 relation and the dashed green line is the best fit to the data points. We note that the properties of the neutral atomic phase are inferred from binned data, whereas the ionized lines can be fit in the individual spaxel. In order to account for that, we took the average of all ionized outflow velocities for each bin of neutral outflow velocity. Each

colour represents the data points of one galaxy with outflows in both phases. In general, most data points lie below the black lines, i.e. the neutral outflows seem to have a larger blueshift than in the ionized gas. We remind the reader that the outflow velocity of the neutral phase is measured using v_{50}, the 50th percentile of the whole sodium absorption profile, whereas for the ionized outflow phase, the velocity is the blueshift of the broad component (see Section 3.2.7). It is not possible to use the same definition for the outflow velocity due to the different spectral properties of the two tracers. Thus, we do not expect to see a perfect 1:1 correlation in this plot.

Concerning the extent of the two outflow phases, there is no clear trend. In some galaxies the neutral atomic outflow has a larger radius than the ionized one (e.g. IRAS 14378-3641) while in other galaxies we see the opposite trend (e.g. IRAS 13229-2934). Especially because of the Voronoi binning, which is necessary to characterise the Na ID outflow, the need to have a strong stellar continuum for Na ID detection, different SNRs in both phases and also because of the faintness of outflow features, we are unable to draw unbiased conclusions about the relative sizes of outflows in different phases.

3.4 Summary and Conclusions

This chapter investigates the properties of multiphase outflows in local (U)LIRGs. We used MUSE observations of 26 (U)LIRGs, which include both AGN hosts and starburst-dominated objects, to study the ionized gas phase including estimates of the electron density and visual extinction of the ionized gas. In addition, we investigate the neutral atomic gas phase traced by the Na I doublet. To study the connection between different outflow phases, we supplemented our sample with outflow studies from the literature. This brings our sample of galaxies with outflows detected in at least two phases to 31 objects, out of which 13 galaxies have outflows in all three phases, molecular, neutral atomic and ionized. This makes it the largest resolved study of multiphase outflows to date. Our main findings are:

- Out of the 26 galaxies observed with MUSE/VLT, 12 galaxies show clear signs of ionized outflows, 10 galaxies have neutral atomic outflows and 8 galaxies have outflow in both phases simultaneously.
- Outflowing gas has on average an electron density a factor of three higher than the disc ($< n_{\mathrm{e,disc}} > = 144$ cm^{-3} and $< n_{\mathrm{e,outflow}} > = 485$ cm^{-3}) (see Fig. 3.2). This is also the case individually for nearly all galaxies. This finding could indicate that cloud compression is more important than cloud dissipation in the outflow. However, some star forming galaxies show the reverse trend with enhanced densities in the disc (e.g. IRAS 21453-3511).

- The average visual extinction is twice as high in the narrow component than in the broad component (see Fig. 3.3). This is interpreted as the approaching side of the outflow (the one most easily detected) being less obscured than the disc. The most massive ionized outflows, however, show higher visual extinction in the outflow, possibly because of their high dust content (inside the outflow).
- The difference in extinction between the broad and narrow components increases with higher ionized outflow mass, which could be explained by mainly dusty material being swept up by the outflow.
- The molecular mass outflow rate accounts for the majority of the total outflow rate, amounting from 60 to 95 per cent in 11 out of 13 objects. The atomic phase contributes slightly less than the molecular phase, while the ionized phase is negligible in most objects studied here. Star forming galaxies have less molecular gas in the outflow and the molecular phase is not always the dominant phase in these galaxies.
- In many galaxies, the ionized and neutral atomic phases are co-spatial and show a similar kinematic structure (e.g. correlated velocities), hinting at the possibility that the two phases are linked.
- The relative contribution of the ionized and molecular phase varies little with increasing AGN luminosity, but if anything, the ratio of ionized to molecular mass outflow rate declines slightly with higher AGN luminosity (with a large scatter).

3.5 Appendix

3.5.1 Electron Density

3.5.1.1 Density of AGN and Star Forming Hosts

Fig. 3.11 shows the electron density in the disc for star forming (teal) and AGN host galaxies (light red). The centroids for the two distributions are $n_{\mathrm{e,narrow,SF}} = 85.6$ cm^{-3} and $n_{\mathrm{e,narrow,AGN}} = 207.4$ cm^{-3}.

3.5.2 Density of IRAS 21453-3511

We show the electron density histogram of IRAS 21453-3511 in Fig. 3.12. In this galaxy, the electron density in the disc (in blue) and in the outflow (in red) are very similar.

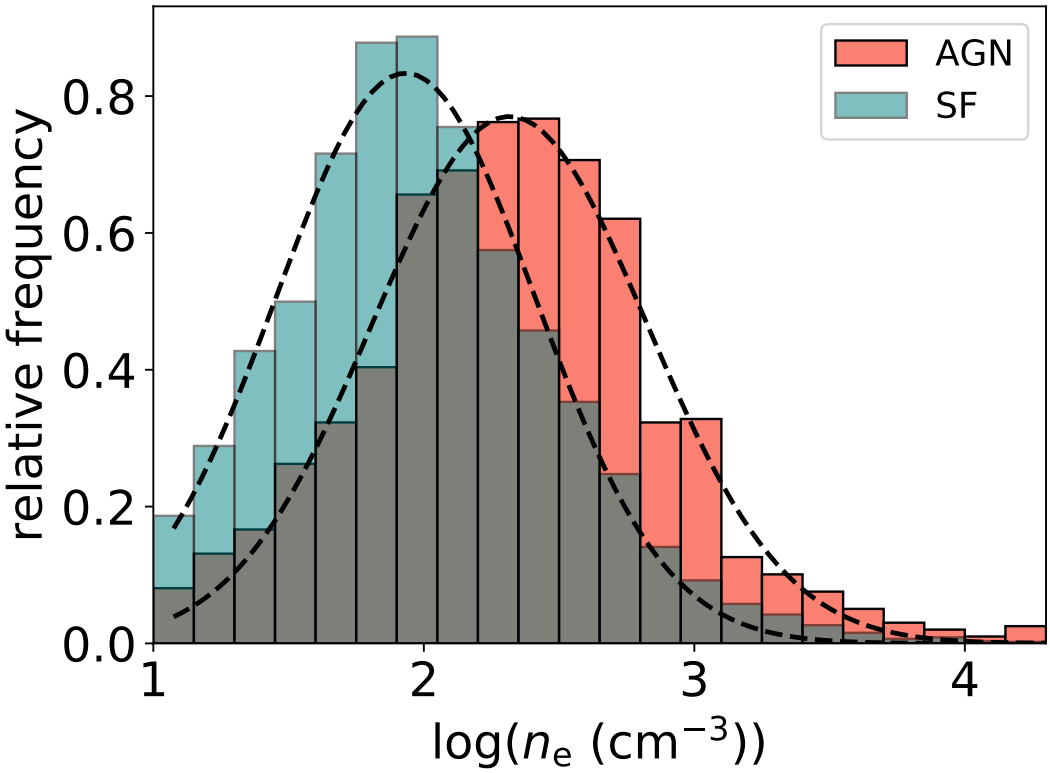

Figure 3.11: In teal and light red, the distribution of the electron densities (n_e) of the narrow component for star forming and AGN host galaxies are shown, respectively. The dashed lines are the Gaussian fit to the distributions.

3.5.3 Relative Importance of Ionized and Molecular Phase as Function of Star Formation

The ratio of ionized to molecular mass outflow rate as a function of the SFR is shown in Fig. 3.13. There is a large scatter, but no clear trend.

3.5.4 Target List

The list of all targets (including the extended sample) is shown in Table 3.2. However, it does not include the ionized outflows from Rose et al. (2017), which were used for Fig. 3.4 as in these galaxies outflows have (so far) only been detected in the ionized phase.

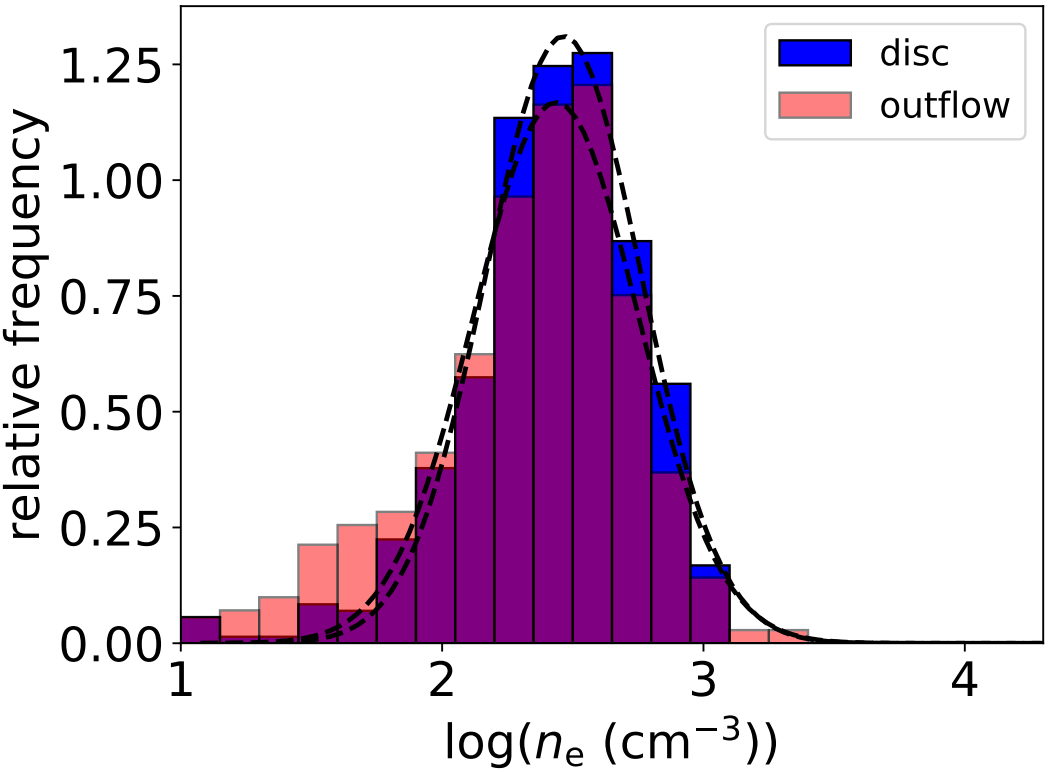

Figure 3.12: In blue and red, the distribution of the electron densities of the narrow and broad components of IRAS 21453-3511 are shown, respectively. The dashed black lines are Gaussian fits to the electron density distributions.

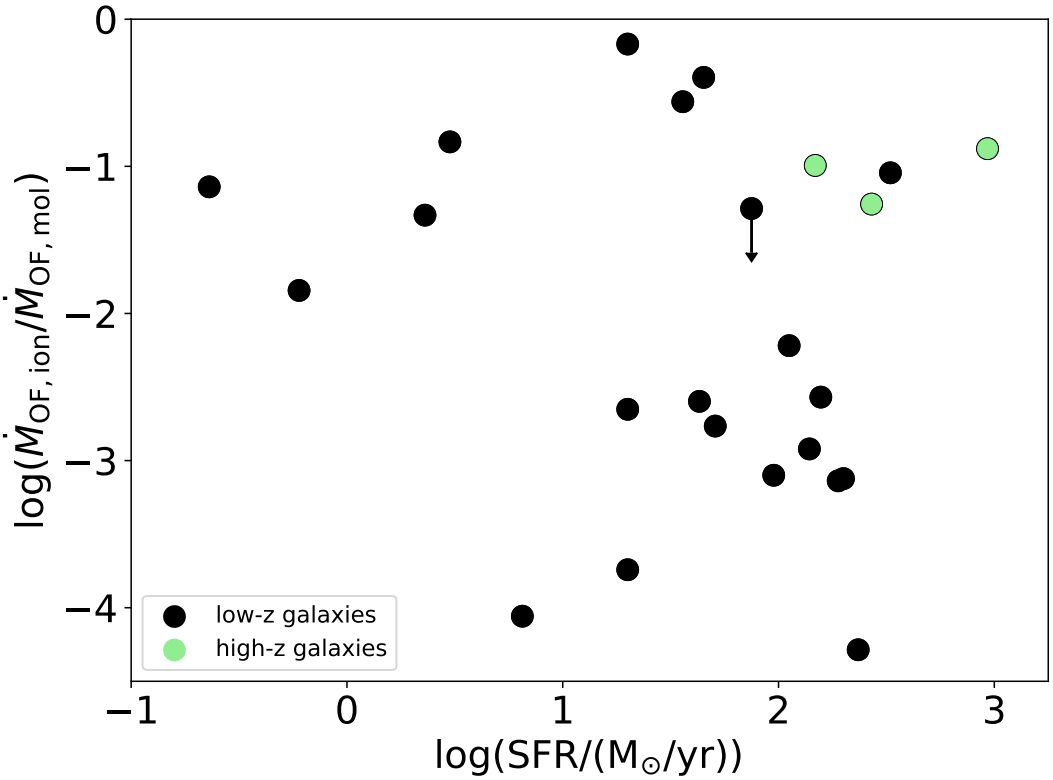

Figure 3.13: Ratio of ionized to molecular mass outflow rate as a function of SFR. The green data points represent high-redshift galaxies and the black data points low-redshift galaxies.

Table 3.1: Galaxy properties of the sample

Galaxy	z	D_L [Mpc]	class	$\log(L_{\rm AGN})$ [erg s^{-1}]	$\alpha_{\rm bol} = L_{\rm AGN}/L_{\rm bol}$	io	no	mo	References
(1)	(2)	(3)	(4)	(5)	(6)	(7)	(8)	(9)	10
MUSE sample									
IRAS 23128-5919	0.0448	198	SF	≤42.93	≤0.0019	✓			(a)
IRAS 14544-4255	0.015728	68	SF	≤41.94	≤0.0017				(b)
IRAS 13229-2934	0.01369	59	AGN	44.65	0.54	✓			(c)
IRAS 17207-0014	0.04281	189	SF	≤43.67	≤ 0.0042		✓	✓	(d)
IRAS 21130-4446	0.092554	424	SF	≤44.54	≤0.057				(e)
Mrk 463	0.050382	190	AGN	44.74	0.19	✓			(f)
IRAS 19542+1110	0.064955	292	SF	≤43.76	≤0.0093	✓	✓		(g)
IRAS 22491-1808	0.0760	344	SF	≤41.83	≤0.00010			✓	(a)
IRAS 23389+1300	0.145	687	AGN	45.63	0.49				(h)
IRAS 00509+1225	0.0608	272	AGN (type I)	45.37	0.59	✓	✓	(✓)	(i)
IRAS 13156+0435N	0.1130	525	SF						
IRAS 13156+0435S	0.1130	525	AGN						
IRAS 20551-4250	0.0430	190	comp.	43.39	0.0047	✓	✓	✓	(d)
IRAS 06259-4708N	0.038790	171	comp.	≤42.10	≤0.00037				(j)
IRAS 10257-4339	0.009354	40	SF	≤41.88	≤0.00038		✓	✓	(k)
IRAS 10409-4556	0.021011	91	SF						

Continued on next page

Table 3.1 – *Continued from previous page*

Galaxy	z	D_L [Mpc]	class	$\log(L_{\rm AGN})$ [erg s^{-1}]	$\alpha_{\rm bol} = L_{\rm AGN}/L_{\rm bol}$	io	no	mo	References
IRAS 12043-3140	0.023203	101	comp.						
IRAS 21453-3511	0.016151	70	AGN	44.25	0.16	✓	✓		(b)
IRAS 01159-4443	0.022903	100	SF						
IRAS 01341-3735	0.01731	75	SF	≤42.11	≤0.0025				(b)
IRAS 18093-5744	0.017345	75	SF	≤41.66	≤0.00038				(b)
IRAS 15115+0208	0.095482	452	SF	≤43.49	≤0.014	✓	✓	✓	(l)
IRAS 23060+0505	0.17301	861	AGN	46.06	0.35	✓		(✓)	(l)
IRAS 14378-3651	0.067637	314	comp.	45.12	0.21	✓	✓	✓	(l)
IRAS 13120-5453	0.030761	139	AGN	44.35	0.028	✓	✓	✓	(l)
IRAS 20100-4156	0.12958	608	SF	≤42.93	≤0.00038	✓	✓	✓	(l)
Extended sample									
zC400528	2.387	19282	AGN	46.31*		✓		✓	(m)
XID 2028	1.5930	11750	AGN	47.21*		✓		✓	(n)
3C 298	1.43812	10357	AGN (type I)	46.99	0.276	✓		✓	(o)
IRAS 08572+3915	0.05835	261	AGN	45.72	0.86	✓	✓	✓	(l)
IRAS 10565+2448	0.0431	191	AGN	44.81	0.170	✓	✓	✓	(l)
Mrk 273	0.03778	167	AGN	44.16	0.080	✓	✓	✓	(l)
Mrk 231	0.04217	186	AGN	45.72	0.340	✓	✓	✓	(l)
IRAS 05189-2524	0.04256	188	AGN (type I)	44.47	0.05	✓	✓	✓	(l)

Continued on next page

Table 3.1 – *Continued from previous page*

Galaxy	z	D_L [Mpc]	class	$\log(L_{\rm AGN})$ [erg s^{-1}]	$\alpha_{\rm bol} = L_{\rm AGN}/L_{\rm bol}$	io	no	mo	References
IRAS 07599+5506	0.1483	704	AGN (type I)			✓	✓		
NGC 253	0.00081	3.47	SF	≤40.66	≤0.0004	✓		✓	(l)
VV 705: NW	0.04019	177	comp.			✓	✓		
IRAS 13218+0552	0.2051	1008	AGN (type I)			✓	✓		
IRAS F13342+3932	0.17931	868	AGN (type I)			✓	✓		
Mrk 876	0.129	605	AGN (type I)	45.84	0.93	✓		(✓)	(l)
HE 1353-1917	0.03502	154	AGN	44.23*		✓		✓	(p)
IC 5063	0.01135	49	AGN	44.30	0.9	✓		✓	(l)
NGC 1614	0.01594	69.1	SF	≤42.07	≤0.0006	✓	✓	✓	(l)
SDSS J1356+1026	0.12297	575	AGN	46	0.43	✓		✓	(l)
ESO 320-G030	0.01078	46.6	SF	≤41.09	≤0.0001	✓	✓	✓	(l)
NGC 1433	0.00359	15.4	AGN	42.24	0.20	✓		✓	(l)

Table 3.1: Columns: (1): Galaxy name, (2) redshift, (3) luminosity distance, (4): optical class, star forming (SF), AGN-dominated (AGN) or composite (comp.), (5) AGN luminosity, *: no estimate of total bolometric luminosity (6) AGN contribution, (7)-(9) evidence of outflow in the ionized (io), neutral atomic (no) and molecular (mo) phase, (10) references for AGN luminosity: (a): Franceschini et al. (2003), (b): Alonso-Herrero et al. (2011), (c): Burtscher et al. (2015), (d): Nardini et al. (2010), (e): Farrah et al. (2003), (f): Yamada et al. (2018), (g): Laha et al. (2018), (h): Imanishi & Saito (2014), (i): Veilleux et al. (2009), (j): Iwasawa et al. (2011), (k): Pereira-Santaella et al. (2011), (l): Fluetsch et al. (2019) and references therein, (m): Herrera-Camus et al. (2019), (n): Brusa et al. (2015), (o): Vayner et al. (2017), (p): Husemann et al. (2019)

3.5.5 Kinematic Maps

In Figs 3.14 - 3.27 we show the kinematic maps of all galaxies with outflow signatures in at least one phase. In panel (a) from left to right, the Hα flux, the [OIII] flux, the gas velocity and the gas velocity dispersion is displayed for the narrow (top row) and broad components (bottom row). Since the lines have been tied (see Section 3.2.3), the velocity and velocity dispersion displayed refer to the parameters of all emission lines. In panel (b), we show the integrated spectrum of the sodium absorption (light blue) including the fit (red). In subfigure (c), the gas velocity of the neutral outflow is shown as well as the dispersion of the narrow and broad components. In panel (d) we show the measured integrated spectrum (light blue), our fit (green) and the broad (cyan) and narrow (navy blue) component fit for Hα and Hβ. The spatial region used for the integrated spectrum is defined in Section 3.2.4.

Table 3.2: Outflow properties of the sample

Galaxy	$\dot{M}_{\rm OF,ion}$ [$M_\odot$/yr]	$\dot{M}_{\rm OF,neu}$ [$M_\odot$/yr]	$\dot{M}_{\rm OF,mol}$ [$M_\odot$/yr]	References
MUSE sample				
IRAS 23128-5919	1.62			(a),
IRAS 13229-2934	0.60			(a),
IRAS 17207-0014	0.13	138	176	(a), (1)
IRAS 19542+1110	2.9	123		(a), (α)
IRAS 00509+1225	13.1	11.1	≤47.7	(a), (α), (1)
IRAS 20551-4250	0.66	25.60	263	(a), (α), (1)
IRAS 10257-4339		51.4	11.27	(α), (1)
IRAS 21453-3511	0.95	6.97		(a), (α)
IRAS 15115+0208	0.09	6.42	54.6	(a), (α), (1)
IRAS 23060+0505	26		≤504	(a), (1)
IRAS 14378-3651	1.23	91.9	204	(a), (α), (1)
IRAS 13120-5453	3.1	175	1134	(a), (α), (1)
IRAS 20100-4156	130	189	1435	(a), (α), (1)
Extended sample				
zC400528	32		323	(b), (2)
XID 2028	6.1		110	(c), (3)
3C 298	84		636	(d), (4)
IRAS 08572+3915	0.07	11.3	365	(e), (β), (1)
IRAS 10565+2448	0.07	37.7	92.1	(e), (β), (1)
Mrk 273	0.22	9.5	187	(e), (β), (1)
Mrk 231	0.017	38.8	323	(e), (β, γ). (1)
IRAS 05189-2524	0.16	40.4	216	(f), (γ), (1)
IRAS 07599+5506	0.004	32.3		(f), (γ)
NGC 253	0.49		3.34	(g), (1)
VV 705: NW	0.07	27.8		(e), (β)
IRAS 13218+0552	0.35	3.85		(f), (γ)
IRAS F13342+3932	0.71	4.86		(f), (γ)
Mrk 876	0.05		≤609	(f), (1)
HE 1353-1917	1.36		29.2	(h), (5)
IC 5063	0.30		21.2	(i), (1)
NGC 1614	8.42	62.9	20.9	(j), (δ), (1)
SDSS J1356+1026	0.26		117	(k), (1)
ESO 320-G030	0.68	37.0	1.0	(j), (δ), (1)
NGC 1433	0.05		0.63	(a), (1)

Columns: (1): Galaxy name, (2): ionized mass outflow rate, (3): molecular mass outflow rate, (4): neutral outflow rate, (5) references: ionized outflow: (a): this work, (b): Herrera-Camus et al. (2019), (c): Cresci et al. (2015b), (d): Vayner et al. (2017), (e): Rupke & Veilleux (2013), (f): Rupke et al. (2017), (g): Westmoquette et al. (2011), (h): Husemann et al. (2019), (i): Morganti et al. (2007), (j): Arribas et al. (2014), (k): Greene et al. (2012); neutral outflow: (α): this work, (β): Rupke & Veilleux (2013), (γ): Rupke et al. (2017), (δ): Cazzoli et al. (2016); molecular outflow: (1): Fluetsch et al. (2019) and references therein, (2): Herrera-Camus et al. (2019), (3) Brusa et al. (2018), (4): Vayner et al. (2017), (5): Husemann et al. (2019)

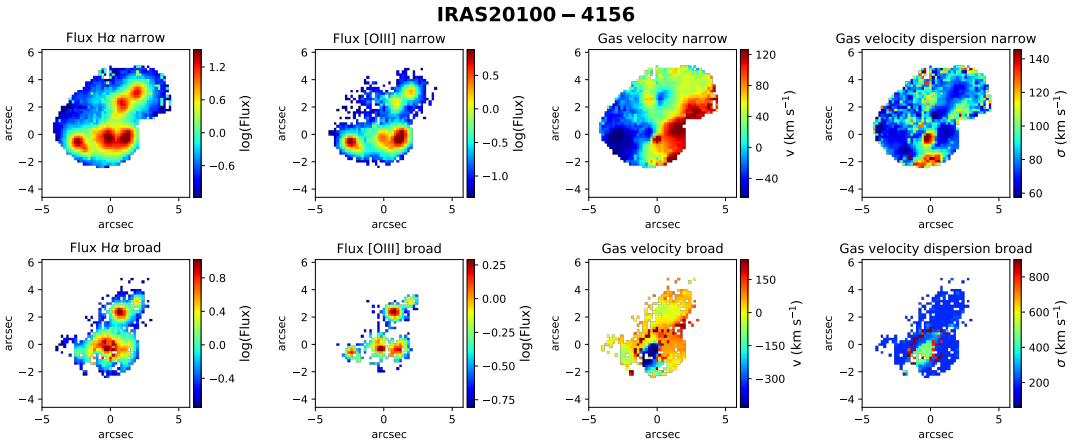

(a) Maps of the ionized gas: The Hα flux, the [OIII] flux, the gas velocity and velocity dispersion are shown for the narrow (top) and broad (bottom) component.

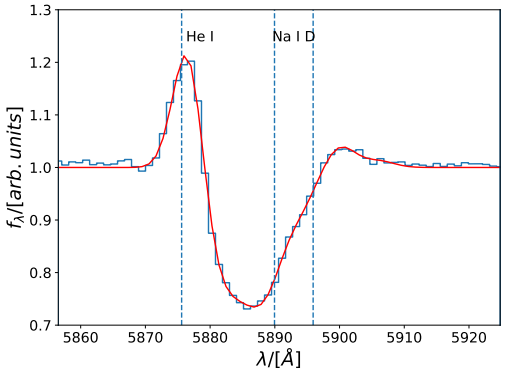

(b) Integrated spectrum of the He I emission and the sodium absorption feature (blue) with fit (red). The dashed lines indicate where we expect the He I emission (5876 Å) and the Na I D absorption lines (5889 Å and 5896 Å).

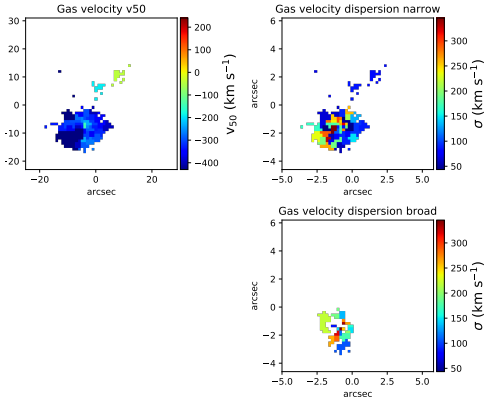

(c) Maps of the neutral atomic gas: Velocity (v_{50}) (right) and gas velocity dispersion (left) of the two components.

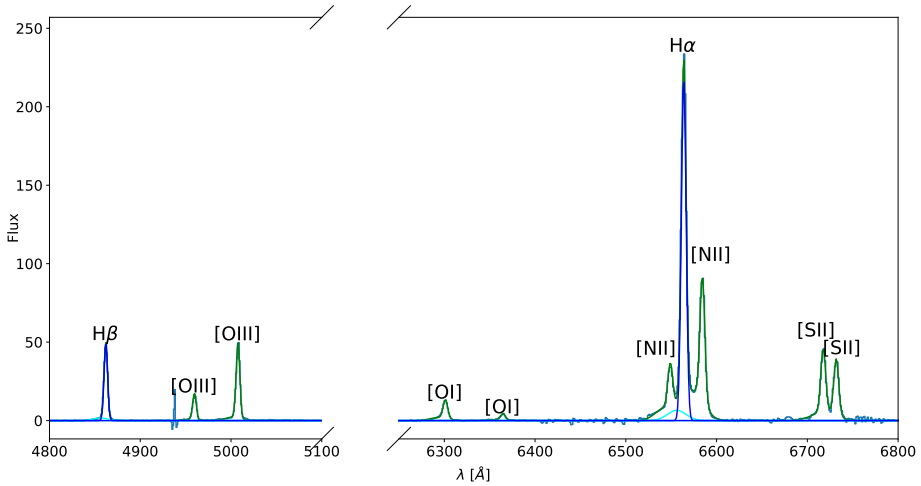

(d) Integrated spectrum: The spectrum is shown in light blue, the two component fit in green, the one component fit in dark blue and for the broad component of Hα and Hβ in cyan.

Figure 3.14: IRAS 20100-4156

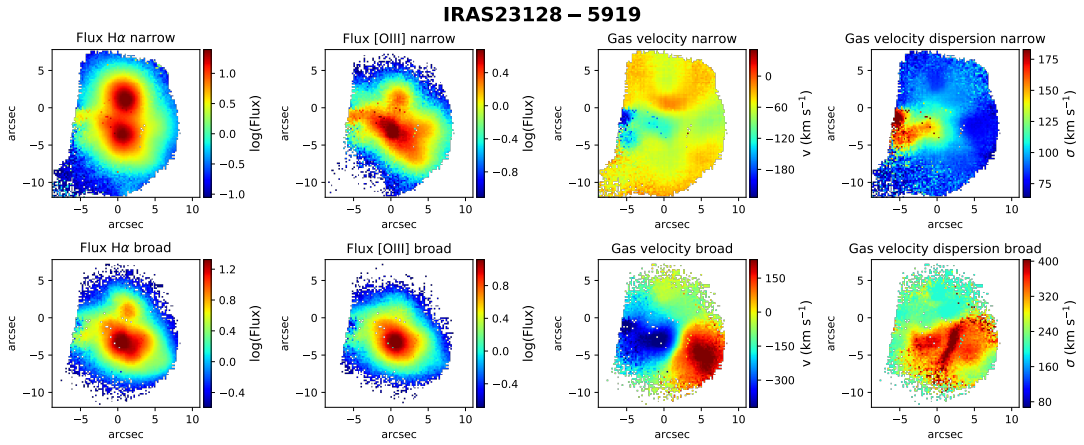

(a) Maps of the ionized gas: The Hα flux, the [OIII] flux, the gas velocity and velocity dispersion are shown for the narrow (top) and broad (bottom) component.

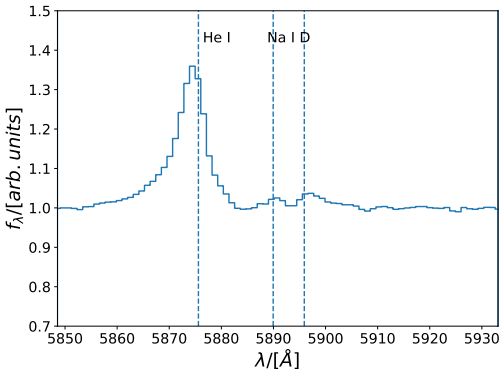

(b) Integrated spectrum of the He I emission and the sodium absorption feature (blue) with fit (red). The dashed lines indicate where we expect the He I emission (5876 Å) and the Na I D absorption lines (5889 Å and 5896 Å).

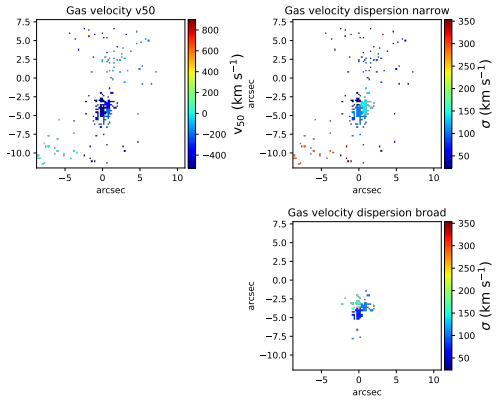

(c) Maps of the neutral atomic gas: Velocity (v_{50}) (right) and gas velocity dispersion (left) of the two components.

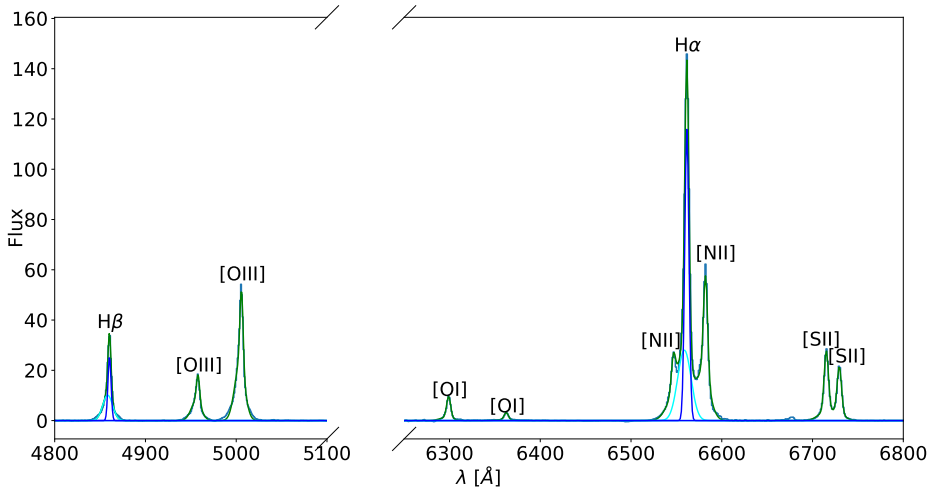

(d) Integrated spectrum: The spectrum is shown in light blue, the two component fit in green, the one component fit in dark blue and for the broad component of Hα and Hβ in cyan.

Figure 3.15: IRAS 23128-5919

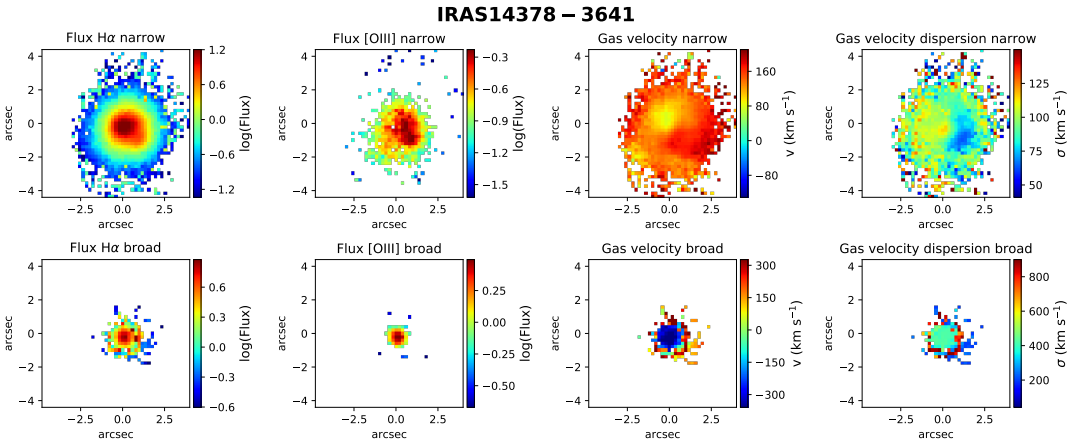

(a) Maps of the ionized gas: The Hα flux, the [OIII] flux, the gas velocity and velocity dispersion are shown for the narrow (top) and broad (bottom) component.

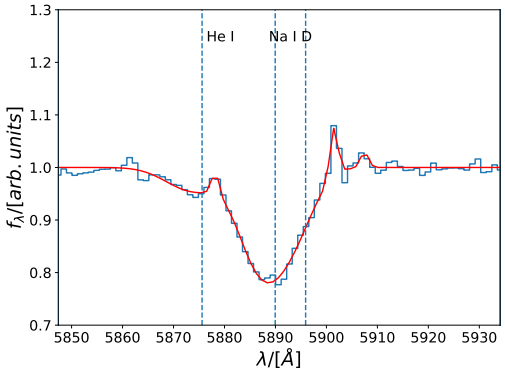

(b) Integrated spectrum of the He I emission and the sodium absorption feature (blue) with fit (red). The dashed lines indicate where we expect the He I emission (5876 Å) and the Na I D absorption lines (5889 Å and 5896 Å).

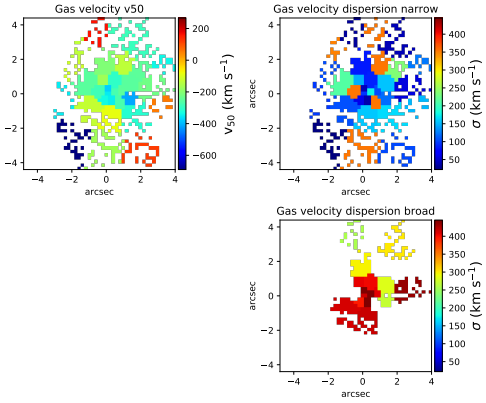

(c) Maps of the neutral atomic gas: Velocity (v_{50}) (right) and gas velocity dispersion (left) of the two components.

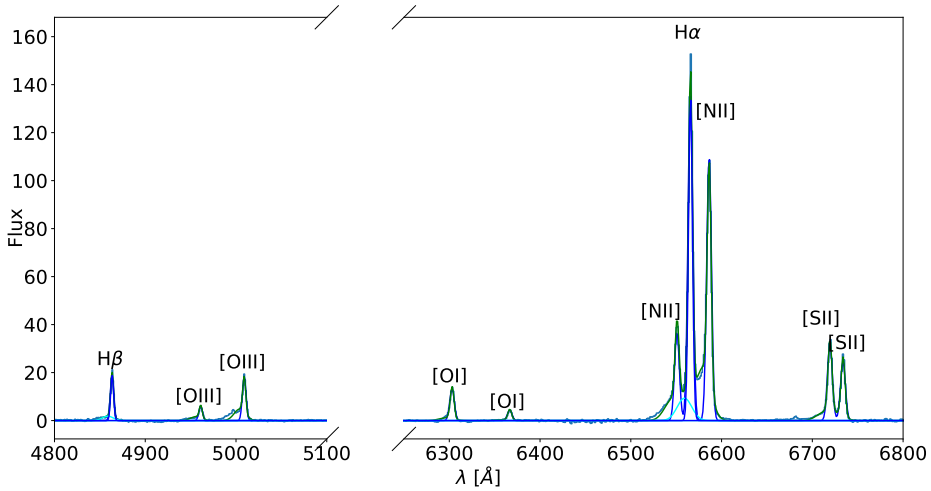

(d) Integrated spectrum: The spectrum is shown in light blue, the two component fit in green, the one component fit in dark blue and for the broad component of Hα and Hβ in cyan.

Figure 3.16: IRAS 14378-3651

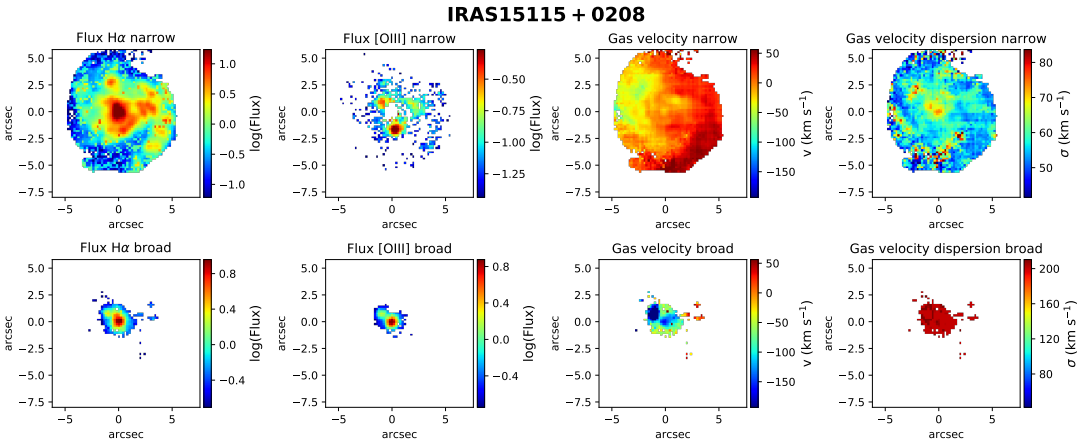

(a) Maps of the ionized gas: The Hα flux, the [OIII] flux, the gas velocity and velocity dispersion are shown for the narrow (top) and broad (bottom) component.

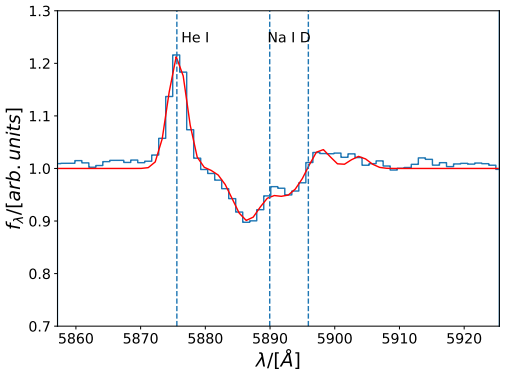

(b) Integrated spectrum of the He I emission and the sodium absorption feature (blue) with fit (red). The dashed lines indicate where we expect the He I emission (5876 Å) and the Na I D absorption lines (5889 Å and 5896 Å).

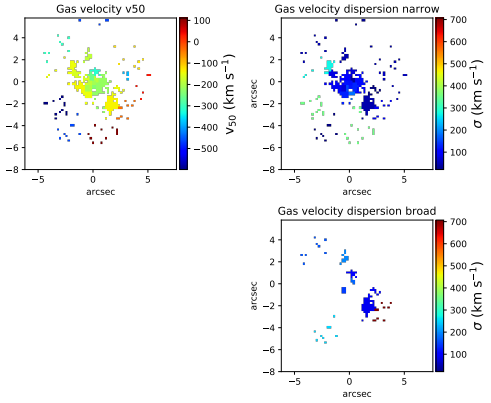

(c) Maps of the neutral atomic gas: Velocity (v_{50}) (right) and gas velocity dispersion (left) of the two components.

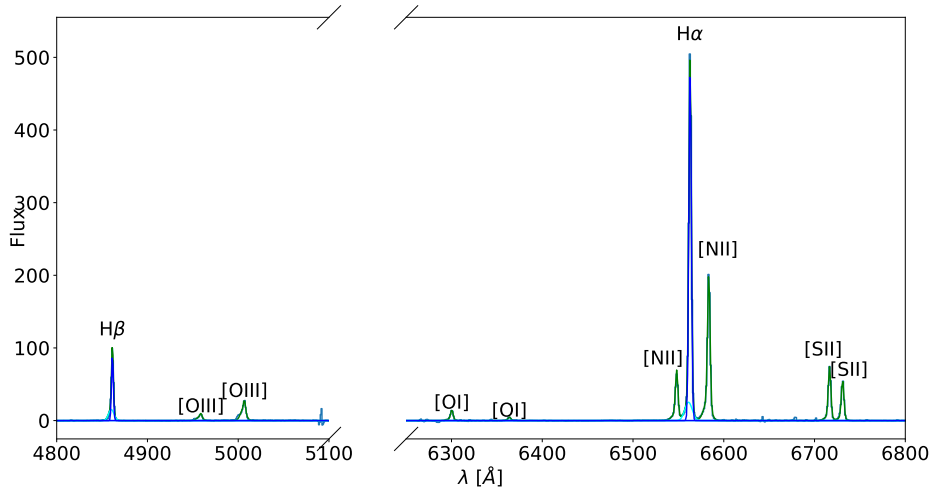

(d) Integrated spectrum: The spectrum is shown in light blue, the two component fit in green, the one component fit in dark blue and for the broad component of Hα and Hβ in cyan.

Figure 3.17: IRAS 15115+0208

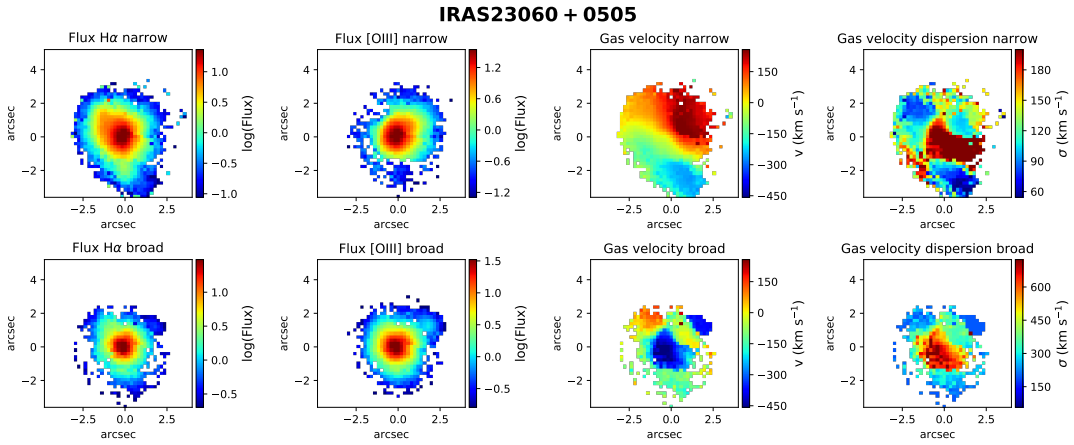

(a) Maps of the ionized gas: The Hα flux, the [OIII] flux, the gas velocity and velocity dispersion are shown for the narrow (top) and broad (bottom) component.

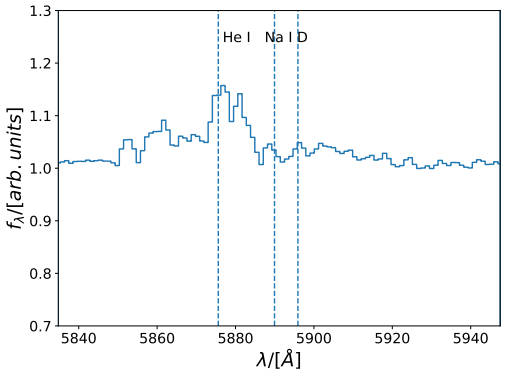

(b) Integrated spectrum of the He I emission and the sodium absorption feature (blue) with fit (red). The dashed lines indicate where we expect the He I emission (5876 Å) and the Na I D absorption lines (5889 Å and 5896 Å).

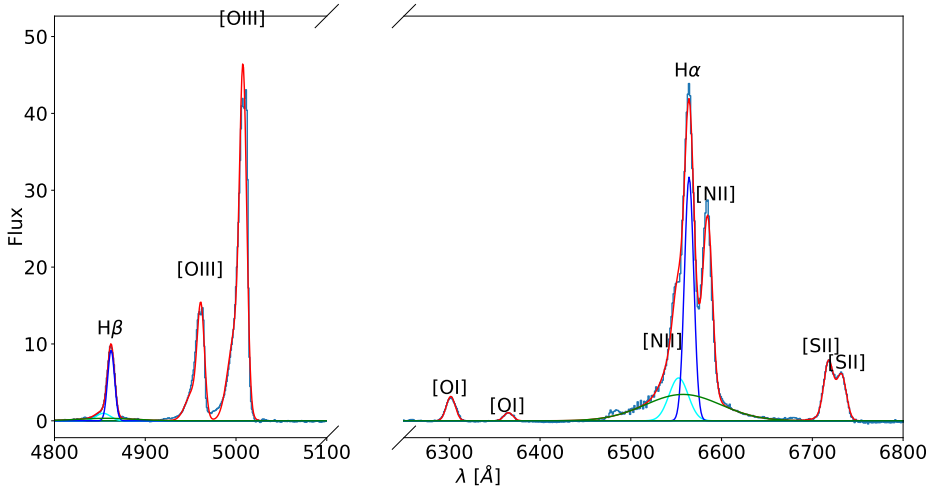

(c) Integrated spectrum: The spectrum is shown in light blue, the two component fit in green, the one component fit in dark blue and for the broad component of Hα and Hβ in cyan.

Figure 3.18: IRAS 23060+0505

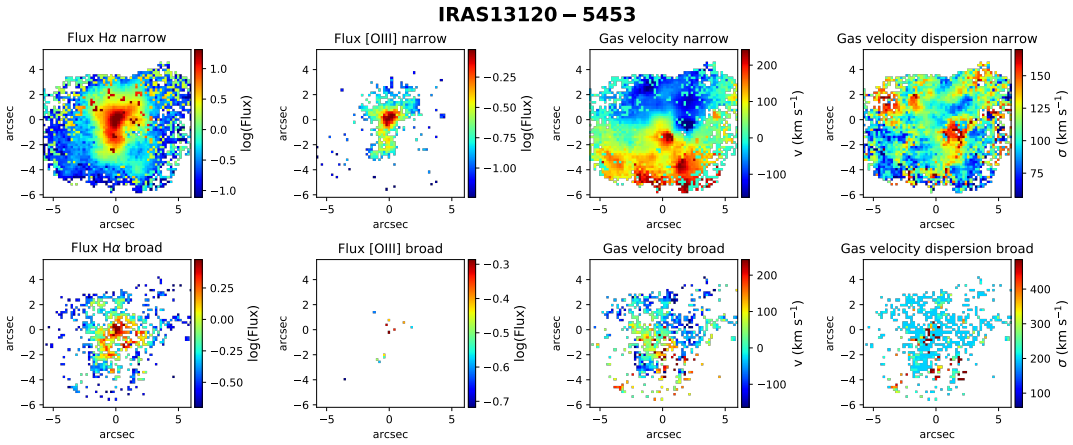

(a) Maps of the ionized gas: The Hα flux, the [OIII] flux, the gas velocity and velocity dispersion are shown for the narrow (top) and broad (bottom) component.

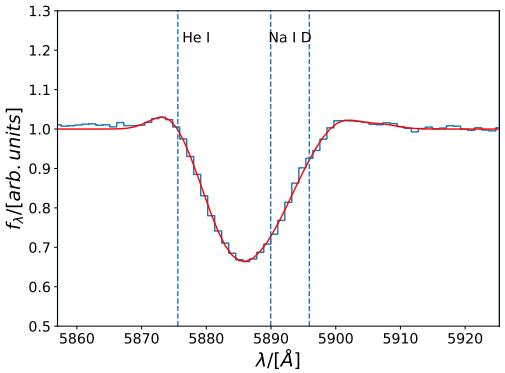

(b) Integrated spectrum of the He I emission and the sodium absorption feature (blue) with fit (red). The dashed lines indicate where we expect the He I emission (5876 Å) and the Na I D absorption lines (5889 Å and 5896 Å).

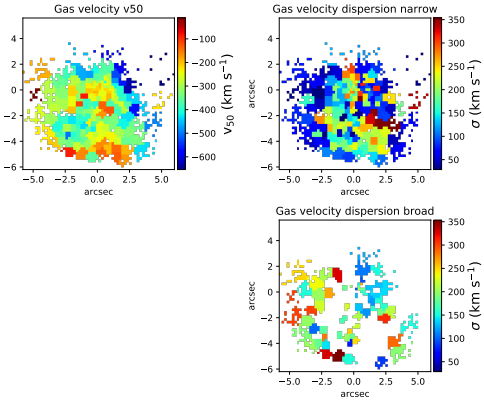

(c) Maps of the neutral atomic gas: Velocity (v_{50}) (right) and gas velocity dispersion (left) of the two components.

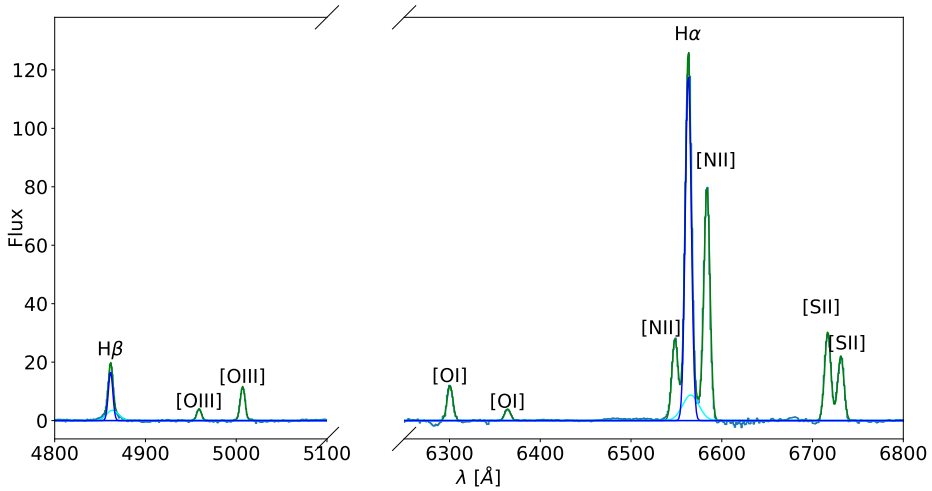

(d) Integrated spectrum: The spectrum is shown in light blue, the two component fit in green, the one component fit in dark blue and for the broad component of Hα and Hβ in cyan.

Figure 3.19: IRAS 17207-0014

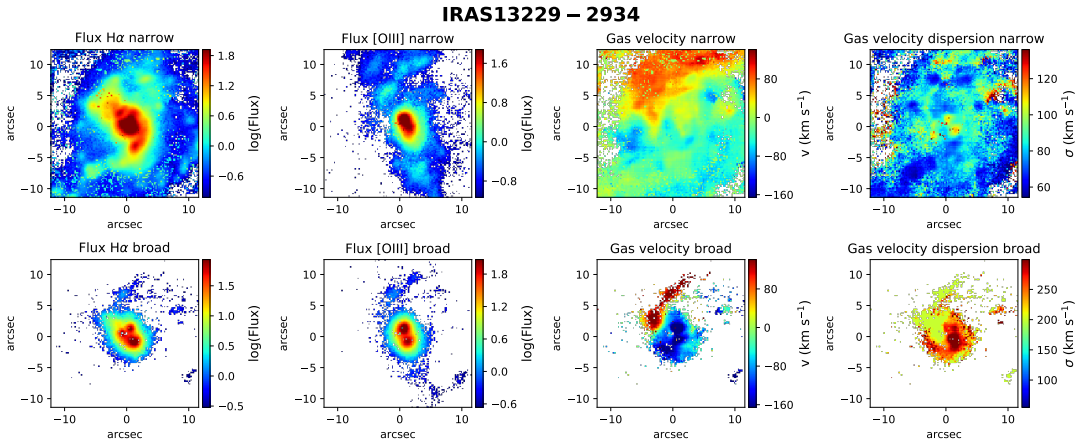

(a) Maps of the ionized gas: The Hα flux, the [OIII] flux, the gas velocity and velocity dispersion are shown for the narrow (top) and broad (bottom) component.

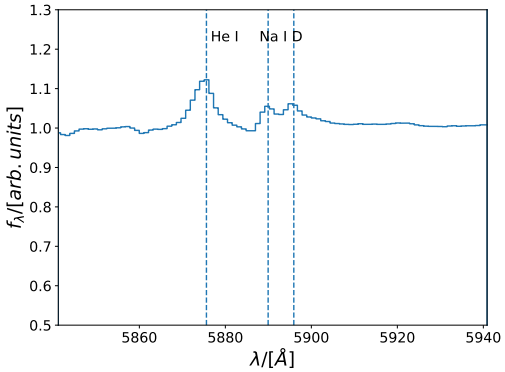

(b) Integrated spectrum of the He I emission and the sodium absorption feature (blue) with fit (red). The dashed lines indicate where we expect the He I emission (5876 Å) and the Na I D absorption lines (5889 Å and 5896 Å).

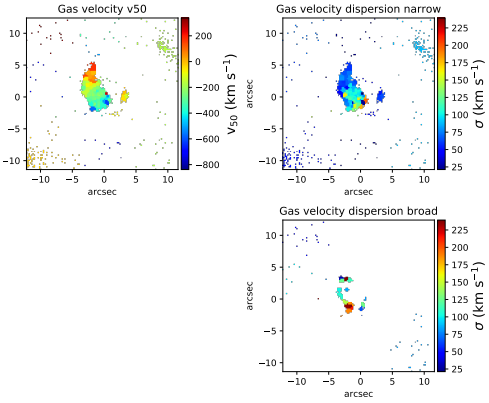

(c) Maps of the neutral atomic gas: Velocity (v_{50}) (right) and gas velocity dispersion (left) of the two components.

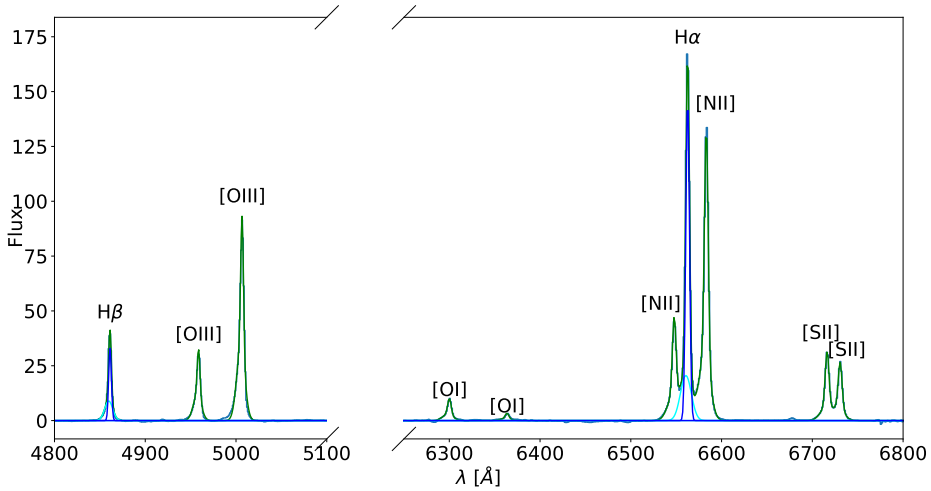

(d) Integrated spectrum: The spectrum is shown in light blue, the two component fit in green, the one component fit in dark blue and for the broad component of Hα and Hβ in cyan.

Figure 3.20: IRAS 13229-2934

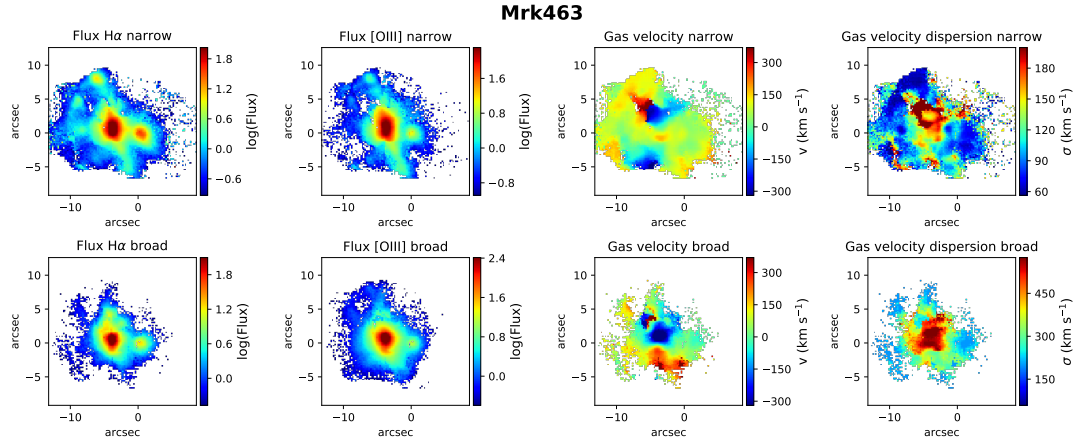

(a) Maps of the ionized gas: The Hα flux, the [OIII] flux, the gas velocity and velocity dispersion are shown for the narrow (top) and broad (bottom) component.

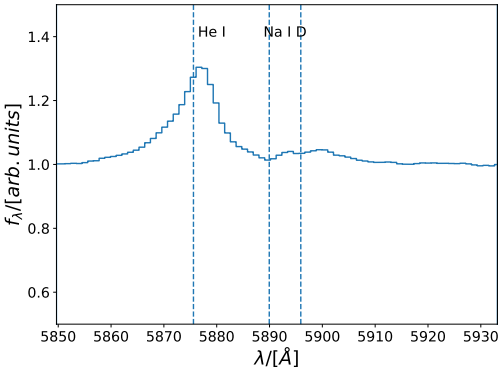

(b) Integrated spectrum of the He I emission and the sodium absorption feature (blue) with fit (red). The dashed lines indicate where we expect the He I emission (5876 Å) and the Na I D absorption lines (5889 Å and 5896 Å).

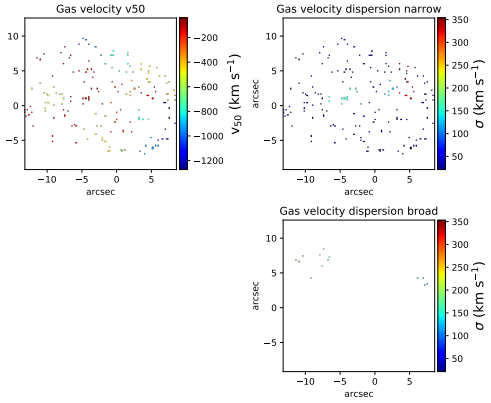

(c) Maps of the neutral atomic gas: Velocity (v_{50}) (right) and gas velocity dispersion (left) of the two components.

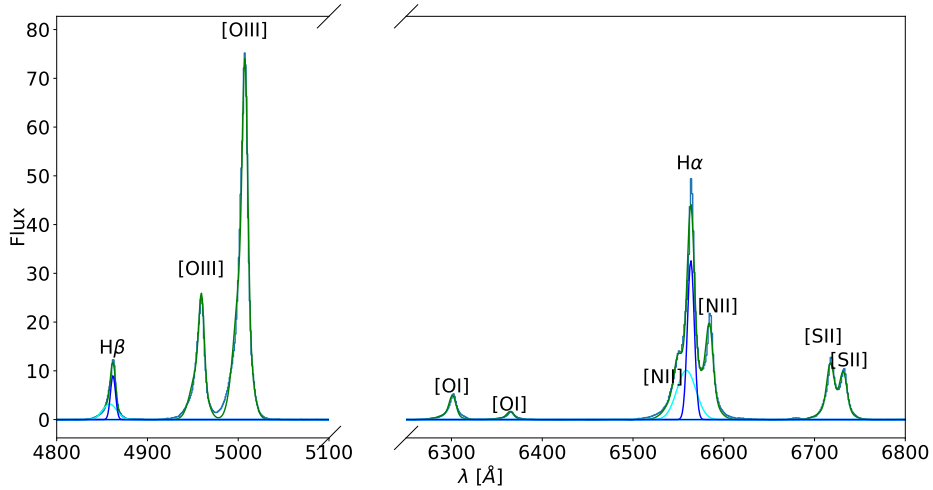

(d) Integrated spectrum: The spectrum is shown in light blue, the two component fit in green, the one component fit in dark blue and for the broad component of Hα and Hβ in cyan.

Figure 3.21: Mrk 463

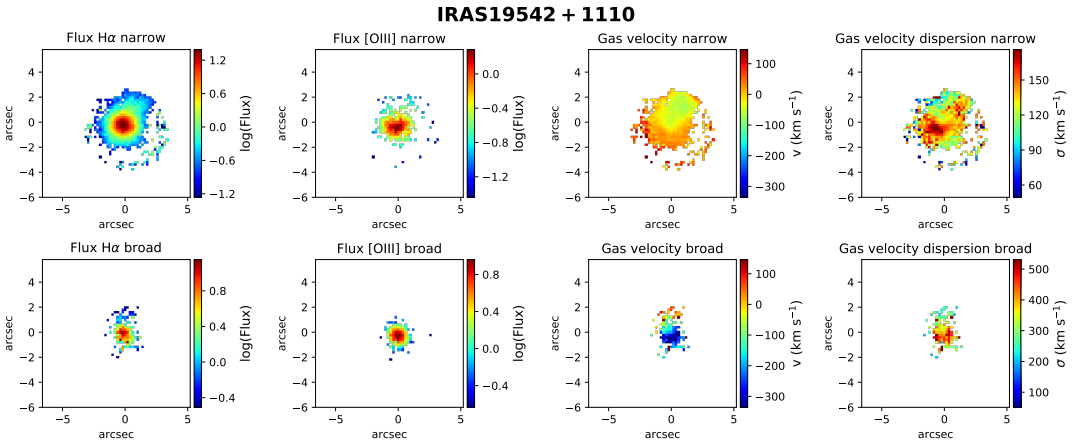

(a) Maps of the ionized gas: The Hα flux, the [OIII] flux, the gas velocity and velocity dispersion are shown for the narrow (top) and broad (bottom) component.

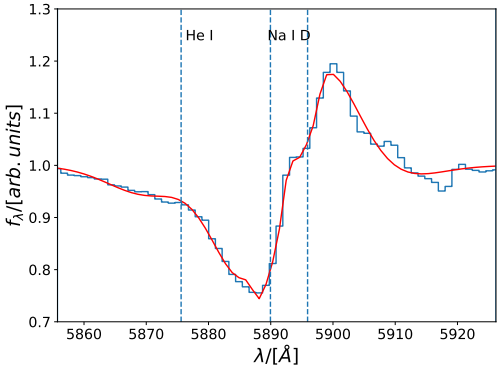

(b) Integrated spectrum of the He I emission and the sodium absorption feature (blue) with fit (red). The dashed lines indicate where we expect the He I emission (5876 Å) and the Na I D absorption lines (5889 Å and 5896 Å).

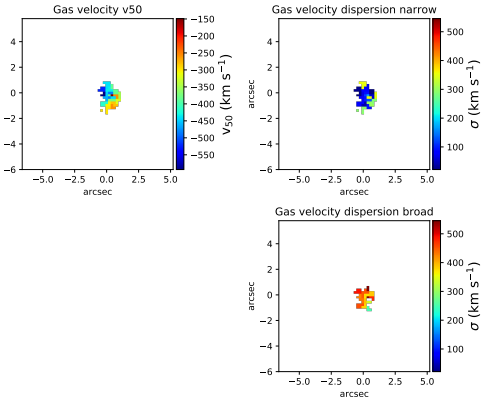

(c) Maps of the neutral atomic gas: Velocity (v_{50}) (right) and gas velocity dispersion (left) of the two components.

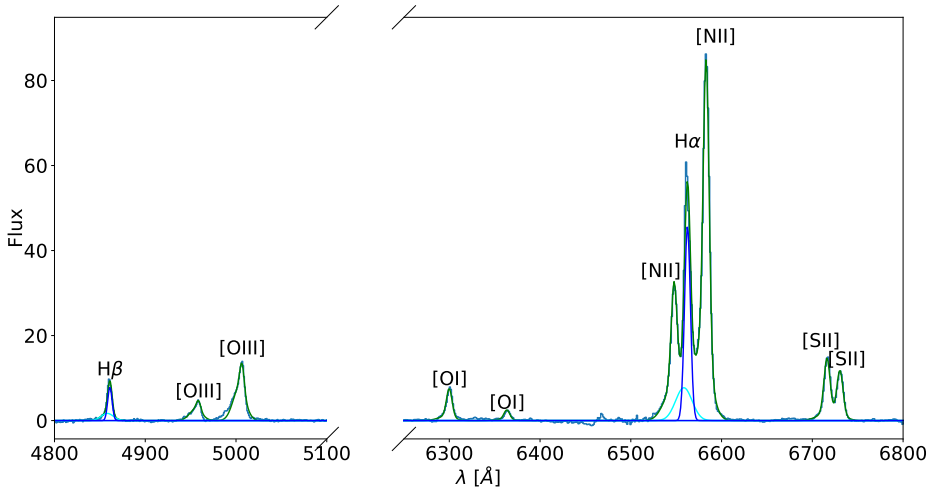

(d) Integrated spectrum: The spectrum is shown in light blue, the two component fit in green, the one component fit in dark blue and for the broad component of Hα and Hβ in cyan.

Figure 3.22: IRAS 19542+1110

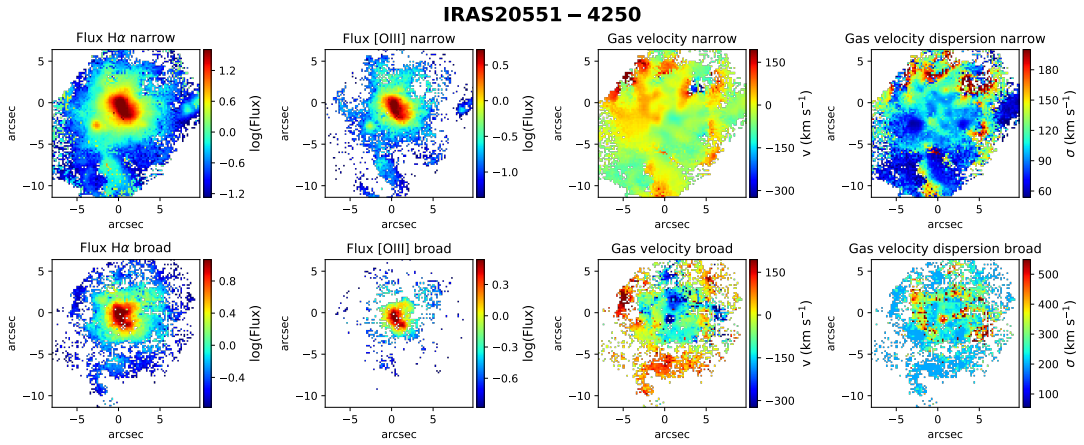

(a) Maps of the ionized gas: The Hα flux, the [OIII] flux, the gas velocity and velocity dispersion are shown for the narrow (top) and broad (bottom) component.

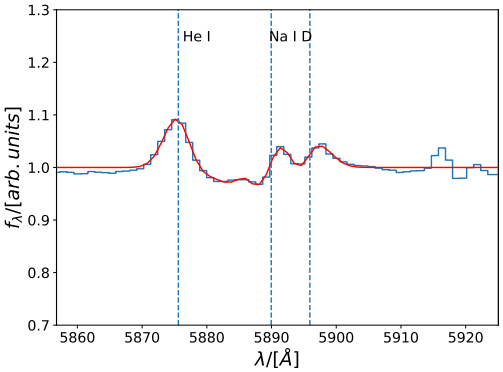

(b) Integrated spectrum of the He I emission and the sodium absorption feature (blue) with fit (red). The dashed lines indicate where we expect the He I emission (5876 Å) and the Na I D absorption lines (5889 Å and 5896 Å).

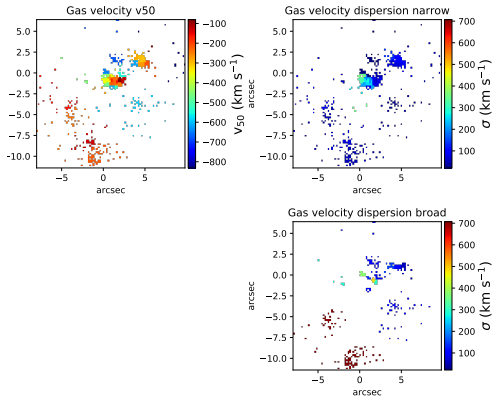

(c) Maps of the neutral atomic gas: Velocity (v_{50}) (right) and gas velocity dispersion (left) of the two components.

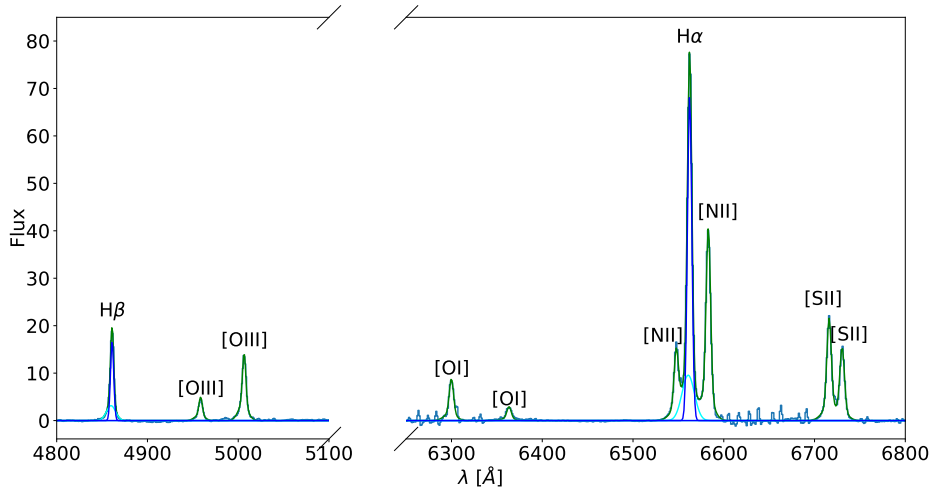

(d) Integrated spectrum: The spectrum is shown in light blue, the two component fit in green, the one component fit in dark blue and for the broad component of Hα and Hβ in cyan.

Figure 3.23: IRAS 20551-4250

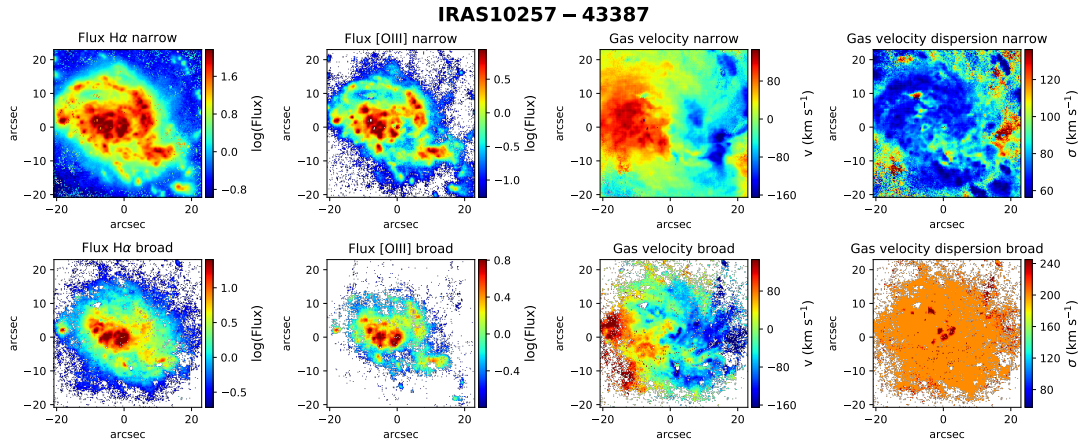

(a) Maps of the ionized gas: The Hα flux, the [OIII] flux, the gas velocity and velocity dispersion are shown for the narrow (top) and broad (bottom) component.

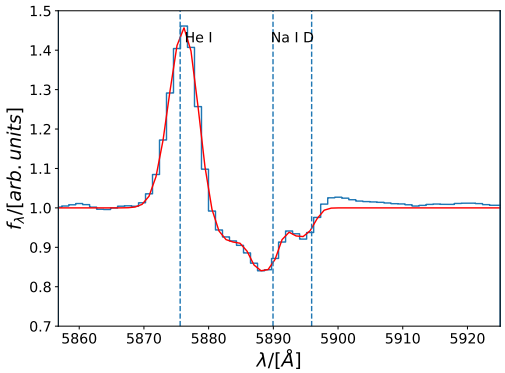

(b) Integrated spectrum of the He I emission and the sodium absorption feature (blue) with fit (red). The dashed lines indicate where we expect the He I emission (5876 Å) and the Na I D absorption lines (5889 Å and 5896 Å).

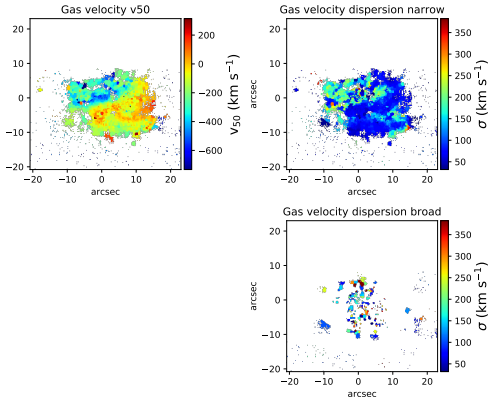

(c) Maps of the neutral atomic gas: Velocity (v_{50}) (right) and gas velocity dispersion (left) of the two components.

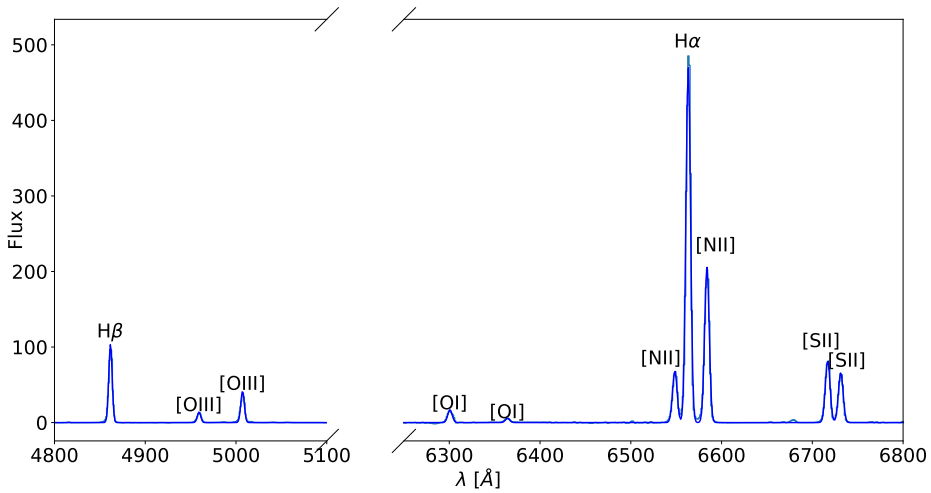

(d) Integrated spectrum: The spectrum is shown in light blue and the one component fit in dark blue.

Figure 3.24: IRAS 10257-4339

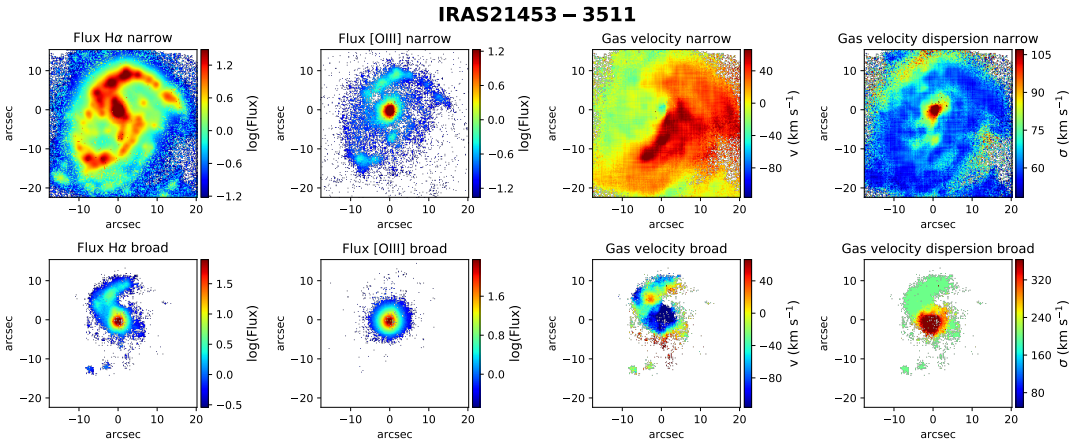

(a) Maps of the ionized gas: The Hα flux, the [OIII] flux, the gas velocity and velocity dispersion are shown for the narrow (top) and broad (bottom) component.

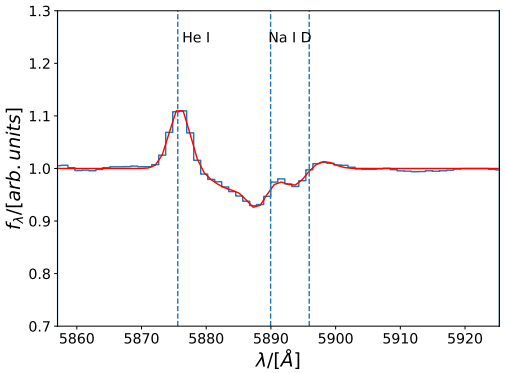

(b) Integrated spectrum of the He I emission and the sodium absorption feature (blue) with fit (red). The dashed lines indicate where we expect the He I emission (5876 Å) and the Na I D absorption lines (5889 Å and 5896 Å).

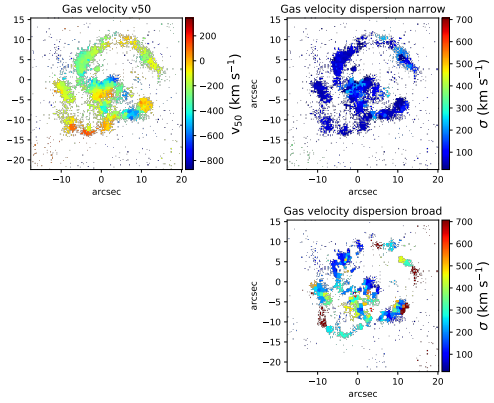

(c) Maps of the neutral atomic gas: Velocity (v_{50}) (right) and gas velocity dispersion (left) of the two components.

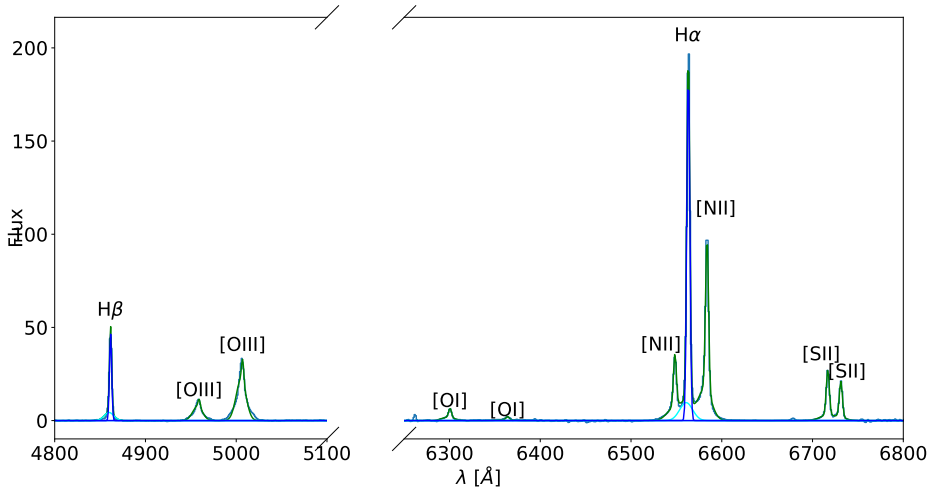

(d) Integrated spectrum: The spectrum is shown in light blue, the two component fit in green, the one component fit in dark blue and for the broad component of Hα and Hβ in cyan.

Figure 3.25: IRAS 21453-3511

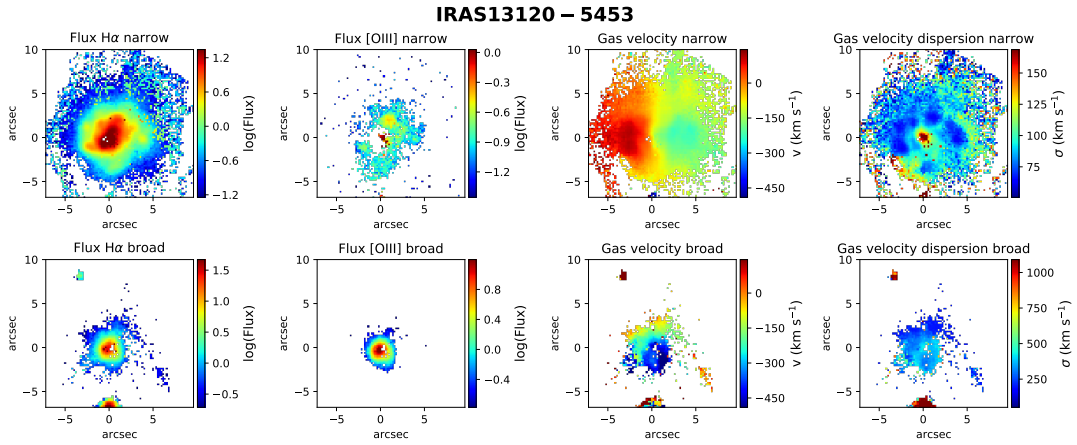

(a) Maps of the ionized gas: The Hα flux, the [OIII] flux, the gas velocity and velocity dispersion are shown for the narrow (top) and broad (bottom) component.

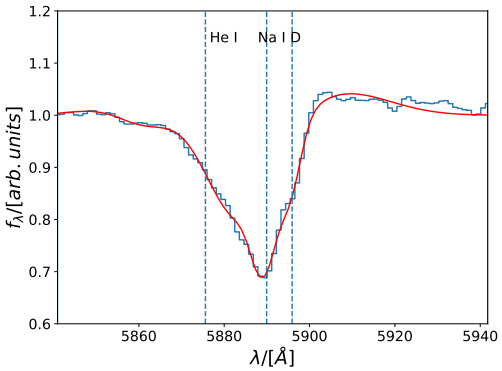

(b) Integrated spectrum of the He I emission and the sodium absorption feature (blue) with fit (red). The dashed lines indicate where we expect the He I emission (5876 Å) and the Na I D absorption lines (5889 Å and 5896 Å).

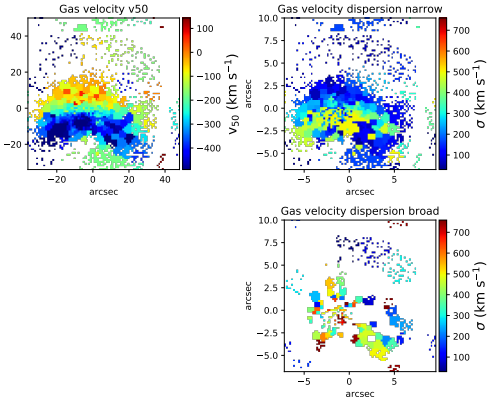

(c) Maps of the neutral atomic gas: Velocity (v_{50}) (right) and gas velocity dispersion (left) of the two components.

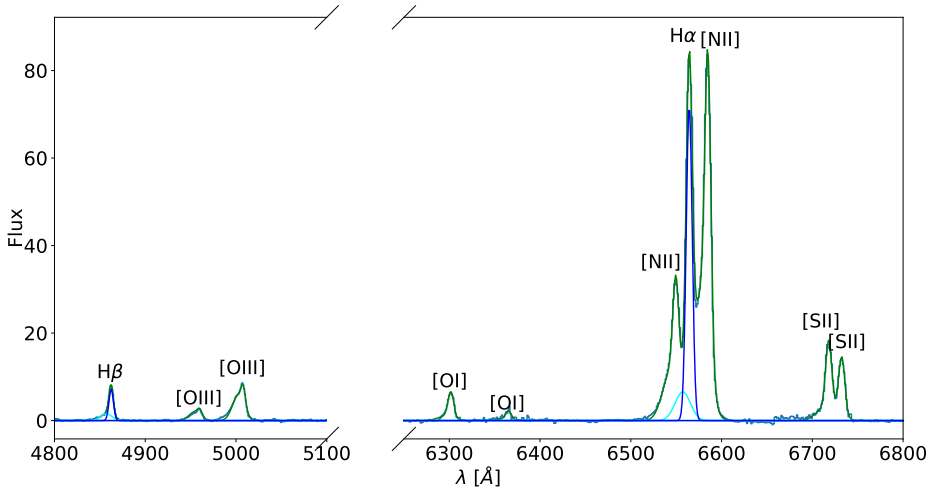

(d) Integrated spectrum: The spectrum is shown in light blue, the two component fit in green, the one component fit in dark blue and for the broad component of Hα and Hβ in cyan.

Figure 3.26: IRAS 13120-5453

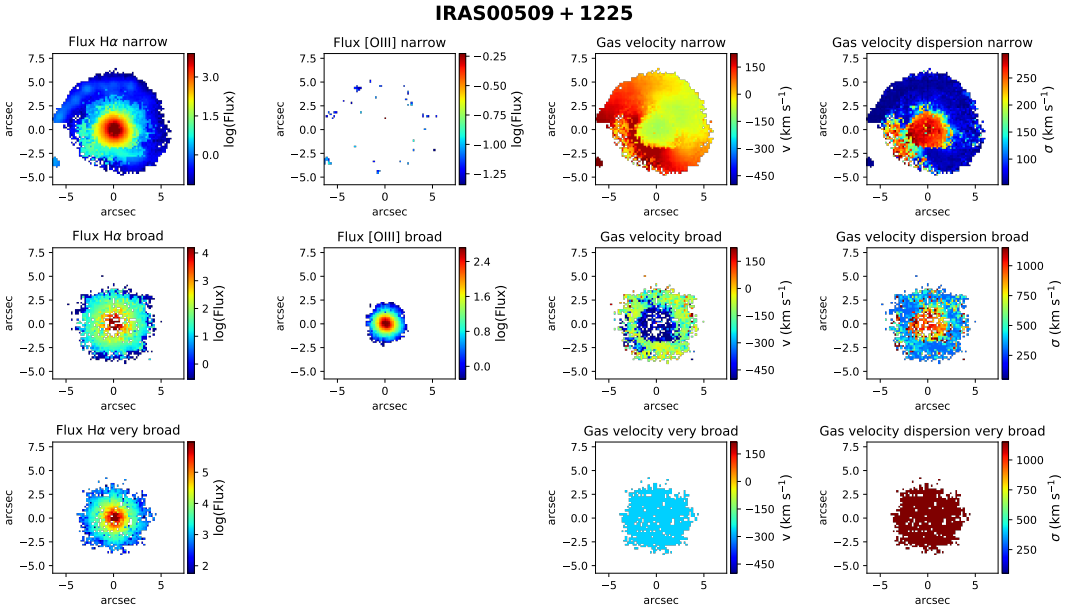

(a) Maps of the ionized gas: The Hα flux, the [OIII] flux, the gas velocity and velocity dispersion are shown for the narrow (top), broad (middle) and very broad (bottom) component.

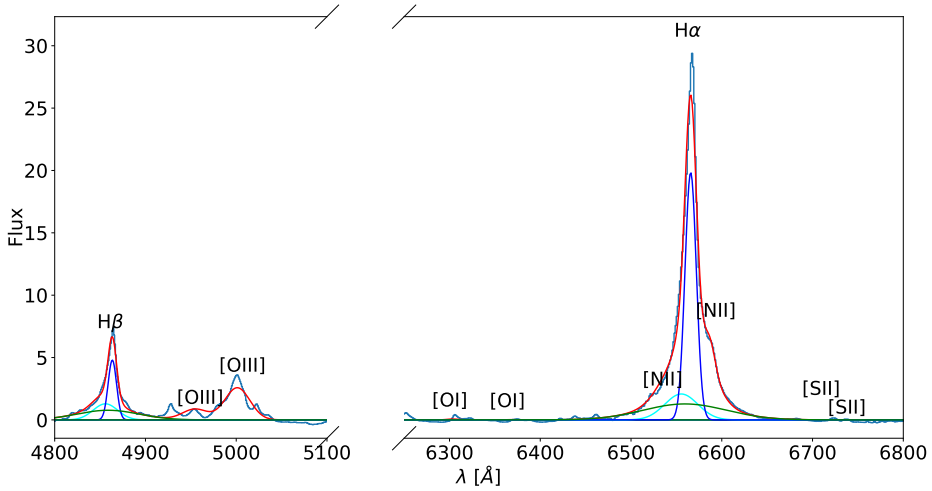

(b) Integrated spectrum: The spectrum is shown in light blue, the three component fit in red, the narrow, broad and very broad component of Hα and Hβ in blue, cyan and green, respectively.

Figure 3.27: IRAS 00509+1225

Chapter 4

Star Formation Inside Galactic Outflows of Local (Ultra)luminous Infrared Galaxies

4.1 Introduction

Not only can outflows suppress star formation, but they can also *induce* or *enhance* the formation of stars. As discussed in Chapter 1, this so-called positive feedback can operate in two different modes. Briefly, in the first mode, outflowing gas (or jets), driven either by star formation or an AGN, compresses gas in the galaxy's disc (or CGM (Croft et al. 2006; Elbaz et al. 2009; Lacy et al. 2017)), leading to fragmentation and gravitational collapse of clouds and therefore enhanced star formation in the disc. A second mode has recently been proposed, in which outflowing gas collapses, fragments and stars are formed in situ, i.e. inside the outflowing gas (Zubovas et al. 2013a; Ishibashi et al. 2013; El-Badry et al. 2016; Mukherjee et al. 2018; Wang & Loeb 2018; Decataldo et al. 2019).

In this chapter, we shall focus on this second mode. Although we now have observational evidence owing to the first detection by Maiolino et al. (2017) that this mode of positive feedback does indeed exist, it remains unclear how widespread this phenomena is. An analysis of galaxies from the Mapping Nearby Galaxies at APO (MaNGA) survey (Bundy et al. 2015) by Gallagher et al. (2019) found that about 30 % of outflows have nebular emission line ratios consistent with ionization by star formation. Studying the ionization parameter, they also found

that the ionization is mostly likely due to stars in the outflow and not due to stars in the disc illuminating the outflowing gas. Rodriguez del Pino et al. (2019) confirmed that about 20–40 % of outflows in their sample of MaNGA galaxies show signs of positive feedback. The star formation rates in these galactic outflows is modest (SFR < 10 $M_\odot$/yr) and in most cases even below 1 $M_\odot$/yr. However, this could be due to their sample consisting of mostly main-sequence galaxies with small outflow rates. Indeed, Gallagher et al. (2019) found a correlation between the ionized outflow rate and the SFR inside the outflow, suggesting that massive outflows such as those observed in high-z quasars (with outflow rates > 100 $M_\odot$/yr) could have significant amounts of star being formed in their outflows. In these objects, the star formation rate in outflows is expected to reach up to 100 $M_\odot$/yr or even more (Ishibashi & Fabian 2012; Silk 2013b). Star formation in galactic winds (even if modest relative to the global star formation in the disc) might in turn have far-reaching consequences for galaxy evolution, such as giving rise to high-velocity stars (Dugan et al. 2014), which might even escape the galaxy, or affecting the morphological evolution of the galaxy and contribute to the formation of the spheroidal component of galaxies (Gaibler et al. 2012). This phenomena could even give rise to the observed galaxy-black hole correlations (Kormendy & Ho 2013) or the metal enrichment of the CGM/IGM (Gallagher et al. 2019). For this reason, we will study possible evidence for positive feedback in a sample local ($z < 0.2$) (Ultra-)luminous infrared galaxies. (U)LIRGs, formally defined as a class of galaxies with an infrared luminosity $> 10^{12}$ $L_\odot$ (ULIRGs) (or $> 10^{11}$ $L_\odot$ for LIRGs). These are galaxies which often have a strong AGN, significant star formation or a combination of the two. Usually, (U)LIRGs are (advanced) mergers and have significant amounts of gas and dust (Lonsdale et al. 2006; Kartaltepe et al. 2010) and resemble massive galaxies at higher redshift. This makes them suitable laboratories to study feedback as the are likely to exhibit faster and more massive outflows than main-sequence galaxies (see e.g. Rodríguez-Zaurín et al. 2013; Rose et al. 2017). (U)LIRGs have been targeted in previous studies (see e.g. Bellocchi et al. 2013; Arribas et al. 2014), which have managed to detect two kinematically distinct components in these systems. However, due to the lack of sensitivity and spatial resolution, these works often have not been able to detect the full extent of outflows or structures on scales smaller than ≈ 1 kpc.

While being similar to high-z galaxies, the (U)LIRGs in our sample can be studied in great spatial detail because these galaxies are local. Observing them with MUSE provides spatially resolved information on the kinematics with an unprecedented resolution ($\approx$ 0.6–0.8 arcsec (but seeing-limited), corresponding to $\sim$ 100–2000 pc for our sample depending on the galaxy).

The aims of this chapter are threefold. First, we want to establish how common star formation in galactic outflows of (U)LIRGs are. Second, we investigate whether this mode of star formation is more prominent in powerful and massive outflows. This will help us infer

how important in situ star formation is at higher redshifts. Finally, leveraging on the BPT diagnostics developed to investigate the first two points, we study how outflow properties of the neutral atomic and ionized outflow phases vary as a function of the position of the host and the outflow in the BPT diagrams.

Throughout this chapter, a $H_0 = 70$ km s^{-1} Mpc^{-1}, $\Omega_M = 0.27$ and $\Omega_\Lambda = 0.73$ cosmology is adopted as in previous chapters.

4.2 Methods

4.2.1 Sample

The sample used in this chapter is identical to the one used in Chapter 3 and it consists of 26 local (U)LIRGs with redshifts below 0.2. A more detailed description of the sample can be found in Chapter 3. Briefly, these galaxies are characterised by an infrared luminosity of $L_{IR} > 10^{11}$ L$_\odot$ in the case of LIRGs and $> 10^{12}$ L$_\odot$ in the case of ULIRGs. We include a combination of star formation and AGN-dominated galaxies. All galaxies were observed with the ESO Multi Unit Spectroscopic Explorer (MUSE) at the Very Large Telescope. For a description of the instrument see Section 3.2.1.

4.2.2 Data Analysis

The MUSE data cubes were used in their reduced form after running the MUSE pipeline. These data cubes provide access to all nebular emission lines of interest: Hβ, [OIII]$\lambda\lambda$4959, 5007, [OI]$\lambda\lambda$6300, 6366, [NII]$\lambda\lambda$6548, 6584, Hα and [SII]$\lambda\lambda$6717, 6731. The emission and absorption line-fitting was performed as explained in Chapter 3. Briefly, the fitting approach relies on a penalized Pixel-Fitting (pPXF) routine by Cappellari (2017) and emission lines and stellar continuum are fitted simultaneously. To establish the number of emission line components (one, two or three), the model with the lowest χ^2_{red} is selected. The narrow component is identified as the disc, the broad component as the outflow and the very broad component is used to fit emission lines from the broad line region (BLR).

4.2.3 Mass Outflow Rates

Ionized mass outflow rates are calculated from the integrated spectrum according to prescription in Chapter 3. We assume time-average thin shells or clumps (Rupke et al. 2005a; Lutz et al. 2020). The mass outflow rate is then given by:

$$\dot{M}_{OF,ion} = \frac{M_{OF,ion}}{\tau_{OF,ion}} = \frac{M_{OF,ion} v_{OF,ion}}{r_{OF,ion}}, \tag{4.1}$$

where $v_{\rm OF,ion}$ and $r_{\rm OF,ion}$ are the ionized outflow velocity and radius, respectively. As in previous chapters, we define the outflow velocity as $v_{\rm OF,ion} = \Delta v + {\rm FWHM_{broad}}/2$, where Δv is the offset between the narrow and broad velocity centroid. The radius of the ionized outflow is defined as the radius which includes 50 % of the total flux of the broad Hα component. The mass of the outflow, $M_{\rm OF,ion}$, is calculated using the luminosity of the broad component of Hα, $L_{\rm H\alpha,broad}$, following the prescription in Gallagher et al. (2019):

$$M_{\rm OF,ion}[{\rm M_\odot}] = 1.5 \times 10^9 {\rm M_\odot} \left(\frac{L_{\rm H\alpha,broad}}{10^{44}\ {\rm erg\ s^{-1}}}\right) \left(\frac{n_{\rm e}}{200\ {\rm cm^{-3}}}\right)^{-1}, \tag{4.2}$$

or the broad component of the [OIII]λ5007 line, $L_{\rm [OIII],broad}$,

$$M_{\rm OF,ion}[{\rm M_\odot}] = 2 \times 10^8 {\rm M_\odot} 10^{-[{\rm O/H}]} \left(\frac{L_{\rm [OIII],broad}}{10^{44}\ {\rm erg\ s^{-1}}}\right) \left(\frac{n_{\rm e}}{200\ {\rm cm^{-3}}}\right)^{-1}. \tag{4.3}$$

The [OIII]-based outflow rate estimate is generally lower because it does not include lower ionization phases of the outflow (see Chapter 3). Unlike in Chapter 3 we use the median of the measured electron density in their outflows rather than the sample average.

4.2.4 Calculation of Star Formation Rates

To infer the star formation rate we use Hα, which is sensitive to star formation from the last 10 Myr (Kennicutt & Evans 2012). We correct the Hα luminosity for extinction using the Balmer decrement and apply a Calzetti et al. (2000) attenuation curve for a galactic diffuse ISM ($R_{\rm V} = 4.05$). The star formation rate in the disc (outflow) is obtained from the extinction-corrected narrow (broad) Hα luminosity (assuming a Kroupa IMF) via (Kennicutt & Evans 2012):

$$\log\left(\frac{\rm SFR}{\rm M_\odot/yr}\right) = \log\left(\frac{L_{\rm H\alpha}}{\rm erg\ s^{-1}}\right) - 41.27. \tag{4.4}$$

For the SFR in the outflow, we consider only the contribution to the Hα luminosity, $L_{\rm H\alpha}$, from outflowing spaxels which are classified as star forming in the [SII]-BPT diagram. The true star formation is likely higher as there could be a contribution from spaxels which are not classified as star forming according to the BPT diagram but might still contribute to the total SFR in the outflow. If we have a combination of star formation and AGN activity, the BPT diagnostic is likely dominated by even a weak AGN and classified as AGN/shock-like (see Gallagher et al. (2019) for a discussion on how even a faint AGN can rapidly move the BPT line ratios towards the Seyfert region even if prominent star formation is present).

One caveat is that Hα-based SFRs might underestimate the true SFR (even when corrected for extinction inferred from the Balmer decrement). This is because in many (U)LIRGs the

optical extinction is so high that most of the optical emission lines are affected by an opacity much larger than unity. Hence, their flux is nearly completely suppressed and cannot be recovered even by correcting with the extinction inferred from the Balmer decrement. Indeed, previous works have already found that in ULIRGs (and thus maybe also in their outflows) Hα-derived SFRs are a factor of a few up to an order magnitude lower than the SFR estimates based on the IR luminosities (Flores et al. 2004; Rodríguez-Zaurín et al. 2011). In these heavily obscured systems a much more accurate measure of the SFR can be obtained from the 8–1000 μm IR luminosity, which is unaffected by extinction. However, as this is an integrated property of the galaxy, without any kinematic information, it is not possible to discriminate directly what fraction of the IR luminosity comes from the galaxy and what fraction comes from the outflows. We can assume that the IR-estimated SFR is distributed in the same relative fraction among disc and outflow as calculated form the two Hα components. In this case the IR-based SFR in the outflow is given by (Sturm et al. 2011):

$$\mathrm{SFR}_{\mathrm{OF,IR}} = \frac{\mathrm{SFR}_{\mathrm{H}\alpha,\mathrm{broad}}}{\mathrm{SFR}_{\mathrm{H}\alpha,\mathrm{narrow}}} \times (1 - \alpha_{\mathrm{bol}}) L_{\mathrm{IR}} * 10^{-10}, \tag{4.5}$$

where α_{bol} is the AGN contribution to the total IR luminosity.

4.2.5 Baldwin-Phillips-Terlevich (BPT) Diagrams

To determine the dominant ionization mechanism and physical properties of the ionized gas, we use the Baldwin-Phillips-Terlevich (BPT) diagrams (Baldwin et al. 1981). Originally, the emission line ratios of [NII]λ6584/Hα versus [OIII]λ5007/Hβ ([NII]-BPT) were used to distinguish HII regions (excited by young, massive hot stars) from regions photoionized by a harder radiation field. This harder radiation field can by produced by either shock excitation or by an AGN. In addition to [NII], also other tracers are used ([SII]$\lambda\lambda$6716,6731 ([SII]-BPT) and [OI]λ6300 ([OI]-BPT)). The demarcation line between star forming objects and regions which cannot be explained by star formation alone was calculated by Kewley et al. (2001) using population synthesis models in combination with photoionization and shock models. The line was slightly modified by Kauffmann et al. (2003) to match the observed SDSS galaxies. For all our BPT diagrams, we require a SNR > 3 on all emission lines required by the BPT diagrams. For instance, for the [NII]-BPT diagram, we require SNR(Hα), SNR(Hβ), SNR([NII]) and SNR([OIII]) > 3 for both (broad and narrow) components.

4.2.6 Identification of Positive Feedback Candidates

One of the main goals of this chapter is to find evidence for positive feedback in our sample. To establish the presence of positive feedback, we require four criteria to be satisfied:

1) The broad component is kinematically distinct from the narrow component and is identified as an outflow in the regions where we look for positive feedback. This means that the gas velocites of the narrow and broad components should be different (more than 50 km s^{-1} apart). Similarly, the gas velocity dispersion (σ) of the broad component has to exceed the gas velocity dispersion of the narrow component by at least 50 km s^{-1};
2) At least 30 % of the outflowing spaxels are classified as star forming in the [SII]-BPT diagram;
3) The proxy for the ionization parameter (as traced by the RS_{23} parameter) is not significantly lower in the outflow than in the disc (this ensures that the SF-like diagnostics are due to in situ excitation and not due to illumination by the young stars in the disc);
4) The median electron density in the outflow ($n_{e,OF}$) is equal or higher than in the disc ($n_{e,disc}$). This is to ensure that the ionization parameter is not high purely because of a low density in the outflow (see point 3)).

4.3 Prevalence of Positive Feedback

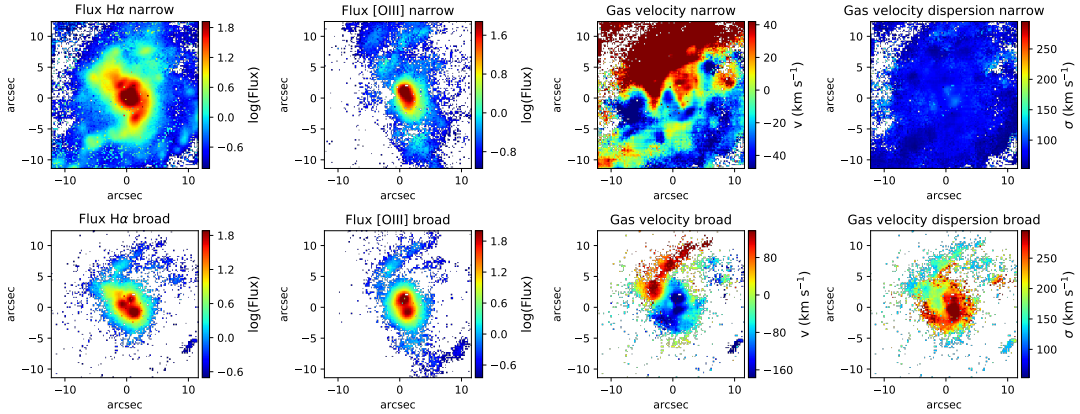

Figure 4.1: Maps of the narrow (top) and broad (bottom) component of IRAS 13229-2934. From left to right, we show Hα and [OIII] flux maps, gas velocity and gas velocity dispersion map.

Many (U)LIRGs show complex kinematics (e.g. Bellocchi et al. 2013; Piqueras López et al. 2013), often because of past or current interactions with other galaxies. To establish the presence of an outflow, we therefore study the emission line maps first. We require that the broad component is kinematically distinct from the narrow component (criterion 1 in Section 4.2.6). Outflows are often characterised by blueshifted (with respect to the systemic emission lines) emission lines and large velocity dispersions (see e.g. Mullaney et al. 2013; Harrison et al. 2016). Our goal is to find evidence for that to distinguish outflows from mergers or other

gas interactions. In Fig. 4.1, we show the Hα and [OIII]λ5007 flux maps (two columns on the left), the gas velocity (3rd column) and the gas velocity dispersion (4th column) for the narrow (top row) and the broad component (bottom row) of IRAS 13229-2934. As displayed in the third column, the broad component is blueshifted with velocities up to –150 km s^{-1} compared to the narrow component. Furthermore, the gas velocity dispersion reaches values of almost 300 km s^{-1} (the broad and narrow components are shown on different scales). There are several interpretations of these features, but the strong blueshift found here and also in Bellocchi et al. (2013) suggests the presence of outflowing gas. The kinematic maps for the remaining three positive feedback candidates can be found in Section 3.5.5.

In a second step (criterion 2 in Section 4.2.6), to evaluate whether stars are being formed in the outflowing gas, we study the BPT diagrams of the outflow and the disc. For some galaxies, we find a large fraction (> 30 % or even > 50 %) of spaxels in the outflow are classified as star forming according to the [SII]-BPT diagram. In Fig. 4.2 the BPT diagrams for the systemic (top row) and the outflowing components (bottom row) of all positive feedback candidates are displayed. The median locations in the BPT diagrams are shown as bright green stars. In IRAS 23128-4919 and IRAS 19541+1110, the vast majority of spaxels in the broad component are SF-dominated. In the [SII]-BPT diagram of these two galaxies almost all outflowing spaxels are classified as star forming, while only about 50 % of the narrow components have SF-like diagnostics. In the [NII]- and [SII]-BPT diagrams of IRAS 13229-2934 about 30–50 % of outflowing spaxels are classified as composite/star forming in the [NII]-BPT and as star forming in the [SII]-BPT. About 70–80 % of the outflowing spaxels are classified as star forming or star forming and composite in the [SII]- and [NII]-BPT diagrams of IRAS 20551-4250, respectively. In the [OI]-BPT diagram of all four galaxies, most spaxels are Seyfert- or LINER-like, but the SNR for the [OI] line is generally significantly lower and hence a large number of spaxels cannot even be classified in the [OI]-BPT diagram. In addition, we found that due to SNR constraint (> 3), the [OI]-BPT diagram predominantly selects spaxels which were classified as Seyfert-like in the other BPT diagrams and discards SF-dominated spaxels. Hence the [OI]-BPT is likely biased towards shock/AGN-dominated regions. For the analysis in this chapter, we mainly focus on the [SII]-BPT diagram as the strength of the [NII]-BPT diagram classification depends strongly on the N/O abundance and thus also on stellar mass (Pérez-Montero & Contini 2009; Masters et al. 2016). [SII] on the other hand is an alpha process element and does not suffer from this issue (Burbidge et al. 1957).

4.3.1 Spatially Resolved BPT Diagrams

MUSE allows us to also produce spatially resolved BPT diagrams. The spatial BPT diagrams of IRAS 23128-5919, IRAS 13229-2934, IRAS 20551-4250 and IRAS 19542+1110 are shown

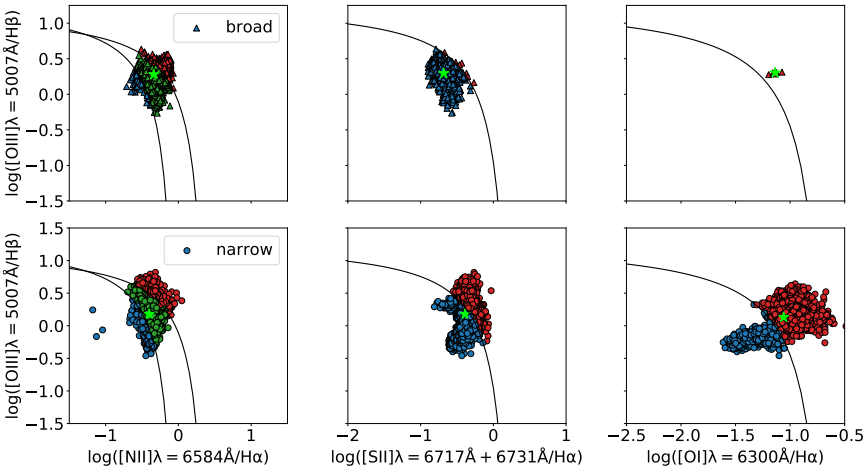

(a) BPT diagrams of IRAS 23128-5919

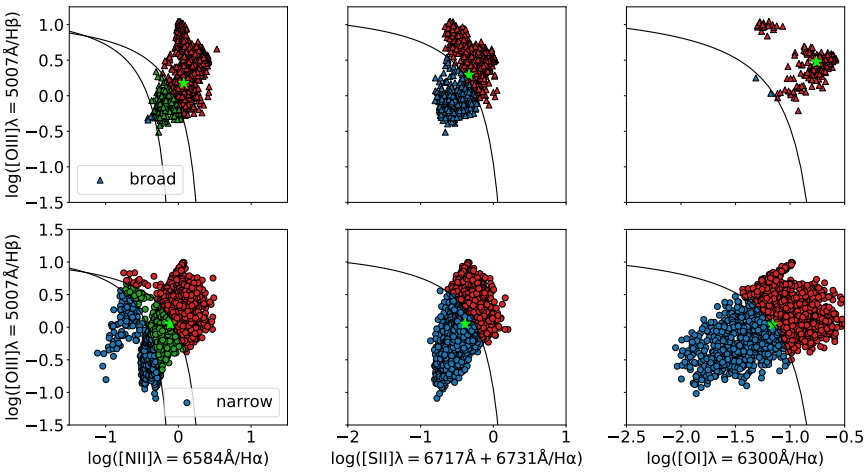

(b) BPT diagrams of IRAS 13229-2934

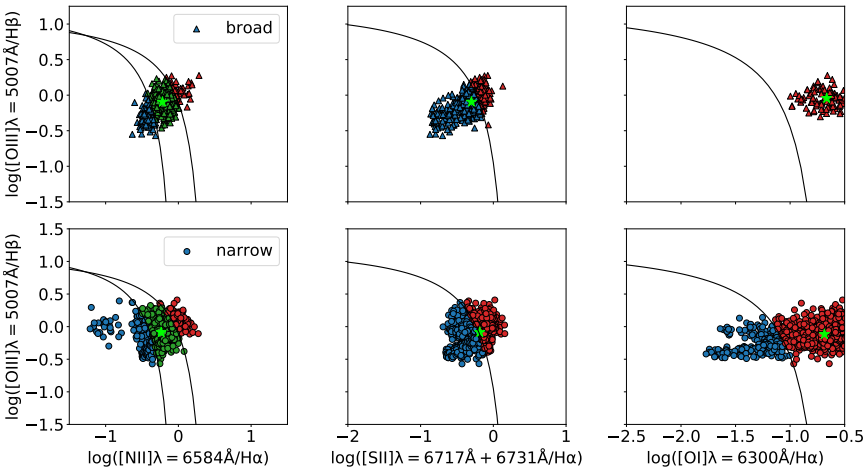

(c) BPT diagrams of IRAS 20551-4250

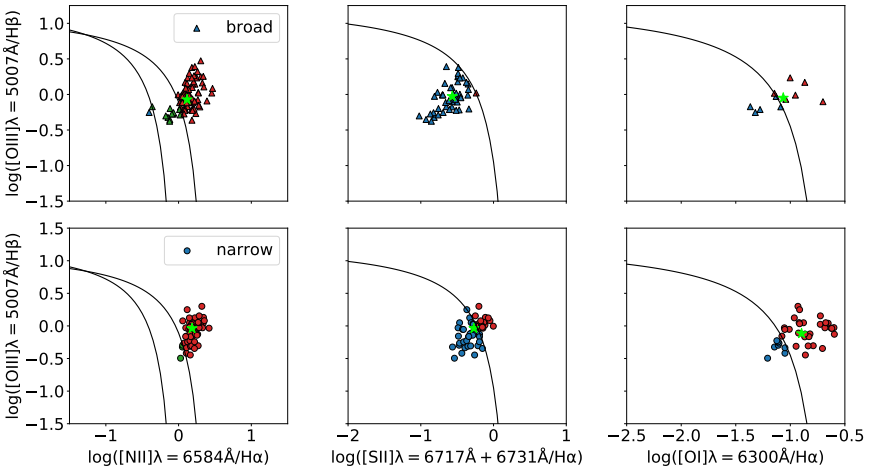

(d) BPT diagrams of IRAS 19542+1110

Figure 4.2: BPT diagrams of the broad (top row) and narrow (bottom row) component of all galaxies with positive feedback. We show the [NII]- (left), [SII]- (centre) and [OI]- (right) BPT diagrams. The green star indicates the median position in the BPT diagrams. The demarcation lines between AGN and starburst-dominated objects were obtained by Kewley et al. (2001), who calculated a maximum starburst line based on stellar population synthesis, photoionization and shock models. For the [NII]-BPT diagram, Kauffmann et al. (2003) revised this line (upper line of the two) to include galaxies with a combination of AGN and starbursts.

in Fig. 4.3, where each spaxel is coloured according to its BPT classification. From left to right, we show the [NII]-, [SII]- and [OI]-BPT classified spaxels. Again, we require a SNR > 3 for all lines to classify a spaxel. For IRAS 23128-5919, the whole galaxy is classified as star forming according to the [SII]-BPT diagram, whereas the [NII] demarcation lines classify a number of spaxel near the centre as Seyfert, but the majority as composite. While the centre of IRAS 13229-2934 is dominated by Seyfert-like emission (shown in red), a large part of the outflowing gas in the north-east is mainly photo-ionized by star formation (shown in blue) in the [SII]-diagram or it is classified as composite in the NII diagram (shown in green). In IRAS 20551-4250 large parts are composite or star forming in the [NII] and [SII]-BPT, respectively. Only the very centre is Seyfert-dominated, probably because of the deeply buried AGN in this object (see e.g Imanishi et al. 2016, and references therein). In IRAS 19542+1110, there is a mix between star forming and Seyfert-dominated spaxels.

These figures also illustrate that [OI] is only above the SNR cut in a very small part of the galaxy compared to [NII] and [SII]. As discussed above, the [OI]-BPT diagram is likely biased towards shock/AGN-dominated regions, i.e. [OI] is more likely to be above the required SNR cut in these regions.

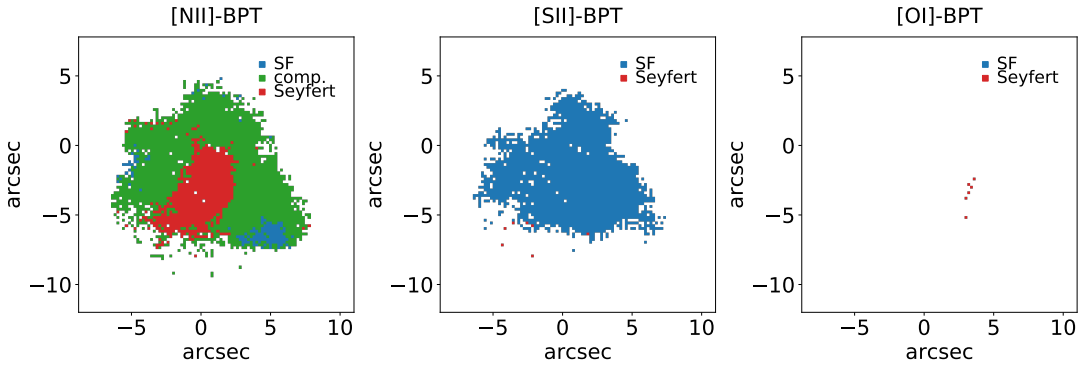

(a) spatial BPT diagrams of IRAS 23128-5919

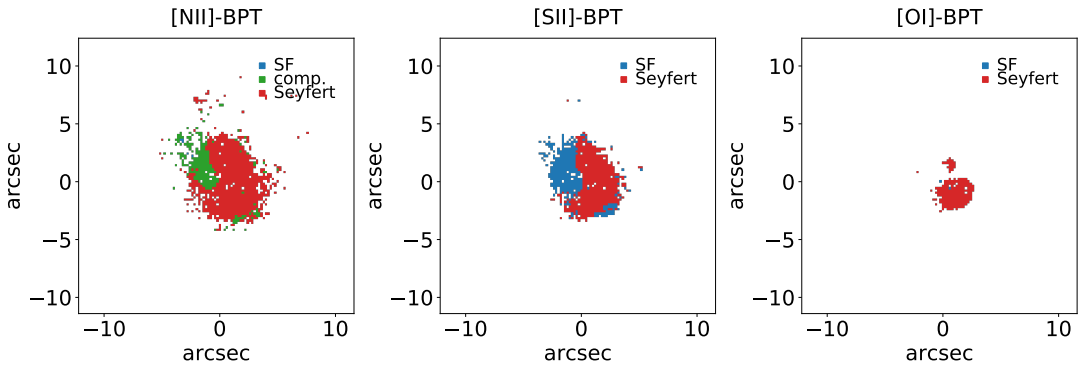

(b) spatial BPT diagrams of IRAS 13229-2934

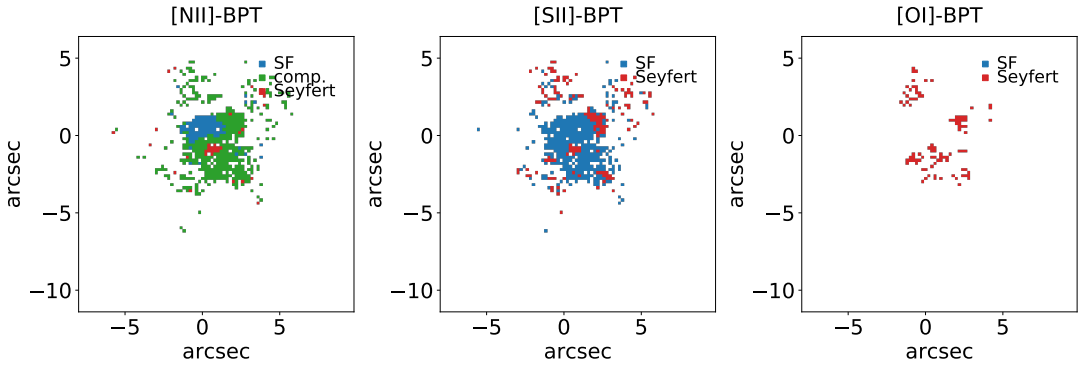

(c) spatial BPT diagrams of IRAS 20551-4250

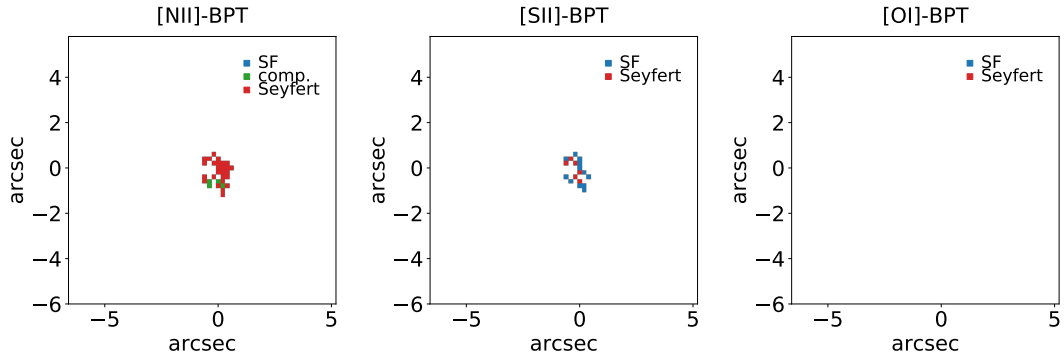

(d) spatial BPT diagrams of IRAS 19542+1110

Figure 4.3: Spatial BPT diagrams of the broad (outflowing) component based on the demarcation lines in the [NII]-(left), [SII]-(centre) and [OI]-(right) BPT diagrams for all galaxies with signs of positive feedback. SF- dominated regions are shown in blue, composite regions (in the [NII]-BPT) in green and Seyfert-dominated regions in red. Composite regions are datapoints lying between the Kewley et al. (2001) and Kauffmann et al. (2003) lines in Fig. 4.2.

4.3.2 Ionization Parameter

One potential concern is that the outflowing spaxels are solely classified as star forming because the outflow is illuminated externally by young stars in the disc rather than in situ star formation. To test this, we study the ionization parameter, U (criterion 3 in Section 4.2.6). U is related to the flux of ionizing photons ($Q_{\rm ion}/4\pi r^2$) via:

$$U = \frac{Q_{\rm ion}}{4\pi r^2 c n_{\rm e}} \tag{4.6}$$

where c is the speed of light and $n_{\rm e}$ the electron density. As in Chapter 3, we define the outflow radius as the radius which encompasses half of the total broad Hα flux above 3σ (for more details, see Section 3.2.7) Since the outflow is at much larger distances (i.e. larger r in equation 4.6) than the ISM surrounding the stars and it also has higher density (see Chapter 3 and discussion later on), we would expect U to be much lower in case it was illuminated externally by stars in the galactic disc. We test this by comparing the ionization parameter values in the disc and the outflow.

Usually the ionization parameter is measured using the [OIII]λ5007/[OII]λ3727 or the [SIII]$\lambda\lambda$9069,9532/[SII]$\lambda\lambda$6716,6731 line ratios (Diaz & Pérez-Montero 2000). Unfortunately, [OII] and [SIII] are not in the wavelength range covered by MUSE. Instead of [OIII]/[OII] we thus use the [OIII]/[SII] ratio, which is closely correlated with the former (Venturi et al., in prep.). Hence, we measure the ionization parameter using log(RS$_{23}$), where RS$_{23}$ is defined as the [OIII]/[SII] line ratio.

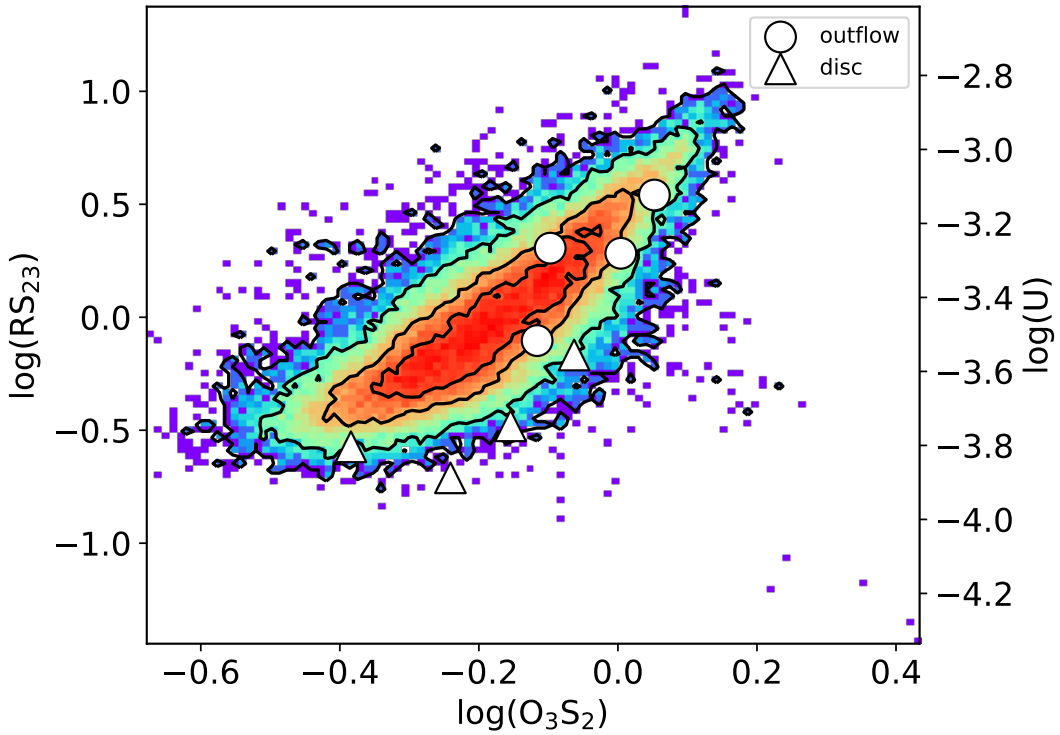

Figure 4.4: Ionization parameter ($U \sim \log(RS_{23})$) values for the outflow (white circle) and disc (white triangle) of all positive feedback candidates. The contours represent the ionization parameter values of star forming galaxies from the MaNGA survey.

In Fig. 4.4, we compare the ionization parameter in the disc and the outflow. The horizontal axis is $\log(O_3S_2)$ = log ([OIII]+[SII])/Hα, which is a proxy of metallicity (Kumari et al. 2019). The coloured region with contours shows the distribution of these parameters among MaNGA star forming galaxies and illustrates a well-known correlation between ionization parameter and metallicity. The median ionization parameter values for the disc are shown as triangles and lie slightly below the typical local star forming galaxies in the MaNGA survey (shown as contours in Fig. 4.4). The outflowing regions of these galaxies (shown as circles) do not lie below the disc values of typical star forming regions as would be expected if they were illuminated by the disc. In the latter case they would be expected to lie one or two orders of magnitude below the relation for normal star forming regions because of the larger distance, r. Instead, the outflows have ionization parameter values typical of star forming regions, which reinforces the idea that star formation takes place within these outflows.

However, a potential caveat might be that the outflow is less dense, thereby compensating for the lower flux of ionizing photons (see equation 4.6). This would then lead to a higher ionization parameter. However, as already discussed in Chapter 3 we demonstrated that outflowing gas is

Table 4.1: Positive feedback candidates

Galaxy	z	$\dot{M}_{\rm OF,ion}$* [$M_\odot$/yr]	$SFR_{H\alpha}$ (in outflow) [$M_\odot$/yr]	SFR_{IR} (in outflow) [$M_\odot$/yr]
IRAS 23128-5919	0.0448	1.79	7.0	55.2
IRAS 13229-2934	0.01369	0.55	0.25	6.11
IRAS 20551-4250	0.0430	2.00	1.39	24.7
IRAS 19542+1110	0.064955	4.10	0.55	79.3

Table 4.2: Columns: (1): galaxy name, (2): redshift, (3): ionized mass outflow rate derived using Hα, (4): Hα-based SFR in outflow and (5): IR-derived SFR in outflow.
*the ionized mass outflow rates quoted here differ from those in Chapter 3 as we use the electron density measured in each galaxy instead of n_e = 500 cm^{-3}.

on average about a factor of two to three denser than the ISM in the disc. In this section, we will study whether this also holds for the specific galaxies which display signs of positive feedback. The electron densities of the four positive feedback candidates are shown Fig. 4.5. In these panels, we show the electron density maps for the narrow (top) and broad (bottom) component on the left. The density was measured using the line ratio of the [SII] doublet as discussed in Chapter 3. For each spaxel we require a SNR of at least 2 on each of the two [SII] lines. Since the broad component usually has a smaller SNR, fewer spaxel are displayed in the bottom plot. On the right, the histogram of the broad and narrow components for the same galaxy is shown in regions where both components are detected. The blue and red bars represent the narrow and broad component, respectively. Evidently, the broad components are characterised by higher densities in all four galaxies with median electron densities of $10^{2.5}$ cm^{-3} to almost 10^3 cm^{-3}, whereas the narrow components peak around densities of $n_e \sim 10^2$ cm^{-3}–$10^{2.5}$ cm^{-3}.

4.3.3 Role of Shocks

Shocks can reproduce the line ratios we see in LI(N)ER and Seyfert regions of the BPT diagram. Yet if the shocks are slow, they could potentially even mimic SF-like line ratios. However, it is unlikely that the SF-like line ratios seen here are due to shocks. First, as Gallagher et al. (2019) pointed out, only a small number of the ratios found in our objects can reproduced by shock models from MAPPINGS III library of fast radiative shock models (Allen et al. 2008) (assuming very specific parameters). The majority of data points in our BPT diagrams are inconsistent with shock models. Moreover, shock models are unable to reproduce the high ionization parameter values measured in outflows as shown in Fig. 4.4. Finally, they are unlikely to account for the high nebular luminosities in the outflow as the typical Hα luminosities in the outflow are about 1–2 orders of magnitude higher than what we would expect from shocks (Gallagher et al. 2019).

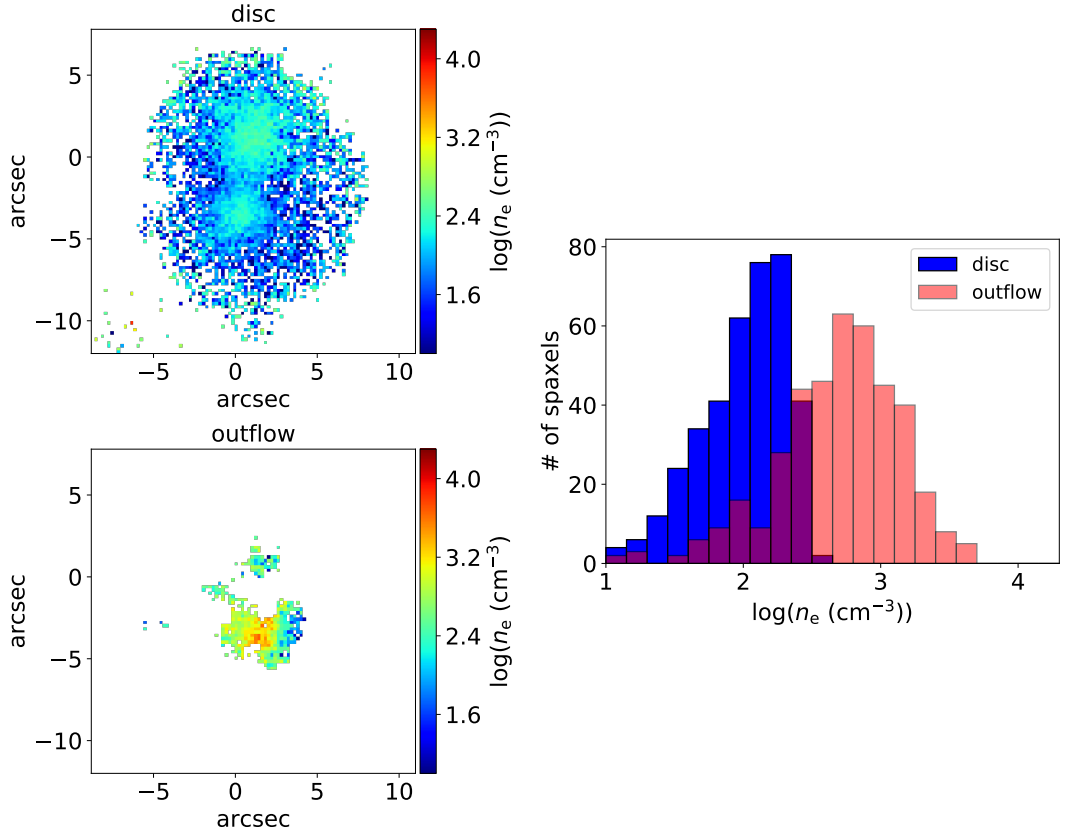

(a) Electron density of IRAS 23128-5919

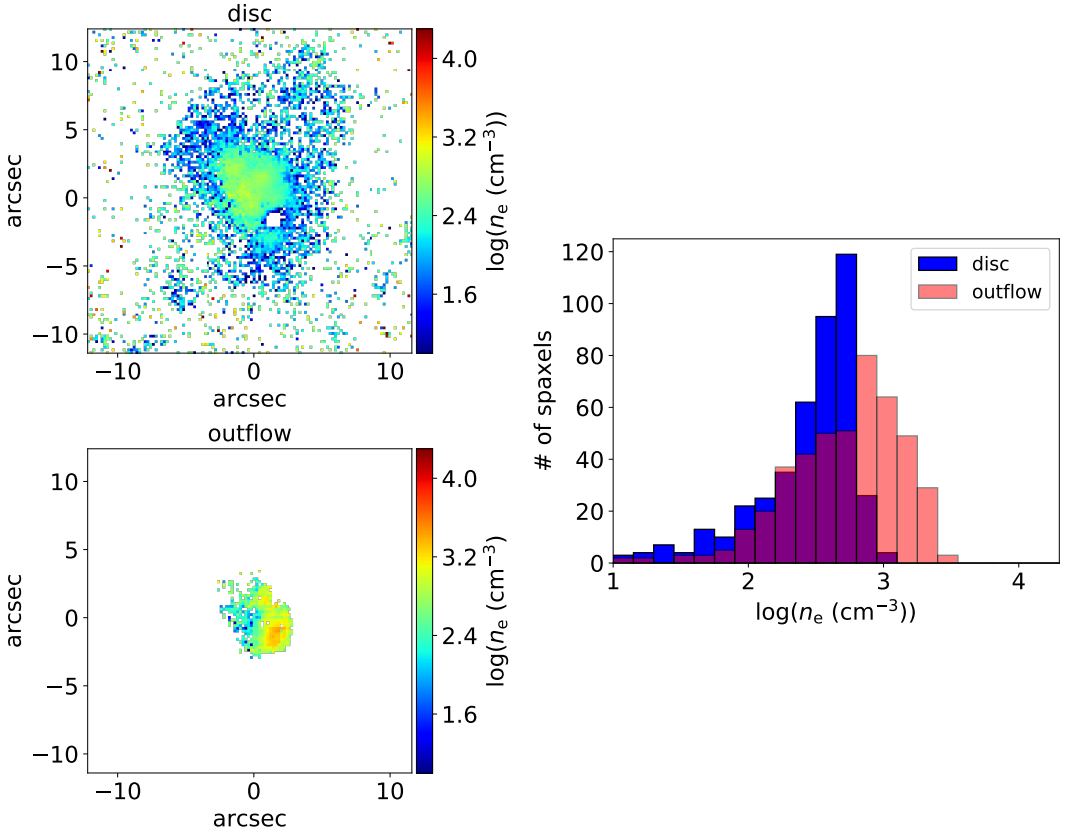

(b) Electron density of IRAS 13229-2934

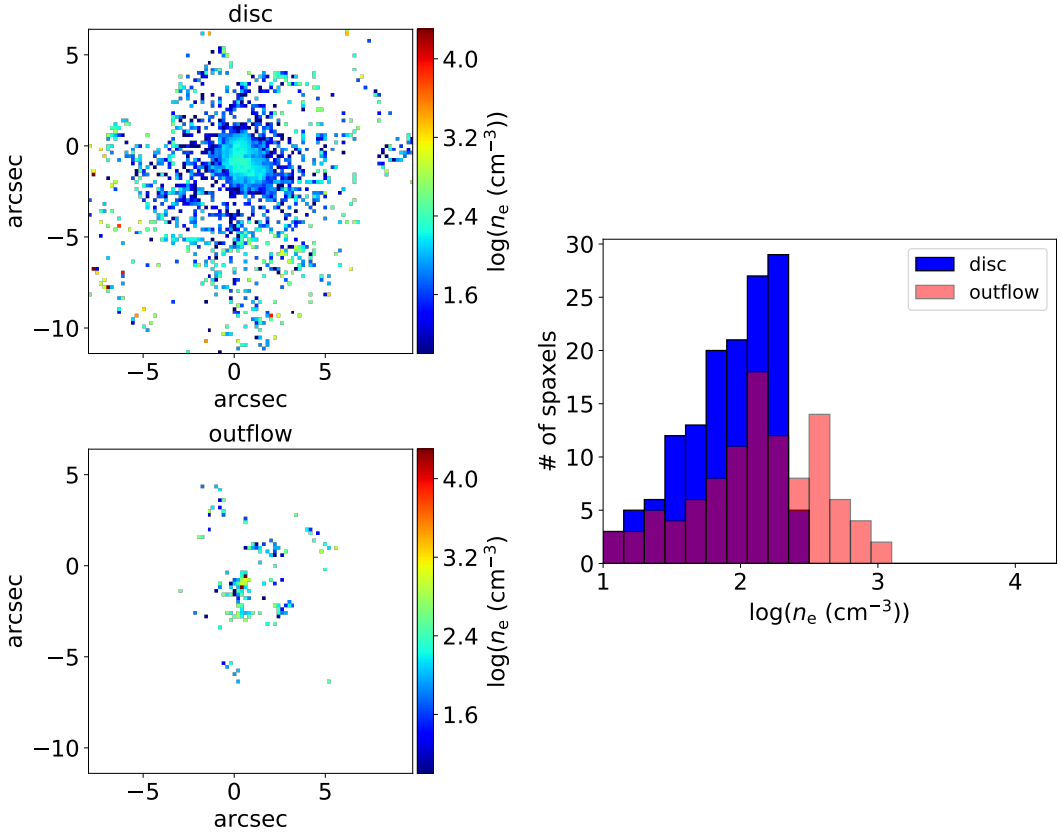

(c) Electron density of IRAS 20551-4250

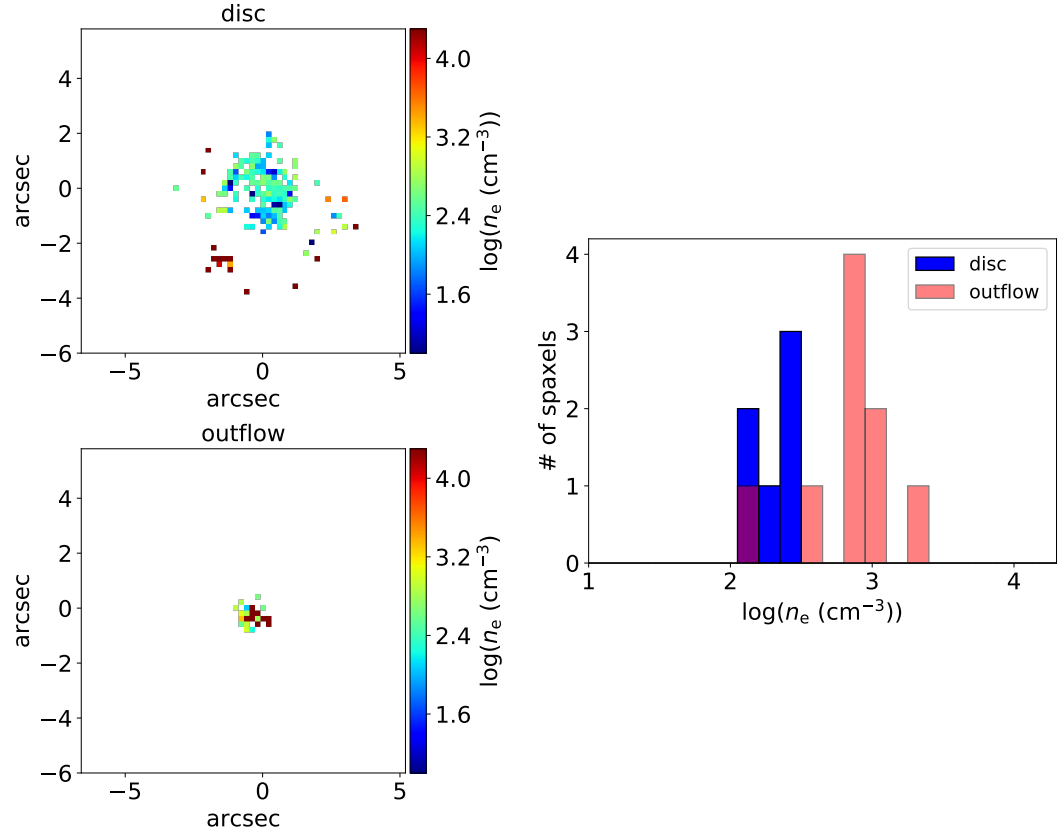

(d) Electron density of IRAS 19542+1110

Figure 4.5: Left: Electron density maps for the narrow (top) and broad (bottom) component. Right: Histogram of the electron densities in the region where electron densities for both components are measured.

4.3.4 Occurrence of SF in Outflows

To summarize, we find that out of our sample of 26 (U)LIRGs, 12 galaxies have an ionized outflow (see Chapter 3). After applying the criteria in Section 4.2.6, we conclude that four (33 %) of these show signs of positive feedback. This fraction is roughly consistent with the fraction of outflows with significant star formation inside the outflow (30 %) found by Gallagher et al. (2019) for their MaNGA sample.

4.3.5 Importance of Positive Feedback in Powerful Outflows

Gallagher et al. (2019) suggested that the star formation rate in the outflow correlates with the ionized outflow rate. This would imply that powerful quasars or starburst galaxies at higher redshifts with large outflow rates ($\dot{M}_{\rm OF}$ ~ 100–1000 $M_\odot$/yr) (e.g. Carniani et al. 2015; Bischetti et al. 2019a) could contribute significantly to the total star formation rate and thus also affect the evolution of the galaxy as a whole. As our sample of (U)LIRGs are characterised by higher outflow rates than the MaNGA galaxies in Gallagher et al. (2019), we can test whether the correlation between SFR and mass outflow rate extends beyond the MaNGA's parameter range ($\log(M_\star/M_\odot)$ ~ 9.5–11.5, $\log(\mathrm{SFR}/(M_\odot/\mathrm{yr}))$ ~ -2–1) . This in turn allows us to draw conclusions about the importance of in situ star formation in even more powerful outflows. We investigate this in Fig. 4.6, where we plot the star formation rate inside the outflow as a function of the mass outflow rate inferred from Hα. The black line is the fit to the outflows in the MaNGA galaxies in Gallagher et al. (2019) (blue data points). While IRAS 23128-5919 (red circle) follows the trend, the other galaxies in our sample (green circles) have SFR about an order of magnitude lower than expected given their outflow rate. One possible explanation for such low SFR is, as discussed above, that Hα-based SFRs (shown as circles in Fig. 4.6) underestimate the true SFR (even when corrected for extinction inferred from the Balmer decrement). To account for this issue, we also estimate the SFR in the outflow using the 8–1000 μm infrared luminosity ($L_{\rm IR}$) taking into account the AGN contribution, $\alpha_{\rm bol}$ as dicussed in Section 4.2.4. We plot these IR-based SFRs as triangles in Figs 4.6 and 4.7. They agree well with the relation suggested in Gallagher et al. (2019). Whether the IR- or Hα-based estimates are more accurate, is difficult to determine. It seems likely that Hα is an unreliable tracer also in outflows and not just ULIRGs host given their heavy dust obscuration. On the other hand, it is not clear that the Hα ratio can be readily be applied to the outflow. For instance, the outflow may have a relatively larger amount of recent star formation traced by the Hα emission, but little older star formation (traced by $L_{\rm IR}$). Overall, we conclude that more powerful outflow do have higher rates of in situ star formation, although the relation might have a large scatter. In addition, as pointed out by Gallagher et al. (2019), even a weak AGN would dominate the diagnostics and

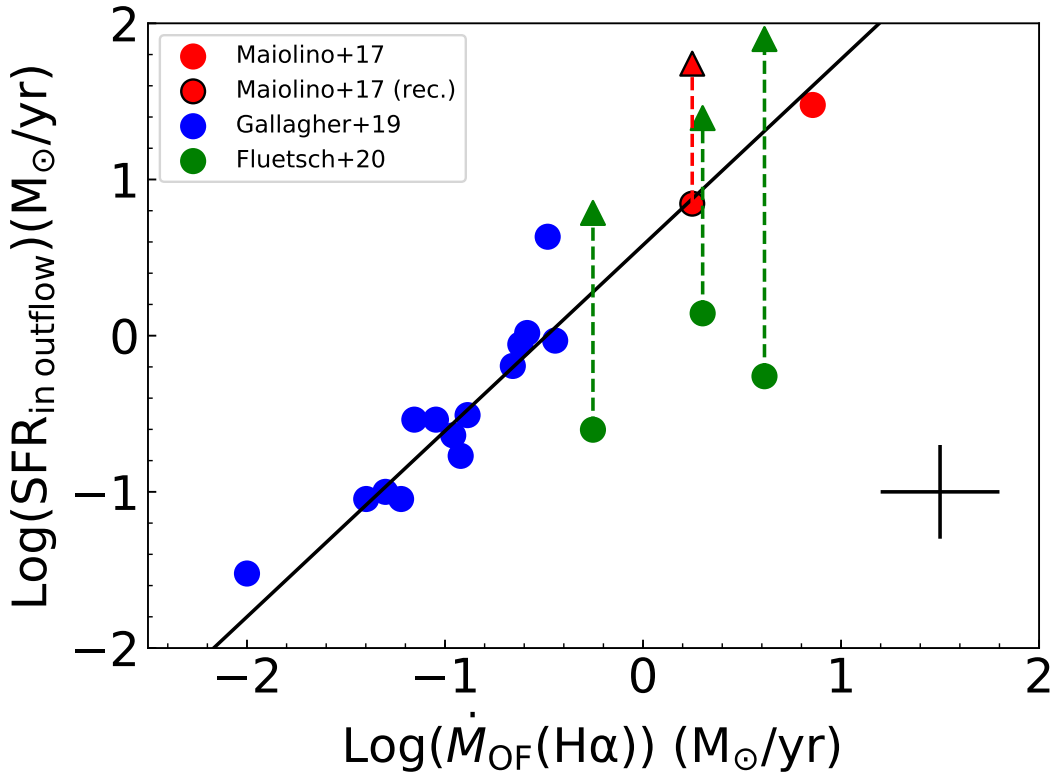

Figure 4.6: SFR inside the outflow as a function of the ionized outflow rate (calculated based on the broad Hα component). The blue data points are from Gallagher et al. (2019), the red data point without a black contour from Maiolino et al. (2017) and the green data points from this work. The red data point with a black contour is the same galaxy as in Maiolino et al. (2017), but recalculated using the method and assumptions used in this paper. The triangles represent the data points from this sample where the SFR was calculated using the galaxy's infrared rather than its Hα luminosity. The black line is the fit to the MaNGA galaxies in Gallagher et al. (2019).

by only using the SF-classified spaxels in the calculation, we likely underestimate the true SFR.

One potential concern with this figure is that both the x- and the y-axis are calculated based on the flux of the broad Hα flux and this may induce a spurious correlation. To address this issue, we also computed the outflow rate using the broad [OIII] line. This is shown in Fig. 4.7, where we plot the star formation rate versus the outflow rate calculated based on flux of the broad [OIII] line. The IR-derived SFRs are shown as triangles, while the Hα-based SFRs are represented by circles. Overall, the result is the same as for the Hα-derived outflow rates, but there is a larger scatter.

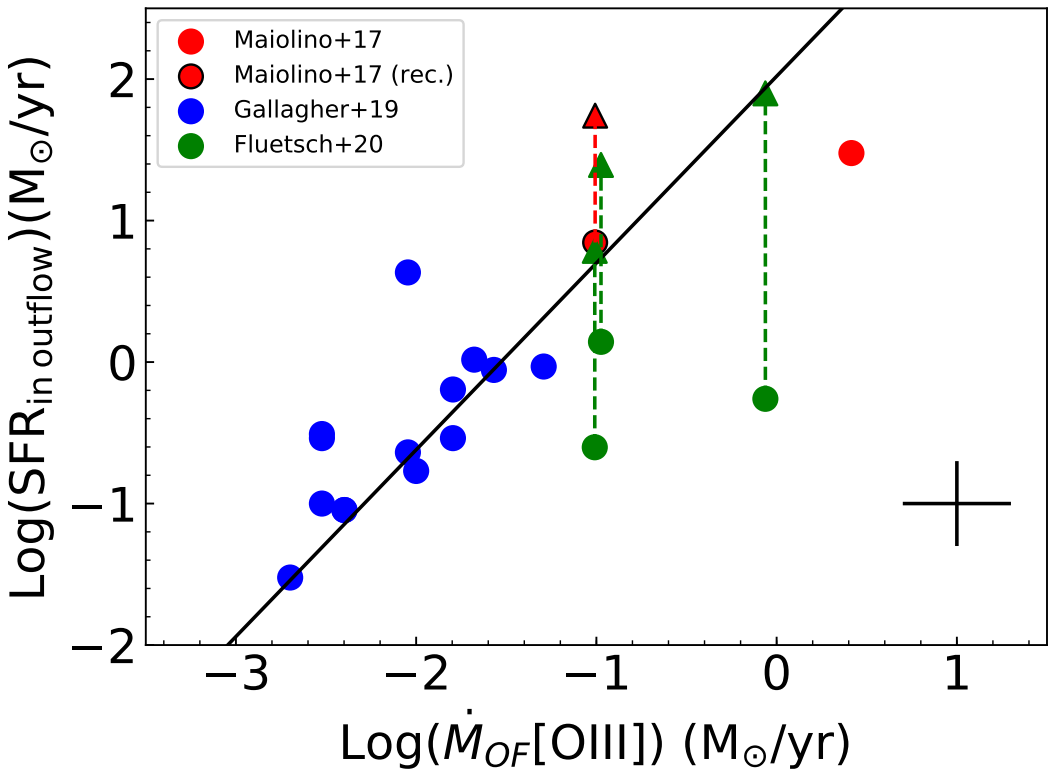

Figure 4.7: SFR inside the outflow as a function of the ionized outflow rate (calculated based on the broad [OIII] component). The blue data points are from Gallagher et al. (2019), the red data point without a black contour from Maiolino et al. (2017) and the green data points from this work. The red data point with a black contour is the same galaxy as in Maiolino et al. (2017), but recalculated using the method and assumptions used in this paper. The triangles represent the data points from this sample where the SFR was calculated using the galaxy's infrared luminosity. The black line is the fit to the MaNGA galaxies in Gallagher et al. (2019).

4.4 Dependence of Outflow Properties on Their BPT Classification

In this section, we investigate, how outflow properties vary based on the galaxy's position in the [NII]- and [SII]-BPT diagram.

We first focus on the ionized gas outflow phase. We study how the dynamical time-scales differs between SF- and AGN-driven outflows. It is important to investigate this quantity as it quantifies the impact of outflows on the evolutionary time-scales of galaxies, both in terms of halo heating and also ejection of gas that can temporarily suppress star formation but also provide a reservoir of gas in the halo. This can then later be re-accreted (if cold enough) for subsequent star formation. The dynamical time, $\tau_{\rm OF}$, is defined as the time the ionized outflow

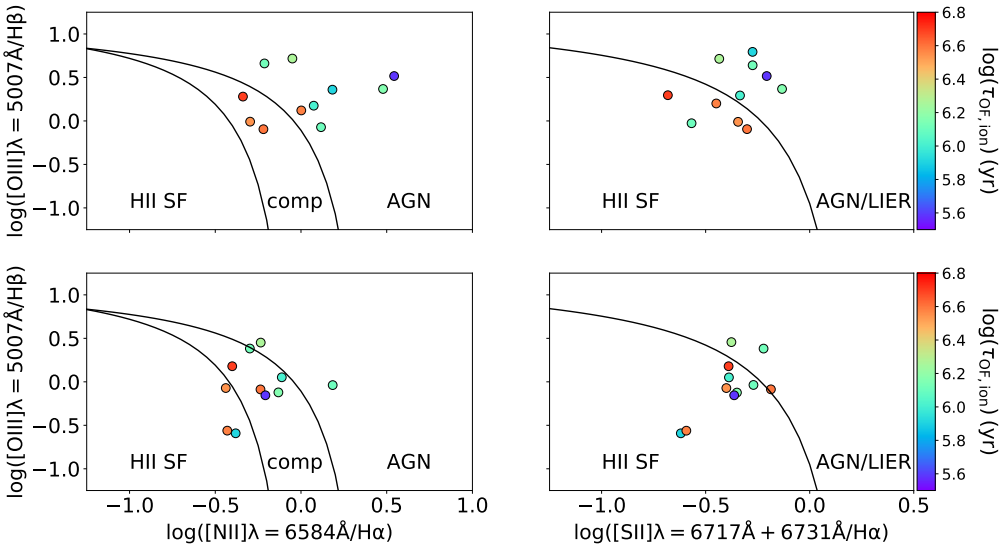

Figure 4.8: [NII]- and [SII]-BPT diagram for the median spaxel of the host (top panel) and outflow (bottom panel) of the ULIRGs with outflows in our sample. The data points are colour-coded by the dynamical time-scale of their ionized outflow, $\tau_{\mathrm{OF,ion}}$.

needs to reach the distance r_{OF} from its centre assuming a constant outflow velocity, v_{OF}.

In Fig. 4.8, we show the [NII]-(left) and [SII]-(right) BPT diagrams for the disc (top panels) and the outflow (bottom panels). The data points are colour-coded by the dynamical times of their outflows (in yrs). The [NII]-BPT diagrams suggest that outflows driven by star formation or composite have larger dynamical times than AGN-driven outflows. The difference is about a factor of 3. That means AGN-driven outflows are capable of affecting the gas reservoir at shorter time-scales than outflows powered by star formation. This difference in dynamical time-scales is due to both, different velocities in AGN- and SF-driven winds and different extents. Overall, SF-driven outflows (especially if the disc is classified as SF) seem to be more extended compared to AGN-driven outflows. The radii of SF-driven outflows are on average 2 kpc, compared to 1 kpc looking at the narrow component. The radii according to the broad component classification are comparable. This difference in the host is possibly because the driving sources (stellar winds and SNe) are distributed across the whole disc. AGN-driven outflows are slightly faster than SF-driven outflows. As expected by models (e.g. Zubovas & King 2012) and simulations (e.g. Costa et al. 2015), AGN-driven outflows can reach velocities in excess of 1000 km s^{-1}, whereas SF-driven outflows typically only reach a few hundred km s^{-1}.

We also investigate whether mass outflow rate, kinetic power or mass loading factor depends on the disc's or galaxy's position in the BPT diagram, but we found no clear trends. This might

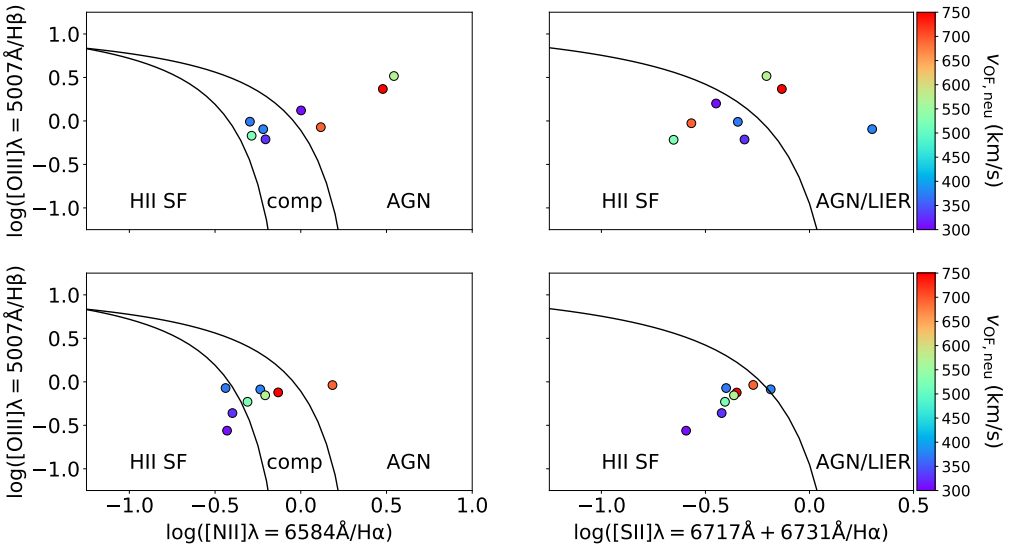

Figure 4.9: [NII]- and [SII]-BPT diagram for the median spaxel of the host (top panel) and outflow (bottom panel) of the ULIRGs with outflows in our sample. The data points are colour-coded by the neutral atomic outflow velocity, $v_{\mathrm{OF,neu}}$.

also be due to the small sample and does not necessarily rule out a physical difference.

Next, we study how the properties of the neutral atomic outflow vary with their position in the BPT-diagrams. We find high-velocity outflows in the AGN regions of the BPT diagrams as well as in the star forming part. This is shown in Fig. 4.9, where we show the [NII]- and [SII]-BPT diagrams, colour-coded by their neutral outflow velocity. The mass-loading factors of star forming and AGN-driven outflows are shown in Fig. 4.10. In this figure, the [NII]- and [SII]-BPT diagrams are displayed and the data points are colour-coded by the neutral mass loading factor ($\eta_{\mathrm{neu}} = \dot{M}_{\mathrm{OF,neu}}/\mathrm{SFR}$). Galaxies, where the outflow rates approach the current SFR (and most likely even exceed it if we take into account the contribution from the molecular and ionized phases), can be found both in the star forming part and in the AGN part of the diagram.

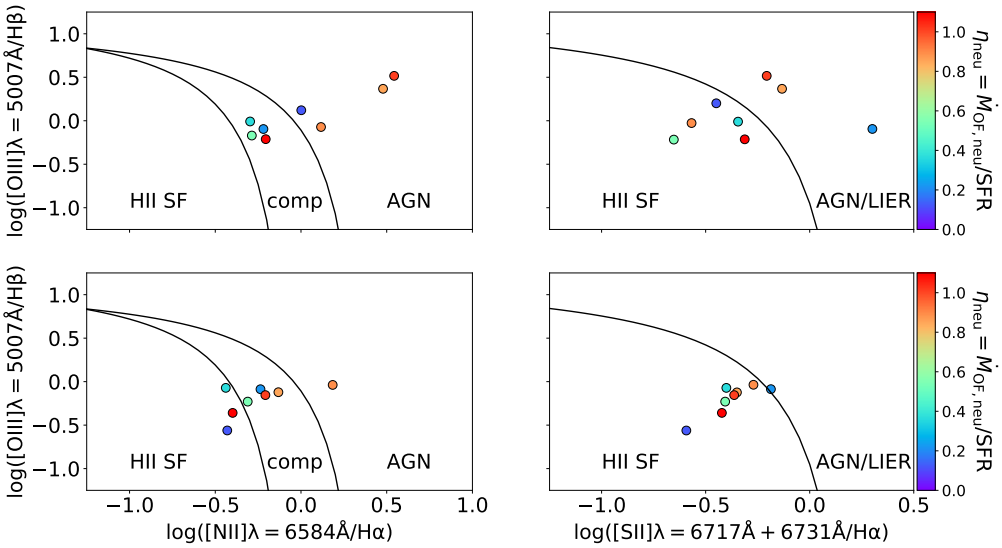

Figure 4.10: [NII]- and [SII]-BPT diagram for the median spaxel of the host (top panel) and outflow (bottom panel) of the ULIRGs with outflows in our sample. The data points are colour-coded by the neutral mass loading factor (for which we used the total IR-derived SFR of the galaxy).

4.5 Conclusions

In this chapter we investigated a sample of 26 galaxies, 12 of which have an ionized outflow and 11 a neutral atomic outflow. We investigated the prevalence of positive feedback in these outflows and analysed how outflow properties depend on the BPT classification of their (U)LIRGs hosts and their outflows. We obtain the following results:

- Out of our 12 galaxies, four galaxies show signs of star formation in their outflows. This is a fraction similar to what was found by Gallagher et al. (2019) (30 %) for a sample of outflows in lower luminosity galaxies probed by the MaNGA survey.
- The gas in these outflows is characterised by SF-like diagnostics and has ionization parameters similar or higher than normal star forming regions. Together with the enhanced gas density in the outflows, this strongly favours the scenario, in which the gas is photoionized by star formation inside the outflows, and rules out external photoionization from stars in the disc.
- The star formation rates inside the galactic winds are likely correlated with their ionized outflow rate. However, this relation might have a large scatter.
- The ionized dynamical time-scale is shorter for AGN-driven outflows ($\sim 10^6$ yr) than for star formation-driven ones ($\sim 10^{6.5-7}$ yr).
- The neutral loading factor approaches or even exceeds unity in AGN-powered objects, whereas in SF-driven outflows it is mostly below 1.

4.6 BPT Diagrams of Galaxies Without Positive Feedback

In the following, we present the BPT-diagrams of all other galaxies in our sample without signs of positive feedback.

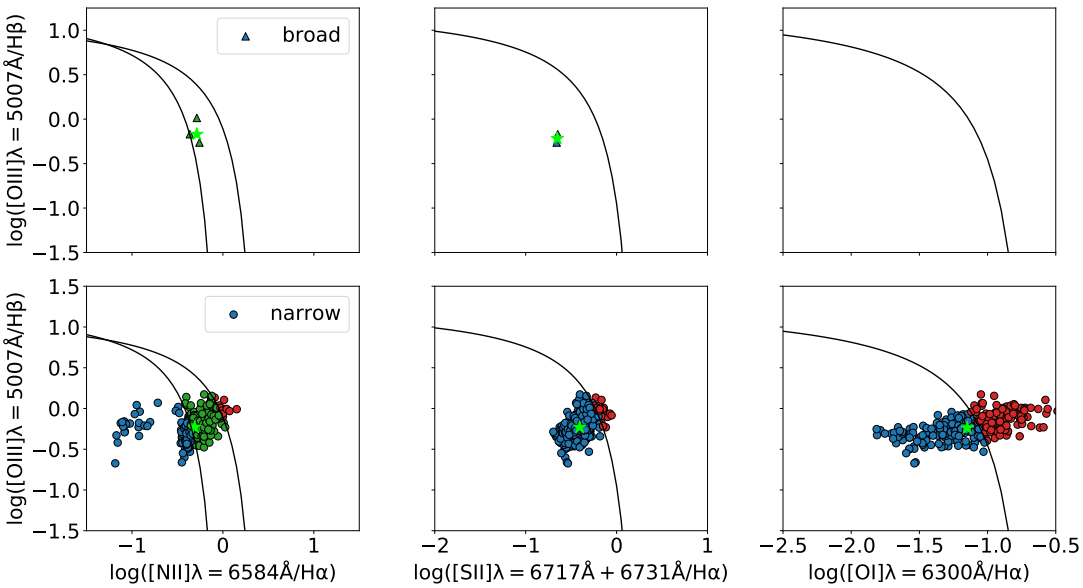

Figure 4.11: BPT diagrams of IRAS 17207, see caption of 4.2

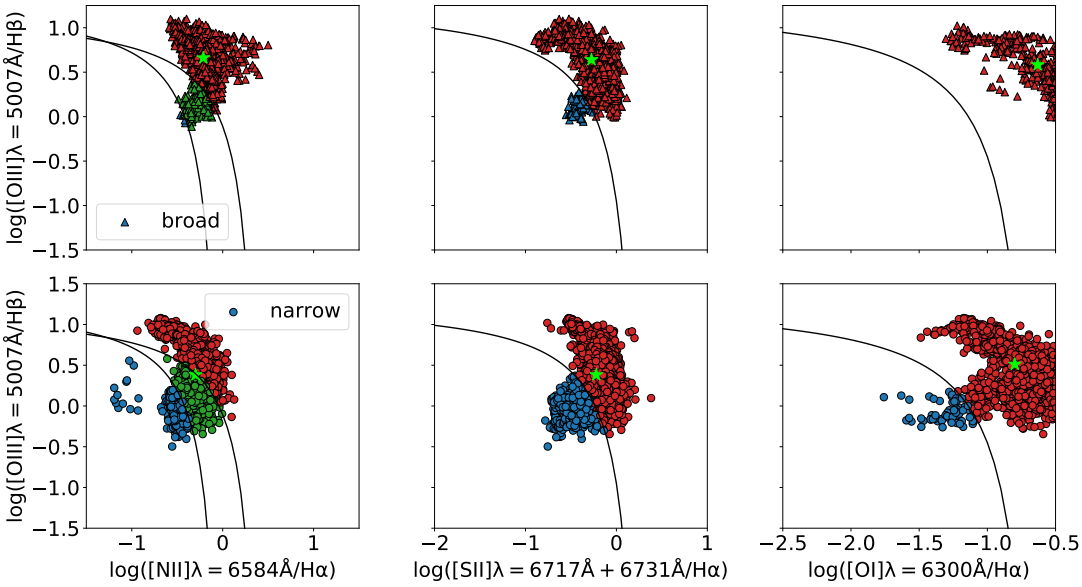

Figure 4.12: BPT diagrams of Mrk 463, see caption of 4.2

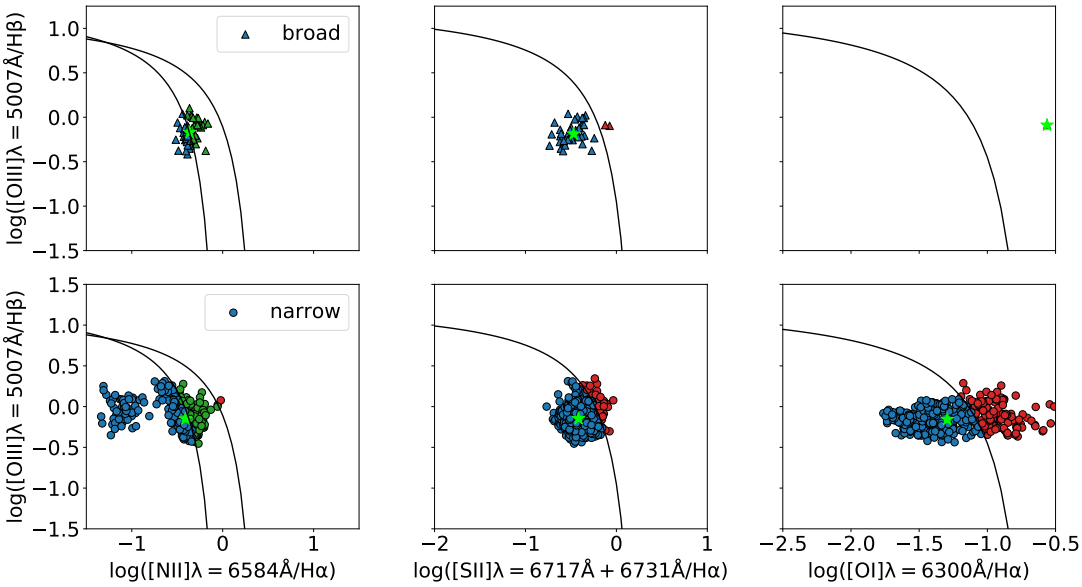

Figure 4.13: BPT diagrams of IRAS 22491, see caption of 4.2

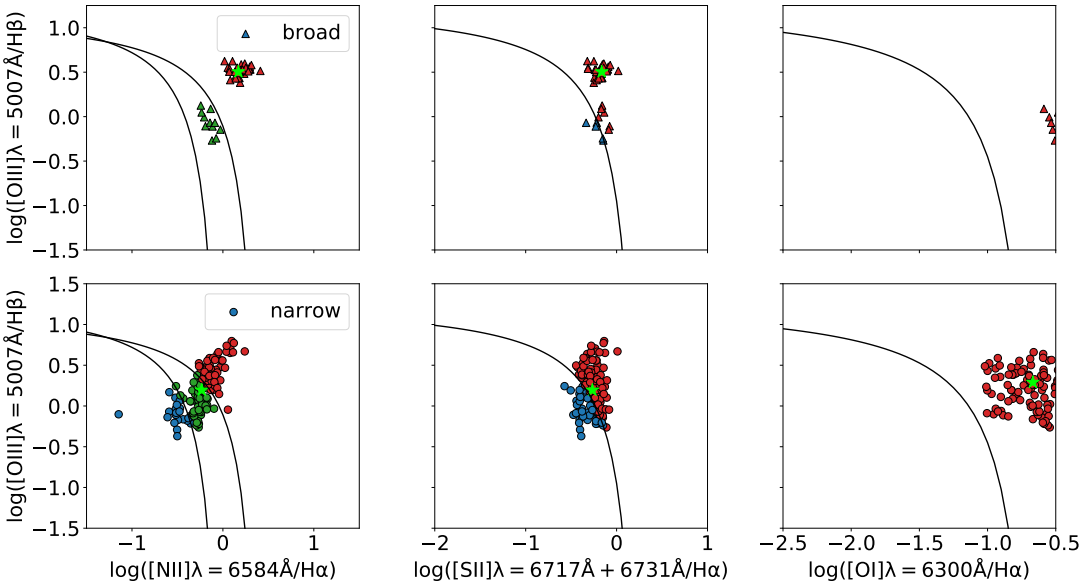

Figure 4.14: BPT diagrams of IRAS 23389, see caption of 4.2

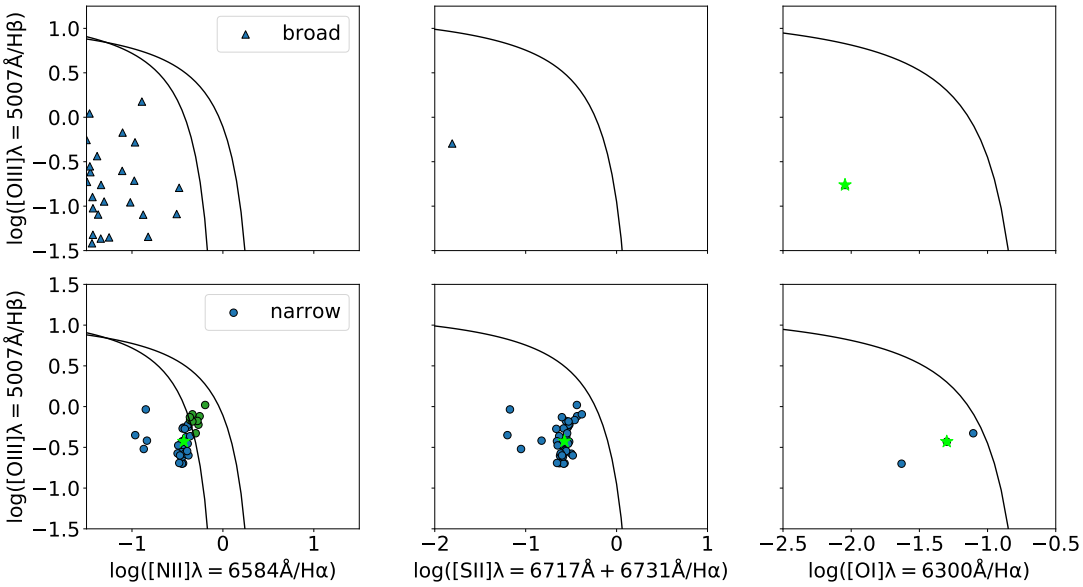

Figure 4.15: BPT diagrams of IRAS 00509, see caption of 4.2

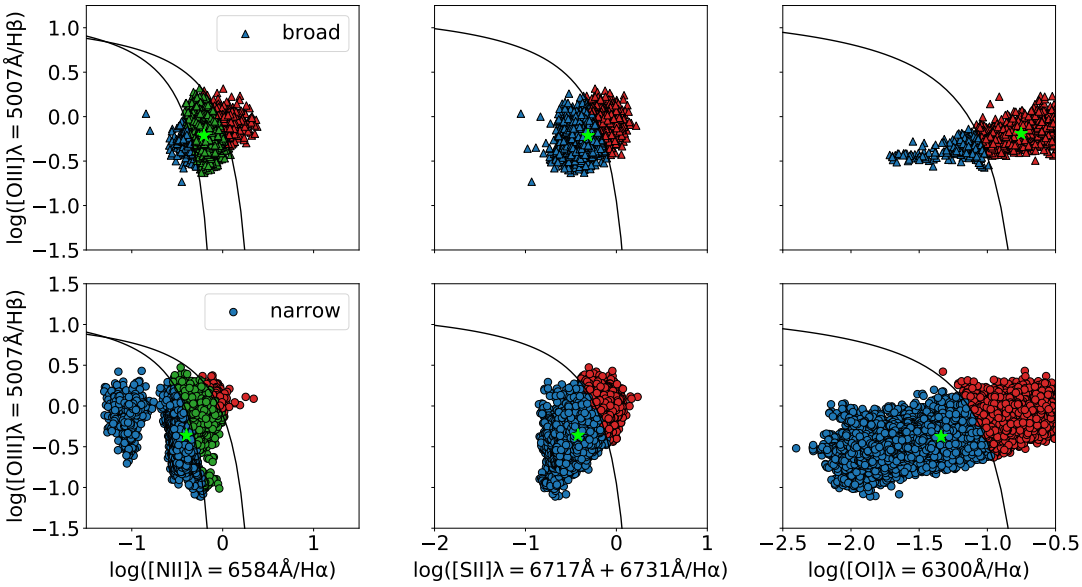

Figure 4.16: BPT diagrams of IRAS 10257, see caption of 4.2

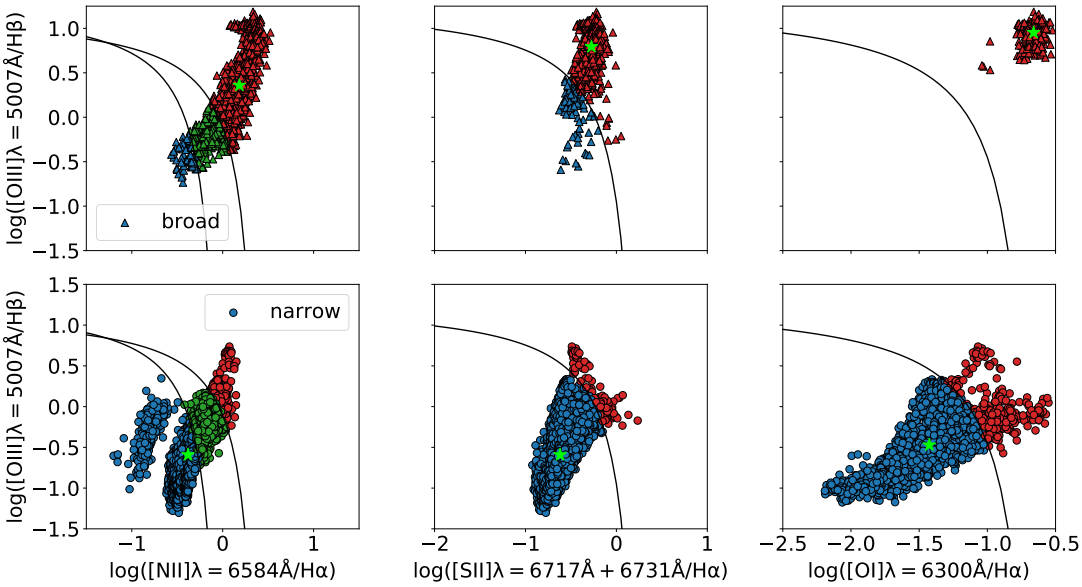

Figure 4.17: BPT diagrams of IRAS 21453, see caption of 4.2

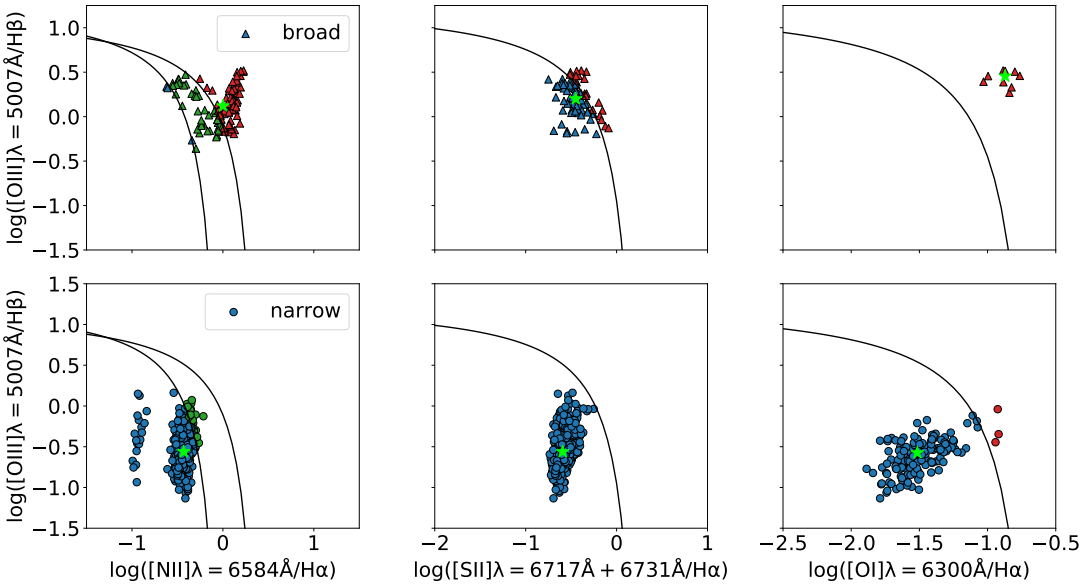

Figure 4.18: BPT diagrams of IRAS 15115, see caption of 4.2

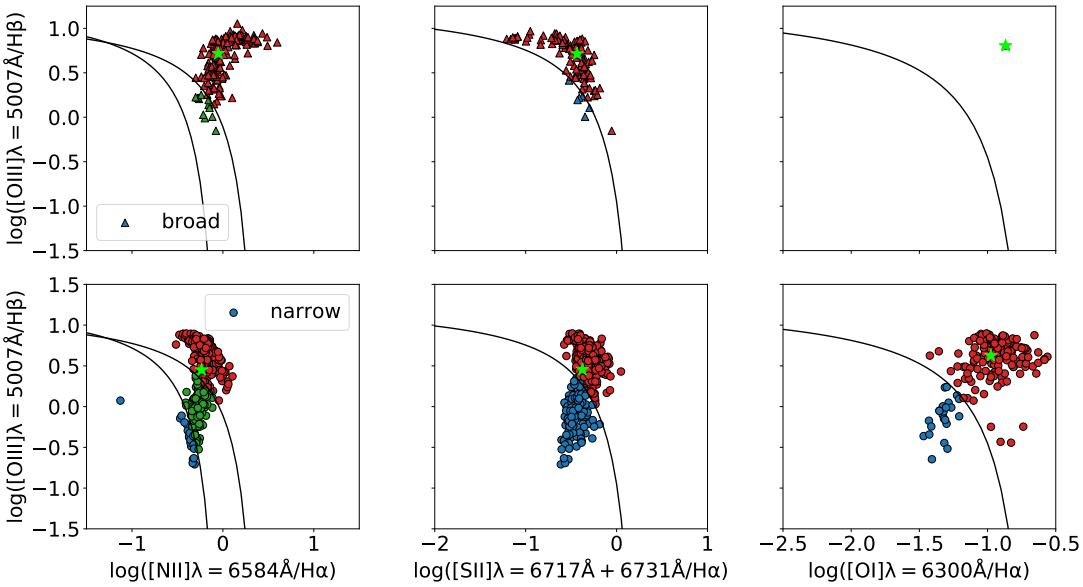

Figure 4.19: BPT diagrams of IRAS 23060, see caption of 4.2

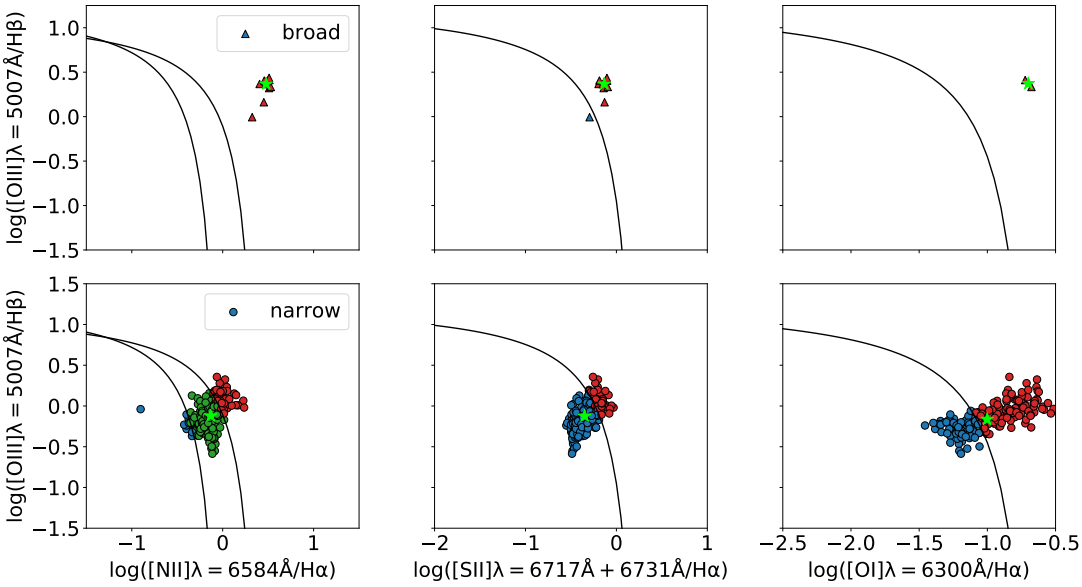

Figure 4.20: BPT diagrams of IRAS 14378, see caption of 4.2

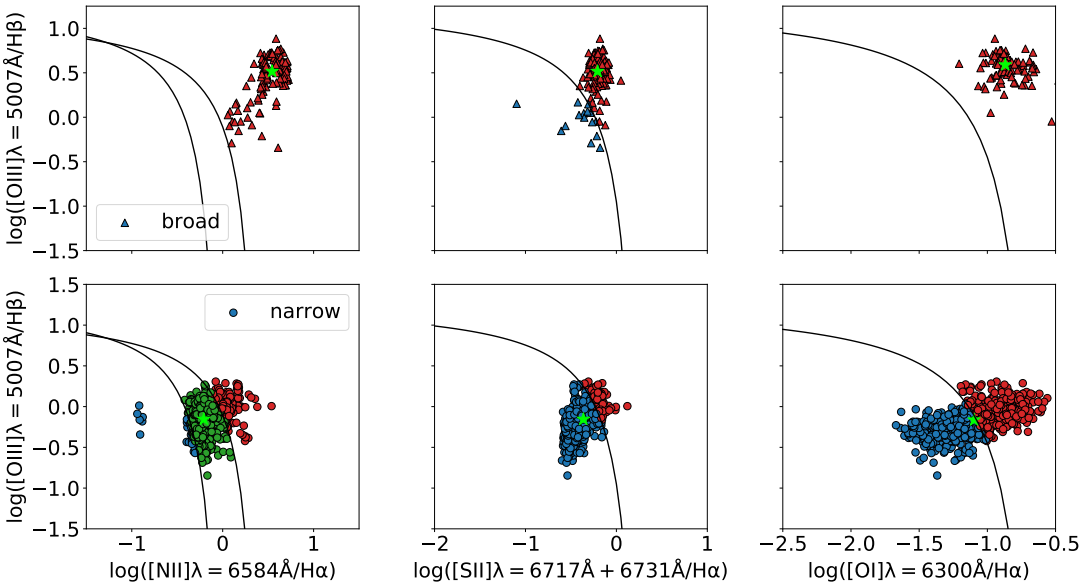

Figure 4.21: BPT diagrams of IRAS 13120, see caption of 4.2

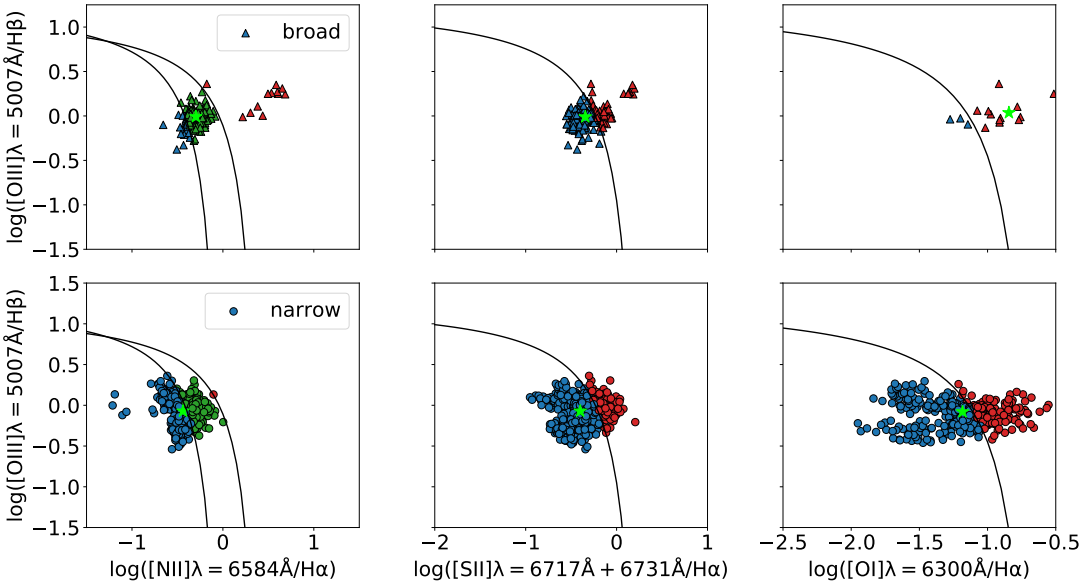

Figure 4.22: BPT diagrams of IRAS 20100, see caption of 4.2

Chapter 5

Conclusions and Future Work

This thesis aims at understanding galactic outflows, which are considered an important pathway for how galaxies regulate and halt their star formation. Indeed, through the injection of momentum and energy into the ISM, outflows are expected to expel large amounts of gas out of the galaxy and hence regulate or completely suppress future star formation. We have studied outflows in this thesis using a multi-wavelength approach, combining MUSE data to trace the neutral atomic and ionized gas phases with millimetre observations with ALMA probing the molecular gas phase. This has allowed us to investigate how outflows properties depend on their host galaxy's physical properties and what are the driving mechanisms of galactic winds. Owing to the multiphase approach, we were able to obtain a more comprehensive view of outflows, and ultimately also of their feedback effect on their host galaxies. Below we list the primary conclusions from this thesis.

5.1 Conclusions

5.1.1 Driving Mechanism

One open issue in the field of galactic outflows is which theoretical model best describes outflows. Three main modes have been proposed: energy-driven, momentum-driven and driven by direct radiation pressure on the dusty clouds in the ISM. Based on our observations of almost 50 local galaxies with outflowing gas presented in Chapter 2, outflows are less powerful than previous studies indicated. Most AGN-driven outflows have kinetic powers ranging from

0.1–5 % $L_{\rm AGN}$ and lie mostly below the theoretical expectation for an energy-driven outflow (assuming a 100 % coupling). Therefore, if these outflows are energy-driven, they must have poor coupling with the ISM, as indeed suggested by some detailed zoom-in simulations (e.g. Costa et al. 2015; Roos et al. 2015). Alternatively, the properties of galactic outflows are consistent with the direct radiation pressure-driven mode as suggested by e.g. Fabian (2012) and Ishibashi et al. (2018). In this mode, the AGN radiation acts directly on dust grains in molecular clouds and, given efficient coupling between dust and gas, transfers momentum on the molecular clouds.

On the other hand, star forming galaxies have outflows which seem consistent with the momentum-driven scenario. However, momentum-driven outflows are known to have little effect and to develop only on scales of a few 100 pc, hence they certainly cannot explain the outflows observed extending up to kpc scales.

There are also a few galaxies (in our sample about 10 %) whose kinetic power, momentum rate and velocity exceed expectations of any model, both for AGN- and starburst-driven winds. These are likely because they are 'fossil outflows' which were powered by an AGN which has now switched off or significantly faded.

5.1.2 Quenching Potential of Outflows

Quenching of star formation is a complex mechanism, however, there is growing evidence that black holes play an important role in this process (see Chapter 1). Many AGN hosts have shown signatures of outflowing gas, but so far we have been missing smoking gun evidence for the fact that it is indeed outflows which suppress star formation. In Chapter 2 we have quantified the effect of molecular outflows on the ISM of their host based on a) whether they are able to escape the galaxy, and b) how quickly they cause the depletion of the galaxy's molecular gas reservoir. We have found that only a small fraction (usually less than 5 %) of the outflow escapes the galaxy (and even less gas escapes the halo). Regarding the depletion time-scale, outflows are expected to clear the total gas reservoir (including the atomic component) on time-scales of the order of 10^8 yr. Although some objects with high AGN luminosities have shorter depletion time-scales, the depletion time-scales are generally longer that the typical AGN lifetime. Both pieces of evidence as well as their low coupling efficiency with the ISM, suggest that, while this ejective mode is effective in rapidly removing gas from the central region, it is unlikely to quickly suppress star formation across the entire galaxy. However, outflows may have an important delayed quenching effect (Cresci & Maiolino 2018). They can heat the halo and therefore suppress cold accretion of gas onto the galaxy which results in a delayed suppression of star formation by starvation (e.g. Peng et al. 2015; Trussler et al. 2020)

5.1.3 Multiphase Nature of Outflows

Several detailed observations of local galaxies have highlighted the multiphase nature of outflows. In Chapter 3 we have established the relative importance of the molecular, the ionized and the neutral atomic phase, by combining MUSE data with sub-millimetre observations from ALMA. The molecular phase was found to be dominant in terms of mass outflow rate and kinetic power, accounting for more than 50 % of the total mass outflow rate and kinetic power in most objects. The ionized component, on the other hand, is almost negligible, but it is more important in star forming galaxies. However, even in these objects, it contributes at most a few per cent. Even though there are very large uncertainties, the ionized contribution is unlikely to be much larger given the high electron densities found using different methods (which further reduce the estimated outflow rates). Therefore it is impossible to use the existing studies of large samples of ionized outflows as a comparison to predictions from theory or simulations. The neutral atomic component can be of the order of 10 % and is sometimes almost as prominent as the molecular component. The molecular component is equally important in objects with high AGN luminosity or might even increase relative to the ionized and neutral atomic components, possibly due to gas compression in the high AGN luminosity objects.

Based on our analysis of MUSE observations presented in Chapter 3 we have also established that in many galaxies the ionized and the neutral atomic gas outflow phases are co-spatial and share certain kinematic features, such as correlated velocities, which indicates that these two phases are linked in some objects.

5.1.4 Physical Conditions of Ionized Outflows

To characterise outflows in greater detail it is important to determine their physical conditions. In Chapter 3, we studied the electron density using the [SII] doublet in (U)LIRGs hosts and their outflows and found that the average electron density is more than three times higher in the outflow than in the disc ($< n_{\rm e,outflow} >$ = 500 cm^{-3} vs $< n_{\rm e,disc} >$ = 150 cm^{-3}). This suggests that cloud compression is more important than cloud dissipation in most outflows. This in turn would also explain the enhanced HCN/CO ratio in some molecular outflows (Aalto et al. 2015; Walter et al. 2017). However, a small number of star forming galaxies have similar densities in the disc and the outflow.

The outflows studied here are also characterised by lower dust extinction than the disc. Furthermore, we found that the difference in dust extinction between the outflow and the disc correlates with the ionized gas outflow mass, which hints at the fact that the most massive outflows are associated with the expulsion of dusty clouds.

5.1.5 Positive Feedback in (U)LIRGs

There are a number of galaxies which show signs of enhanced star formation associated with outflows. Overall, the evidence is sparse and it is unclear what role positive feedback plays in the evolution of galaxies. In this thesis, in Chapter 4, we have shown that around 30 % of (U)LIRGs with outflows show signs of star formation inside their outflows based on their BPT diagrams and the analysis of the ionization parameter in the disc and the outflow. This highlights their frequent occurrence, even though the first detection by Maiolino et al. (2017) is unique in its strength. In addition, we confirm the result of previous studies that more powerful outflows have higher in situ star formation rates, although with large scatter. The presence of star formation inside galactic outflows may contribute significantly to the formation of the spheroidal component of galaxies.

5.2 Future Work

Although we presented the largest study of molecular gas outflows using carbon monoxide in Chapter 2, the sample studied here still suffers from selection biases. In this thesis as well as other molecular outflow studies, there has been a clear focus on unusual or extreme objects, such as quasars, ULIRGs or powerful starbursts, which are more likely to host massive and fast outflows (Faucher-Giguère & Quataert 2012; Bischetti et al. 2017). While for the ionized or neutral atomic outflow phase, we do have large-scale studies of normal star forming galaxies (Cicone et al. 2016; Concas et al. 2017, 2019), a comparable extensive study of the molecular outflow phase is missing. As a result, it is still difficult to assess to what degree outflows affect the evolution of a typical (main-sequence) galaxy, especially because the molecular phase likely dominates the total mass and energy budget of the outflow (see Chapter 3). A natural next steps would therefore be to study molecular outflows in an unbiased sample of galaxies in the local Universe. Ideally, we would focus on objects with available information about the ionized and/or the neutral atomic outflows for instance from the SDSS or the MaNGA survey, so as to obtain a multiphase view of these outflows. In principle, such a study can be carried out using current facilities, such as ALMA or the Northern Extended Millimetre Array (NOEMA).

In recent years, outflow studies went from focusing on single galaxies to including dozens of objects with spatially resolved information (like this thesis) or even tens of thousands (e.g. Concas et al. 2017; Roberts-Borsani & Saintonge 2019). Some works, including this thesis, have studied outflows combining information from different gas phases to obtain a more complete picture of outflows and allow detailed comparisons to simulations. Almost all of these multiphase outflow studies, however, have focused on the local Universe. Yet, negative feedback and hence quenching of galaxies is expected to be most prominent at $z > 1$ when

black holes grow more rapidly and star formation activity peaks (Shankar et al. 2009; Madau & Dickinson 2014; Heckman & Best 2014). In addition, the quenching mechanism needs to be able to explain the large fraction of passive galaxies already present at $z > 2$ (e.g. Cimatti et al. 2004; Straatman et al. 2014). Some studies targeted high-z objects, using for instance the [CII] emission line to study the atomic phase (Bischetti et al. 2019b) or the [OIII] line to study the ionized gas phase (Harrison et al. 2016). Yet, apart from very few examples (see Chapter 3), little is known about the physical properties and relative importance of different gas phases in these outflows at higher redshifts. Thus, a fair comparison to models of galactic winds and an evaluation of the quenching potential of these high-redshift outflows remains difficult. An additional difficulty is that we use different tracers (e.g. CO(J = 1–0) for local galaxies vs [CII] or high-J CO lines for high-redshift objects) and/or instruments (spatially resolved IFU vs integrated measurements or IFU with very low angular resolution) for low- and high-redshift sources which makes it challenging to assess how outflows shape galaxy evolution across cosmic times. Current facilities such as NOEMA and ALMA already allow us to probe the cold component at higher redshift by observing higher-J CO or [CII] transitions, but significant time is required. Further advancements will be possible with the Next Generation Very Large Array (ngVLA), which offers a ten times better sensitivity than ALMA and thirty times longer baselines which allow milliarcsecond resolution (Selina et al. 2018). ngVLA will be able to probe low-J CO transitions at higher redshifts. Ionized outflows at higher redshifts have already been investigated using KMOS (e.g. Förster Schreiber et al. 2019) or SINFONI (e.g. Carniani et al. 2015; Kakkad et al. 2016) at the VLT. In addition, the James Webb Space Telescope will enable us to probe the warm molecular phase (through near-IR ro-vibrational and rotational H_2 lines) in outflows, which according to some models may account for the bulk of the total outflow mass (Richings & Faucher-Giguère 2018). Future studies will not only enable the detection of high-z galaxies with outflows, but also the comprehensive, multiphase study of these outflows. Some efforts to study multiphase outflows at higher redshifts are already under way such as the SUPER-ALMA programme, which combines SINFONI near-IR IFU spectra with CO(3–2) observations from ALMA for AGN hosts at $z \sim 2$.

In Chapter 4 we have provided further evidence for positive feedback occurring in galactic winds. Although there is now a large amount of evidence for positive feedback in some outflows using various diagnostics (e.g. BPT- and NIR-diagnostics), ultimately direct signatures of young hot stars inside outflows are needed to confirm the existence of positive feedback. The next step will therefore be to use stellar features of OB stars such as the CIII] 1176 Å line and investigate whether they are blueshifted (and hence are formed in outflowing gas). First efforts are already under way by Belfiore et al. (in prep) and by Loiacono et al. (in prep) who use stellar features in Hubble Space Telescope-Cosmic Origins Spectrograph (HST-COS) spectra to find

direct evidence of OB stars being formed in outflows. The Large Ultraviolet/Optical/Infrared Surveyor (LUVOIR) will offer order of magnitude better sensitivity and a several times better resolution than HST-COS and will even enable the detection of even very small amounts of star formation in galactic outflows.

In this thesis, we have looked into molecular outflows and star formation taking place inside them. The missing link between the two is the study of the dense gas phase in the outflow as star formation takes place in the dense cores of molecular clouds. In a few individual objects, dense gas tracers such as HCN, HCO^+ or CS have been studied (e.g. Aalto et al. 2015; Michiyama et al. 2018). Yet, it is unclear whether most molecular outflows host very dense gas and hence are potentially suitable for star formation. Interferometric observations of the distribution of dense gas tracers could also help understand long-standing questions such as whether molecules in outflows are formed in situ or whether the molecular gas was entrained in the ISM expelled from the galaxy. Therefore a large study of dense gas tracers with ALMA could advance our standing tremendously, from purely detecting outflows to characterising them in detail and understanding the physics behind them.

Bibliography

Aalto S., Garcia-Burillo S., Muller S., Winters J., van der Werf P., Henkel C., Costagliola F., Neri R., 2012, Astronomy and Astrophysics, 537, A44

Aalto S., et al., 2015, Astronomy and Astrophysics, 574, A85

Aird J., Coil A., Georgakakis A., Nandra K., Barro G., Pérez-González P., 2015, Monthly Notices of the Royal Astronomical Society, 451, 1892

Allen M. G., Groves B. A., Dopita M. A., Sutherland R. S., Kewley L. J., 2008, The Astrophysical Journal Supplement Series, 178, 20

Alonso-Herrero A., et al., 2011, The Astrophysical Journal, 736, 82

Alonso-Herrero A., et al., 2018, The Astrophysical Journal, 859, 144

Andrae R., Schulze-Hartung T., Melchior P., 2010, arXiv e-prints, p. arXiv:1012.3754

Antonucci R., 1993, Annual Review of Astronomy and Astrophysics, 31, 473

Arribas S., Colina L., Bellocchi E., Maiolino R., Villar-Martin M., 2014, Astronomy and Astrophysics, 568, A14

Bacon R., et al., 2001, Monthly Notices of the Royal Astronomical Society, 326, 23

Bacon R., et al., 2015, Astronomy and Astrophysics, 575, A75

Baldry I. K., Glazebrook K., Brinkmann J., Ivezić Ž., Lupton R. H., Nichol R. C., Szalay A. S., 2004, The Astrophysical Journal, 600, 681

Baldry I., Balogh M., Bower R., Glazebrook K., Nichol R., Bamford S., Budavari T., 2006, Monthly Notices of the Royal Astronomical Society, 373, 469

Baldwin J., Phillips M., Terlevich R., 1981, Publications of the Astronomical Society of the Pacific, 93, 5

Bamford S. P., et al., 2009, Monthly Notices of the Royal Astronomical Society, 393, 1324

Bardeen J. M., Steinhardt P. J., Turner M. S., 1983, Physical Review D, 28, 679

Barger A., Cowie L., Mushotzky R., Yang Y., Wang W. H., Steffen A., Capak P., 2005, The Astronomical Journal, 129, 578

Belfiore F., et al., 2016, Monthly Notices of the Royal Astronomical Society, 461, 3111

Bell E. F., de Jong R. S., 2001, The Astrophysical Journal, 550, 212

Bell E. F., McIntosh D. H., Katz N., Weinberg M. D., 2003, The Astrophysical Journal

Supplement Series, 149, 289

Bellocchi E., Arribas S., Colina L., Miralles-Caballero D., 2013, Astronomy & Astrophysics, 557, A59

Best P., Kauffmann G., Heckman T., Brinchmann J., Charlot S., Ivezić Ž., White S., 2005, Monthly Notices of the Royal Astronomical Society, 362, 25

Bieri R., Dubois Y., Rosdahl J., Wagner A., Silk J., Mamon G. A., 2017, Monthly Notices of the Royal Astronomical Society, 464, 1854

Biernacki P., Teyssier R., 2018, Monthly Notices of the Royal Astronomical Society, 475, 5688

Binney J., 1977, The Astrophysical Journal, 215, 483

Bischetti M., et al., 2017, Astronomy and Astrophysics, 598, A122

Bischetti M., et al., 2019a, Astronomy & Astrophysics, 628, A118

Bischetti M., Maiolino R., Carniani S., Fiore F., Piconcelli E., Fluetsch A., 2019b, Astronomy & Astrophysics, 630, A59

Bolatto A. D., Wolfire M., Leroy A. K., 2013, Annual Review of Astronomy and Astrophysics, 51, 207

Bourne M. A., Nayakshin S., Hobbs A., 2014, Monthly Notices of the Royal Astronomical Society, 441, 3055

Bourne M. A., Zubovas K., Nayakshin S., 2015, Monthly Notices of the Royal Astronomical Society, 453, 1829

Bower R., Benson A., Crain R. A., 2012, Monthly Notices of the Royal Astronomical Society, 422, 2816

Brammer G., et al., 2009, The Astrophysical Journal Letters, 706, L173

Brammer G. B., et al., 2011, The Astrophysical Journal, 739, 24

Briggs D. S., Schwab F. R., Sramek R. A., 1999, in Taylor G., Carilli C., Perley R., eds, Astronomical Society of the Pacific Conference Series Vol. 180, Synthesis Imaging in Radio Astronomy II. p. 127

Brusa M., et al., 2015, Monthly Notices of the Royal Astronomical Society, 446, 2394

Brusa M., et al., 2016, Astronomy & Astrophysics, 588, A58

Brusa M., et al., 2018, Astronomy & Astrophysics, 612, A29

Bundy K., et al., 2015, The Astrophysical Journal, 798, 7

Burbidge E. M., Burbidge G., Fowler W. A., Hoyle F., 1957, Reviews of Modern Physics, 29, 547

Burtscher L., et al., 2015, Astronomy & Astrophysics, 578, A47

Calzetti D., 2001, Publications of the Astronomical Society of the Pacific, 113, 1449

Calzetti D., Armus L., Bohlin R. C., Kinney A. L., Koornneef J., Storchi-Bergmann T., 2000, The Astrophysical Journal, 533, 682

Cano-Diaz M., et al., 2012, Astronomy & Astrophysics, 537, L8

Cappellari M., 2017, Monthly Notices of the Royal Astronomical Society, 466, 798

Cappellari M., Copin Y., 2003, Monthly Notices of the Royal Astronomical Society

Cappellari M., Emsellem E., 2004, Publications of the Astronomical Society of the Pacific, 116, 138

Carniani S., et al., 2015, arXiv.org, 1506, 3096

Carniani S., et al., 2016, Astronomy & Astrophysics, 591, A28

Cazzoli S., Arribas S., Maiolino R., Colina L., 2016, Astronomy and Astrophysics, 590, A125

Chisholm J., Tremonti C. A., Leitherer C., Chen Y., 2017, Monthly Notices of the Royal Astronomical Society, 469, 4831

Churazov E., Sazonov S., Sunyaev R., Forman W., Jones C., Böhringer H., 2005, Monthly Notices of the Royal Astronomical Society, 363, L91

Cicone C., et al., 2014, Astronomy & Astrophysics, 562, A21

Cicone C., et al., 2015, Astronomy & Astrophysics, 574, A14

Cicone C., Maiolino R., Marconi A., 2016, Astronomy & Astrophysics, 588, A41

Cicone C., et al., 2018, The Astrophysical Journal, 863, 143

Cicone C., Maiolino R., Aalto S., Muller S., Feruglio C., 2020, Astronomy & Astrophysics, 633, A163

Cimatti A., et al., 2004, Nature, 430, 184

Colless M., et al., 2001, Monthly Notices of the Royal Astronomical Society, 328, 1039

Combes F., et al., 2013, Astronomy & Astrophysics, 558, A124

Concas A., Popesso P., Brusa M., Mainieri V., Erfanianfar G., Morselli L., 2017, Astronomy & Astrophysics, 606, A36

Concas A., Popesso P., Brusa M., Mainieri V., Thomas D., 2019, Astronomy & Astrophysics, 622, A188

Conselice C. J., Wilkinson A., Duncan K., Mortlock A., 2016, The Astrophysical Journal, 830, 83

Costa T., Sijacki D., Haehnelt M. G., 2014, Monthly Notices of the Royal Astronomical Society, 444, 2355

Costa T., Sijacki D., Haehnelt M. G., 2015, Monthly Notices of the Royal Astronomical Society: Letters, 448, L30

Costa T., Rosdahl J., Sijacki D., Haehnelt M. G., 2018a, Monthly Notices of the Royal Astronomical Society, 473, 4197

Costa T., Rosdahl J., Sijacki D., Haehnelt M. G., 2018b, Monthly Notices of the Royal Astronomical Society, 479, 2079

Cowie L. L., Songaila A., Hu E. M., Cohen J., 1996, Astronomical Journal, 112, 839

Cresci G., Maiolino R., 2018, Nature Astronomy, 2, 179

Cresci G., et al., 2015a, Astronomy & Astrophysics, 582, A63

Cresci G., et al., 2015b, The Astrophysical Journal, 799, 82

Croft S., et al., 2006, The Astrophysical Journal, 647, 1040

Dasyra K. M., Combes F., Novak G. S., Bremer M., Spinoglio L., Pereira Santaella M., Salomé P., Falgarone E., 2014, Astronomy & Astrophysics, 565, A46

Dasyra K. M., Bostrom A. C., Combes F., Vlahakis N., 2015, Astrophysical Journal, 815, 34

Dasyra K. M., Combes F., Oosterloo T., Oonk J. B. R., Morganti R., Salomé P., Vlahakis N., 2016, Astronomy & Astrophysics, 595, L7

Davé R., Oppenheimer B. D., Finlator K., 2011, Monthly Notices of the Royal Astronomical Society, 415, 11

Davies R., et al., 2020, arXiv e-prints, p. arXiv:2003.06153

Debuhr J., Quataert E., Ma C.-P., 2011, Monthly Notices of the Royal Astronomical Society, 412, 1341

Decataldo D., Pallottini A., Ferrara A., Vallini L., Gallerani S., 2019, Monthly Notices of the Royal Astronomical Society, 487, 3377

Dekel A., Birnboim Y., 2006, Monthly Notices of the Royal Astronomical Society, 368, 2

Dekel A., Silk J., 1986, The Astrophysical Journal, 303, 39

Dekel A., Sari R., Ceverino D., 2009, The Astrophysical Journal, 703, 785

Diaz A. I., Pérez-Montero E., 2000, Monthly Notices of the Royal Astronomical Society, 312, 130

Driver S., et al., 2006, Monthly Notices of the Royal Astronomical Society, 368, 414

Duffy A. R., Schaye J., Kay S. T., Vecchia C. D., 2008, Monthly Notices of the Royal Astronomical Society: Letters, 390, 1

Dugan Z., Bryan S., Gaibler V., Silk J., Haas M., 2014, The Astrophysical Journal, 796, 113

El-Badry K., Wetzel A., Geha M., Hopkins P. F., Kereš D., Chan T., Faucher-Giguère C.-A., 2016, The Astrophysical Journal, 820, 131

Elbaz D., Jahnke K., Pantin E., Le Borgne D., Letawe G., 2009, Astronomy & Astrophysics, 507, 1359

Emonts B., Piqueras-López J., Colina L., Arribas S., Villar-Martin M., Pereira-Santaella M., Garcia-Burillo S., Alonso-Herrero A., 2014, Astronomy and Astrophysics, 572, A40

Emonts B., Colina L., Piqueras-López J., Garcia-Burillo S., Pereira-Santaella M., Arribas S., Labiano A., Alonso-Herrero A., 2017, Astronomy and Astrophysics, 607, A116

Fabian A., 1999, Monthly Notices of the Royal Astronomical Society, 308, L39

Fabian A., 2012, Annual Review of Astronomy and Astrophysics, 50, 455

Fabian A. C., Vasudevan R. V., Gandhi P., 2008, Monthly Notices of the Royal Astronomical

Society: Letters, 385

Farrah D., Afonso J., Efstathiou A., Rowan-Robinson M., Fox M., Clements D., 2003, Monthly Notices of the Royal Astronomical Society, 343, 585

Fath E. A., 1909, Lick Observatory Bulletin, 149, 71

Faucher-Giguère C.-A., Quataert E., 2012, Monthly Notices of the Royal Astronomical Society, 425, 605

Ferrarese L., Ford H., 2005, Space Science Reviews, 116, 523

Feruglio C., Maiolino R., Piconcelli E., Menci N., Aussel H., Lamastra A., Fiore F., 2010, Astronomy and Astrophysics, 518, L155

Feruglio C., et al., 2015, Astronomy & Astrophysics, 583, A99

Finlator K., Davé R., 2008, Monthly Notices of the Royal Astronomical Society, 385, 2181

Finlez C., Nagar N. M., Storchi-Bergmann T., Schnorr-Müller A., Riffel R. A., Lena D., Mundell C., Elvis M. S., 2018, Monthly Notices of the Royal Astronomical Society, 479, 3892

Fiore F., et al., 2017, Astronomy and Astrophysics Astrophysics, 601, A143

Fischer J., et al., 2010, Astronomy and Astrophysics, 518, L41

Flores H., Hammer F., Elbaz D., Cesarsky C., Liang Y., Fadda D., Gruel N., 2004, Astronomy & Astrophysics, 415, 885

Fluetsch A., et al., 2019, Monthly Notices of the Royal Astronomical Society, 483, 4586

Förster Schreiber N., et al., 2019, The Astrophysical Journal, 875, 21

Franceschini A., et al., 2003, Monthly Notices of the Royal Astronomical Society, 343, 1181

Gabor J. M., Bournaud F., 2014, Monthly Notices of the Royal Astronomical Society, 441, 1615

Gaibler V., Khochfar S., Krause M., Silk J., 2012, Monthly Notices of the Royal Astronomical Society, 425, 438

Gallagher R., Maiolino R., Belfiore F., Drory N., Riffel R., Riffel R. A., 2019, Monthly Notices of the Royal Astronomical Society, 485, 3409

García-Burillo S., et al., 2015, Astronomy & Astrophysics, 580, A35

Gebhardt K., et al., 2000, The Astrophysical Journal Letters, 543, L5

Genzel R., et al., 2017, Nature, 543, 397

Geréb K., Maccagni F., Morganti R., Oosterloo T., 2015, Astronomy and Astrophysics, 575, A44

Gil de Paz A., et al., 2007, The Astrophysical Journal Supplement Series, 173, 185

Gilli R., Maiolino R., Marconi A., Risaliti G., Dadina M., Weaver K., Colbert E., 2000, Astronomy & Astrophysics, 355, 485

Gilli R., Calura F., D'Ercole A., Norman C., 2017, Astronomy & Astrophysics, 603, A69

Glazebrook K., et al., 2004, Nature, 430, 181

Gofford J., Reeves J. N., Tombesi F., Braito V., Turner T. J., Miller L., Cappi M., 2013, Monthly Notices of the Royal Astronomical Society, 430, 60

González-Alfonso E., et al., 2017, The Astrophysical Journal, 836, 11

Gowardhan A., et al., 2018, The Astrophysical Journal, 859, 35

Greene J. E., Zakamska N. L., Smith P. S., 2012, The Astrophysical Journal, 746, 86

Gunn J. E., Gott J. Richard I. I. I., 1972, The Astrophysical Journal, 176, 1

Guth A. H., 1981, Physical Review D, 23, 347

Häring N., Rix H.-W., 2004, The Astrophysical Journal Letters, 604, L89

Harrison E., 1970, Physical Review D, 1, 2726

Harrison C. M., 2017, Impact of supermassive black hole growth on star formation (arXiv:1703.06889), doi:10.1038/s41550-017-0165

Harrison C., Alexander D., Mullaney J., Swinbank A., 2014, Monthly Notices of the Royal Astronomical Society, 441, 3306

Harrison C., et al., 2016, Monthly Notices of the Royal Astronomical Society, 456, 1195

Harrison C., Costa T., Tadhunter C., Flütsch A., Kakkad D., Perna M., Vietri G., 2018, Nature Astronomy, 2, 198

Heckman T. M., Best P. N., 2014, Annual Review of Astronomy and Astrophysics, 52, 589

Heckman T. M., Armus L., Miley G. K., 1990, The Astrophysical Journal Supplement Series, 74, 833

Heckman T. M., Kauffmann G., Brinchmann J., Tremonti C., White S. D. M., Charlot S., Tremonti C., White S. D. M., 2004, The Astrophysical Journal, 613, 109

Heckman T. M., Alexandroff R. M., Borthakur S., Overzier R., Leitherer C., 2015, The Astrophysical Journal, 809

Hernquist L., 1990, The Astrophysical Journal, 356, 359

Herrera-Camus R., et al., 2019, The Astrophysical Journal, 871, 37

Herrera-Camus R., et al., 2020, Astronomy & Astrophysics, 635, A47

Hickox R. C., Alexander D. M., 2018, Annual Review of Astronomy and Astrophysics, 56, 625

Ho L., Filippenko A., Sargent W., 1993, The Astrophysical Journal, 417, 63

Högbom J., 1974, Astronomy and Astrophysics Supplement, 15, 417

Holt J., Tadhunter C., Morganti R., Emonts B., 2011, Monthly Notices of the Royal Astronomical Society, 410, 1527

Hoopes C. G., et al., 2005, The Astrophysical Journal, 619, L99

Hubble E., 1926, The Astrophysical Journal, 64, 321

Hubble E., 1936, Realm of the Nebulae

Husemann B., Scharwächter J., Bennert V., Mainieri V., Woo J. H., Kakkad D., 2016, Astronomy & Astrophysics, 594, A44

Husemann B., et al., 2019, Astronomy & Astrophysics, 627, A53

Ilbert O., et al., 2013, Astronomy and Astrophysics, 556, A55

Imanishi M., Saito Y., 2014, The Astrophysical Journal, 780, 106

Imanishi M., Nakanishi K., Izumi T., 2016, The Astrophysical Journal, 825, 44

Ishibashi W., Fabian A., 2012, Monthly Notices of the Royal Astronomical Society, 427, 2998

Ishibashi W., Fabian A. C., 2015, Monthly Notices of the Royal Astronomical Society, 451, 93

Ishibashi W., Fabian A. C., 2016, Monthly Notices of the Royal Astronomical Society, 457, 2864

Ishibashi W., Fabian A., Canning R., 2013, Monthly Notices of the Royal Astronomical Society, 431, 2350

Ishibashi W., Banerji M., Fabian A. C., 2017, Monthly Notices of the Royal Astronomical Society, 469, 1496

Ishibashi W., Fabian A. C., Maiolino R., 2018, Monthly Notices of the Royal Astronomical Society, 476, 512

Ivison R. J., et al., 2010, Monthly Notices of the Royal Astronomical Society, 402, 245

Iwasawa K., et al., 2011, Astronomy & Astrophysics, 529, A106

Jahnke K., Macciò A. V., 2011, The Astrophysical Journal, 734, 92

Janssen A. W., et al., 2016, The Astrophysical Journal, 822, 1

Jeans J., 1902, Philosophical Transactions of the Royal Society of London Series A, 199, 1

Kakkad D., et al., 2016, Astronomy and Astrophysics, 592, A148

Kakkad D., et al., 2020, Astronomy & Astrophysics, 642, A147

Kartaltepe J. S., et al., 2010, The Astrophysical Journal, 721, 98

Kauffmann G., et al., 2003, Monthly Notices of the Royal Astronomical Society, 346, 1055

Kelly B. C., 2007, The Astrophysical Journal, 665, 1489

Kennicutt R. C., 1998, The Astrophysical Journal, 498, 541

Kennicutt R. C., Evans N. J., 2012, Annual Review of Astronomy and Astrophysics, 50, 531

Kewley L., Dopita M., Sutherland R., Heisler C., Trevena J., 2001, The Astrophysical Journal, 556, 121

Kewley L. J., Groves B., Kauffmann G., Heckman T., 2006, Monthly Notices of the Royal Astronomical Society, 372, 961

King A. R., 2010, Monthly Notices of the Royal Astronomical Society, 402, 1516

King A., Pounds K., 2015, Annual Review of Astronomy and Astrophysics, 53, 115

King A. R., Zubovas K., Power C., 2011, Monthly Notices of the Royal Astronomical Society: Letters, 415

Kormendy J., Ho L., 2013, Annual Review of Astronomy and Astrophysics, 51, 511

Koudmani S., Sijacki D., Bourne M. A., Smith M. C., 2019, Monthly Notices of the Royal

Astronomical Society, 484, 2047
Kumari N., Maiolino R., Belfiore F., Curti M., 2019, Monthly Notices of the Royal Astronomical Society, 485, 367
Lacy M., Croft S., Fragile C., Wood S., Nyland K., 2017, The Astrophysical Journal, 838, 146
Laha S., Guainazzi M., Piconcelli E., Gand hi P., Ricci C., Ghosh R., Markowitz A. G., Bagchi J., 2018, The Astrophysical Journal, 868, 10
Leavitt H. S., 1908, Annals of Harvard College Observatory, 60, 87
Leroy A. K., et al., 2015, The Astrophysical Journal, 814, 83
Levenberg K., 1944, Quarterly of Applied Mathematics, 2, 164
Licquia T. C., Newman J. A., 2015, The Astrophysical Journal, 806, 96
Liddle A. R., 2007, Monthly Notices of the Royal Astronomical Society, 377, L74
Lonsdale C., Farrah D., Smith H., 2006, Ultraluminous Infrared Galaxies. p. 285, doi:10.1007/3-540-30313-8_9
López-Corredoira M., Allende Prieto C., Garzón F., Wang H., Liu C., Deng L., 2018, Astronomy and Astrophysics, 612, L8
Lovell M. R., et al., 2018, Monthly Notices of the Royal Astronomical Society, 481, 1950
Lutz D., et al., 2020, Astronomy & Astrophysics, 633, A134
Madau P., Dickinson M., 2014, Annual Review of Astronomy and Astrophysics, 52, 415
Madau P., Ferguson H. C., Dickinson M. E., Giavalisco M., Steidel C. C., Fruchter A., 1996, Monthly Notices of the Royal Astronomical Society, 283, 1388
Magorrian J., et al., 1998, The Astronomical Journal, 115, 2285
Maiolino R., Rieke G., 1995, The Astrophysical Journal, 454, 95
Maiolino R., et al., 2012, Monthly Notices of the Royal Astronomical Society: Letters, 425
Maiolino R., et al., 2017, Nature, 544, 202
Mannucci F., Pozzetti L., Thompson D., Oliva E., Baffa C., Comoretto G., Gennari S., Lisi F., 2002, Monthly Notices of the Royal Astronomical Society, 329, 57
Marconi A., Risaliti G., Gilli R., Hunt L. K., Maiolino R., Salvati M., 2004, Monthly Notices of the Royal Astronomical Society, 351, 169
Marquardt D. W., 1963, Journal of the Society for Industrial and Applied Mathematics, 11, 431
Masters D., Faisst A., Capak P., 2016, The Astrophysical Journal, 828, 18
Matthews T. A., Sandage A. R., 1963, The Astrophysical Journal, 138, 30
McConnell N. J., Ma C.-P., 2013, The Astrophysical Journal, 764, 184
McIntosh D. H., et al., 2005, The Astrophysical Journal, 632, 191
McMullin J. P., Waters B., Schiebel D., Young W., Golap K., 2007, Astronomical Data Analysis Software and Systems XVI, 376, 127
McNamara B. R., Nulsen P. E. J., 2007, Annual Review of Astronomy and Astrophysics, 45,

117
McNamara B. R., Nulsen P. E. J., 2012, New Journal of Physics, 14, 055023
Merloni A., 2004, Monthly Notices of the Royal Astronomical Society, 353, 1035
Michiyama T., et al., 2018, The Astrophysical Journal, 868, 95
Miller C. J., Nichol R. C., Gomez P. L., Hopkins A. M., Bernardi M., 2003, The Astrophysical Journal, 597, 142
Mingozzi M., et al., 2019, Astronomy & Astrophysics, 622, A146
Mitra S., Davé R., Finlator K., 2015, Monthly Notices of the Royal Astronomical Society, 452, 1184
Monreal-Ibero A., Arribas S., Colina L., 2006, The Astrophysical Journal, 637, 138
Morganti R., Tadhunter C. N., Oosterloo T. A., 2005, Astronomy and Astrophysics, 444, L9
Morganti R., Holt J., Saripalli L., Oosterloo T., Tadhunter C., 2007, Astronomy & Astrophysics, 476, 735
Morganti R., Fogasy J., Paragi Z., Oosterloo T., Orienti M., 2013, Science, 341, 1082
Morganti R., Oosterloo T., Raymond Oonk J. B., Frieswijk W., Tadhunter C., 2015, Astronomy & Astrophysics, 580, A1
Morton D. C., 1991, The Astrophysical Journal Supplement Series, 77, 119
Moster B. P., Naab T., White S. D. M., 2013, Monthly Notices of the Royal Astronomical Society, 428, 3121
Mukherjee D., Sutherland R. S., Bicknell G. V., Wagner A. Y., Silk J., 2018, Monthly Notices of the Royal Astronomical Society, 479, 5544
Mulchaey J. S., 2000, Annual Review of Astronomy and Astrophysics, 38, 289
Mullaney J. R., Alexander D. M., Fine S., Goulding A. D., Harrison C. M., Hickox R. C., 2013, Monthly Notices of the Royal Astronomical Society, 433, 622
Murray N., Quataert E., Thompson T. A., 2005, The Astrophysical Journal, 618, 569
Muzzin A., et al., 2013, The Astrophysical Journal, 777, 18
Nan R., et al., 2011, International Journal of Modern Physics D, 20, 989
Nardini E., Risaliti G., Salvati M., Sani E., Watabe Y., Marconi A., Maiolino R., 2009, Monthly Notices of the Royal Astronomical Society, 399, 1373
Nardini E., Risaliti G., Watabe Y., Salvati M., Sani E., 2010, Monthly Notices of the Royal Astronomical Society, 405, 2505
Navarro J. F., Frenk C. S., White S. D. M., 1995, The Astrophysical Journal, 462, 563
Nayakshin S., 2014, Monthly Notices of the Royal Astronomical Society, 437, 2404
Nayakshin S., Zubovas K., 2012, Monthly Notices of the Royal Astronomical Society, 427, 372
Nelson D., et al., 2019, Monthly Notices of the Royal Astronomical Society, 490, 3234
Newville M., Stensitzki T., Allen D. B., Ingargiola A., 2014, LMFIT: Non-Linear Least-Square

Minimization and Curve-Fitting for Python, doi:10.5281/zenodo.11813

Nims J., Quataert E., Faucher-Giguère C.-A., 2015, Monthly Notices of the Royal Astronomical Society, 447, 3612

Oosterloo T., Raymond Oonk J., Morganti R., Combes F., Dasyra K., Salomé P., Vlahakis N., Tadhunter C., 2017, Astronomy & Astrophysics, 608, A38

Osterbrock D. E., Ferland G. J., 2006, Astrophysics of gaseous nebulae and active galactic nuclei

Peng Y., Maiolino R., Cochrane R., 2015, Nature, 521, 192

Pereira-Santaella M., et al., 2011, Astronomy & Astrophysics, 535, A93

Pereira-Santaella M., et al., 2016, Astronomy & Astrophysics, 594, A81

Pérez-Montero E., Contini T., 2009, Monthly Notices of the Royal Astronomical Society, 398, 949

Perna M., Lanzuisi G., Brusa M., Cresci G., Mignoli M., 2017, Astronomy & Astrophysics, 606, A96

Peterson B. M., 2006, The Broad-Line Region in Active Galactic Nuclei. Springer Berlin Heidelberg, Berlin, Heidelberg, pp 77–100, doi:10.1007/3-540-34621-X_3, https://doi.org/10.1007/3-540-34621-X{_}3

Pineda J., Langer W., Velusamy T., Goldsmith P., 2013, Astronomy and Astrophysics, 554, A103

Piqueras López J., Colina L., Arribas S., Alonso-Herrero A., 2013, Astronomy & Astrophysics, 553, A85

Planelles S., Schleicher D., Bykov A., 2015, Space Science Reviews, 188, 93

Puchwein E., Springel V., 2013, Monthly Notices of the Royal Astronomical Society, 428, 2966

Querejeta M., et al., 2016, Astronomy and Astrophysics, 593, A118

Ramos Almeida C., Acosta-Pulido J., Tadhunter C., González-Fernández C., Cicone C., Fernández-Torreiro M., 2019, Monthly Notices of the Royal Astronomical Society, 487, L18

Read J., Trentham N., 2005, Philosophical Transactions of the Royal Society of London Series A, 363, 2693

Rees M., Ostriker J., 1977, Monthly Notices of the Royal Astronomical Society, 179, 541

Renzini A., Peng Y.-j., 2015, The Astrophysical Journal Letters, 801, L29

Ricci C., et al., 2017, Nature, 549, 488

Richings A. J., Faucher-Giguère C. A., 2018, Monthly Notices of the Royal Astronomical Society, 474, 3673

Roberts-Borsani G., Saintonge A., 2019, Monthly Notices of the Royal Astronomical Society, 482, 4111

Rodríguez-Zaurín J., Arribas S., Monreal-Ibero A., Colina L., Alonso-Herrero A., Alfonso-Garzón J., 2011, Astronomy & Astrophysics, 527, A60

Rodríguez-Zaurín J., Tadhunter C. N., Rose M., Holt J., 2013, Monthly Notices of the Royal Astronomical Society

Rodriguez del Pino B., Arribas S., Piqueras López J., Villar-Martin M., Colina L., 2019, Monthly Notices of the Royal Astronomical Society, 486, 344

Rohlfs K., Wilson T., 2004, Tools of radio astronomy. Berlin, Heidelberg

Romanowsky A. J., Fall S. M., 2012, The Astrophysical Journal Supplement Series, 203, 17

Roos O., Juneau S., Bournaud F., Gabor J. M., 2015, Astrophysical Journal, 800

Rose M., Tadhunter C., Ramos Almeida C., Rodríguez Zaurín J., Santoro F., Spence R., 2017, Monthly Notices of the Royal Astronomical Society, 474, 128

Roussel H., et al., 2007, The Astrophysical Journal, 669, 959

Rupke D. S., Veilleux S., 2013, Astrophysical Journal, 768

Rupke D. S., Veilleux S., 2015, Astrophysical Journal, 801, 126

Rupke D. S., Veilleux S., Sanders D., 2005a, The Astrophysical Journal Supplement Series, 160, 87

Rupke D. S., Veilleux S., Sanders D., 2005b, The Astrophysical Journal Supplement Series, 160, 115

Rupke D. S., Gültekin K., Veilleux S., 2017, The Astrophysical Journal, 850, 40

Salak D., Nakai N., Hatakeyama T., Miyamoto Y., 2016, The Astrophysical Journal, 823, 68

Salim S., et al., 2007, The Astrophysical Journal Supplement Series, 173, 267

Salomé Q., Salomé P., Miville-Deschênes M. A., Combes F., Hamer S., 2017, Astronomy and Astrophysics, 608, A98

Sánchez-Blázquez P., et al., 2006, Monthly Notices of the Royal Astronomical Society, 371, 703

Sanders R. L., et al., 2015, The Astrophysical Journal, 816, 23

Sarzi M., et al., 2006, Monthly Notices of the Royal Astronomical Society, 366, 1151

Sarzi M., et al., 2010, Monthly Notices of the Royal Astronomical Society, 402, 2187

Savage B. D., Sembach K. R., 1996, Annual Review of Astronomy and Astrophysics, 34, 279

Schawinski K., et al., 2014, Monthly Notices of the Royal Astronomical Society, 440, 889

Schawinski K., Koss M., Berney S., Sartori L. F., 2015, Monthly Notices of the Royal Astronomical Society, 451, 2517

Schechter P., 1976, The Astrophysical Journal, 203, 297

Scholtz J., et al., 2020, Monthly Notices of the Royal Astronomical Society, 492, 3194

Selina R. J., et al., 2018, in Proceedings of the SPIE. p. 107001O (arXiv:1806.08405), doi:10.1117/12.2312089

Seyfert C. K., 1943, The Astrophysical Journal, 97, 28

Shankar F., Weinberg D. H., Miralda-Escudé J., 2009, The Astrophysical Journal, 690, 20

Shimizu T. T., et al., 2019, Monthly Notices of the Royal Astronomical Society, 490, 5860

Silk J., 2013a, Astrophysical Journal

Silk J., 2013b, The Astrophysical Journal, 772, 112

Silk J., Mamon G. A., 2012, Research in Astronomy and Astrophysics, 12, 917

Silk J., Rees M., 1998, Astronomy and Astrophysics, 331, L1

Skrutskie M. F., et al., 2006, The Astronomical Journal, 131, 1163

Slater R., et al., 2019, Astronomy and Astrophysics, 621, A83

Solomon P. M., Vanden Bout P. A., 2005, Annual Review of Astronomy and Astrophysics, 43, 677

Soltan A., 1982, Monthly Notices of the Royal Astronomical Society, 200, 115

Somerville R. S., Popping G., Trager S. C., 2015, Monthly Notices of the Royal Astronomical Society, 453, 4337

Speagle J., Steinhardt C., Capak P., Silverman J., 2014, The Astrophysical Journal Supplement Series, 214, 15

Springel V., et al., 2005, Nature, 435, 629

Springel V., Frenk C. S., White S. D., 2006, Nature, 440, 1137

Straatman C. M., et al., 2014, The Astrophysical Journal Letters, 783, L14

Strateva I., et al., 2001, The Astronomical Journal, 122, 1861

Sturm E., et al., 2011,] 10.1088/2041-8205/733/1/L16

Sun A.-L., Greene J. E., Zakamska N. L., Nesvadba N. P. H., 2014, The Astrophysical Journal, 790, 160

Tadhunter C., Morganti R., Rose M., Oonk J., Oosterloo T., 2014, Nature, 511, 440

Takeuchi T. T., Buat V., Iglesias-Páramo J., Boselli A., Burgarella D., 2005, Astronomy & Astrophysics, 432, 423

Taylor E. N., et al., 2011, Monthly Notices of the Royal Astronomical Society, 418, 1587

Tegmark M., Silk J., Rees M. J., Blanchard A., Abel T., Palla F., 1997, The Astrophysical Journal, 474, 1

Thompson T. A., Quataert E., Murray N., 2005, The Astrophysical Journal, 630, 167

Thompson T. A., Fabian A. C., Quataert E., Murray N., 2015, Monthly Notices of the Royal Astronomical Society, 449, 147

Tombesi F., Tazaki F., Mushotzky R., Ueda Y., Cappi M., Gofford J., Reeves J., Guainazzi M., 2014, Monthly Notices of the Royal Astronomical Society, 443, 2154

Tombesi F., Meléndez M., Veilleux S., Reeves J. N., González-Alfonso E., Reynolds C. S., 2015, Nature, 519, 436

Trussler J., Maiolino R., Maraston C., Peng Y., Thomas D., Goddard D., Lian J., 2020, Monthly Notices of the Royal Astronomical Society, 491, 5406

Ueda Y., Akiyama M., Ohta K., Miyaji T., 2003, The Astrophysical Journal, 598, 886

Urry C. M., Padovani P., 1995, Publications of the Astronomical Society of the Pacific, 107, 803

Vayner A., Wright S. A., Murray N., Armus L., Larkin J. E., Mieda E., 2017, The Astrophysical Journal, 851, 126

Veilleux S., Kim D., Sanders D. B., 2002, The Astrophysical Journal Supplement Series, 143, 315

Veilleux S., Cecil G., Bland-Hawthorn J., 2005, Annual Review of Astronomy and Astrophysics, 43, 769

Veilleux S., et al., 2009, The Astrophysical Journal Supplement Series, 182, 628

Veilleux S., Bolatto A., Tombesi F., Meléndez M., Sturm E., González-Alfonso E., Fischer J., Rupke D. S. N., 2017, The Astrophysical Journal, 843, 18

Venturi G., et al., 2018, Astronomy & Astrophysics, 619, A74

Véron-Cetty M.-P., Véron P., 2010, Astronomy and Astrophysics, 518, A10

Vijayan A., Kim C.-G., Armillotta L., Ostriker E. C., Li M., 2020, The Astrophysical Journal, 894, 12

Villar-Martín M., Emonts B., Humphrey A., Cabrera Lavers A., Binette L., 2014, Monthly Notices of the Royal Astronomical Society, 440, 3202

Vogelsberger M., et al., 2014, Monthly Notices of the Royal Astronomical Society, 444, 1518

Volonteri M., 2012, Science, 337, 544

Walch S., Naab T., 2015, Monthly Notices of the Royal Astronomical Society, 451, 2757

Walter F., et al., 2017, The Astrophysical Journal, 835, 265

Wang X., Loeb A., 2018, New Astronomy, 61, 95

Weilbacher P. M., et al., 2020, arXiv e-prints, p. arXiv:2006.08638

Weller J., Ostriker J., Bode P., Shaw L., 2005, Monthly Notices of the Royal Astronomical Society, 364, 823

Werner N., McNamara B., Churazov E., Scannapieco E., 2019, Space Science Reviews, 215, 5

Westmoquette M., Exter K., Christensen L., Maier M., Lemoine-Busserolle M., Turner J., Marquart T., 2009

Westmoquette M., Smith L., Gallagher J.S. 2011, Monthly Notices of the Royal Astronomical Society, 414, 3719

White S., Rees M., 1978, Monthly Notices of the Royal Astronomical Society, 183, 341

Woo J.-H., et al., 2010, The Astrophysical Journal, 716, 269

Woo J.-H., Bae H.-J., Son D., Karouzos M., 2016, The Astrophysical Journal, 817, 108

Woo J.-H., Son D., Bae H.-J., 2017, The Astrophysical Journal, 839, 120

Yamada S., Ueda Y., Oda S., Tanimoto A., Imanishi M., Terashima Y., Ricci C., 2018, The Astrophysical Journal, 858, 106

York D. G., et al., 2000, The Astronomical Journal, 120, 1579

Yu S., et al., 2020, Monthly Notices of the Royal Astronomical Society, 494, 1539

Yun M. S., Reddy N. A., Condon J. J., 2001, The Astrophysical Journal, 554, 803

Zeldovich Y. B., 1972, Monthly Notices of the Royal Astronomical Society, 160, 1P

Zhang Z., Shi Y., Rieke G. H., Xia X., Wang Y., Sun B., Wan L., 2016, The Astrophysical Journal Letters, 819, 0

Zibetti S., Charlot S., Rix H.-W., 2009, Monthly Notices of the Royal Astronomical Society, 400, 1181

Zschaechner L. K., et al., 2016, The Astrophysical Journal, 832, 1

Zubovas K., 2015, Monthly Notices of the Royal Astronomical Society, 451, 3627

Zubovas K., King A., 2012, The Astrophysical Journal, 745, L34

Zubovas K., Nayakshin S., Sazonov S., Sunyaev R., 2013a, Monthly Notices of the Royal Astronomical Society, 431, 793

Zubovas K., Nayakshin S., King A., Wilkinson M., 2013b, Monthly Notices of the Royal Astronomical Society, 433, 3079

Zubovas K., Sabulis K., Naujalis R., 2014, Monthly Notices of the Royal Astronomical Society, 442, 2837

Zwicky F., 1937, The Astrophysical Journal, 86, 217

da Cunha E., et al., 2013, The Astrophysical Journal, 766, 13